UNIVERSITY OF CALIFORNIA

Los Angeles

Dynamic Stresses in Foundation Soils from Soil-Structure Interaction

A dissertation submitted in partial satisfaction of the requirements for the degree of Doctor of Philosophy in Civil and Environmental Engineering

by

Bahareh Heidarzadeh

2016

ABSTRACT OF THE DISSERTATION

Dynamic Stresses in Foundation Soils

from Soil-Structure Interaction

by

Bahareh Heidarzadeh

Doctor of Philosophy in Civil and Environmental Engineering

University of California, Los Angeles, 2016

Professor Jonathan P. Stewart, Co-Chair

Professor George Mylonakis, Co-Chair

This research concerns the impacts of Soil-Structure Interaction (SSI) on the seismic stress demands in soil materials beneath the foundation, referred to as 'foundation soils'. Engineering procedures for evaluation of these stress demands are needed for a variety of applications including ground failure evaluation in foundation soils and possible impacts of SSI on buried structures such as pipelines. Conventional engineering practice typically ignores SSI during evaluation of the seismic stress demands in foundation soils based on the perception that this demand is dominated by wave propagation from site response. The goals of this study are to show how the presence of a structure affects wave propagation in the vicinity of the foundation due to SSI and to propose rigorous procedures by which to assess these demands due to vertical

or horizontal point loads, line loads, or arbitrary combinations of these acting within a foundation area.

Following an exhaustive literature review, I find that while integral transform methods exist to evaluate the response of foundation soils to surface loads, such approaches have two major limitations: (1) the resulting equations are so complex that closed form solutions for stresses produced by harmonic surface loads are absent in the literature, despite over a century of research in this subject; and (2) the resulting equations can be solved numerically, but only one such study has been conducted, and that work has limited practical applicability.

Accordingly, I solve the governing equations numerically for harmonically applied surface loads (horizontal and vertical, point and line) acting on a visco-elastic halfspace using the Boundary Element Method via a well-verified software platform (ISoBEM). The results are interpreted within a framework derived from dimensional analysis considerations, specifically applying the Buckingham π theorem to determine the dimensionless fundamental parameters applicable to these problems. I demonstrate that induced stresses normalize using appropriate dimensionless variables, and that these normalized stresses have clear dependencies on dimensionless frequency, location within the soil, and soil Poisson's ratio. Moreover, I demonstrate that phase angle is associated with wave travel times from source to the point of interest in the foundation soil, and as such varies with aperture angle due to variations in body and surface wave radiation patterns from horizontal and vertical surface loads.

Results for the amplitude and phase of all relevant stress components are presented in dimensionless graphical forms and the effects of fundamental parameters for each case are discussed. For the case of loads applied to rigid surface foundations, I evaluate the distribution of

normal and shear stresses at the base of the foundations. Finally, for the flexible foundation case I have developed and verified a numerical code that applies superposition principles to combine soil stress demands associated with uniformly distributed surface loads.

The dissertation of Bahareh Heidarzadeh is approved.

Scott J. Brandenberg

Ertugrul Taciroglu

Anne Lemnitzer

George Mylonakis, Committee Co-Chair

Jonathan P. Stewart, Committee Co-Chair

University of California, Los Angeles

2016

To my loving parents

CONTENTS

LIST OF FIGURES

LIST OF TABLES

ACKNOWLEDGMENTS

I would like to express my deepest gratitude to my advisor and co-advisor, Jonathan P. Stewart and George Mylonakis, for their excellent guidance, caring, and patience. They provided me with an excellent atmosphere for doing research all these years. They taught me how to question thoughts and express ideas. Their patience and support helped me overcome many crisis situations and finish this dissertation. I hope that one day I would become as good an advisor to my students as Jonathan and George have been to me.

For this dissertation, I would like to thank my defense committee members: Scott Brandenberg, Ertugrul Taciroglu, and Anne Lemnitzer for their time, interest, helpful comments, and insightful questions.

I am also grateful to Dimitri Beskos and Demosthenes Polyzos of University of Patras, and Stephanos Tsinopoulos of Technological Educational Institute of Patras, for providing the full version of ISoBEM and supporting me in the use of the software. I thank Farhang Ostadan, Eduardo Kausel of University of Massachusetts Institute of Technology, and Winfried Schepers for correspondence related to this topic that advanced the work. I would also like to thank Tajendra Vir Singh for helping me using the Hoffman2 Cluster at UCLA.

This research was supported in part by grant from the National Science Foundation with award number CMMI 1208170. Partial support was also provided by the UCLA Civil & Environmental Engineering Department. This support is gratefully acknowledged.

I would like to express my deepest gratitude to Saeed and Elnaz. For not just sharing their scientific knowledge with me which helped me a lot in this work, but for proving to be my true friends for life.

Most importantly, I would like to thank my parents Mah Monir and Mohammad Hassan. This research could have not been possible without their support. They have been the constant source of love, concern, support and strength throughout my life.

BIOGRAPHICAL SKETCH

Bahareh Heidarzadeh earned her Bachelor's degree in 2008 at Tehran Polytechnic in Iran, and her Master's degree in 2010 at the University of California, Los Angeles. She is a member of the American Society of Civil Engineers (ASCE), the Earthquake Engineering Research Institute (EERI), and the California Geoprofessionals Association (CalGeo). She earned her EIT in the state of California in 2010 (No. 139550). She has been a Teaching Assistant at UCLA for graduate course of Ground Motion Characterization (2011) and undergraduate courses of Advanced Geotechnical Design (2012) and Design of Foundations and Earth Structures (2015). She has worked as a student intern at Fugro Consultant Inc, (2012). She has been a graduate student researcher at UCLA from April 2009 to March 2014.

Her published work is listed below:

Heidarzadeh, B., Mylonakis, G. Stewart, J.P, (2015). Stresses beneath Dynamically Applied Vertical Point Loads, presented at 6th International Conference on Earthquake Geotechnical Engineering, New Zealand, 2015.

1 Introduction

Earthquake ground shaking induces strains and stresses in soil materials as a result of the wave propagation from site response. In the absence of an overlying structure, these seismic demands on the soil materials are considered free-field. Such demands on soil materials can cause pore pressure generation and associated losses in shear strength and stiffness. The presence of a structure modifies the characteristics of wave propagation in the vicinity of the foundation due to soil-structure interaction (SSI), and hence also modifies local demands on soil elements that may or may not trigger various forms of ground failure.

The general field of SSI is in a period of transition. As documented by NIST (2012), while SSI has traditionally been ignored in analysis of the seismic response of structures, the increasing application of Performance Based Earthquake Engineering (PBEE) procedures in structural evaluations has motivated increased consideration of SSI as well. These applications are most often in the context of nonlinear static procedures and nonlinear response history analyses. The procedures employed concern SSI effects on ground motions and the flexibility and energy dissipation at the foundation-soil interface. While procedures for these analyses have reached a level of maturity that allows them to be applied in practice, what remains much more poorly understood is the effect of SSI on stresses in foundation soil.

This introduction is organized to provide context for the research presented in this dissertation by answering the following questions:

1. What is SSI?
2. How are SSI effects accounted for in an analysis of seismic structural response?
3. How are SSI effects accounted for in the seismic response of foundation soils?

1.1 WHAT IS SOIL-STRUCTURE INTERACTION?

Considering soil and structure as independent systems, soil-structure interaction can be described as a *system of systems* which creates more complexity than simply the sum of constituent systems. In other words, in SSI problems, the motion of the soil affects the structural response and the motion of the structure modifies the soil response and neither the structural response nor the soil response, are independent of each other.

From the structural standpoint, SSI effects reflect the difference between the actual response of the structure and the response for the theoretical, rigid base condition where the motions at the base of the structure and on the ground away from it match. In other words, there is neither flexibility at the foundation-soil interface, nor damping in case of a rigid-base structure. The presence of the foundation for a structure causes the ground motions on the foundation to deviate from free-field motions due to averaging of incoherent wave fields, which is referred to as kinematic effects, and the relative foundation-free field displacements and rotations associated with structure and foundation inertia. The inertial response, in turn, is affected by the flexibility and damping at the foundation soil interface. Therefore in this context, the SSI analysis involves evaluation of ground shaking demands at the base of structures in consideration of realistic inputs and analysis of structural response in consideration of the complex interface behavior.

From the foundation soil standpoint, SSI effects account for the difference between the actual stress and strain demands placed upon foundation soil and the corollary demands from free-field wave propagation. In this case, the SSI effect describes how the presence of a structure causes the characteristics of wave propagation and associated stress/strains to deviate from the free-field condition as a result of aforementioned kinematic and inertial effects.

1.2 SOIL STRUCTURE INTERACTION EFFECTS ON SEISMIC RESPONSE OF STRUCTURES

To properly address the seismic response of structure, one approach is to use the finite element method to model the structure, foundation soil, and portions of the surrounding soil media, which is known as direct modeling. As presented in Figure 1.1, in this approach, appropriate boundary conditions should be applied to truncate the discretized domain such that it properly accounts for the semi-infinite soil domain. Despite difficulties in formulating appropriate boundary conditions and the requirement for a large number of input parameters for soil constitutive models, the direct approach is increasingly being used in unique projects involving complex structural configurations such as the Transbay Terminal in San Francisco (Ellison et al., 2015).

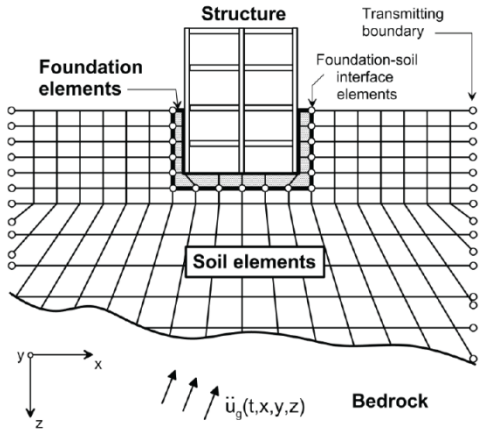

Figure 1.1: Schematic illustration of a direct analysis of soil-structure interaction using continuum modeling by finite elements- Adapted from NIST (2012)

The substructure approach, as shown in Figure 1.2, breaks the structure-foundation-soil system into several parts to capture various effects of SSI on the seismic response of structures (NIST, 2012). This approach also accounts for the modified input motion at the soil-foundation interface, which is termed a Foundation Input Motion (FIM).

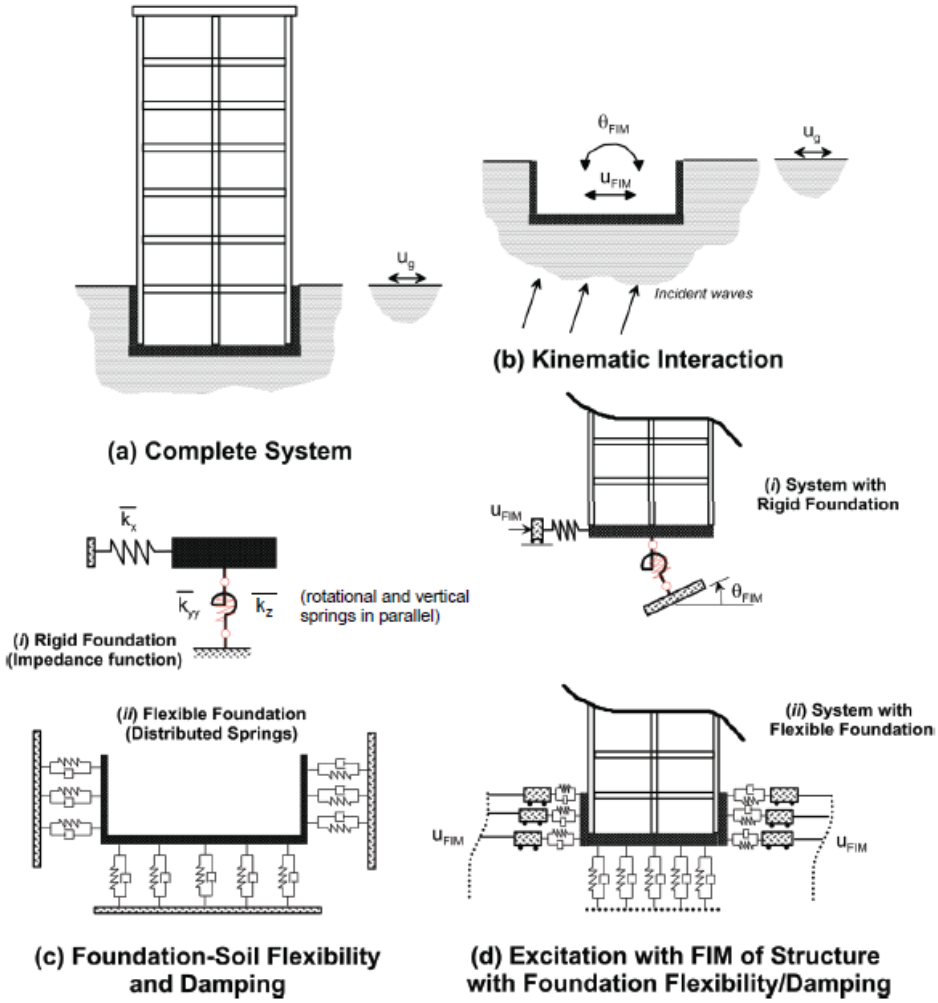

Figure 1.2: Schematic illustration of a substructure approach to analysis of soil-structure interaction using either: (i) rigid foundation; or (ii) flexible foundation assumptions- Adapted from NIST (2012)

Figure 1.3 illustrates inertial interaction effects through a single-degree-of-freedom (SDOF) system. Figure 1.3(a) shows a fixed-based SDOF system with height h, period T and

damping ratio β, which ignores SSI effects. Figure 1.3(b) shows the deformable nature of soil-foundation system by using vertical, horizontal, and rotational springs, (k_x, k_z, k_{yy}).

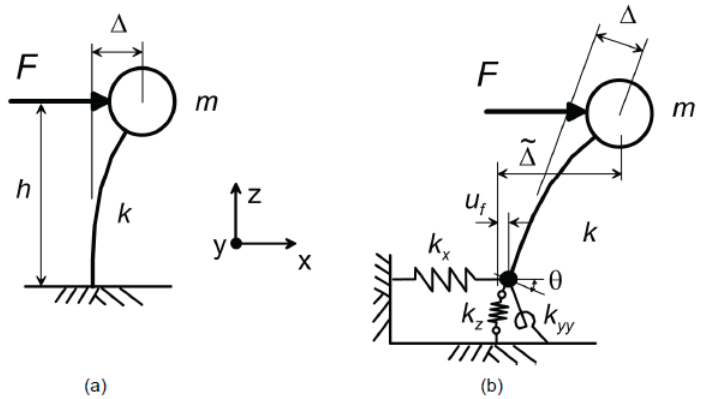

Figure 1.3: Schematic illustration of deflections caused by force applied to: (a) fixed-based structure; and (b) structure with vertical, horizontal, and rotational flexibility at its base- Adapted from NIST (2012)

As observed in this figure, inertial interaction introduces base flexibility, which lengthens the SDOF oscillator period. The ratio of the flexible-to-fixed-base period is known as period lengthening, $\tilde{T}/T$. Analysis of period lengthening is developed by Jennings and Bielak (1973) and Veletsos and Meek (1974), as shown in Equation 1.1.

$$\frac{\tilde{T}}{T} = \sqrt{1 + \frac{k}{k_x} + \frac{kh^2}{k_{yy}}} \tag{1.1}$$

It is shown in NIST (2012) that for a rectangular foundation, the period lengthening is controlled by following dimensionless parameters:

$$\frac{h}{V_s T}, \frac{h}{B}, \frac{B}{L}, \frac{m}{\rho_s 4BLh}, \text{and } \nu$$

where B and L refer to the half-width and half-length of the rectangular foundation, and respectively, h, m, ρ, and ν represent the distance from the base to the center of mass in the

first mode shape, the effective modal mass, soil mass density, and the soil Poisson's ratio. These parameters are discussed in detail in NIST (2012).

Aside from period lengthening, foundation damping is a significant contributor to the system behavior. Foundation damping derives from soil hysteretic and radiation damping. The damping of the flexible-base system as a whole includes contributions from foundation damping as well as damping in the super structure (e.g., Veletsos and Nair, 1975, Bielak 1976).

Figure 1.4 illustrates the effect of inertial SSI on force-based seismic demand (i.e., base shear). For the long period structures for which the slope of the response spectrum with respect to period is negative, inertial SSI typically reduces the base shear. At short periods, where the spectrum slope is ascending, SSI can increase the base shear demand.

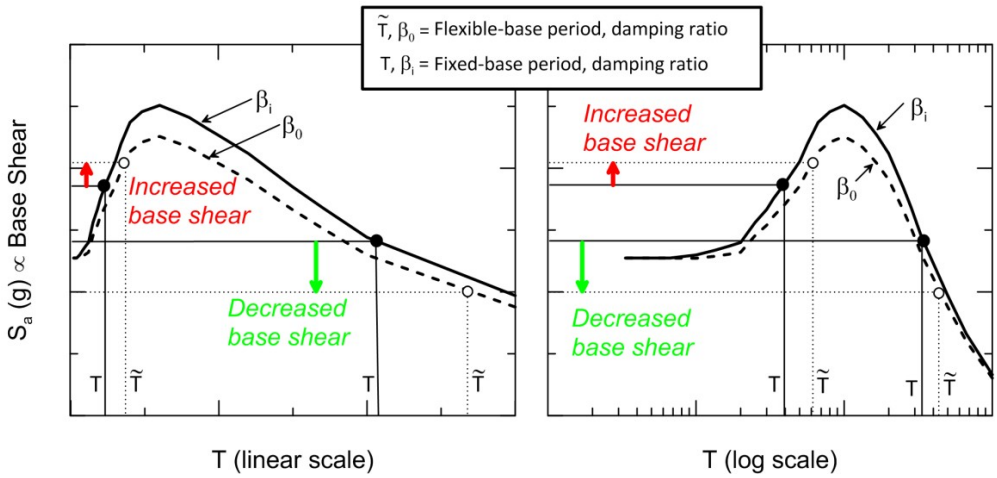

Figure 1.4: Effect of inertial SSI on spectral acceleration (base shear) associated with period lengthening and change in damping- Adapted from NIST (2012)

In addition, kinematic interaction causes deviation of FIM at the base of the foundation from free-field motions due to base slab averaging and embedment effects. Base slab averaging refers to the phenomenon in which stiffness and strength of the foundation system average out the spatially variable ground motions within the building envelop. Embedment effects also cause ground motion reduction with depth below the free-surface. To properly account for kinematic

SSI effects, frequency dependent transfer functions should be used to modify the free-field motion into a suitable FIM. Formulations that account for base slab averaging and embedment effects on this transfer function are given in NIST (2012).

NIST (2012) summarizes the required steps for a complete SSI evaluation in the assessment of the seismic response of a structure:

1. Evaluation of free-field ground motion and soil material properties.
2. Evaluation of transfer function as the ratio of foundation to free-field motion in frequency domain in order to convert the free-field input motion to a suitable FIM.
3. Selection of sets of springs and dashpots to model the effects of stiffness and damping at the soil-foundation interface due to translational and rotational modes of foundation vibration.
4. Implementation of a response analysis of the combined system of structure-spring/dashpot system with excitation provided by the FIM.

1.3 SOIL STRUCTURE INTERACTION EFFECTS ON SEISMIC RESPONSE OF FOUNDATION SOIL

As discussed earlier, SSI effects have been typically investigated by consideration of their impact on the vibrating structure and its foundation. In this research, the question is turned around by asking – *what is the effect of the structure on the soil*? More specifically, the objective is to seek the impacts of SSI on the seismic stress demands in the soil materials beneath the foundation, referred to as 'foundation soils'. As schematically shown in Figure 1.5, the seismic stress demand of the overall foundation soil is obtained by the proper combination of stress induced in

the soil mass due to the vibrating structure and its foundation (SSI problem) and the stresses associated with site response if the structure were not present (free-field problem).

There are many examples of infrastructure that could be affected by local ground failure in foundation soils, including various structures (buildings, bridges), earth structures such as levees, and buried structures such as pipelines. Among these, SSI-induced ground failure beneath building foundations is the most well documented, which has been attributed to liquefaction of granular soils and cyclic softening of cohesive soils (Bray and Stewart, 2000; Chu et al., 2008; Ashford et al., 2011, Cubrinovski et al., 2011). The levee problem is also of great interest. Levees are earth fills used to provide flood protection around water bodies (often rivers). Levees are often constructed on soft foundation soils that can be highly susceptible to ground failure from liquefaction, cyclic softening, and post-cyclic volumetric deformations associated with peats (Shafiee et al., 2015). Our concern in this research is not the ground failure mechanisms per se, but the stress demands associated with SSI that could potentially contribute to the triggering of ground failure associated with any applicable mechanism.

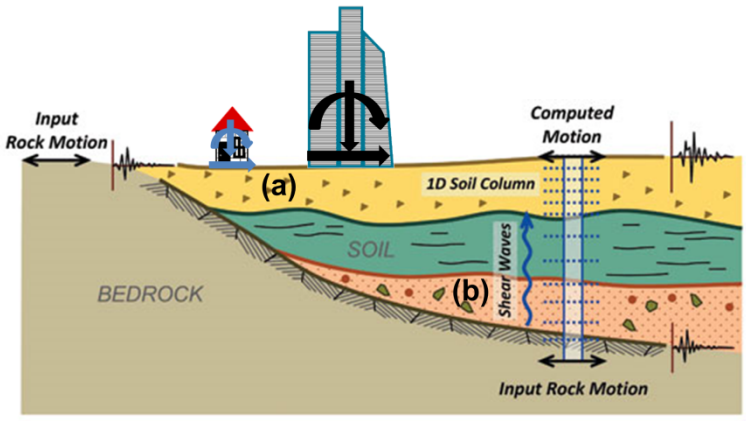

Figure 1.5: Seismic stress demand on foundation soil due to (a) vibrating structure and its foundation (SSI problem), and (b) upward propagating seismic waves (free-field problem) - Adapted from Nikolaou and Go (2009)

Engineering assessments of ground failure potential express seismic demands in the form of shear stresses or shear strains (e.g., Seed and Idriss, 1971; Dobry and Ladd, 1980). Of these, demand characterization in the form of stresses is more common because peak shear stresses can readily be related to peak horizontal ground accelerations. It is common to normalize the shear stress by the pre-shaking vertical effective stress to form the Cyclic Stress Ratio (CSR):

$$CSR = \frac{\tau_{hv}}{\sigma'_{v0}} \tag{1.2}$$

where τ_{hv} is shear stress on horizontal and vertical planes and σ'_{v0} is the pre-shaking vertical effective stress. These stresses are depicted graphically in Figure 1.6. Seed and Idriss (1971) compute CSR as:

$$CSR = 0.65 \frac{PHA}{g} \frac{\sigma_v}{\sigma'_{v0}} r_d(z) \tag{1.3}$$

where PHA is peak horizontal acceleration at the ground surface and σ_v is the total vertical stress. The r_d factors in Equation 1.3 are based on free-field ground response analyses, and as such CSR computed from Equation 1.3 only reflects free-field demands. The effects of a vibrating structure and its foundation on seismic stress demand (SSI problem) is ignored in this classical definition of seismic demands. As described further in Chapter 2, other than by performing relatively complex finite element analyses of structure-foundation-soil systems, there are no current methods for estimating stress demands from SSI. The principle objective of the present work is to develop such procedures.

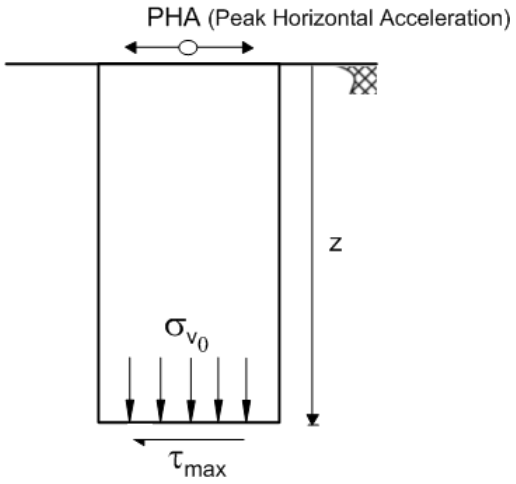

Figure 1.6: Schematic illustration of seismic stress demand in a rigid soil column due to 1-D propagating seismic waves (free-field problem)

1.4 RESEARCH OBJECTIVE AND SCOPE

The principal objective of the work presented in this dissertation was to study the problem of stress distribution in soil beneath a vibrating foundation, gain insights into the physical processes controlling these stresses, and devise practical procedures for estimating SSI-induced stress demands.

I investigated the use of boundary element methods as tools for analysis of dynamic stress fields in soil, and then applied these simulation procedures to problems with known solutions to verify the simulation results. I performed simulations using the verified code to evaluate dynamic stress fields in soils beneath foundations. As part of this process, vertical and horizontal cyclic foundation loads were applied in the form of both concentrated (point) loads and line loads. I then identified the principle factors governing foundation soil stress amplitudes and phasing in consideration of appropriate normalization procedures. I then presented the results of the stress computations in the form of dimensionless plots.

Using the verified code, I also performed simulations to evaluate the dynamic traction (stress) distributions directly beneath rigid foundations subject to cyclic loading. Results are

presented in the form of graphs as well as parametric equations. The devised stresses can then be converted to input surface loads applied to foundation soils to simulate the effects of vibration of a rigid foundation. I developed a tool in MATLAB for computing stresses produced by surficial loads with any arbitrary distribution across a defined foundation area. This computational tool applies the principles of superposition through integration of point and line load solutions developed as part of this research.

1.5 ORGANIZATION OF THE TEXT

This document is structured as follows: In Chapter 2, I provide an overview of the historical development of analytical expressions for the response of a solid medium to static and dynamic loads on or within the soil medium. Then, I present existing numerical solutions for evaluating the stress response due to dynamic point loads at the surface of a semi-infinite soil mass. Some shortcomings of those solutions for the present application are identified.

In Chapter 3, I begin by reviewing the Buckingham π theorem as the basis for normalization. This theorem is then applied to the static and dynamic problems of vertical and horizontal point loads applied on surface of a half-space to evaluate the fundamental dimensionless parameters. I then describe the numerical technique and the appropriate software that was selected for the analysis of stress demands beneath dynamically applies surface forces. I subsequently verify the results produces by this software by comparing to available solutions in the literature. Verification is also conducted for the normalization of the dynamic stress results with respect to proposed dimensionless parameters. The variations of the six components of the three-dimensional stress tensor with respect to the identified fundamental parameters are then investigated through suites of sensitivity analyses. Results for stress amplitudes are presented in

the form of stress bulbs. Time delays between surface loads and stresses are represented with phase shifts, which are also presented in a graphical form.

Chapter 4 is very similar to Chapter 3, except that vertical and horizontal point loads are replaced by corresponding line loads, representing the plane strain problem. In this case, results are provided for three components of the two-dimensional stress tensor.

In Chapter 5, I also perform simulations to evaluate the dynamic stress distributions directly beneath rigid foundations subject to cyclic loading. I present the results in the form of graphs as well as parametric equations. The devised stresses can then be converted to input surface loads applied to foundation soils to simulate the effects of vibration of a rigid foundation. Moreover, I apply the principle of superposition to fundamental dynamic stress solutions in order to obtain the resulting stress distributions in the soil medium due to surficial loads applied at different locations on the ground surface. The accuracy of the integration techniques is verified by comparing to the available solutions as well as the stress solutions obtained by direct modeling of distributed loads using the selected software package. The corresponding computational tools are implemented in Matlab. Finally, in Chapter 6, conclusions from the study are summarized and several recommendations for future work are presented.

.

2 Historical Development

Perhaps not many problems are more familiar, yet more complicated to solve to most engineers than the assessment of effects of an applied load onto body of material(s) modeled as a continuum. The early fundamental solutions to static-type problems were developed during the early 19th century (Kelvin 1848, Cerruti 1882, and Boussinesq 1885) by researchers being mostly interested in applied mathematics and physics. Over time, dynamic cases involving transient loads attracted many researchers mostly for seismological purposes (Stokes 1848, Lamb 1904). In fact, this group was more interested in finding the solution in terms of displacements due to any source on or within a full space semi-infinite half-space. In recent decades, the stresses induced by a source load have been the focus of investigations. Modern geotechnical engineers dealing with liquefaction-related analysis, transportation engineers studying the dynamic behavior of pavement structures under moving loads, and biomedical and bio-material engineers working on modeling of cutting force for surgical simulations (Peng and Zhou, 2013) are only a few groups working on assessment of stresses within an elastic continuum due to a surface load.

Although first developed mostly by mathematicians and applied physicists, the assessment of strains and stresses caused by loads applied onto the surface of an elastic continuum have proven to have value in engineering applications that likely far exceeds the early pioneers' imaginations. In this chapter, a brief review of solutions to various types of loading is presented with the purpose of summarizing fundamental developments and highlighting the level

of difficulty in obtaining analytical solutions, especially for dynamic loads. Detailed description of methodologies and derivation of solutions are beyond the scope of this work. The actual solutions in terms of equations and graphs are presented only for the cases to be used in Chapter 3 for verification purposes.

2.1 TERMINOLOGY, NOTATION AND DEFINITION

Full-space:

An idealization in which all the boundaries are infinitely far away. The medium under consideration is usually assumed to be perfectly homogeneous and isotropic.

Half-space:

A mathematical model in which only one planar boundary exists, all others being infinitely far away. The medium under consideration is usually assumed to be perfectly homogeneous and isotropic (Allaby and Allaby, 2008). Unless otherwise specified, in most of the developments provided in this chapter, the medium is a linear elastic, homogeneous, isotropic half-space. For simplicity, this medium is referred to as half-space throughout this work.

Cylindrical Coordinates:

Figure 2.1 shows the cylindrical coordinate system with respect to a Cartesian coordinate system. This coordinate system is widely used in geotechnical engineering, in cases where an axis of symmetry exists. The location of a point in cylindrical coordinates is defined by horizontal distance r from the origin, vertical distance z from the origin, and angle θ as measured from the x-axis. As shown in Figure 2.1, a new set of axes can also be defined as follows:

$\hat{\boldsymbol{r}}$: radial coordinate

$\hat{z}$: axial coordinate

$\hat{\theta}$: circumferential coordinate

However, it is more common in geotechnical practice to simply use r, z, and θ as shown in Figure 2.1 and that convention is followed here.

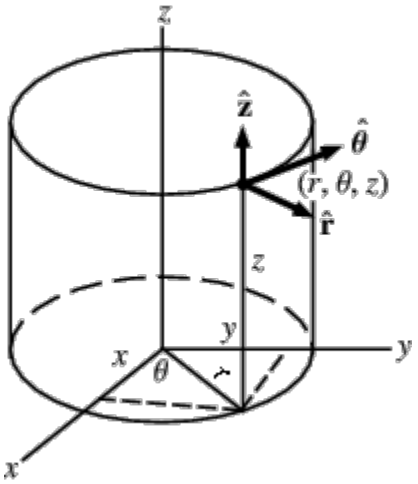

Figure 2.1 The cylindrical coordinates- adapted from Weisstein (2007)

Axisymmetric Formulation:

The basis of axisymmetric formulation is that all the functions defined in the problem are functions of r and z only, i.e. independent of the circumferential coordinate, θ. Therefore, three-dimensional problems are reduced to two-dimensional ones where, however, both hoop strain and stress (ε_θ and σ_θ) are nonzero, although angular displacement (u_θ) is zero (Hughes, 2012). The axisymmetric coordinate parameters are as follows:

$x_1 = r$: radial coordinate

$x_2 = z$: axial coordinate

$x_3 = \theta$: circumferential coordinate

With the constraint of $u_\theta = 0$, four nonzero components of stress and strain are expressed in equations 2.1 and 2.2.

$$\sigma = \begin{Bmatrix} \sigma_{11} \\ \sigma_{22} \\ \tau_{12} \\ \sigma_{33} \end{Bmatrix} = \begin{Bmatrix} \sigma_{rr} \\ \sigma_{zz} \\ \tau_{rz} \\ \sigma_{\theta\theta} \end{Bmatrix} \tag{2.1}$$

$$\varepsilon = \begin{Bmatrix} \varepsilon_{11} \\ \varepsilon_{22} \\ \varepsilon_{12} \\ \varepsilon_{33} \end{Bmatrix} = \begin{Bmatrix} \varepsilon_{rr} \\ \varepsilon_{zz} \\ \varepsilon_{rz} \\ \varepsilon_{\theta\theta} \end{Bmatrix} \tag{2.2}$$

Integral Transform:

In mathematics, integral transform is an operator that maps the function within the integrand, *f*, from its original domain into another function, *Tf*, in a target domain where manipulation and solving of the equation is much easier. The solution is then mapped back to the original domain by means of inverse integral transform. Each integral transform is specified by a choice of the function *K* of two variables, the kernel function or nucleus of the transform. Equations 2.3 and 2.4 show integral transform and inverse integral transform, respectively.

$$(Tf)(u) = \int_{t_1}^{t_2} K(t,u) f(t) dt \tag{2.3}$$

$$f(t) = \int_{u_1}^{u_2} K^{-1}(u,t)(\mathrm{T}(f(u))du \tag{2.4}$$

Among numerous integral transforms, Fourier transform, Hankel transform, and Laplace transform are generally the most applicable in the elasto-dynamics field. By means of equations

such as 2.3 and 2.4, the order of a partial differential equation is reduced by one, and an ordinary differential equation is transformed to an algebraic one. The difficulty typically lies in solving the inversion Equation 2.4 as shown later on.

Phase Angle:

In dynamic problems, the responses of the system, i.e. displacements and stresses, are complex numbers which can be described as either a pair of real and imaginary parts or as amplitudes and phase angles. The latter form is chosen in this research for the graphical presentation of stress response due to vertical and horizontal harmonic loading.

As shown in Figure 2.2 and Equation 2.5, the phase angle (ϕ) is the angle of a vector having length (r) with respect to the positive real axis for any complex number (z):

$$z = x + iy = r(\cos\phi + i\sin\phi) \tag{2.5}$$

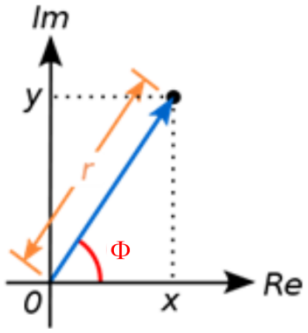

Figure 2.2: Phase angle definition

This coordinate system is known as Argand diagram in which angle ϕ is defined as:

$$\phi = \arg(z) = \begin{cases} \arctan(\frac{y}{x}) & \text{if } x>0 \\ \arctan(\frac{y}{x})+\pi & \text{if } x<0 \text{ and } y\geq 0 \\ \arctan(\frac{y}{x})-\pi & \text{if } x<0 \text{ and } y<0 \\ \frac{\pi}{2} & \text{if } x=0 \text{ and } y>0 \\ -\frac{\pi}{2} & \text{if } x=0 \text{ and } y<0 \\ \text{indeterminate} & \text{if } x=0 \text{ and } y=0 \end{cases} \tag{2.6}$$

It is important to note that the phase angle calculated by Equation 2.6 is called the wrapped phase angle, which is constrained to the range [$-\pi$ π]. However, the actual phase angle is continuous and may take any value within or outside of this range. In Equation 2.6, when the actual phase angle is not within the range [$-\pi$ π], the value is increased or decreased by multiples of 2π to keep it within this range. This procedure causes discontinuities in the phase diagram. The process of recovering the true, or unwrapped, value of phase angle involves adding or subtracting multiples of 2π. Phase unwrapping is a particularly challenging numerical problem for which various algorithms have been developed that can produce different results from the same input data. The challenges associated with this process, and a suggested algorithm, are discussed by Ghiglia and Pritt (1998).

2.2 KELVIN PROBLEM

The problem of static point load acting within a full-space, shown on Figure 2.3, was first solved by Lord Kelvin and published in a short paper (Kelvin, 1848). Kelvin's fundamental solution in modern terminology is also known as Green's function (Favata, 2012). The complete set of equations for both displacements and stresses in cylindrical coordinates can be found in Poulos and Davis (1974) and are partly obtainable by pure dimensional means. The dynamic counterpart

to Kelvin problem's was solved by George Stokes (1849) considering body waves of both types, i.e. longitudinal and transverse, radiating from the point source, yet not reflected body or surface waves as no boundary exists. The solution to this problem is known in closed-from in both time and frequency domains (Eringen and Shuhubi, 1975), being suggested as a fundamental solution in elastostatics and elastodynamics and implemented as a so-called *Boundary Element Method* (BEM) in recent years.

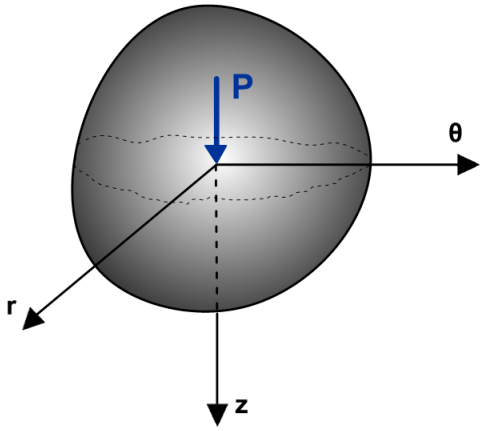

Figure 2.3 Kelvin problem

2.3 STATIC POINT LOAD ON HALF-SPACE

The problem of a vertical point load acting on the surface of a half-space is known in three-dimensional (3-D) and two-dimensional (2-D) forms as the Boussinesq problem and the Flamant problem, respectively. The Flamant problem also contains the horizontal point load on 2-D half-space, while the 3-D case of a horizontal point load is known as the Cerruti problem. The difficulty in solving them over the Kelvin problem lies in the need to satisfy a stress-free condition over the whole surface of the half-space, where the loads are applied.

2.3.1 Boussinesq Problem

Figure 2.4 illustrates the 3-D problem on the action of a static normal concentrated force on the surface of a half-space, which was first solved by Boussinesq (1885) for both displacement and stress fields. This problem has the axisymmetric property both in geometry and loading. Equations 2.7 to 2.10 show the solution to the stress field in cylindrical coordinates. This solution is used in Chapter 3 for validation purposes. In the following equations, P is the point load in units of force, z, r and R are distances shown in Figure 2.4 in units of length, and v is the Poisson's ratio. Variables σ_z, σ_r, σ_θ, and τ_{rz} are vertical, radial, hoop, and shear stresses in cylindrical (polar) coordinates, respectively.

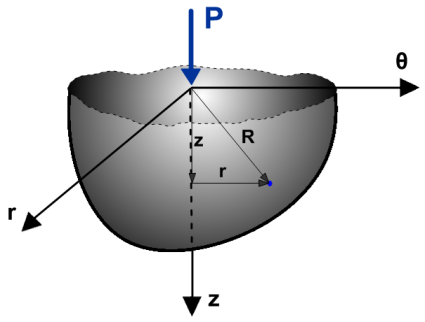

Figure 2.4 Boussinesq problem

$$\sigma_r = \frac{P}{2\pi R^2}\left[3\cos\varphi\sin^2\varphi - \frac{1-2\nu}{(1+\cos\varphi)^2}\right] \tag{2.7}$$

$$\sigma_\theta = \frac{P(1-2\nu)}{2\pi R^2}\left[\frac{1}{1+\cos\varphi} - \cos\varphi\right] \tag{2.8}$$

$$\sigma_z = \frac{3P}{2\pi R^2}\cos^3\varphi \tag{2.9}$$

$$\tau_{rz} = -\frac{3P}{2\pi R^2}\sin\varphi\cos^2\varphi \tag{2.10}$$

Figure 2.5 depicts the case of distributed load over a circular area. The solution is obtained from the Boussinesq's solution by integration over a circular area. Because of the complexities associated with the analytical evaluation of the particular problem, the closed-form solutions are available only for σ_z, σ_r, and σ_θ along the vertical axis ($r = 0$). In Equations 2.11 and 2.12, the load p, in unit of force per length square, is applied on a circular area of radius a.

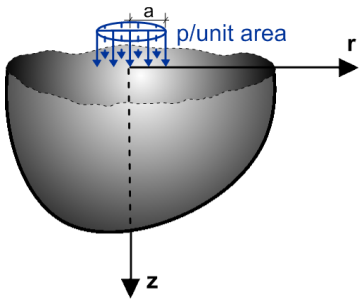

Figure 2.5: Uniform vertical loading on a circular area

$$\sigma_z = p\left[1-\left(\frac{a}{z}\right)^2\right]^{-\frac{3}{2}} \tag{2.11}$$

$$\sigma_r = \sigma_\theta = -\frac{p}{2}\left[(1+2\nu)-\frac{2z(1+\nu)}{(a^2+z^2)^{1/2}}+\frac{z^3}{(a^2+z^2)^{3/2}}\right] \tag{2.12}$$

Numerical solutions to all components of stress, strain, and displacement are tabulated by Ahlvin and Ulery (Ahlvin and Ulery, 1962). For the case of shear stress, the key to the use of Table 2.1 is shown in Equation 2.13.

$$\tau_{rz} = \tau_{zr} = pG_1 \tag{2.13}$$

The value of G_1 could be found in Table 2.1 for corresponding r/a and z/a.

Table 2.1 Function "G_1"- adapted from Ahlvin and Ulery (1962)

r/a / z/a	0	0.2	0.4	0.6	0.8	1	1.2	1.5	2	3	4	5	6	7	8	10	12	14
0	0	0	0	0	0	.31831	0	0	0	0	0	0	0	0	0	0	0	0
0.1	0	.00315	.00802	.01951	.06682	.31405	.05555	.00865	.00159	.00025	.00007	.00003						
0.2	0	.01163	.02877	.06441	.16214	.30474	.13592	.03060	.00614	.00091	.00026	.00010	.00005	.00003	.00002			
0.3	0	.02301	.05475	.11072	.21465	.29228	.18216	.05747	.01302	.00201	.00059							
0.4	0	.03460	.07883	.14477	.23442	.27779	.20195	.08233	.02138									
0.5	0	.04429	.09618	.16426	.23652	.26216	.20731	.10185	.03033	.00528	.00158	.00063	.00030	.00016	.00009	.00004	.00002	.00001
0.6	0	.04966	.10729	.17192	.22949	.24574	.20496	.11541										
0.7	0	.05484	.11256	.17126	.21772	.22924	.19840	.12373	.04718									
0.8	0	.05590	.11225	.16534	.20381	.21295	.18953	.12855										
0.9	0	.05496	.10856	.15628	.18904	.19712	.17945	.28881										
1	0	.05266	.10274	.14566	.17419	.18198	.16884	.12745	.06434	.01646	.00555	.00233	.00113	.00062	.00036	.00015	.00007	.00004
1.2	0	.04585	.08831	.12523	.14615	.15408	.14755	.12038	.06967	.02077	.00743	.00328	.00159	.00087	.00051			
1.5	0	.03483	.06688	.09293	.11071	.11904	.11830	.10477	.07075	.02599	.01021	.00460	.00235	.00130	.00078	.00033	.00016	.00009
2	0	.02102	.04069	.05721	.06948	.07738	.08067	.07804	.06275	.03062	.01409	.00692	.00369	.00212	.00129	.00055	.00027	.00015
2.5	0	.01293	.02534	.03611	.04484	.05119	.05509	.05668	.05117	.03099	.01650	.00886	.00499	.00296	.00185	.00082	.00041	.00023
3	0	.00840	.01638	.02376	.02994	.03485	.03843	.04124	.04039	.02886	.01745	.01022	.00610	.00376	.00241	.00110	.00057	.00032
4	0	.00382	.00772	.01149	.01480	.01764	.02004	.02271	.02475	.02215	.01639	.01118	.00745	.00499	.00340	.00167	.00090	.00052
5	0	.00214				.00992		.01343	.01551	.01601	.01364	.01105	.00782	.00560	.00404	.00216	.00122	.00073
6	0					.00602		.00845	.01014	.01148	.01082	.00917	.00733	.00567	.00432	.00243	.00150	.00092
7	0					.00396			.00687	.00830	.00842	.00770	.00656	.00539	.00432	.00272	.00171	.00110
8	0					.00270			.00481	.00612	.00656	.00631	.00568	.00492	.00413	.00278	.00185	.00124
9	0					.00177			.00347	.00459	.00513	.00515	.00485	.00438	.00381	.00276	.00192	.00133
10	0							.00199	.00258	.00351	.00407	.00420	.00411	.00382	.00346			

2.3.2 Cerruti Problem

Figure 2.6 illustrates a horizontal point load acting parallel to the surface of a half-space, known as the Cerruti problem (Cerruti, 1882). The solution is available for both stress and displacements in cylindrical coordinates. This solution is partly presented in Equations 2.14 to 2.19, corresponding to stress components in cylindrical (polar) coordinates.

$$\sigma_r = -\frac{P}{2\pi R^2}\cos\theta\sin\varphi\left[3\sin^2\varphi - \frac{1-2\nu}{(1+\cos\varphi)^2}\right] \tag{2.14}$$

$$\sigma_\theta = \frac{P(1-2\nu)}{2\pi R^2}\frac{\cos\theta(2+\cos\varphi)\sin\varphi\cos\varphi}{(1+\cos\varphi)^2} \tag{2.15}$$

$$\sigma_z = \frac{3P}{2\pi R^2}\cos\theta\sin\varphi\cos^2\varphi \tag{2.16}$$

$$\tau_{r\theta} = -\frac{P(1-2\nu)}{2\pi R^2}\frac{\sin\theta\sin\varphi}{(1+\cos\varphi)^2} \tag{2.17}$$

$$\tau_{rz} = -\frac{3P}{2\pi R^2}\left[\cos\theta \sin^2\varphi \cos\varphi\right] \tag{2.18}$$

$$\tau_{z\theta} = 0 \tag{2.19}$$

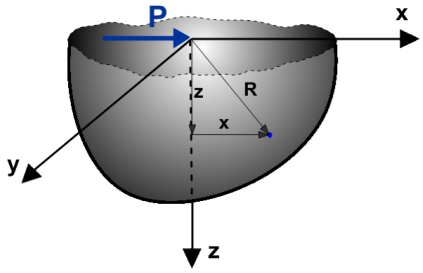

Figure 2.6: Cerruti Problem

2.3.3 Flamant Problem

Figure 2.7 represents the 2-D half-space under a horizontal or vertical line load, commonly known as the Flamant problem (Saad, 2009). The solution to this problem is developed for both stresses and displacements. However, the displacement solution contains logarithmic terms that cause unbounded outcomes at infinity as a result of two-dimensional modeling in an unbounded homogeneous domain (Saad, 2009). Stress components resulting from vertical load are calculated from Equations 2.20 to 2.22. The stress results corresponding to horizontal load are shown in Equations 2.23 to 2.25. Variables P_x and P_y in these equations are measured in units of force per length.

$$\sigma_x = \frac{2P_y x^2 y}{\pi(x^2+y^2)^2} \tag{2.20}$$

$$\sigma_y = \frac{2P_y y^3}{\pi(x^2+y^2)^2} \tag{2.21}$$

$$\tau_{xy} = \frac{2P_y xy^2}{\pi(x^2+y^2)^2} \tag{2.22}$$

$$\sigma_x = \frac{2P_x x^3}{\pi(x^2+y^2)^2} \tag{2.23}$$

$$\sigma_y = \frac{2P_x xy^2}{\pi(x^2+y^2)^2} \tag{2.24}$$

$$\tau_{xy} = \frac{2P_x x^2 y}{\pi(x^2+y^2)^2} \tag{2.25}$$

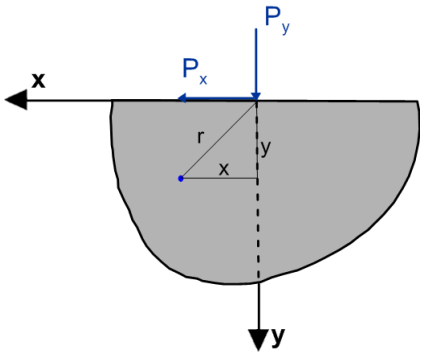

Figure 2.7: Flamant problem

It is worth mentioning that all the static stress solutions are independent of Young's modulus of the half-space, and some components (vertical and shear in point load problems) are independent of Poisson's ratio as well. The latter, however, is not true for dynamic loading as demonstrated below.

2.4 DYNAMIC POINT LOAD ON HALF-SPACE: LAMB'S PROBLEM

The solutions discussed in previous sections correspond to the case of static loading which is described by elliptic partial differential equations and, thereby, does not involve propagation phenomena (i.e. response to applied loads is instantaneous). The solutions to dynamic-type problems are coupled tightly with the wave propagation theories and correspond to partial

differential equations of the hyperbolic type which are much harder to solve. The first such solution is D'Alembert's solution of one-dimensional waves (Bekefi & Barrett, 1987). In the early 20th century, investigations of the effects of applying a vibratory force at a point entered a new era after Lord Rayleigh's discovery of new types of surface waves, currently known as Rayleigh (R) waves (Figure 2.8). The presence of Rayleigh waves clarified that the influence of the free-surface in modifying the characteristics of the vibration is more significant than what had been suspected earlier using Stokes solution in laws of wave-propagation (Lamb, 1904).

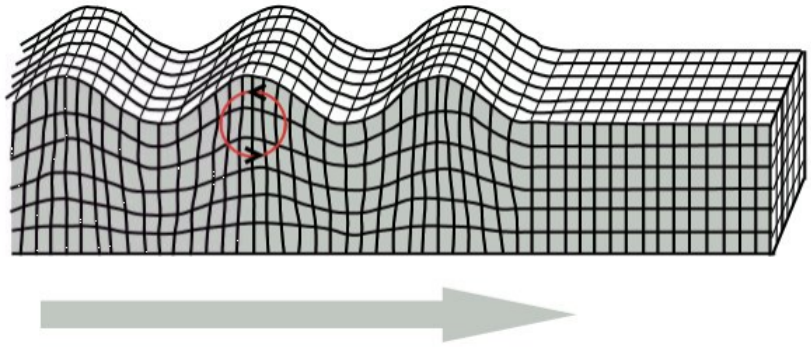

Figure 2.8: Propagating Rayleigh wave- Adapted from Bolt (1993)

In an unbounded elastic medium, i.e. full-space, only two types of waves, primary (or Compression) (P) and shear (S) waves can be propagated. It should also be noted that P and S waves propagate independently in a full-space medium. In the presence of a boundary, as in the half-space problem, two phenomena introduce deviations from classical wave-propagation theory. One is the coupling of the P and S waves through the surface boundary. In other words, an incident wave of sharp angle (i.e. close to vertical), either P or S polarized on the plane of the paper (SV waves), can be converted into two waves on reflection (Graff, 1975). This behavior is called Mode Conversion and is shown in Figure 2.9.

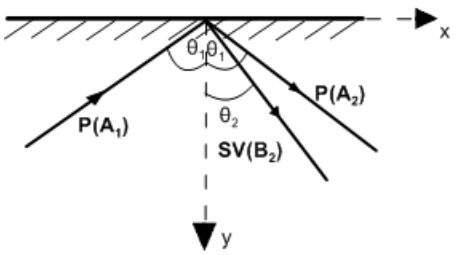

Figure 2.9: Mode Conversion phenomenon, incident P wave with amplitude A1 is reflected as P wave with amplitude A2 and SV wave with amplitude B2

The second phenomenon referenced above is the existence of Rayleigh waves due to the refraction of P and S waves traveling at obtuse angle on the surface boundary. The surface or Rayleigh wave is essentially two-dimensional (although not necessary planar), as no propagation take place in the vertical direction; therefore, it dissipates its energy less rapidly than P and S waves, which propagate in three-dimensional space. Figure 2.10 shows the distribution of displacement and energy due to different types of waves as a result of a harmonic vertical load applied on a half-space. In this figure, the predominance of Rayleigh waves in terms of energy and response is evident, especially close to the surface. It should also be noted that the effects of Rayleigh waves decays rapidly with depth, and the velocity of propagation is slower than that of body waves. An interesting discussion on the importance of Rayleigh waves in foundation dynamics has been provided by Wolf (1994) and Wolf and Deeks (2004).

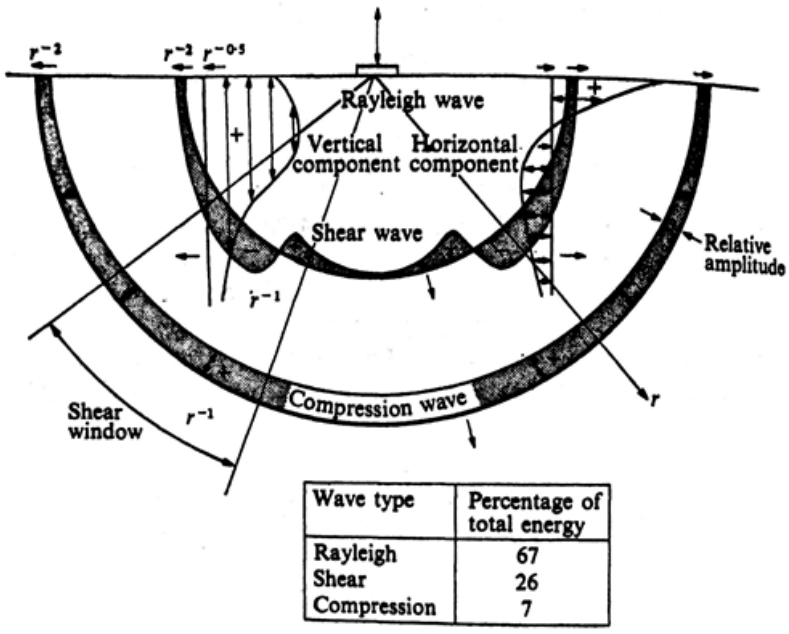

Wave type	Percentage of total energy
Rayleigh	67
Shear	26
Compression	7

Figure 2.10: Distribution of displacement and energy in P, SV, and Rayleigh waves resulting from a harmonic normal load on half-space for $\nu = \frac{1}{4}$ - Adapted from Woods (1968), based on the results from Miller and Pursey (1958).

The classical analysis of the surface dynamic source problem was first conducted by Sir Horace Lamb, Professor of Mathematics at the Victoria University of Manchester (before that in the newly founded University of Adelaide, Australia), and was published in 1904. Lamb considered a half-space under an impulsive 2-D and a suddenly applied 3-D vertical load. Lamb discussed harmonic loading and used superposition techniques to obtain results for pulse loading (Graff, 1975). His procedure was a great contribution to what is known today as the modern integral transform method. However, due to lack of mathematical capacity required for evaluation of associated integrals, he only evaluated the response at large distance from the source load, i.e. the far field response (Kausel, 2012). As part of that study, Lamb laid the foundation of what we call today the integral transform method (Kause, 2012). A great number of contributions have been conducted over time to solve this problem; however, the problem of a

dynamic source applied on the surface of a half-space is referred to as *Lamb's Problem* in the honor of the very first pioneer in this field, Sir Lamb.

Kausel (2012) provides a thorough review of the analysis of Lamb's problem in different studies including Cagniard (1939), Pekeris (1955), De Hoop (1960), Chao (1960), Mooney (1974), Eringen et al. (1975), and Richards (1979).

Four decades after Lamb formulated the problem, Cagniard (1939) developed a technique for performing the inversion of Lamb's integrals. A simplification to Cagniard's method was presented by De Hoop (1960). The latter is currently known as Carniard-De Hoop method. Pekeris (1955) and Chao (1960) obtained closed-form solutions for suddenly applied vertical and horizontal loads on a half-space. But these solutions were limited to a Poisson's ratio of 0.25. Mooney (1974) expanded Perkins' results to obtain the vertical component of displacement due to vertical point loads with arbitrary Poisson's ratio. In the book, *Elastodynamics*, Eringen et. al (1975) completed Mooney's work by providing results for radial components, for Poisson's ratios up to 0.2631 (numerical problems were encountered for larger values of v). Finally, Richards (1979) provided a complete set of equations for both vertical and horizontal components for different values of Poisson's ratio. Recently, Kausel (2012) revisited Lamb's problem for the cases of suddenly applied vertical and horizontal point loads on the surface of an elastic, homogeneous half-space and presented a compact set of equations for space-time displacement response at the surface and at depth underneath the load (i.e. $r = 0$) for any Poisson's ratio from 0 to 0.5, and concluded that the outcomes are in full agreement with those in Richard's study. The advantages of this new set of equations compared to previous works are their simplicity as a result of reducing the number and form of constants, and providing

equations that makes no distinction between real and complex roots associated with the Rayleigh poles. The latter simplifies the task of taking derivatives.

Table 2.2 summarizes the available theoretical solutions to Lamb's problem. Note that aside from some of the original work by Lamb (1904), these solutions do not apply directly for cyclic loads. Moreover, the solutions predict only displacements, and while displacement solutions can be readily converted to stresses for simple 1-D wave propagation, this conversion is not straightforward for the more complex 2-D and 3-D wave propagation associated with surface loading. The third major shortcoming of existing integral transform solutions is that their outcomes (for displacements) are only applicable for limited positions relative to the point load (i.e., at the ground surface and directly beneath the load; i.e., aperture angles of 90º and 0º). Hence, while these solutions represent significant milestones in the development of our theoretical understanding of how foundation soils respond to surface loads, they are not suitable to predict for any location the SSI-induced stresses that are of interest in the present work.

Table 2.2 Available integral transform solutions to Lamb's problem of point loads on the surface of a halfspace.

Developers	**Lamb (1904)**	**Pekeris (1955) Chao (1960)**	**Mooney (1974)**	**Eringen et. al (1975)**	**Richards (1979)**	**Kausel (2012)**
Load Direction	Vertical Horizontal	Vertical Horizontal	Vertical Horizontal	Vertical Horizontal	Vertical Horizontal	Vertical Horizontal
Load Type	Cyclic, Impulsive	Impulsive	Impulsive	Impulsive	Impulsive	Impulsive
Solution for Displacement (u_i)	far field u_z, u_r	u_z, u_r (z = 0)	u_z (z = 0)	u_z, u_r (z = 0)	u_z, u_r (z = 0)	u_z, u_r along r = 0 or z = 0 only
Solution for Stress (σ_{ij})	N.A.	N.A.	N.A.	N.A.	N.A.	N.A.
Poisson's ratio	0 - 0.5	0.25	0 - 0.5	0 - 0.2631	0 - 0.5	0 - 0.5

It should also be noted that although the formulation of integral transforms is exact, in most cases, such complex integrals are not tractable using exact analytical solutions. Therefore, the integrals should be evaluated numerically. As discussed earlier in this chapter, exact solutions are even lacking in the static case, in particular for distributed loads. On the other hand, evaluation of integrals numerically encounters many difficulties due to the singular nature of these loads (Schepers et al., 2010). This is in fact the main cause of the aforementioned limited availability of analytical solutions for: (1) some specific load types (i.e. mostly impulsive point loads), (2) displacements and not stresses, and (3) locations along the ground surface or directly beneath the load, but not at other aperture angles.

An excellent contribution was recently presented by Schepers et al. (2010) to deal with some numerical problems associated with evaluation of integrals for the problem of harmonic vertical and horizontal point load applied on the surface of an elastic or viscoelastic half-space. They also provide solutions in the form of stresses. In a nutshell, the closed-form static solution

is subtracted from the kernel in the wavenumber domain, and is added back in the spatial domain. The focus of this work is to evaluate the contours of stress components for various frequencies and a full range of Poisson's ratios. To illustrate the difficulty in obtaining such response functions, the procedure described in Schepers et al. (2010) for shear stress component evaluation is summarized in Equations 2.26 to 2.40.

$$\tau_{rz} = \mu\left\{\frac{\partial \bar{u}_z}{\partial r} + \frac{\partial \bar{u}_r}{\partial z}\right\} \tag{2.26}$$

where $\bar{u}_z$ and $\bar{u}_r$ are vertical and radial displacement and μ and λ are Lame constants.

The displacement components for horizontal (n = 1) and vertical (n = 0) loads can be written as:

$$u_r = \bar{u}_r(r,z)(\cos n\theta) \tag{2.27}$$

$$u_z = \bar{u}_z(r,z)(\cos n\theta) \tag{2.28}$$

$$u_r(r,z,\omega) = -\frac{1}{2\pi\mu}\int_0^\infty f_{xz} J_1(kr)dk \tag{2.29}$$

$$u_z(r,z,\omega) = -\frac{1}{2\pi\mu}\int_0^\infty f_{zz} J_0(kr)dk \tag{2.30}$$

In these equations J_0 and J_1 are the Bessel functions of the first kind and order 0 and 1, respectively. The kernels of these expressions involve flexibility functions in the frequency-wavenumber domain (f_{xz} ,f_{zz}), which are as shown in Equations 2.31 and 2.32. It should be mentioned that the flexibility functions are related to *actual* Green's functions (G_{xz}, G_{zz}) (Schepers et al., 2010).

$$f_{xz} = \mu k G_{xz} = \frac{1}{2\Delta}\left[pse_e - \frac{1}{2}(1+s^2)e_p \right] \tag{2.31}$$

$$f_{zz} = \mu k G_{zz} = \frac{p}{2\Delta}\left[e_e - \frac{1}{2}(1+s^2)e_p \right] \tag{2.32}$$

$$\Delta = ps - \frac{1}{4}(1+s^2)^2 \tag{2.33}$$

where G_{xz} and G_{zz} are actual Green's functions and Δ is the Rayleigh function in which

$$\frac{1}{C_P^c} = \frac{1-i\xi_p}{C_p} \tag{2.34}$$

$$\frac{1}{C_S^c} = \frac{1-i\xi_S}{C_S} \tag{2.35}$$

are complex *P* and *S* wave velocities, respectively.

$$p = \sqrt{1-\left(\frac{\omega}{kC_P^c}\right)^2}, \mathrm{Im}(p) \geq 0 \tag{2.36}$$

$$s = \sqrt{1-\left(\frac{\omega}{kC_S^c}\right)^2}, \mathrm{Im}(s) \geq 0 \tag{2.37}$$

$$e_p = \exp(kpz) = exp(-kp|z|) \tag{2.38}$$

$$e_s = \exp(ksz) = exp(-ks|z|) \tag{2.39}$$

The wave numbers are also defined as:

$$k_p = \frac{\omega}{C_P}, \quad k_S = \frac{\omega}{C_S}, \quad k_R = \frac{\omega}{C_R} \tag{2.40}$$

where C_p, C_s, and C_R are P, S, and R wave velocities. The full derivations of aforementioned equations can be found in aforementioned publications as well as Schepers et al. (2010) and in Chapter 10 of Kausel (2006).

Figure 2.11 presents one set of pressure bulbs corresponding as determined by Schepers et al. (2010) to vertical load on an elastic and homogenous half-space with Poisson's ratio (ν) of 0.33, damping (ξ) of 0.5%, shear wave velocity (V_S) of 100 m/s, and mass density (ρ) of 1.8 Mg/m^3. The normalization is performed based on the corresponding static stress value at the reference location $R_0(\varphi_0)$ = 1 m (i.e. the radial distance along the ray = 0°, 45°, or 90°, depending on the stress components (Schepers et al., 2010). It should be noted that in their presentation, all bulbs in one tile are lines of "one and only one" constant value of the non-dimensional stress. So in order to compute the dimensional value, the corresponding static stress value at the reference location R_0 should be considered applying the appropriate static closed-form equation, i.e. Boussinesq's solution. Since all bulbs are lines of one and only one constant stress value, the stress value of the static one and the non-scaled dynamic ones are equal at any point on any bulb of a tile.

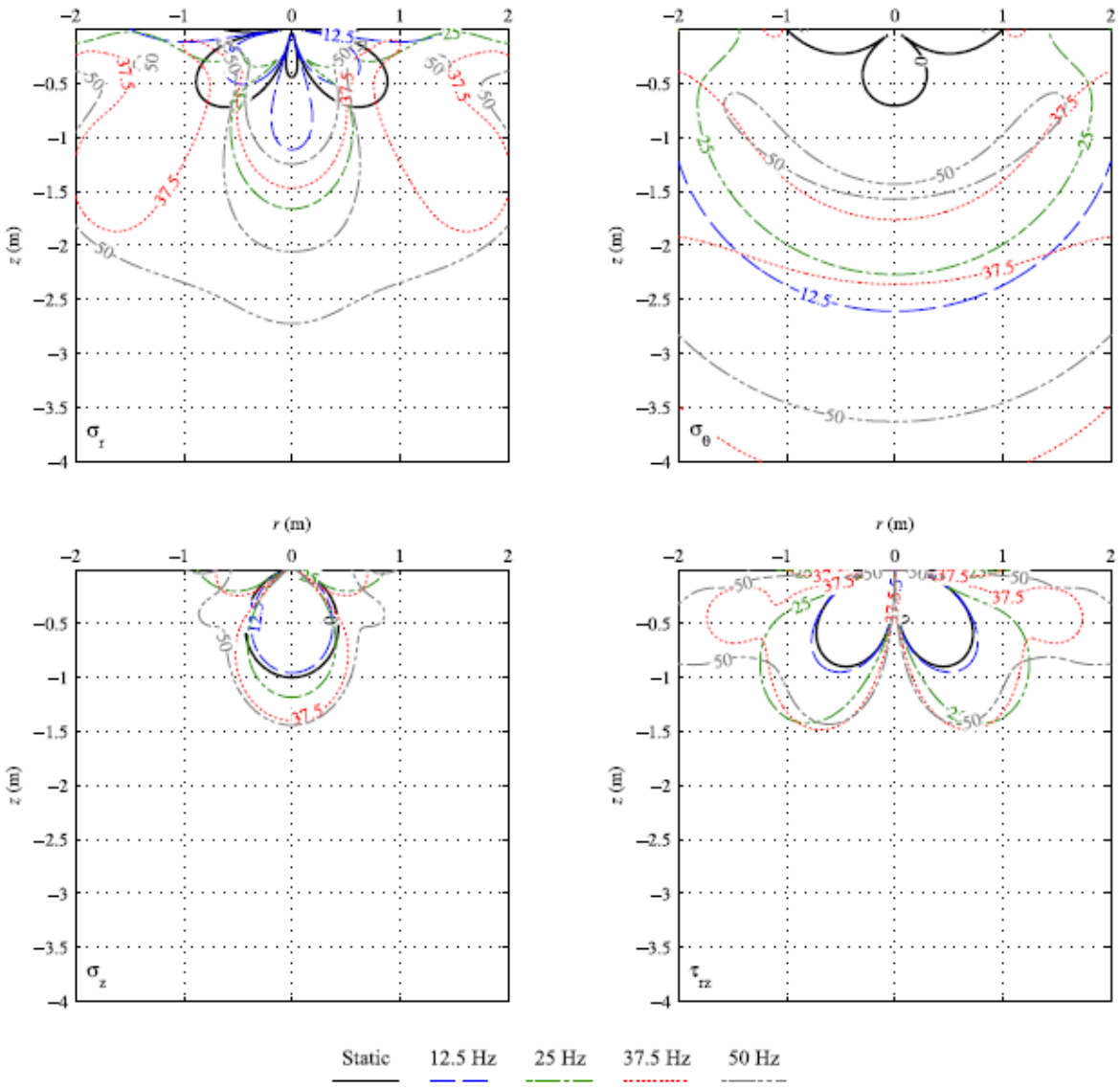

Figure 2.11: Pressure bulbs due to vertical load, ν = 0.33, ξ = 0.005, V_S = 100 m/s, ρ = 1.8 Mg/m^3 - Adapted from Schepers et al. (2010)

This specific set of results is used in Chapter 3 for verification purposes. The pressure bulbs in this work are limited to a few numbers of frequencies as well as a nominal shear wave velocity of 100 m/s. If any other values of shear wave velocity or frequency are of interest, some scaling adjustment procedures need to be performed in order to get the corresponding stress outputs. For the applied nominal shear wave velocity, 10 Hz is the threshold above which dynamic effects become more pronounced and dynamic bulbs deviates from static ones.

Nevertheless, this threshold is strongly a function of actual to nominal shear wave velocity ratio, and tends to decrease with increases of this ratio (Schepers et al., 2010). Moreover, dynamic stresses reach deeper in the soil mass and follow more complex patterns as a result of constructive and destructive wave interference (Schepers et al., 2010). These will be explored in detail in later chapters.

2.5 BEYOND THE SSI PROBLEM

Although mostly familiar to engineers and researchers working in geotechnical earthquake engineering and Soil-Structure Interaction fields, the problem of assessment of strains and stresses caused by loads applied onto surface of a medium has attracted many researchers in other fields such as pavement design, biomedical and bio-material. In the following section, some important developments in such fields are discussed briefly.

2.5.1 Flexible Pavement Design

Flexible pavements typically consist of two or three layers, i.e. the surface layer which is primarily made of asphalt, the granular base course, sub-base as an optional treated subgrade, and subgrade being the existing soil.

Many laboratory investigations as well as in-situ and analytical studies have been conducted to evaluate the effects of speed and frequency of a moving load, i.e. the vehicle, on the response of the flexible pavement. Brown (1967) performed laboratory testing on two models, a single layer of clay, and two layers of granular base on clay subgrade. The applied load was a single bell-shaped pulse of duration between 0.1 and 2 seconds. In addition, pressure and strain cells were used to measure the stresses and strains due to the applied load. The results were then compared with the Boussinesq's solution and the layered system solution both in elastic

theory. In general, the obtained stress outcomes showed a meaningful agreement with theory, but strains were more difficult to predict due to the dependency on modulus. In another study, Hardy and Cebon (1994) proposed a quasi-dynamic analysis, which disregards the effects of frequency of loading but accounts for the speed and fluctuation amplitude of dynamic load. They validated this simplified method by comparing the results in terms of primary load responses and fatigue damage to those predicted by a full dynamic analysis. They concluded that in practice, the quasi-dynamic analysis can successfully predict the response of pavement to the applied load as long as suitable load-damage relationships are used. Analysis of contact stresses on the surface of flexible pavements is another area that has attracted many researchers in recent years. In analysis of rutting and top-down cracking (TDC), shear stress is believed to be one of the critical factors. As opposed to traditional methods that assume uniformly distributed circular vertical contact pressure equal to tire inflation pressure, Su Kai et al. (2008) measured realistic tire-pavement contact pressure in the laboratory using a static test system. They applied the measured pressure on a 3D-FEM of pavement and investigated the effects of tire load and inflation pressure, horizontal stresses, and the asphalt layer thickness. The results indicated that the maximum shear stress that occurs at the tire edge is the major factor causing rutting and TDC developments. Despite the asphalt layer thickness, tire pressure, tire vertical load, and horizontal stress had significant effects on shear stress.

2.5.2 Biomedical and Biomaterial Areas

In this field of research, the materials of interest, i.e. biomaterial, are usually considered to be viscoelastic, indicating both viscous and elastic properties. The elastic property is the tendency of materials to return to their original shape after the applied load is removed. The viscosity is generally the resistance to flow. Therefore, viscoelastic materials have a time-dependent strain

rate even in static problems. Human organs, animal tissue, and most materials in the food industry are classified as viscoelastic materials.

The solution to the Boussinesq problem in viscoelastic materials is developed by Talybly (2010) in which two time-dependent functions were introduced to account for relaxation and Poisson's ratio. Also, equilibrium equations and boundary conditions were used to obtain the equations to solve for the determining functions. Such equations were solved using Volterra integral equation of second kind (Talybly, 2010). In another study, Peng and Zhou (2012) developed the formulation for tangential point force on a half-space, i.e. Cerruti's visco-elastic problem. The derivation of the formulas follows the same approach as of Talybly's; however, the asymmetry due to tangential force makes the formulation much more complicated (Peng and Zhou, 2012). Peng and Zhou (2013) developed a model of cutting force on a viscoelastic body mostly for surgical simulation purposes and presented a closed form solution for stress distribution in a body subjected to the force from the cutting blade. In their analysis, they modeled the body as a linear viscoelastic material and the interaction between the blade and the body as distributive forces acting on the surface of a viscoelastic half-space. The result was presented as a mathematical model and could be used for the stress distribution estimations during biomaterial cutting which could be useful in surgical simulations for the purpose of training new practitioners as well as in the food processing industry where it is desired to know the stress distribution in a food medium under a robot-controlled blade cut. The latter could improve cutting yield and meat harvesting quality (Peng and Zhou, 2013).

In this chapter, the historical development in assessment of effects of an applied load onto a body of material(s) is discussed. As described in this chapter, significant progress has been made over time both in terms of methodology (i.e. integral transforms and inverse integral

transforms) and computational tools. The main objectives were to (1) emphasize the level of complexity in obtaining analytical and numerical solutions to these types of problems, especially in dynamic cases; and (2) demonstrate that currently available solution cover a limited range of conditions and as such are not suitable to practical applications. Moreover, currently available solutions are formulated with a considerable degree of complexity, limiting the potential of practical engineering implementation.

3 Stress beneath Dynamically Applied Vertical and Horizontal Point Loads

As discussed in detail in Chapter 1, based on several studies including NIST (2012) practical guidelines have been developed to help engineers take into account soil-structure interaction (SSI) effects in earthquake engineering. Based on these guidelines, input motions reflect expected levels of ground motion at the base of structures (as opposed to the free field motion) and the structural models include appropriate springs and dashpots that account for the geotechnical and foundation conditions associated with the structure. The aforementioned steps should be taken to answer the most important question in classical SSI; *what are the effects of soil on structural response?* However, what remains is the commonly ignored question: *what are the effects of the structure on soil?*

Earthquake ground shaking induces strains and stresses in soil materials as a result of wave propagation from site response. In the absence of a structure, these seismic demands on the soil materials reflect free-field conditions. Such demands on soil materials can cause, among other effects, pore pressure generation and associated losses in shear strength and stiffness. The presence of a structure modifies the characteristics of wave propagation in the vicinity of the foundation due to SSI. Therefore, dynamic stress demands in the soil beneath the foundation (referred to as 'foundation soils') result from both site response and SSI. In conventional practice, stress demands from SSI are ignored in engineering assessments of ground failure

potential, based on the perception that demands from wave propagation are dominant. However, numerous post-earthquake field investigations [e.g., 1999 Kocaeli, Turkey (Bray and Stewart, 2000); 1999 Chi-Chi, Taiwan (Chu et al., 2004), 2011 Tohoku, Japan (Ashford et al., 2011), 2011 Christchurch, New Zealand (Cubrinovski et al., 2011)] provide evidence for local ground failure beneath foundations, apparently influenced by SSI-related demands. Similar phenomena have been observed and documented in centrifuge modeling (e.g., Dashti et al., 2009).

As explained in Chapter 2, the stress solutions for static vertical and horizontal loads applied on the surface of an elastic half-space are given by exact formulae by Boussinesq (1885) and Cerruti (1882), which are available in engineering textbooks and manuals. Moreover, a few analytical and some numerical solutions exist for more general types of static loading such as circular or square vertical and horizontal loads applied on the surface of an elastic half-space or a finite soil layer over rigid rock, obtained by integration of the above solutions (Poulos & Davis 1974). In the case of dynamic loading, the body of knowledge is much more limited, primarily due to the difficulty in solving the governing differential equations in closed form. The first to successfully perform such an analysis was Lamb (1904), who extended Boussinesq's solution by considering a suddenly applied vertical load of constant amplitude. Despite several subsequent studies (summarized by Kausel 2012), little progress has occurred over the last century for two main reasons: (1) the difficulty in evaluating certain integrals (i.e., inverting the integral transforms) employed in the analysis; and (2) the focus in practice on determining surface motions for seismological purposes, not soil stresses. An exception is a recent study by Schepers et al. (2010) on the problem of harmonic vertical and horizontal point loads on the surface of a visco-elastic half-space. However, the pressure bulbs presented are difficult to use due to necessary scaling adjustments to get the corresponding stress outputs. Inspired by the

aforementioned analyses, the goals of this chapter are to: (1) extend the Boussinesq (1885) and Cerruti (1882) problems to the dynamic regime, by considering a harmonic load applied on the surface of a visco-elastic half-space, (2) develop general normalization schemes to facilitate ease of application, and (3) provide insight into the physics of SSI-induced stresses and thereby take initial steps towards a simplified procedure for evaluating seismic stress demands in foundation soil.

In this chapter, the Buckingham π theorem (Buckingham, 1914) is discussed as part of the normalization scheme. This theorem is applied to the static and dynamic problems of vertical and horizontal point loads imposed on the surface of the half-space to determine the number of dimensionless parameters. Such parameters are then selected with regards to characteristic properties of the systems and investigated throughout the analysis presented in this chapter. Boundary Element Method (BEM) is selected as the numerical method of analysis. The commercial program ISoBEM (2012) is employed as the main software throughout this work. The analyses in this part of research includes two cases for dynamically applied vertical and horizontal point loads on the surface of an elastic half-space. The verification of the solutions in the point load problems is performed by comparing the stress results to the Boussinesq's solution (Boussinesq, 1885), Cerruti's solution (Cerruti, 1882), and Lamb's problem solution by Schepers et al. (2010). Upon verification, the final analysis is performed for a large set of parameters including dimensionless frequencies ($\omega R/V_S$) ranging from 0 to 20, Poisson's ratios of 0.34 and 0.45, and soil damping values of 1% and 5%, to account for sand and incompressible clay soils, respectively. The solutions are then illustrated in the form of dimensionless stress bulbs for amplitude and phase angles. A discussion is also presented on effects of Poisson's ratio,

damping, and most importantly, dimensionless frequency on the stress response of soil mass due to an applied dynamic point load.

3.1 BUCKINGHAM'S THEOREM

The differential equations describing the dynamic response of the soil mass are not solvable analytically; dimensional analysis is employed to identify the governing parameters that characterize the system. The Buckingham π theorem (1914) states that the original expression of a certain physical problem involving N number of parameters with M number of fundamental dimensions is equivalent to an equation involving a set of P = N - M dimensionless parameters, i.e. π groups. In other words, identifying the variables involved in a physical problem would suffice for computing the number of dimensionless parameters, even when the form of the governing equation describing the problem or the solution is unknown, or an analytical solution is not available. It should be noted that the choice of dimensionless parameters is not specified in this theorem; therefore the process of selecting the π groups should be bounded with knowledge of physical characteristics of the corresponding problem and requires judgement. The π theorem is the key scheme in the normalization process and serves as a useful technique in addressing problems being represented by relatively few physical parameters. In the research at hand, as the differential equations describing the response of the soil are not solvable analytically (or even numerically in some occasions), the normalization technique is chosen to capture the dimensionless groups that characterize the system.

3.2 DIMENSIONLESS PARAMETERS OF POINT LOADS ON AN ELASTIC HALF-SPACE

The fundamental units are length *[L]* and force *[F]* in static problems and are length *[L]*, force *[F]* and time *[T]* in dynamic ones. In the following sections, the solution to Boussinesq and Cerruti problems are represented in dimensionless forms for both static and dynamic cases.

3.2.1 Dimensional Analysis of the Classical Boussinesq Problem

With reference to the coordinate system of Figure 3.1(a), the classical Boussinesq problem is presented in Figure 3.1(b).

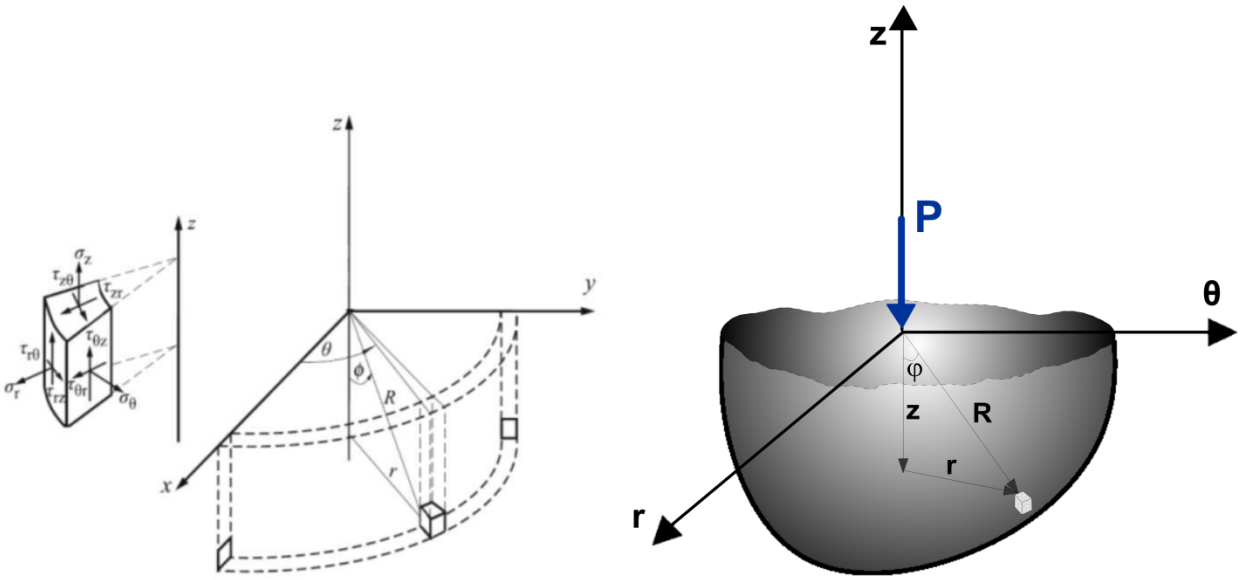

Figure 3.1: (a) Cartesian versus cylindrical coordinates - Adapted from Schepers et al. (2010), (b) Classical Boussinesq problem

In this figure the position of an arbitrary element within the elastic soil medium (with Young's modulus E and Poisson's ratio ν) is defined by radial distance R from the point of application of load P (origin of axes), and the vertical aperture angle, φ. Hence, in this problem, three parameters, E, R, and P have two fundamental units, i.e. length *[L]* and force *[F]*. Two

intrinsically dimensionless parameters, φ and v, complete the definition of the physical system. Accordingly, the number of dimensionless groups required to define this problem is given as (where Q refers to the number of intrinsically dimensionless parameters):

$$(\mathrm{N}-\mathrm{M})+\mathrm{Q}=(3-2)+2=3 \tag{3.1}$$

Therefore, the solution to the classical Boussinesq problem must be represented by an equation involving three dimensionless parameters, two of which are known (φ and v). Additional steps are required to identify the third parameter. Equation 3.2 shows the stress response, σ_{ij}, of a soil element, with the associated units appearing in Equation 3.3.

$$\sigma_{ij} = P^{\alpha} E^{\beta} R^{\gamma} g(\varphi, v) \tag{3.2}$$

$$[\frac{F}{L^2}] = [F^{\alpha}][\frac{F}{L^2}]^{\beta}[L]^{\gamma} \tag{3.3}$$

Parameters α, β, and γ are determined through dimensional analysis per Equation 3.3. Equation 3.4 provides two equations and three unknowns.

$$\begin{aligned} 1 &= \alpha + \beta \\ -2 &= -2\beta + \gamma \end{aligned} \tag{3.4}$$

The linearity of the problem requires $\alpha = 1$. Values of β and γ are then obtained as 0 and -2, respectively, resulting in:

$$\sigma_{ij} = \frac{P}{R^2} g(\varphi, v) \tag{3.5}$$

Equation 3.5 reveals the independence of stresses to the Young's modulus of the half-space, as mentioned in Chapter 2. This equation is rewritten in dimensionless form as Equation 3.6 where the third dimensionless parameter is ($\sigma_{ij}R^2/P$). In other words, for an element located at

distance R from the vertical static point load applied at ground surface, the dimensionless stress depends only on aperture angle and, possibly, ν. This is confirmed by the exact stress solution to the Boussinesq problem as shown in Equations 3.7–10 in dimensionless forms.

$$\frac{\sigma_{ij}R^2}{P} = g(\varphi,\nu) \tag{3.6}$$

$$\frac{\sigma_z R^2}{P} = \frac{3}{2\pi}\cos^3\varphi \tag{3.7}$$

$$\frac{\sigma_r R^2}{P} = \frac{1}{2\pi}\left[3\cos\varphi\sin^2\varphi - \frac{1-2\nu}{1+\cos\varphi}\right] \tag{3.8}$$

$$\frac{\sigma_\theta R^2}{P} = \frac{1-2\nu}{2\pi}\left[\frac{1}{1+\cos\varphi} - \cos\varphi\right] \tag{3.9}$$

$$\frac{\tau_{rz} R^2}{P} = \frac{3}{2\pi}\sin\varphi\cos^2\varphi \tag{3.10}$$

The independence of the right-hand side of the above solutions to R indicates *self-similarity* of the problem, as it reduces the number of independent variables from two (i.e., φ, R) to one (φ), which greatly simplifies the governing equations as an ordinary differential equation is required to solve the problem instead of a partial differential equation. This remarkable property is discussed in detail by Barenblatt (1996). The elegancy of this approach is more pronounced when it comes to problems for which solutions are not fully available in closed-form. The dynamic Boussinesq problem is among those lacking a closed form solution, and is discussed in the following section.

3.2.2 Dimensional Analysis for the Dynamic Vertical Point Load Problem

In the dynamic counterpart to the Boussinesq problem, shown in Figure 3.2(b), the point load is periodic with amplitude P and angular frequency ω. Radial Distance (R), shear wave velocity (V_S), shear modulus (G), and mass density of the soil medium (ρ) are other essential parameters.

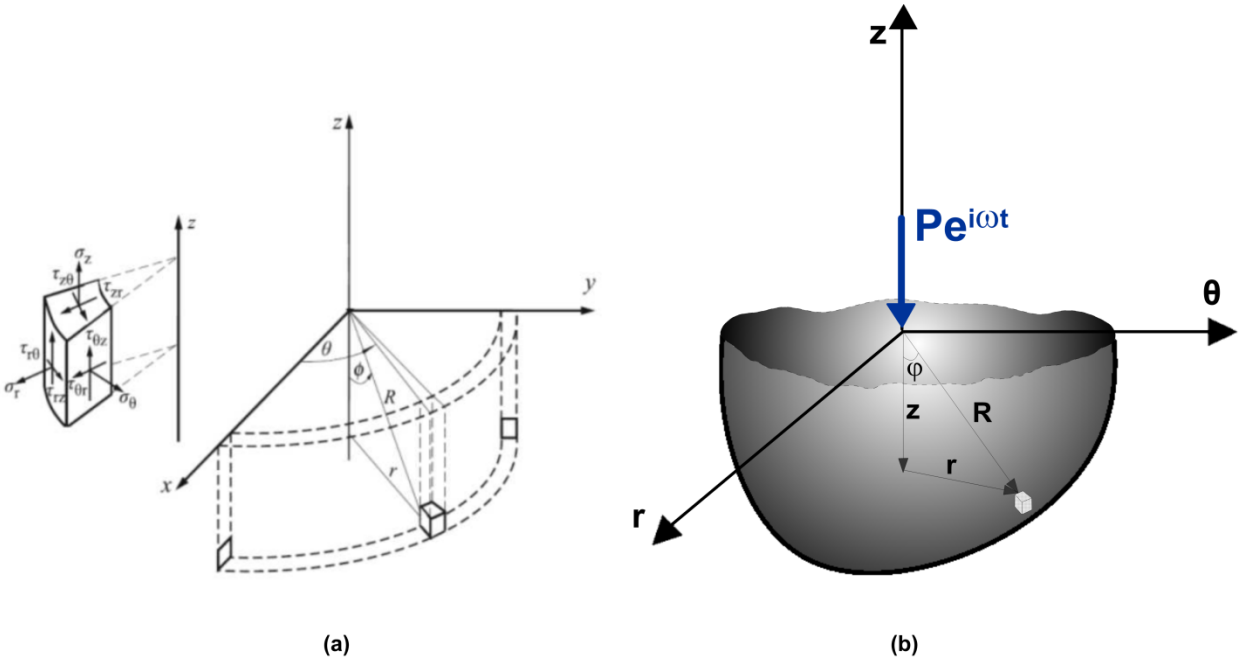

Figure 3.2: (a) Cartesian versus cylindrical coordinates - Adapted from Schepers et al. (2010), (b) Dynamic vertical point load problem

Since G, V_S, and ρ are correlated, only two of them should be considered as fundamental parameters resulting in a total of five (N = 5), three fundamental dimensions, length *[L]*, force *[F]*, and time *[T]*, (M = 3), and three intrinsically dimensionless parameters v, ξ, and φ (Q = 3). Accordingly, the number of dimensionless groups is:

$$(N-M)+Q=(5-3)+3=5 \tag{3.11}$$

Hence, in addition to the three intrinsically dimensionless parameters and ($\sigma_{ij}R^2/P$), another dimensionless parameter is required to fully describe the dynamic solution. This

parameter is selected to be ($\omega R/V_S$), which is recognized in most studies involving dynamic analysis as dimensionless frequency. A difference in the present case is that R is a coordinate, not a characteristic length such as a footing dimension. Alternatively, ($\omega R/V_S$) can be interpreted as proportional to the ratio of R to wavelength. As shown in Equation 3.12 in the dynamic problem ($\sigma_{ij}R^2/P$) is a function of soil ν and ξ, aperture angle, and dimensionless frequency:

$$\frac{\sigma_{ij}R^2}{P} = g\left(\varphi, \nu, \xi, \frac{\omega R}{V_s}\right) \tag{3.12}$$

3.2.3 Dimensional Analysis of the Classical Cerruti Problem

The classical Cerruti problem is presented in Figure 3.3(b).

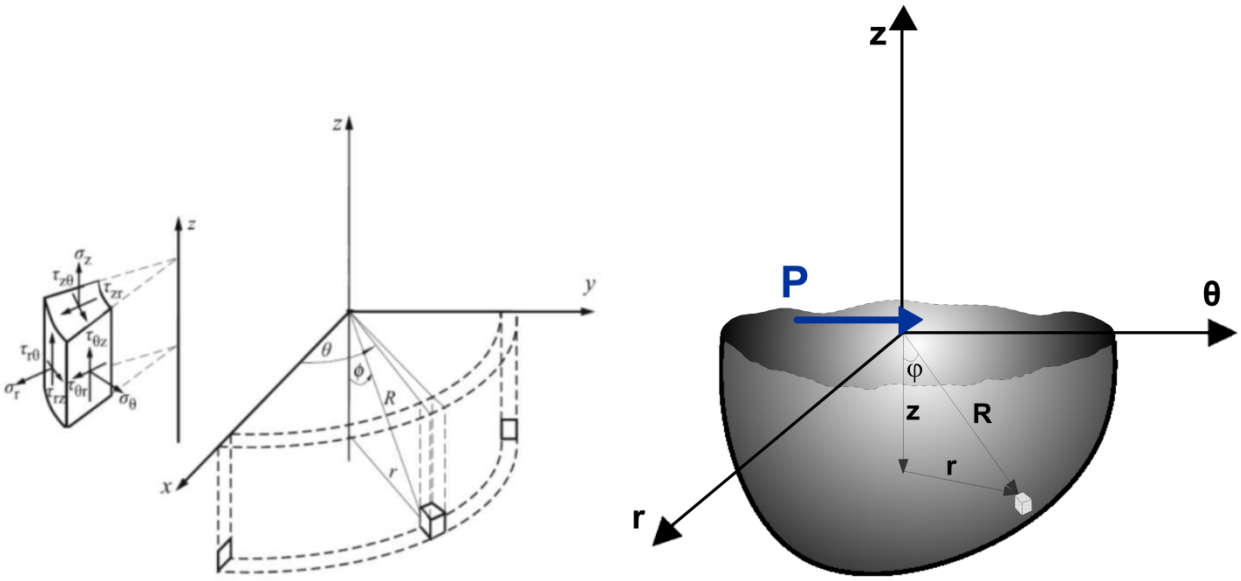

Figure 3.3: (a) Cartesian versus cylindrical coordinates - Adapted from Schepers et al. (2010), (b) Classical Cerruti problem

Considering dimensional analyses, the Cerruti problem is similar to the Boussinesq problem except that whereas the Boussinesq problem is axi-symmetric, the Cerruti problem is

antisymmetric. To account for the additional dimension in the Cerruti problem, azimuthal angle θ should be considered. Equation 3.13 shows the dimensionless presentation of the Cerruti problem. For an element located at distance R from the horizontal static point load applied at the ground surface, the dimensionless stress depends only on aperture angle, azimuthal angle, and ν. This is confirmed by the exact stress solution to the Cerruti problem as shown in Equations 3.14–18 in dimensionless forms.

$$\frac{\sigma_{ij}R^2}{P} = g(\varphi,\theta,\nu) \tag{3.13}$$

$$\frac{\sigma_z R^2}{P} = -\frac{3}{2\pi}\cos\theta\sin\varphi\cos^2\varphi \tag{3.14}$$

$$\frac{\sigma_r R^2}{P} = -\frac{1}{2\pi}\cos\theta\sin\varphi\left[3\sin^2\varphi - \frac{1-2\nu}{(1+\cos\varphi)^2}\right] \tag{3.15}$$

$$\frac{\sigma_\theta R^2}{P} = \frac{1-2\nu}{2\pi}\left[\frac{\cos\theta(2+\cos\varphi)\sin\varphi\cos\varphi}{(1+\cos\varphi)^2}\right] \tag{3.16}$$

$$\frac{\tau_{\theta r}R^2}{P} = -\frac{1-2\nu}{2\pi R^2}\left[\frac{\sin\theta\sin\varphi}{(1+\cos\varphi)^2}\right]$$

(3.17)

$$\frac{\tau_{rz}R^2}{P} = -\frac{3}{2\pi R^2}\cos\theta\sin^2\varphi\cos\varphi \tag{3.18}$$

As mentioned earlier, the remarkable value of this approach is more pronounced when it comes to dynamic problems for which general solutions are not available in closed-form. Dimensional analysis of the dynamic Cerruti problem is addressed in the following section.

3.2.4 Dimensional Analysis for the Dynamic Horizontal Load Problem

As shown in Figure 3.4(b), the dynamic counterpart to the Cerruti problem is the periodic horizontal point load with amplitude P and angular frequency ω. Radial Distance (R), shear wave velocity (V_S), shear modulus (G), and mass density of the soil medium (ρ) are other essential parameters.

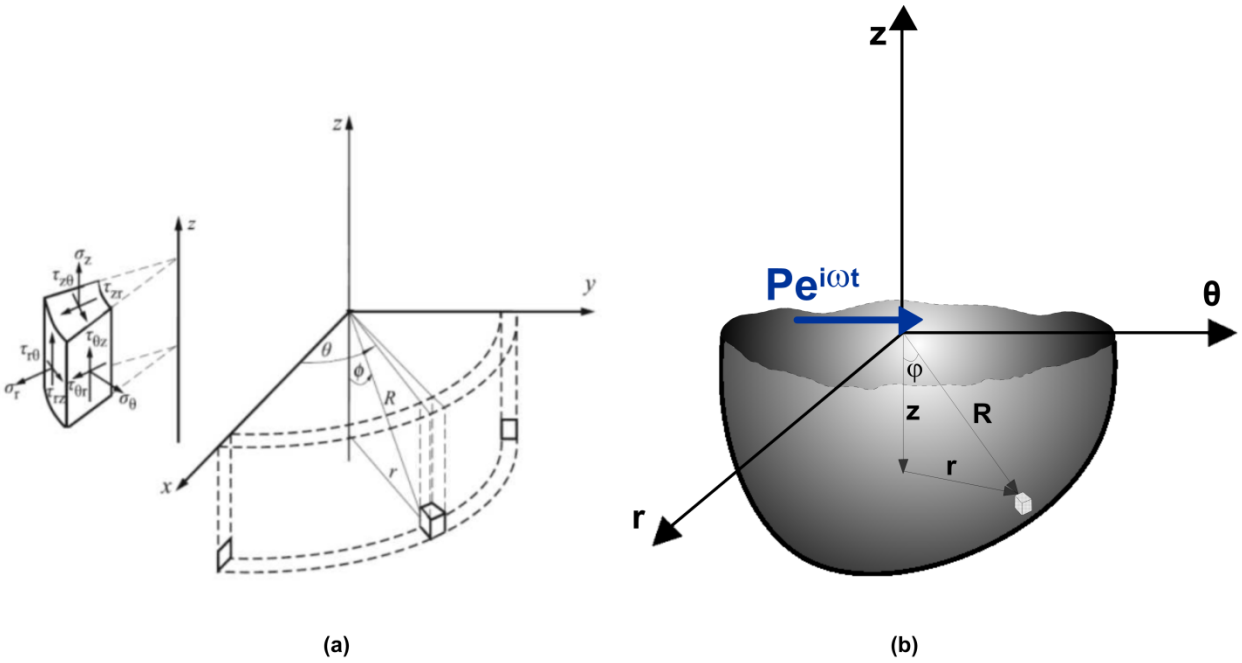

Figure 3.4: (a) Cartesian versus cylindrical coordinates - Adapted from Schepers et al. (2010), (b) Dynamic horizontal point load problem

Following the same approach as the one described in Section 3.2.2 along with considering the three dimensional nature of the problem, Equation 3.19 shows the dimensionless presentation of a harmonically applied horizontal point load. In this dynamic problem ($\sigma_{ij}R^2/P$) is a function of soil v and ξ, aperture angle, azimuthal angle, and dimensionless frequency:

$$\frac{\sigma_{ij}R^2}{P} = g\left(\varphi, \theta, \nu, \xi, \frac{\omega R}{V_S}\right) \tag{3.19}$$

3.3 NUMERICAL TECHNIQUE AND SOFTWARE VERIFICATION

As discussed previously, the stress responses are not fully available in closed-form for two dynamic problems described in Sections 3.2.2 and 3.2.4. Nevertheless, utilization of Buckingham's π theorem together with dimensional analysis provides a basis to redefine such problems in the most physically meaningful dimensionless format. The missing part, however, is the function g in Equations 3.12 and 3.18. Evidently, this function is not unique and changes depending on the stress component of interest. Instead of solving the governing differential equation of the system analytically, which is a formidable task, function g is investigated here numerically.

The selection of a numerical technique is tied to the ability of the technique and the software to address the effects of fundamental parameters of the problem. In the dynamic vertical and horizontal point load problems discussed previously, determinative parameters are the frequency of the applied load and geometric location of the element within the soil medium. Other components to be considered are the accuracy of the technique in dynamic analysis and its capability to properly address the radiation of energy to infinity. Considering the specific parameters that characterize the problem, we selected the boundary element method numerical technique as implemented in software ISoBEM (2012).

BEM is a computational tool for solving a wide range of differential equations numerically. In a particular problem, the fundamental solution of the differential equation, or Green's function, is employed by BEM to develop the solution at any internal point given the solution at its boundary. The fundamental solutions for partial differential equations (PDE) are generally proposed for infinite domains which are free of boundary conditions (and thus of complications resulting from presence of surface waves). For example, Kelvin's and Stoke's

fundamental solutions are developed in elastostatics and elastodynamics problems, respectively. In some problems involving semi-infinite or infinite domains, it is possible to find the solutions of the PDE given the boundary conditions. In such cases, the solutions are called Green's functions, which in many cases can only be obtained numerically (Roach, 1982).

BEM has a number of distinct advantages over FEM for linear elastic problems in semi-infinite domains under dynamic loading. The BEM reduces the dimensions of the problem by one, as discretization is restricted only to the boundary, thereby leading to influence matrices of very small size and simplifying the data input during pre-processing. Moreover, the presence of the fundamental solution increases the accuracy of BEM. The latter advantage over FEM is more pronounced in problems addressing fracture mechanics and semi-infinite domains. The most important strength of BEM in such problems is the accuracy and efficiency of solutions, as the radiation condition at infinity is satisfied spontaneously by the fundamental solution (Banerjee and Wilson, 1989). Moreover in BEM, the solution is obtained in the interior domain at any desired point with no need for considering inter-element continuity as in FEM. Although influence matrices have very small sizes, they are fully populated, non-symmetric and complex-valued which leads to increasing the time required to solve the matrix equations. But the development of efficient solvers in recent years increases the computational capacity and reduces the processing time significantly. It is important to note that fundamental solutions are not fully available for very special categories of problems. In such cases, special integration techniques are required due to the singular nature of the solutions. It is worth mentioning that compared to FEM, BEM is much more sophisticated from the programming perspective; hence, fewer BEM-based platforms are available in the market (ISoBEM, 2012).

ISoBEM (2012) is an advanced, user-friendly platform that employs BEM for solving a wide range of engineering problems including compressible and incompressible elastostatics and elastodynamics, SSI, and propagation of 2-D and 3-D elastic waves in soil. For each problem, a complete set of integral formulation, corresponding Green's function, and numerical implementation are presented in ISoBEM Theory Manual. ISoBEM can accommodate non-uniform soil properties by specifying multiple boundaries at their interfaces. These boundaries, including the ground surface, can be flat or inclined.

The accuracy of ISoBEM analyses are verified for the static vertical and horizontal loading problems as well as corresponding dynamic problems in the following sections. Moreover, a final verification is performed to confirm the normalization of stresses.

3.3.1 Verification of ISoBEM Analyses – Static Problems

The accuracy of ISoBEM analyses are verified for the static vertical and horizontal loading problems in Figures 3.5 and 3.6, which compare vertical, shear, radial, and hoop stress components from ISoBEM analyses to the Boussinesq and the Cerruti solutions, respectively. In both cases, a total of 30 nodes are created at which the internal stresses are calculated by ISoBEM. These nodes are located 1m below the surface boundary and are spaced 0.05m apart. The element types applied for these analyses are considered to be Two-node Linear Line (2LL) for both axisymmetric (vertical point load) and anti-symmetric (horizontal point load) modeling.

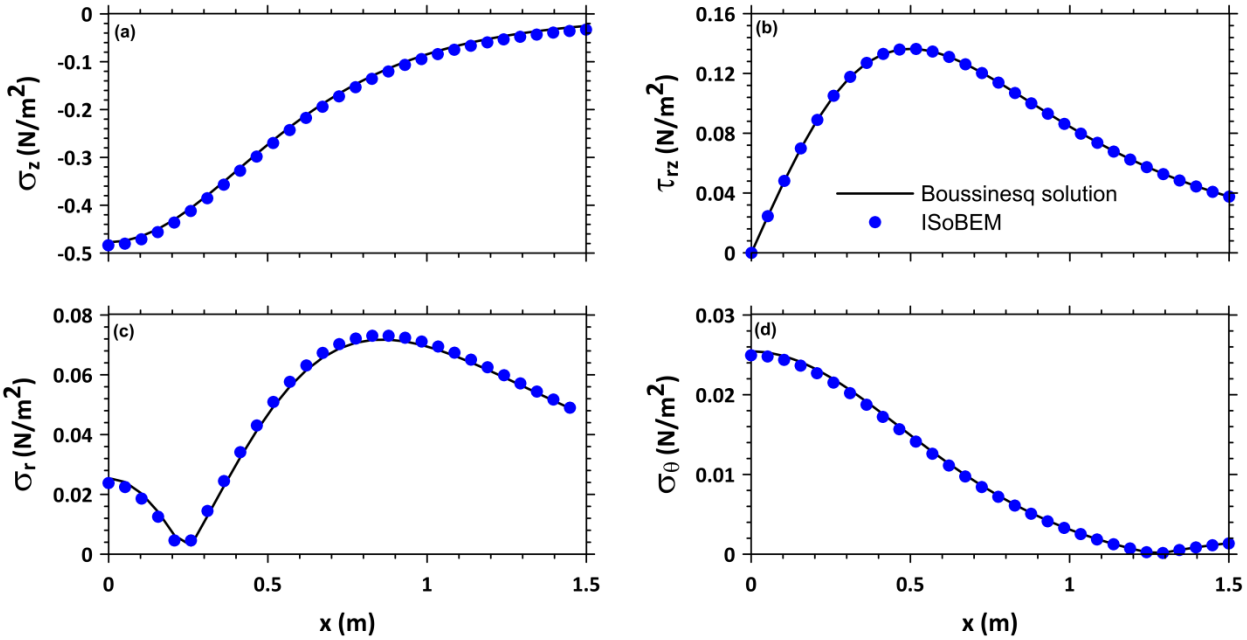

Figure 3.5 Comparison between ISoBEM and analytical solution for classical Boussinesq problem (a) Vertical, (b) Shear, (c) Radial, (d) Hoop stress components (y = 0, z = -1 m, P =1 N, ρ = 1.8 Mg/m3, V_S = 100 m/s, v = 0.33)

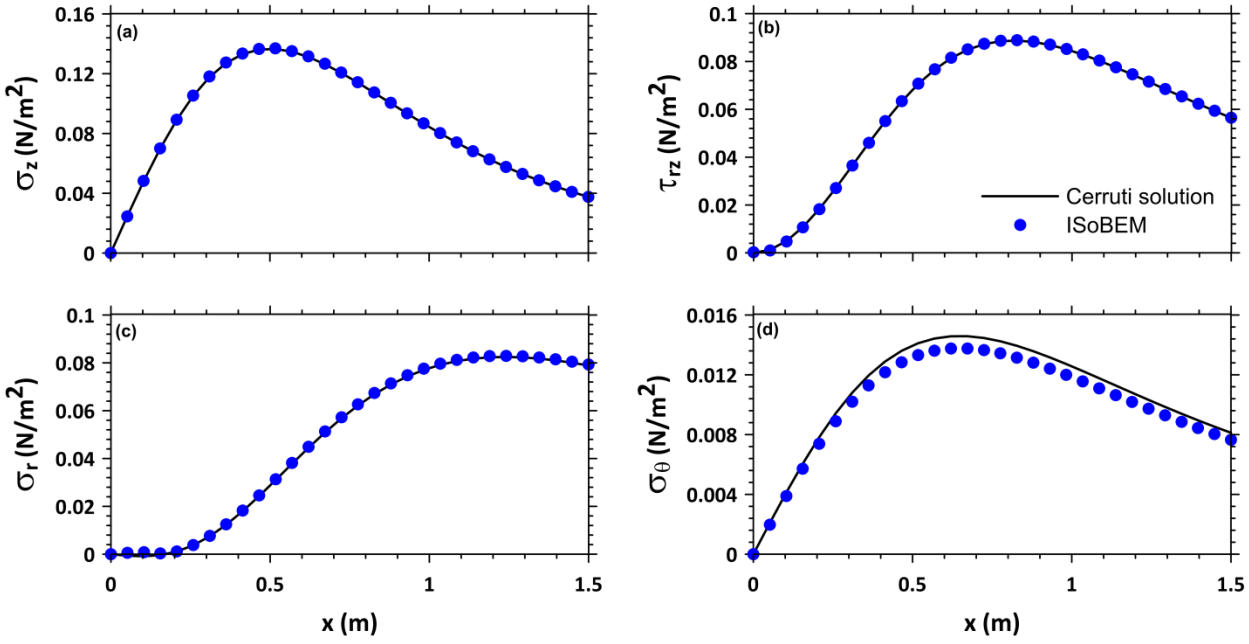

Figure 3.6 Comparison between ISoBEM and analytical solution for classical Cerruti problem (a) Vertical, (b) Shear, (c) Radial, (d) Hoop stress components (*y* = 0, *z* = -1 m, *P* =1 N, *ρ* = 1.8 Mg/m^3, V_S = 100 m/s, *v* = 0.33)

As shown in Figures 3.5 and 3.6, there is nearly perfect compatibility between the stress fields obtained from the Boussinesq and Cerruti closed-form solutions and ISoBEM. It is also confirmed that the axisymmetric and anti-symmetric setups perform well while reducing processing time significantly and enabling the user to apply a denser mesh that helps increasing accuracy in dynamic analyses.

3.3.2 Verification of ISoBEM Analyses – Dynamic Problems

To validate the solutions obtained from ISoBEM analysis in dynamic problems, a comparison is performed with the solution provided by Schepers et al. (2010). As discussed in Chapter 2, Schepers et al. (2010) proposed numerical techniques to evaluate the inversion integrals for the problems of harmonic vertical and horizontal point loads applied on the surface of a visco-elastic half-space. They presented their results in form of dimensionless stress bulbs for various frequencies and a range of Poisson's ratios. In all cases, a damping ratio of 0.5%, shear wave velocity of 100 m/s, and mass density of 1.8 Mg/m^3 were assumed. The last two parameters were employed without loss of generality, as explained below.

The normalization is performed based on the corresponding static stress value at the reference location $R_0(\varphi)$ = 1 m (representing the radial distance along the ray = 0°, 45° , or 90° depending on the stress component). It is important to note that all bulbs in one tile are lines of "one and only one" non-dimensional constant stress value. Thus, the dimensional value is equal to the corresponding static stress at the reference location R_0, which could be calculated from the appropriate static closed-form equation, i.e. Boussinesq or Cerruti solution. As all bulbs are lines of one and only one constant stress value, the stress magnitude of the static case and the non-scaled dynamic ones are equal at any point on any bulb of a tile.

In the cases of a harmonic vertical and horizontal applied point loads, comparisons are performed between vertical and shear stress results from ISoBEM analyses and the solution of Schepers et al. (2010) for $\nu = 0.33$, $\xi = 0.5\%$, $V_S = 100$ m/s, and $\rho = 1.8$ Mg/m^3. The outcomes of these comparisons are presented in Tables 3.1 and 3.2 for vertical and horizontal loads, respectively. The stress values corresponding to Schepers et al. (2010) were computed using a MATLAB script provided by Schepers that evaluates the associated integrals numerically (personal communication, 2013).

Table 3.1 ISoBEM axisymmetric verification models for vertical load.
SEA 2010=Schepers et al. (2010)

Freq f (Hz)	Coord. (r,z) (m)	ISoBEM σ_z (N/m^2)	SEA 2010 σ_z (N/m^2)	σ_z Diff. (%)	Coord. *(r,z)* (m)	ISoBEM τ_{hv} (N/m^2)	SEA 2010 τ_{hv} (N/m^2)	τ_{hv} Diff. (%)
0	(0,-1)	0.484	0.478	1%	(0.704,-0.704)	0.170	0.170	0%
12.5	(0,-0.958)	0.595	0.468	24%	(0.758,-0.758)	0.176	0.168	5%
25	(0,-1.188)	0.530	0.462	14%	(1.032,-1.032)	0.162	0.209	25%
37.5	(0,-1.406)	0.450	0.461	2%	(1.11,-1.11)	0.177	0.166	7%
50	(0,-1.450)	0.453	0.458	1%	(1.176,-1.176)	0.144	0.114	23%

Table 3.2 ISoBEM anti-symmetric verification models for horizontal load.
SEA 2010=Schepers et al. (2010)

Freq f (Hz)	Coord. (r,z) (m)	ISoBEM σ_z (N/m^2)	SEA 2010 σ_z (N/m^2)	σ_z Diff. (%)	Coord. *(r,z)* (m)	ISoBEM τ_{hv} (N/m^2)	SEA 2010 τ_{hv} (N/m^2)	τ_{hv} Diff. (%)
0	(0.704,-0.704)	0.1703	0.170	0%	(0,-1)	0.170	0.170	0%
12.5	(0.758,-0.758)	0.1340	0.116	15%	(0,-0.958)	0.168	0.157	8%
25	(1.032,-1.032)	0.1347	0.115	17%	(0,-1.188)	0.167	0.172	3%
37.5	(1.11,-1.11)	0.1573	0.149	6%	(0,-1.406)	0.219	0.223	2%
50	(1.176,-1.176)	0.1786	0.188	5%	(0,-1.450)	0.243	0.221	10%

While the results are generally compatible, they exhibit differences of up to approximately 25%, which is considered high for this relatively well-defined and simple

problem. Accordingly, we performed additional checks of displacement results between the MATLAB script, ISoBEM, and numerical finite element analyses performed by E. Esmaeilzadeh (personal communication, 2015) using an axisymmetric frequency domain wave solver with perfectly matched layers as absorbing boundary conditions (Esmaeilzadeh et al., 2015). In these finite element analyses, element sizes are determined such that at least 20 nodes are enclosed within the smallest wavelength ($\lambda = V_S/f_{max}$) (Bao et al., 1998), where V_S denotes the smallest shear wave speed and f_{max} denotes the maximum discernible frequency. The material used in finite element analyses is compatible with that used in ISoBEM.

The comparison shown in Figure 3.7 indicates that the results from ISoBEM analyses are generally more consistent with those from finite element simulations than with those from Schepers et al. (2010). Exploring the reasons beyond this discrepancy lies beyond the scope of this work.

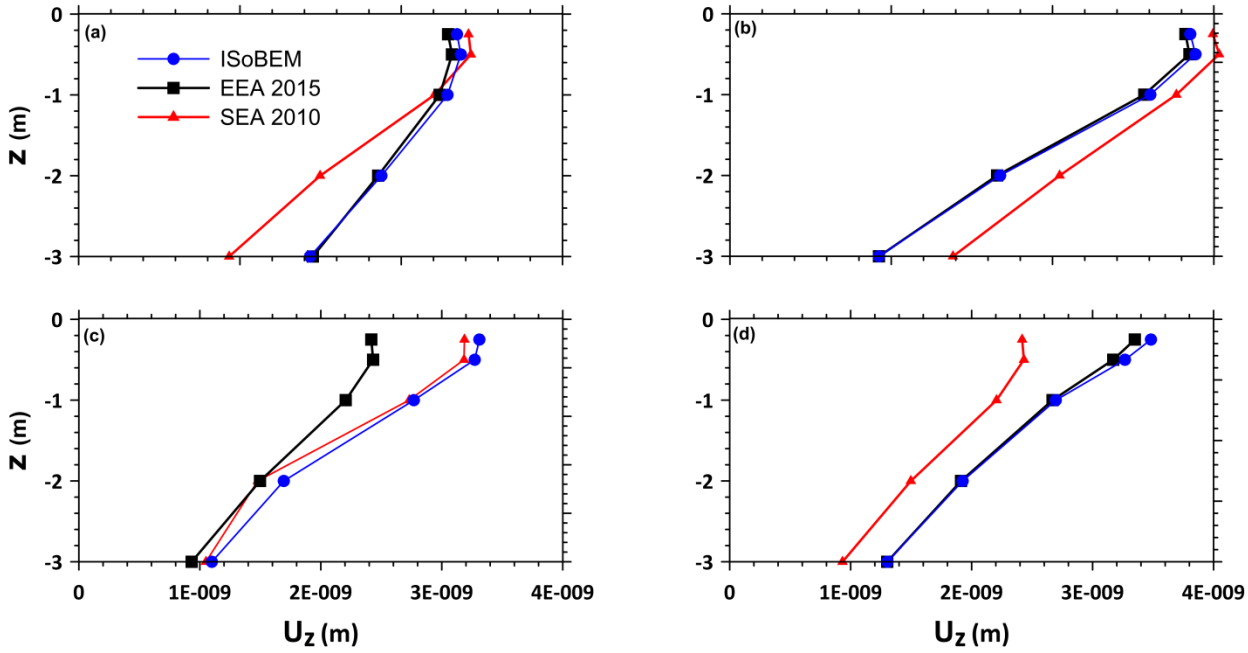

Figure 3.7 Comparison between ISoBEM and solution obtained from FEM (EEA 2015= Esmaeilzadeh et al. (2015)) and SEA 2010 (SEA 2010=Schepers et al. (2010)) for frequencies of (a) 12.5 Hz, (b) 25 Hz, (c) 37.5 Hz, (d) 50 Hz (x = 3 m, P =1 N, ρ = 1.8 Mg/m3, V_S = 100 m/s, v = 0.33)

3.3.3 Verification of ISoBEM Analyses– Normalization

Additional verification is conducted to test the normalization of the dynamic stress results with respect to $(\sigma_{ij}R^2/P)$ and $(\omega R/V_S)$. For this purpose, three models were built in ISoBEM representing different values of frequencies, shear wave velocities, and radial distances, yet identical sets of dimensionless frequencies, $(\omega R/V_S)$. Tables 3.3 and 3.4 summarize the three models used for normalization verifications for vertical and horizontal loads, respectively. Corresponding stress amplitudes are presented in Figures 3.8 and 3.9 in non-normalized and normalized forms for vertical normal stresses σ_z and in-plane shear stresses on horizontal and vertical planes τ_{rz}. The results support the proposed normalization scheme.

Table 3.3 ISoBEM axisymmetric models used to verify normalization for vertical point load; v = 0.34, ξ = 1%.

	Model 1			Model 2			Model 3		
$\omega R/V_S$	ω (rad/s)	V_S (m/s)	R (m)	ω (rad/s)	V_S (m/s)	R (m)	ω (rad/s)	V_S (m/s)	R (m)
0.5	98.06	100.0	0.51	49.75	100.0	1.00	33.26	100.0	1.50
1	196.1	100.0	0.51	99.50	100.0	1.00	66.52	100.0	1.50
2	392.2	100.0	0.51	199.0	100.0	1.00	133	100.0	1.50
4	784.5	100.0	0.51	398.0	100.0	1.00	266	100.0	1.50
6	1177	100.0	0.51	597.0	100.0	1.00	399.1	100.0	1.50
8	1569	100.0	0.51	796.0	100.0	1.00	532.1	100.0	1.50
10	1961	100.0	0.51	995.0	100.0	1.00	665.1	100.0	1.50

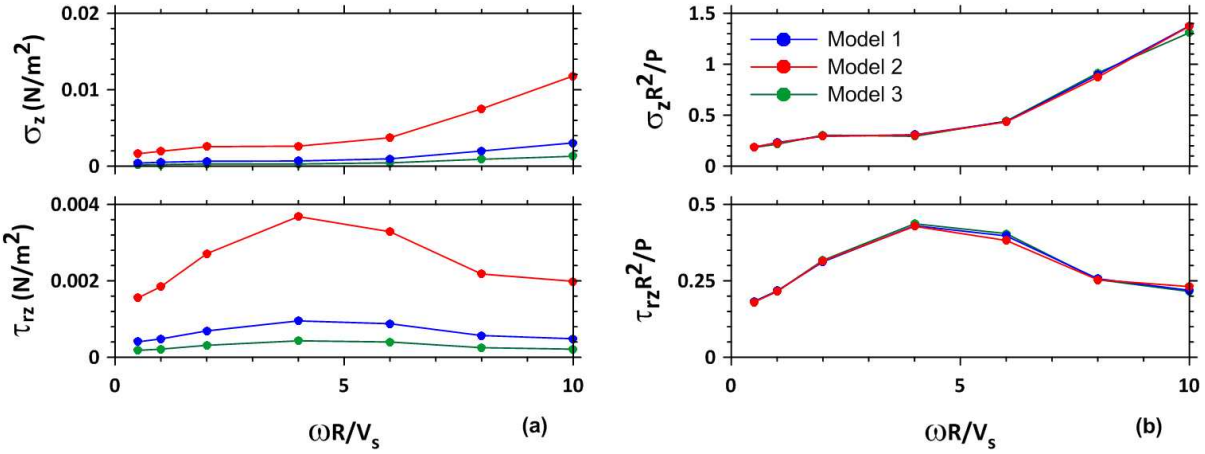

Figure 3.8 Checks of stress normalization using ISoBEM analyses for the conditions described in Table 3.3; (a) stress components (b) normalized stress components

Table 3.4 ISoBEM axisymmetric models used to verify normalization for horizontal point load; v = 0.34, ξ = 1%.

	Model 1			Model 2			Model 3		
$\omega R/Vs$	ω (rad/s)	V_S (m/s)	R (m)	ω (rad/s)	V_S (m/s)	R (m)	ω (rad/s)	V_S (m/s)	R (m)
0.5	98.06	100.0	0.51	49.75	100.0	1.00	49.75	149.6	1.50
1	196.1	100.0	0.51	99.50	100.0	1.00	99.50	149.6	1.50
2	392.2	100.0	0.51	199.0	100.0	1.00	199.0	149.6	1.50
4	784.5	100.0	0.51	398.0	100.0	1.00	398.0	149.6	1.50
6	1177	100.0	0.51	597.0	100.0	1.00	597.0	149.6	1.50
8	1569	100.0	0.51	796.0	100.0	1.00	796.0	149.6	1.50
10	1961	100.0	0.51	995.0	100.0	1.00	995.0	149.6	1.50

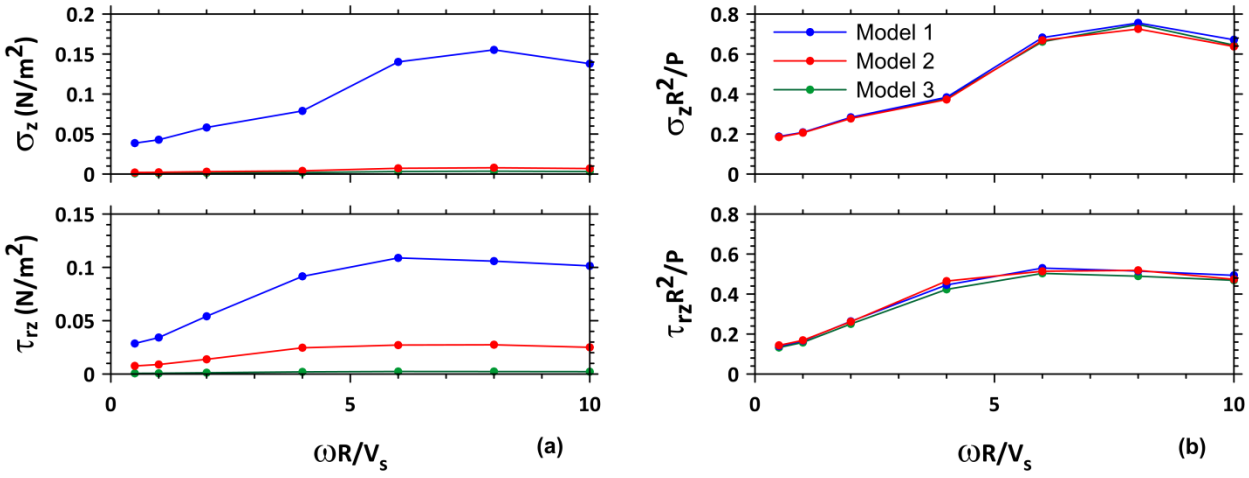

Figure 3.9 Checks of stress normalization using ISoBEM analyses for the conditions described in Table 2; (a) stress components (b) normalized stress components

3.4 A DIMENSIONLESS PRESENTATION OF DYNAMIC STRESS FIELDS

3.4.1 Vertical Point Load

As discussed earlier, stress response due to vertical oscillation of a point load on the surface of the soil mass is represented, in a dimensionless form, at any point inside the half-space using Equation 3.20.

$$\frac{\sigma_{ij}R^2}{P} = g\left(\nu, \xi, \varphi, \frac{\omega R}{V_s}\right) \tag{3.20}$$

Axisymmetric models in ISoBEM were set up to develop dimensionless graphical representations of stress fields resulting from harmonic vertical point loads on a visco-elastic half-space. A total of 40 combinations of dimensionless frequencies, damping and Poisson's ratios are designed to cover the likely parameter range for practical applications. For each combination, locations of internal points are selected such that a full range of angles from 0° to 90° are covered. Such combinations are summarized in four major groups in Table 3.5.

Table 3.5: Summary of model setup in ISoBEM for dynamic point load analysis

Group	Model	φ (°)	$\omega R/V_S$	ω (rad/s)	V_S (m/s)	R (m)	ν	ξ
1	1-10	0 - 90	0 - 20	0 - 12000	300	0.5	0.34	0.01
2	11-20	0 - 90	0 - 20	0 - 12000	300	0.5	0.34	0.05
3	21-30	0 - 90	0 - 20	0 - 12000	300	0.5	0.45	0.01
4	31-40	0 - 90	0 - 20	0 - 12000	300	0.5	0.45	0.05

The models in ISoBEM are set up as axisymmetric where 2LL element types are applied. According to Oudry et al. (2012), a minimum of 16 elements per wavelength is required to ensure accuracy. This is higher that 4-6 nodes per wavelength adopted in finite element analyses (Douglas et al 1972, Wolf 1985). A total of 10,000 elements are considered to mesh the surface boundary. To reduce the processing time, ISoBEM analysis is performed on *HOFFMAN2 Cluster*[1] processors at the University of California Los Angeles (UCLA) and XSEDE[2], which are collections of multiple processors enabling users to run multiple jobs in parallel. The non-zero components of dynamic stress amplitudes and phase angles are generated and plotted as polar graphs. Amplitudes of stress components are presented in Figures 3.11, 3.13, 3.15, and 3.17. To

[1] http://hpc.ucla.edu/hoffman2/hoffman2.php
[2] https://www.xsede.org/

illustrate the effect of dimensionless frequency on the shape of stress bulbs, results are shown in two groups corresponding to ($\omega R/V_S$) = 0 to 2 (left column) and ($\omega R/V_S$) = 4 to 20 (right column).

In these figures, the values read around the radial lines correspond to dimensionless stress amplitudes. To get the dimensional stress values for a specific frequency at a specific location, one should properly calculate the dimensionless frequency ($\omega R/V_S$) then read from the graph the corresponding dimensionless stress values knowing radial distance (R) and aperture angle (φ). The de-normalization should then be performed with respect to known value of vertical point load (P) and R.

The corresponding phase angles are shown in Figures 3.12, 3.14, 3.16, and 3.18. In these figures the values read around the radial lines correspond to actual phase angle in unit of radians. The phase angles are associated with the time shift between the surface load time series and the stress time series at the point of interest. Based on 1-D wave propagation theory, the time shift for a wave travelling at speed V is $\Delta t = R/V$. In turn, the phase shift φ between two sinusoids with frequency ω is related to time shift as $\varphi = \Delta t\omega$. Accordingly, phase shift for 1-D shear wave propagation is equal to $\omega R/V_S$, which is referred to as dimensionless frequency throughout this dissertation.

To help interpret the phase angle behavior, consider the case of the vertical stress component, σ_z, due to a vertical oscillatory surface point load. The axisymmetric models in ISoBEM are set up to investigate phase angles at different aperture angles and the results are presented in Figures 3.10.

The values of phase angles are negative indicating the time lag of vertical stress with respect to the applied load. Moreover, at points along the vertical axis, i.e. aperture angle of 0°, one would expect P-waves to dominant the vertical stress components. According to this expectation, the phase angles should match the theoretical value of $\omega R/V_P$ indicating 1-D P-wave-propagation. As shown in Figure 3.10, this expected behavior is observed at low aperture angles (0 and 10 degrees). At large aperture angles of 70 to 85 degrees, the wave speeds are more akin to those for S-waves or Rayleigh waves, which matches expectation for vertical loads.

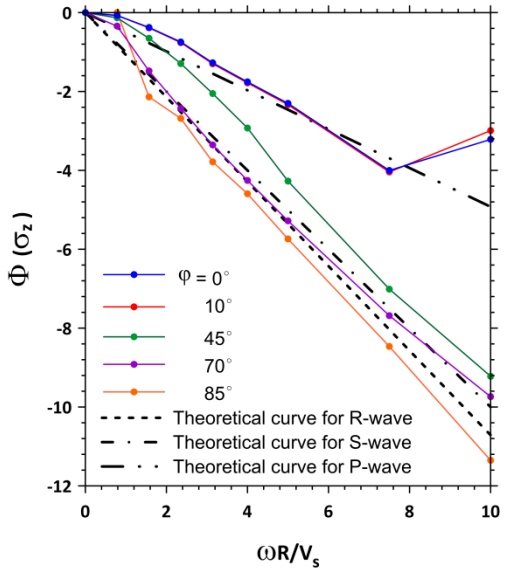

Figure 3.10: Phase angle variation for vertical stress component due to vertical point load, ν = 0.34, ξ = 1%

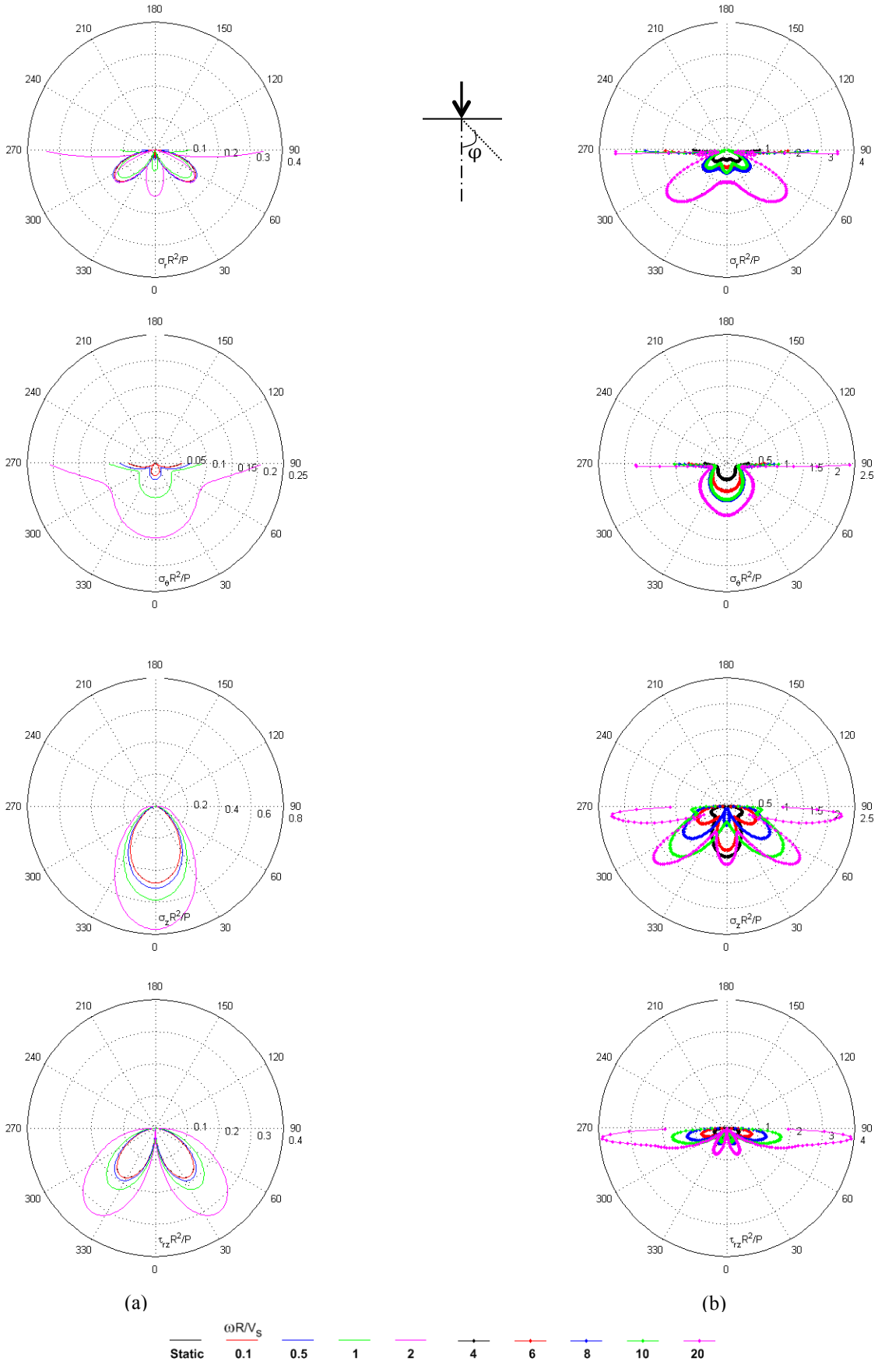

Figure 3.11: Stress amplitude bulbs due to vertical point load, v = 0.34, ξ = 1%; (a) ωR/V_S = 0 (static) to 2, (b) ωR/V_S = 4 to 20

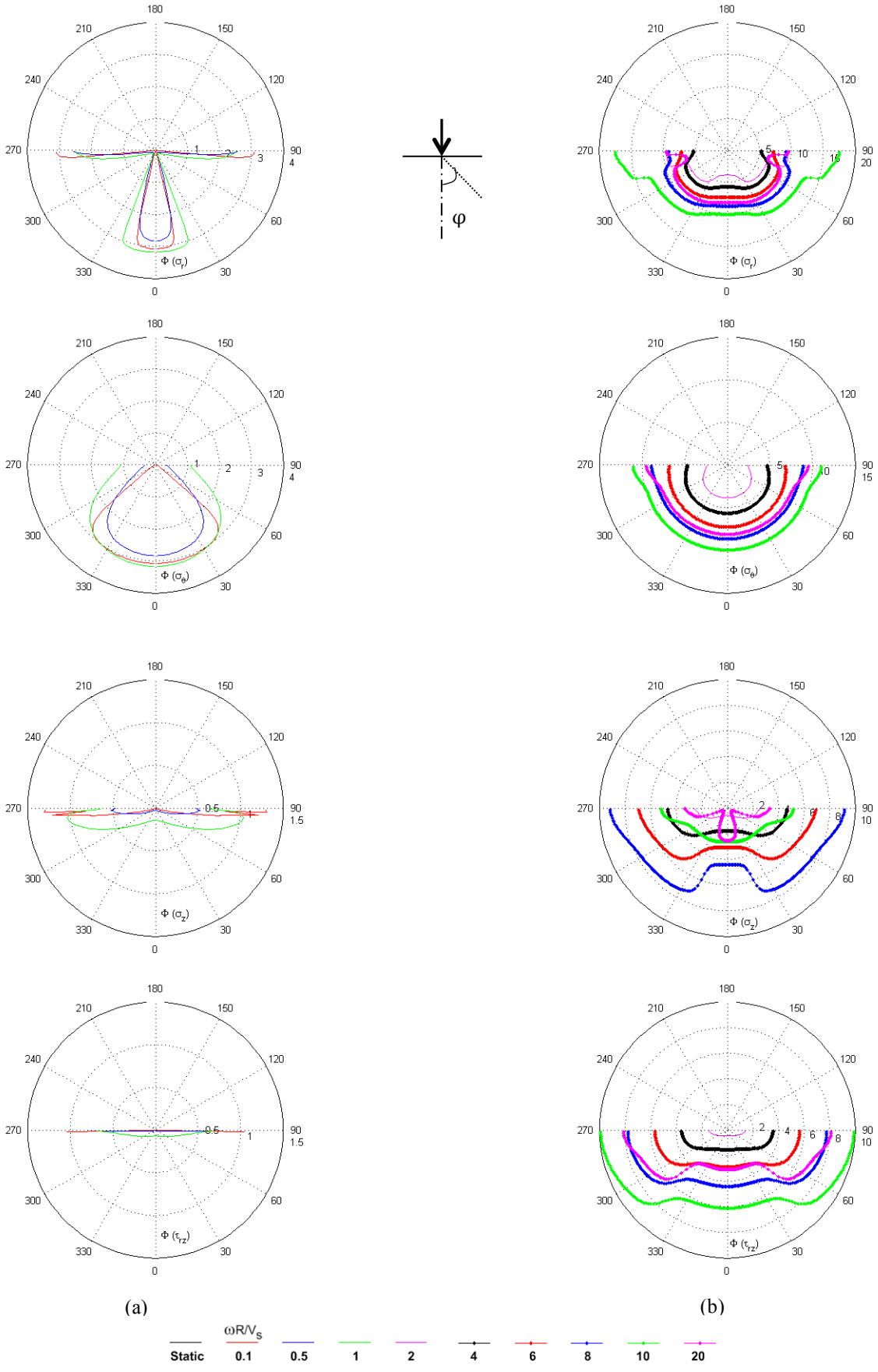

Figure 3.12: Phase angle bulbs due to vertical point load, v = 0.34, ξ = 1%; (a) $\omega R/V_S$ = 0 (static) to 2, (b) $\omega R/V_S$ = 4 to 20

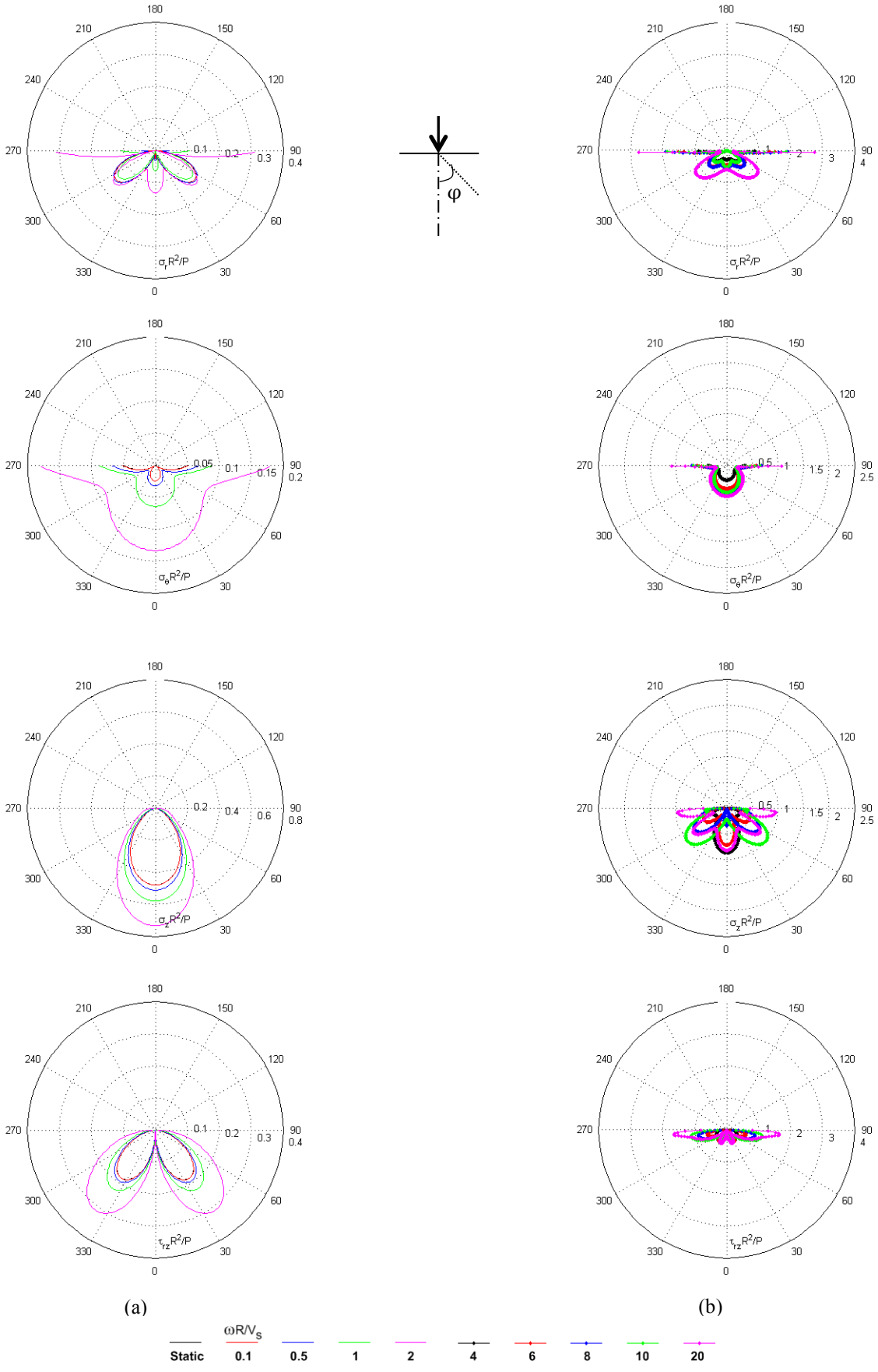

Figure 3.13: Stress amplitude bulbs due to vertical point load, ν = 0.34, ξ = 5%; (a) $\omega R/V_S$ = 0 (static) to 2, (b) $\omega R/V_S$ = 4 to 20

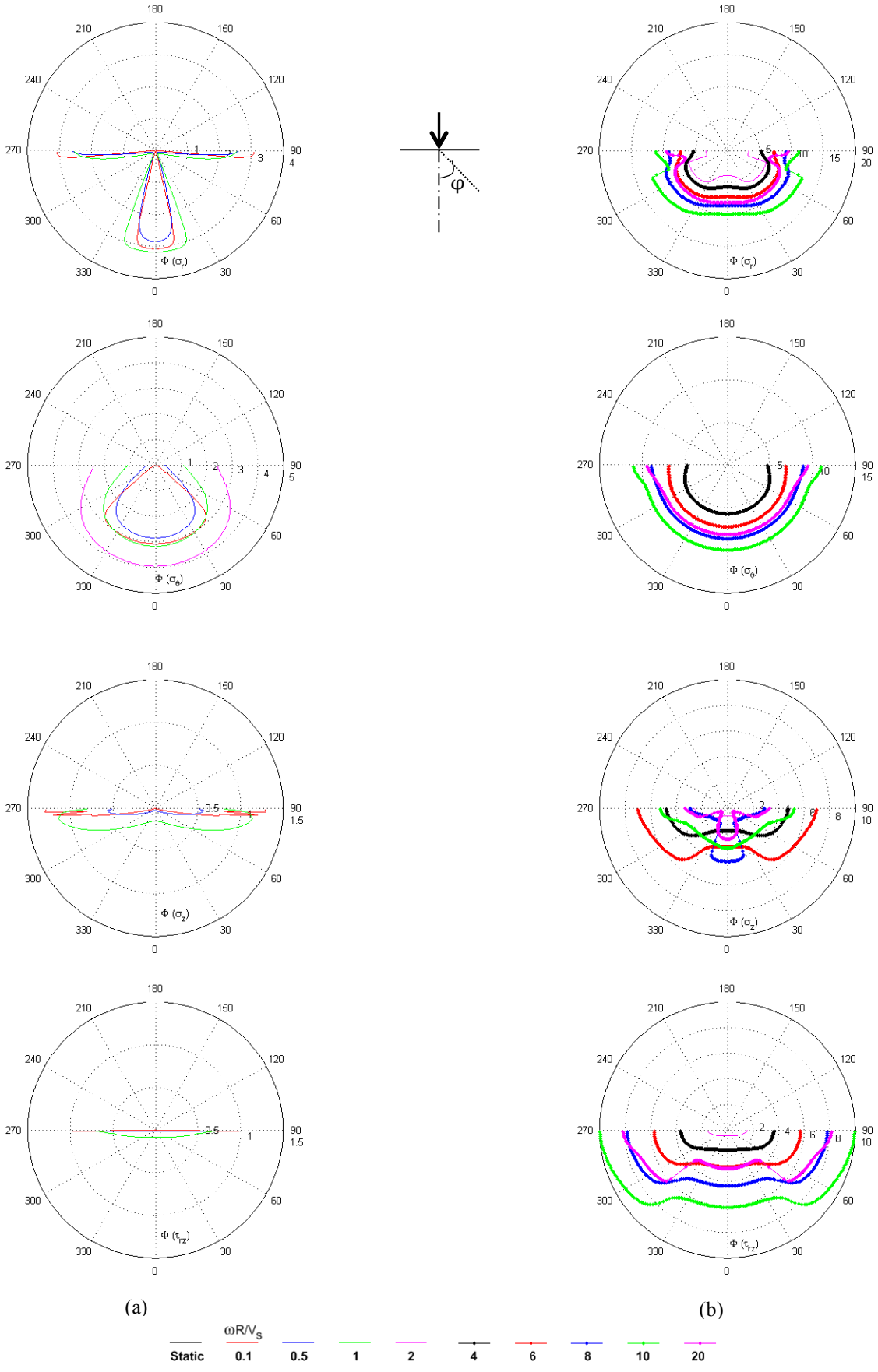

Figure 3.14: Phase angle bulbs due to vertical point load, v = 0.34, ξ = 5%; (a) $\omega R/V_S$ = 0 (static) to 2, (b) $\omega R/V_S$ = 4 to 20

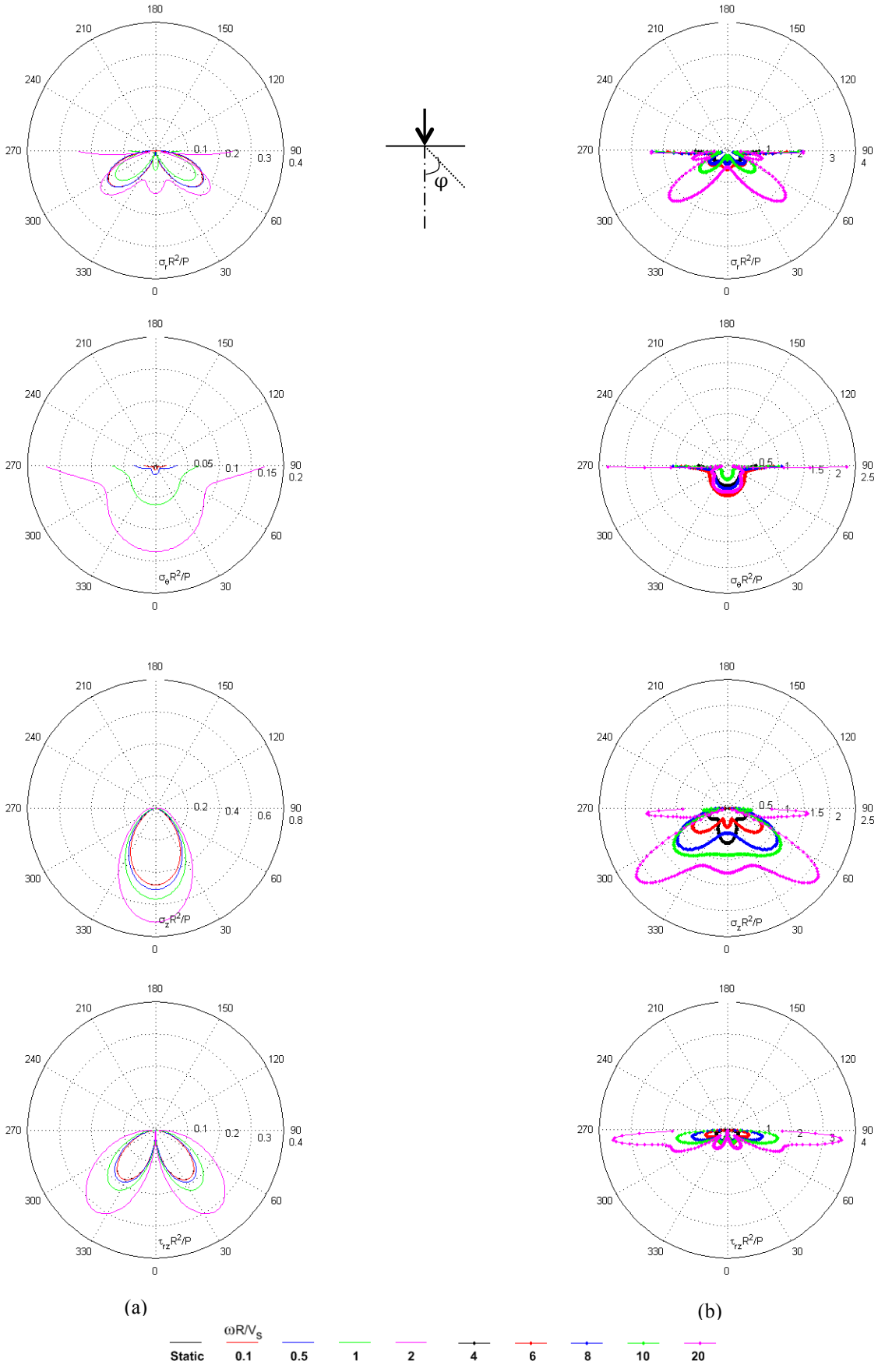

Figure 3.15: Stress amplitude bulbs due to vertical point load, ν = 0.45, ξ = 1%; (a) $\omega R/V_S$= 0 (static) to 2, (b) $\omega R/V_S$ = 4 to 20

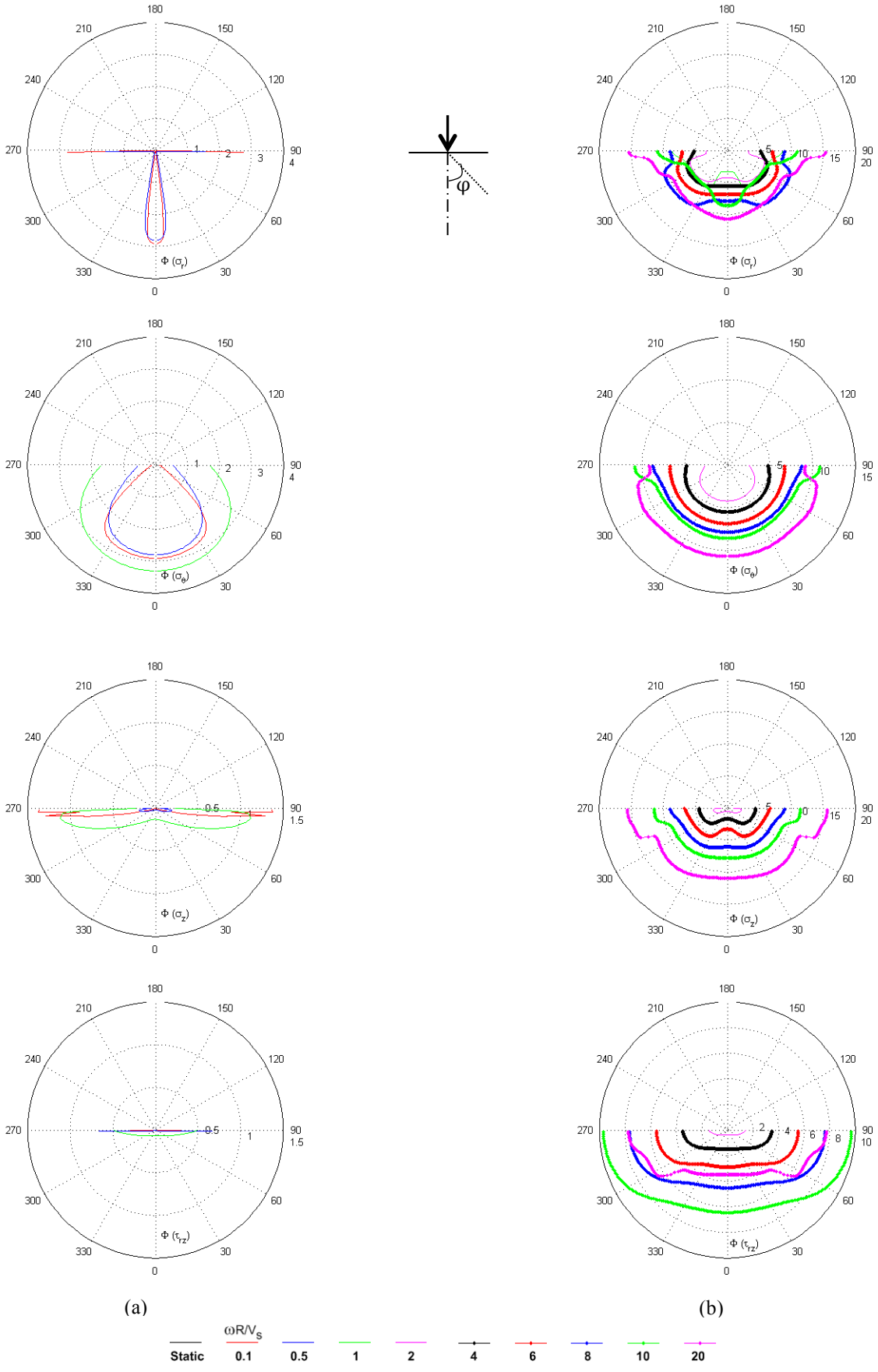

Figure 3.16: Phase angle bulbs due to vertical point load, ν = 0.45, ξ = 5%; (a) $\omega R/V_S$ = 0 (static) to 2, (b) $\omega R/V_S$ = 4 to 20

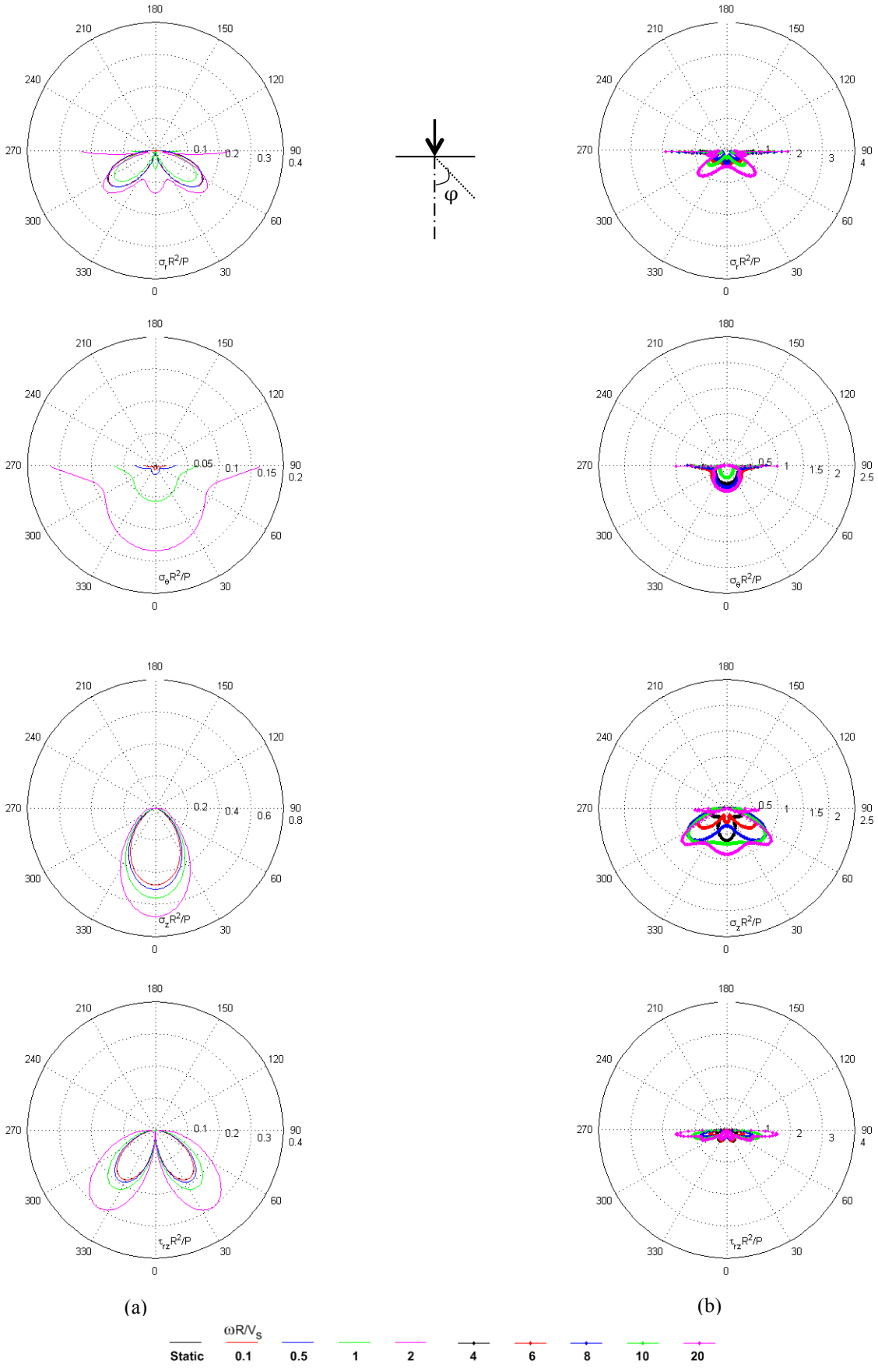

Figure 3.17: Stress amplitude bulbs due to vertical point load, ν = 0.45, ξ = 5%; (a) $\omega R/V_S$ = 0 (static) to 2, (b) $\omega R/V_S$ = 4 to 20

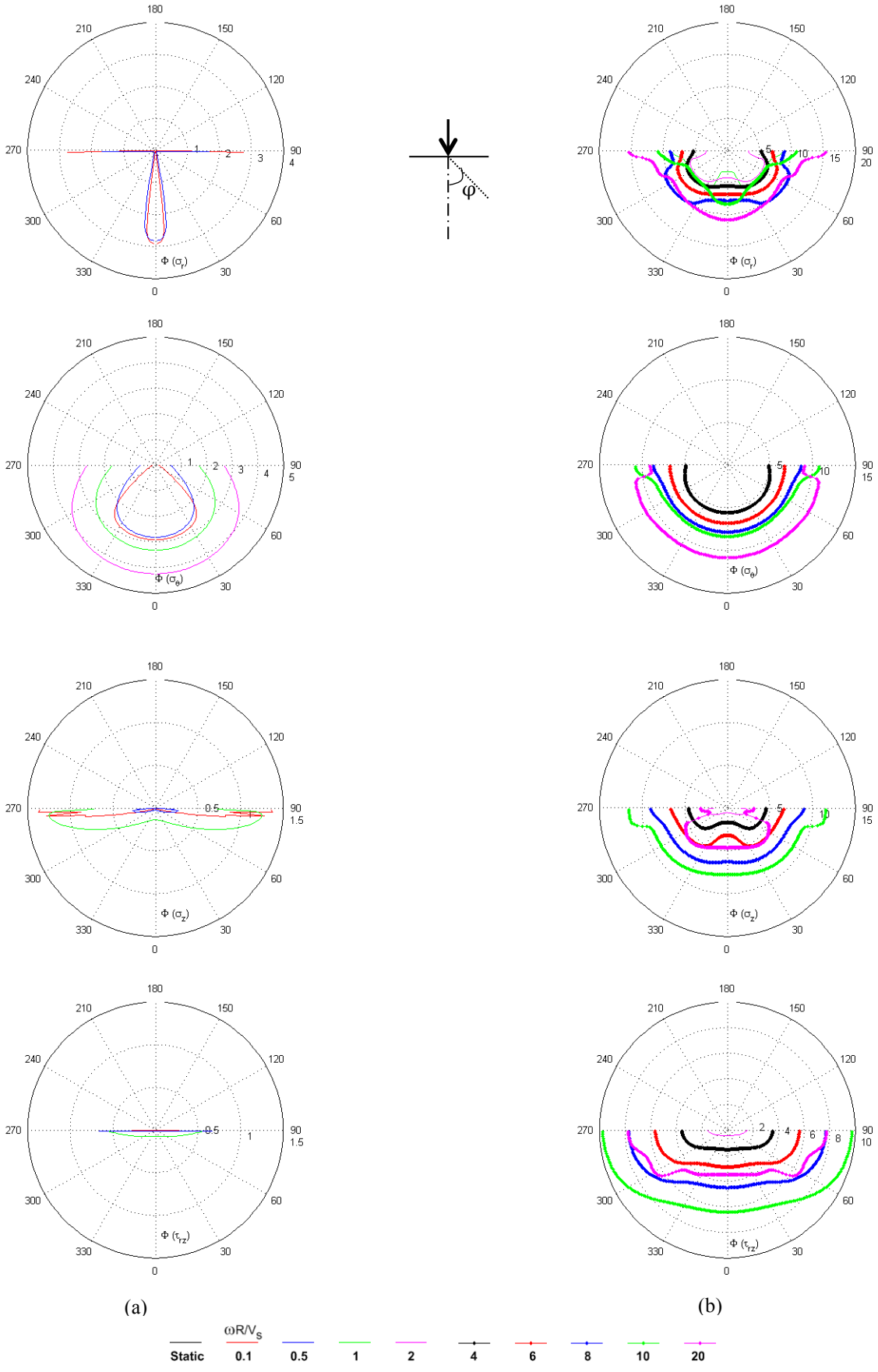

Figure 3.18: Phase angle bulbs due to vertical point load, ν = 0.45, ξ = 5%; (a) $\omega R/V_S$ = 0 (static) to 2, (b) $\omega R/V_S$ = 4 to 20

Stress amplitudes are found to have upper limits of about 2.25 P/R^2 for σ_z and about 4.0 P/R^2 for τ_{rz} in the examined frequency range which far exceeds the corresponding static values. It is also noteworthy that the number of lobes in the stress bulbs increases with frequency, from one under static conditions to five at $(\omega R/V_S) = 20$ for σ_z, and from two in the static case to four at the highest considered dimensionless frequency for τ_{rz}. This pattern can be explained on the basis of successive zones of destructive and constructive interference of P, S and R waves, which is expected to become more pronounced as frequency increases, leading to a flower-like pattern. Similar changes are also observed for the other two stress components, σ_r and σ_θ.

In general, phase angle patterns grow radially with increases of dimensionless frequency, which is expected. As discussed earlier, the phase shift should be roughly equivalent to the dimensionless frequency appropriate to the dominant wave type for the aperture angle under consideration. For instance, for σ_z, at aperture angle of 30°- 60°, phase angle values are close to $\omega R/V_S$; whereas, for higher aperture angles ($\varphi > 60°$), there is a minor increase in phase angle values due to dominancy of Rayleigh waves travelling at velocities slower than that of shear waves. Finally, at aperture angle of 0°, the decrease in phase values is due to the propagating of P-waves along the z-axis.

To help interpret the results, with reference to Figures 3.13 and 3.14, consider the example of a point within the soil media located at r = 1.25 m and z = - 2.16 m. This point is located at radial distance R = 2.5 m from the point of application of the vertical load at a vertical angle of φ = 30 degrees. If V_S = 300 m/s and ω = 60 rad/s, the dimensionless frequency is $\omega R/V_S$ = 0.5. In Figure 3.12, the ray along an aperture angle of 30 degrees intersects the vertical and shear stress bulbs for $\omega R/V_S$ = 0.5 (i.e. solid blue curve) at dimensionless values of 0.34 and 0.19, respectively. For a unit vertical point load (P = 1 kN), vertical and shear stress amplitudes

are obtained by dividing the aforementioned values by R^2 (i.e., σ_z = 54 kN/m^2 and τ_{rz} = 30 kN/m^2).

The corresponding phase angles are 0.01π and 0.003π for vertical and shear components, respectively. At zero frequency (static case), the corresponding stresses are 51 and 28 kN/m^2 and the phase angles are zero.

The results from Figures 3.11 and 3.15 and Figures 3.13 and 3.17 can be compared to show the effects of Poisson's ratio on stress bulbs; while Figures 3.11 and 3.13 and Figures 3.15 and 3.17 can be used to investigate damping effects. The most critical effects of Poisson's ratio are summarized in Figure 3.19, which shows that an increase of Poisson's ratio causes no perceptible change in stress bulb amplitudes or phase angles for aperture angles associated with shear wave propagation (approximately 45º to 60º). However, Poisson's ratio increases produce stress amplitude increases and decreases for aperture angles associated with P-wave (0º − 45º) and Rayleigh wave (45º to 90º) propagation, respectively. Our interpretation is that in the high-ν case, the higher bulk moduli of the soil 'attracts' more P-wave propagation (at the expense of Rayleigh wave energy), thereby modifying stress amplitudes associated with these wave types. These effects are most apparent for relatively high values of dimensionless frequencies ($\omega R/V_S$ = 10, 20).

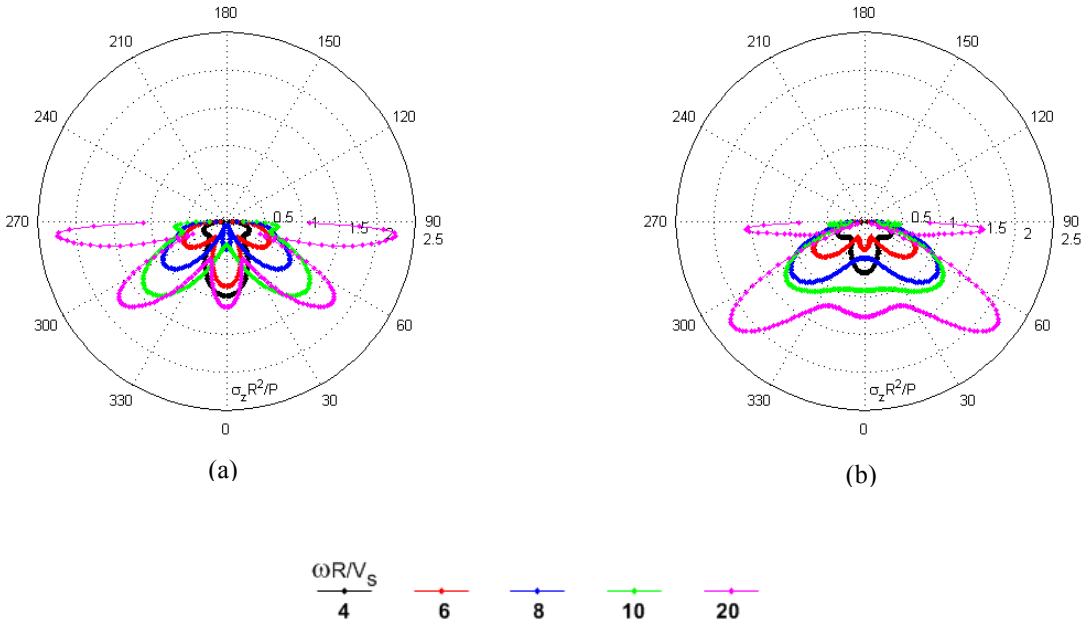

Figure 3.19: Stress amplitudes due to vertical point load, ξ = 1%; (a) v = 0.34, (b) v = 0.45

Figure 3.20 shows the most critical effects of increasing soil damping ratio. As expected, there is a reduction of stresses with increasing damping, which are more obvious for high values of dimensionless frequencies ($\omega R/V_S = 4 - 10$). Aside from stress reductions, increasing damping also serves to smooth the dramatic sharpness in dimensionless stress bulbs for high values of dimensionless frequencies.

It should be noted that the complete sets of results corresponding to 1° increments of azimuthal angle are available in the digital text files (i.e. libraries) and will be used in Chapter 5 to extend the point load solutions to the distributed load cases.

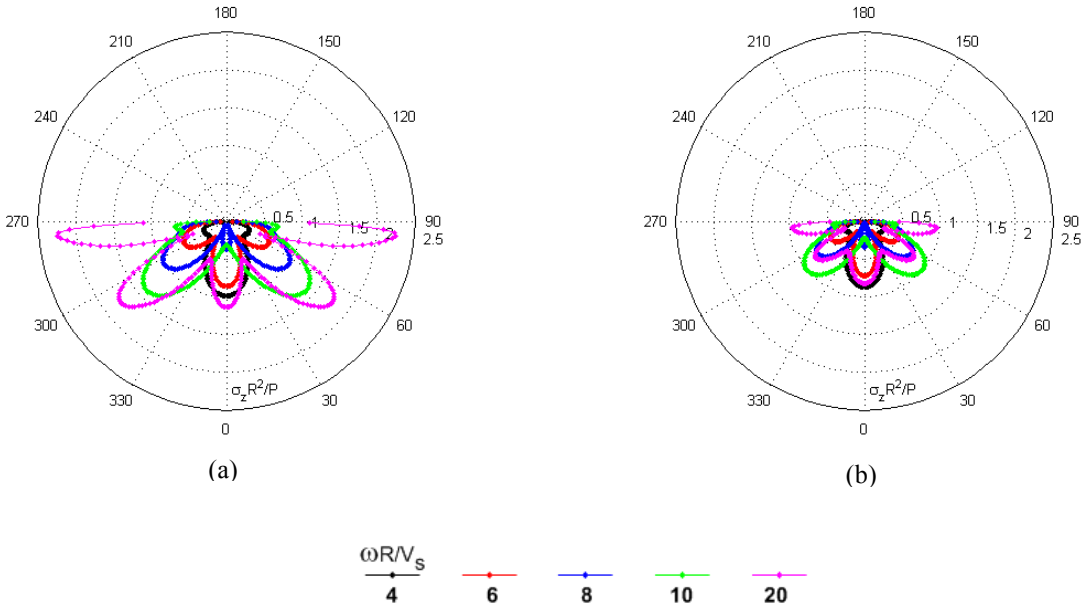

Figure 3.20: Stress amplitudes due to vertical point load, v = 0.34; (a) ξ = 1%, (b) ξ = 5%

3.4.2 A Dimensionless Presentation of Dynamic Stress Field – Horizontal Point Load

As discussed earlier, stress response due to horizontal oscillation of a point load on the surface of the soil mass is represented in a dimensionless form at any point inside the half-space using Equation 3.21.

$$\frac{\sigma_{ij}R^2}{P} = g\left(\varphi,\theta,\nu,\xi,\frac{\omega R}{V_s}\right) \tag{3.21}$$

Similar to the vertical point load case, 40 axisymmetric models in ISoBEM were set up. To account for the three-dimensional aspect of the problem, azimuthal angles from 0° to 360° were considered (strictly, a range of 0-180° would suffice, but ISoBEM uses the larger range by default). To illustrate the behavior, the non-zero components of dynamic stress amplitudes and phase angles at θ = 0° (i.e. σ_r, σ_θ, σ_z, and τ_{rz}) and at θ = 90° (i.e. $\tau_{r\theta}$ and $\tau_{\theta z}$) are generated and plotted as polar graphs. Amplitudes of stress components are presented in Figures 3.22, 3.24,

3.26, and 3.28. Similar to the vertical point load case, results are shown in two groups corresponding to ($\omega R/V_S$) = 0 to 2 (left column) and ($\omega R/V_S$) = 4 to 20 (right column). In these figures, the values read around the radial lines correspond to dimensionless stress amplitudes.

The corresponding phase angles are shown in Figures 3.23, 3.25, 3.27, and 3.29. In these figures the values read around the radial lines correspond to actual phase angle in unit of radians.

As indicated earlier, for 1-D wave propagation, the theoretical value of phase angle should be equal to the corresponding dimensionless frequency considering the dominant wave type. To help interpret the phase angle behavior shown in previous figures, it is useful to consider the case of in-plane shear stress component, τ_{rz}, due to a horizontal oscillatory surface point load. The axisymmetric models in ISoBEM were set up to investigate phase angles at different aperture angles and the results are presented in 3.21.

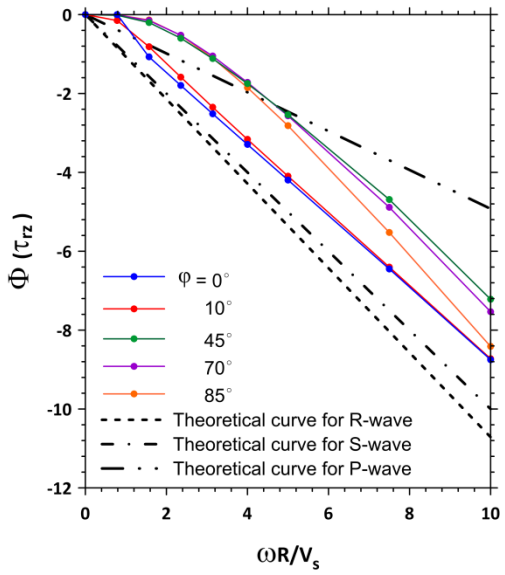

Figure 3.21: Phase angle variation for in-plane shear stress component due to horizontal point load, v = 0.34, ξ = 1%

The values of phase angles are negative indicating the time lag with respect to the applied load. Moreover, the in-plane shear stress component at any points along the vertical axis is

expected to be dominated by the 1-D propagation of shear waves; hence the phase angle should be equal to $\omega R/V_S$. As shown in Figure 3.21, the observed trends nearly match this expectation for aperture angles of 0 and 10 degrees. For larger aperture angles, the wave speeds are considerably faster, likely due in part to P-waves.

It should be noted that the complete sets of results corresponding to 1° increments of azimuthal angle are available in the digital text files (i.e. libraries) and will be used in Chapter 5 to extend the point load solutions to the distributed load cases.

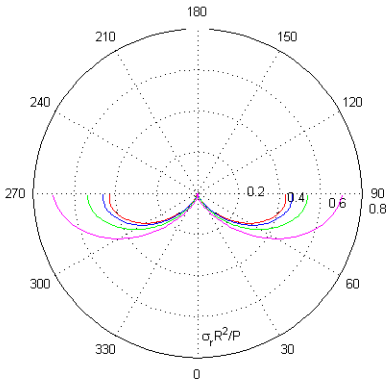
180
210
150
240
120
270
90
300
60
330
30
0
0.2
0.4
0.6
0.8
$\sigma_r R^2/P$

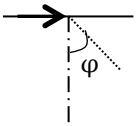
φ

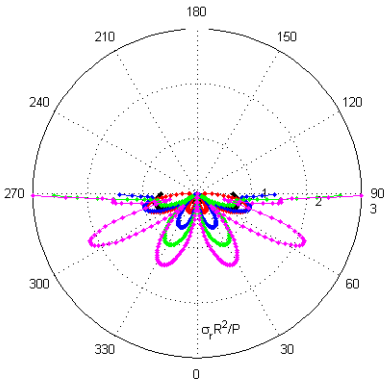
180
210
150
240
120
270
90
300
60
330
30
0
2
3
$\sigma_r R^2/P$

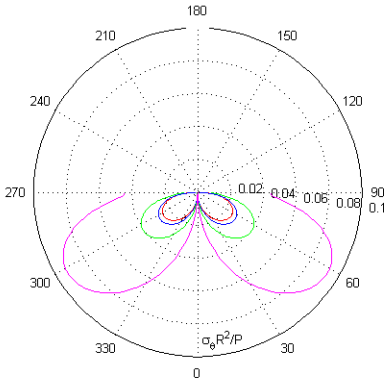
180
210
150
240
120
270
90
300
60
330
30
0
0.02
0.04
0.06
0.08
0.1
$\sigma_\theta R^2/P$

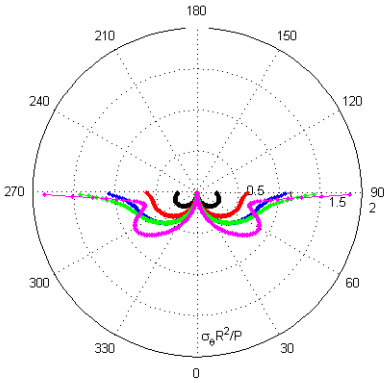
180
210
150
240
120
270
90
300
60
330
30
0
0.5
1.5
2
$\sigma_\theta R^2/P$

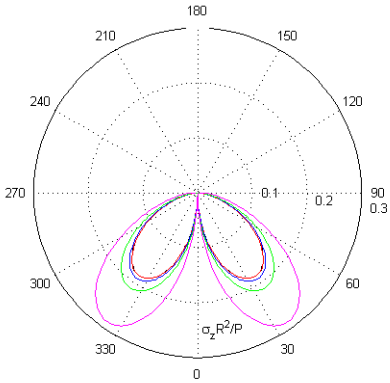
180
210
150
240
120
270
90
300
60
330
30
0
0.1
0.2
0.3
$\sigma_z R^2/P$

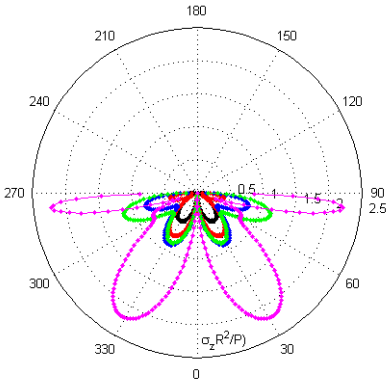
180
210
150
240
120
270
90
300
60
330
30
0
0.5
1
1.5
2
2.5
$\sigma_z R^2/P)$

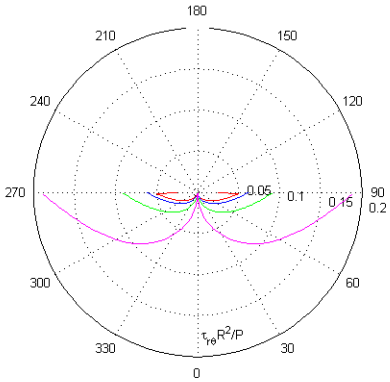
180
210
150
240
120
270
90
300
60
330
30
0
0.05
0.1
0.15
0.2
$\tau_{r\theta} R^2/P$

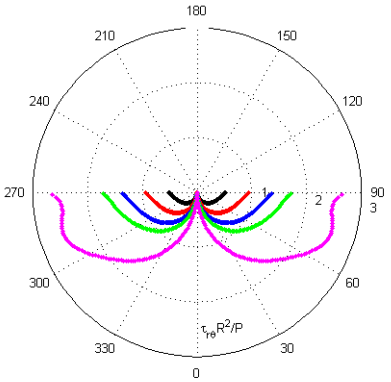
180
210
150
240
120
270
90
300
60
330
30
0
1
2
3
$\tau_{r\theta} R^2/P$

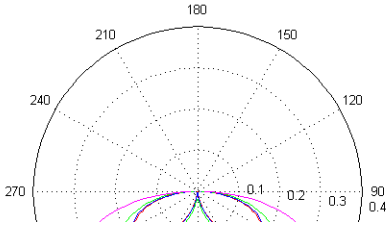
180
210
150
240
120
270
90
300
60
330
30
0
0.1
0.2
0.3
0.4

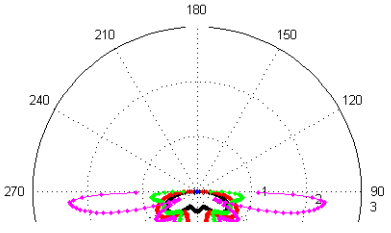
180
210
150
240
120
270
90
300
60
330
30
0
1
2
3

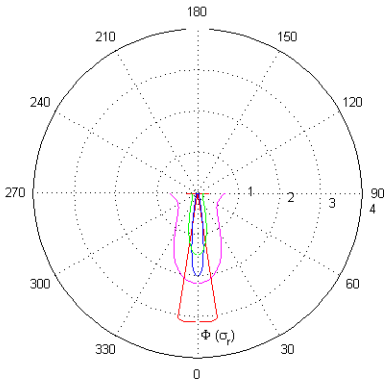
180
210
150
240
120
270
90
300
60
330
30
0
1
2
3
4
Φ (σr)

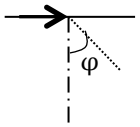
φ

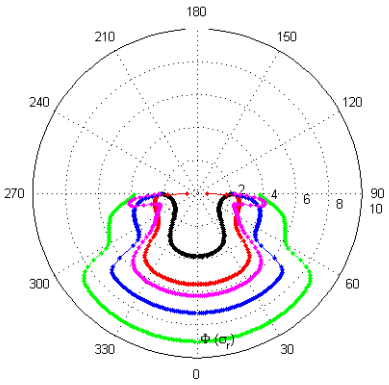
180
210
150
240
120
270
90
300
60
330
30
0
2
4
6
8
10
Φ (σr)

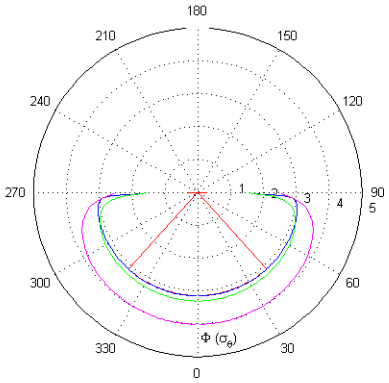
180
210
150
240
120
270
90
300
60
330
30
0
1
2
3
4
5
Φ (σθ)

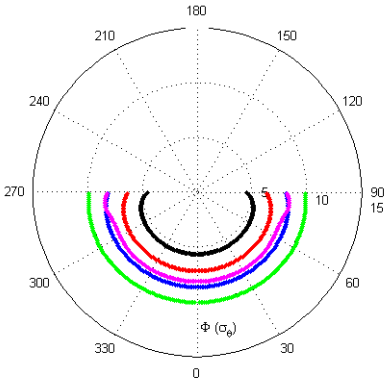
180
210
150
240
120
270
90
300
60
330
30
0
5
10
15
Φ (σθ)

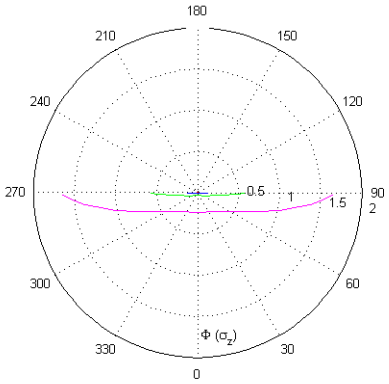
180
210
150
240
120
270
90
300
60
330
30
0
0.5
1
1.5
2
Φ (σz)

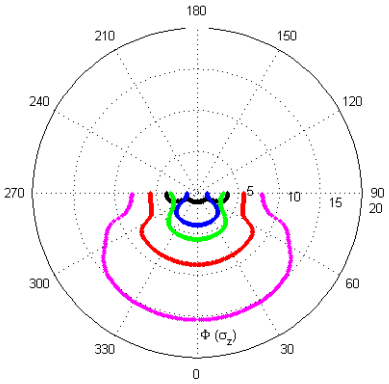
180
210
150
240
120
270
90
300
60
330
30
0
5
10
15
20
Φ (σz)

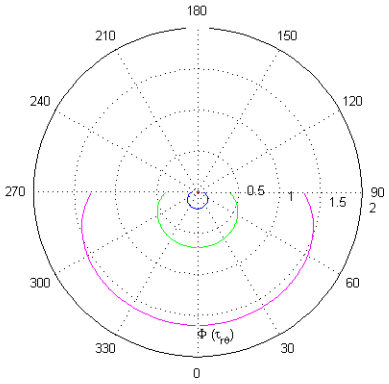
180
210
150
240
120
270
90
300
60
330
30
0
0.5
1
1.5
2
Φ (τrθ)

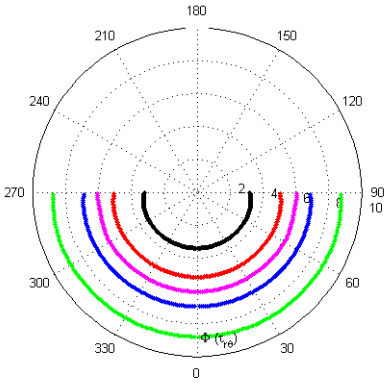
180
210
150
240
120
270
90
300
60
330
30
0
2
4
6
8
10
Φ (τrθ)

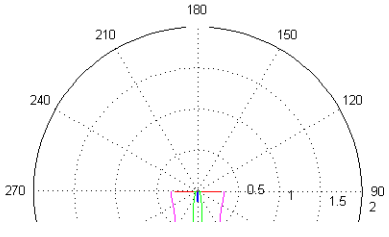
180
210
150
240
120
270
90
300
60
330
30
0
0.5
1
1.5
2

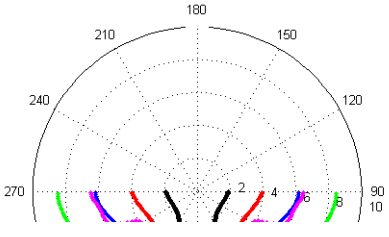
180
210
150
240
120
270
90
300
60
330
30
0
2
4
6
8
10

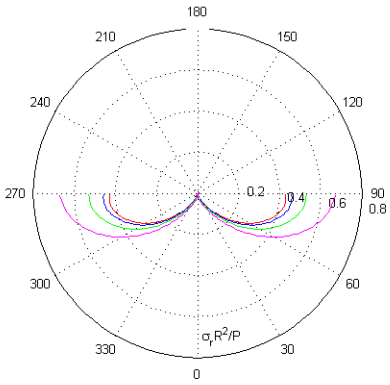
180
210
150
240
120
270
90
300
60
330
30
0
0.2
0.4
0.6
0.8
$\sigma_r R^2/P$

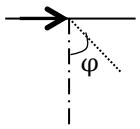
φ

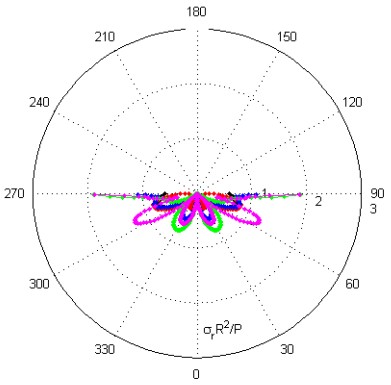
180
210
150
240
120
270
90
300
60
330
30
0
1
2
3
$\sigma_r R^2/P$

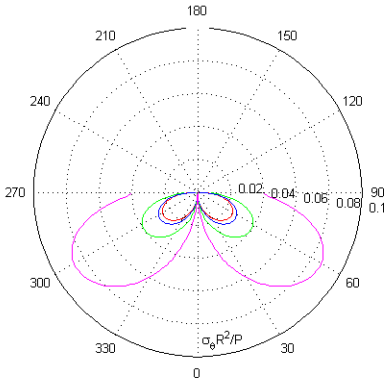
180
210
150
240
120
270
90
300
60
330
30
0
0.02
0.04
0.06
0.08
0.1
$\sigma_\theta R^2/P$

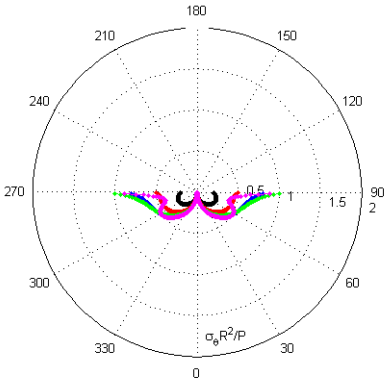
180
210
150
240
120
270
90
300
60
330
30
0
0.5
1
1.5
2
$\sigma_\theta R^2/P$

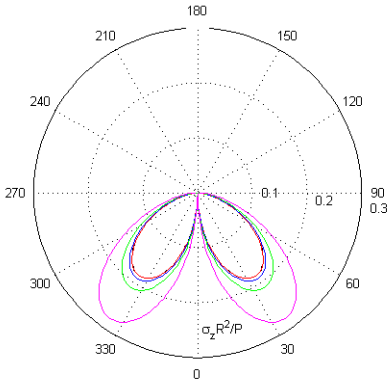
180
210
150
240
120
270
90
300
60
330
30
0
0.1
0.2
0.3
$\sigma_z R^2/P$

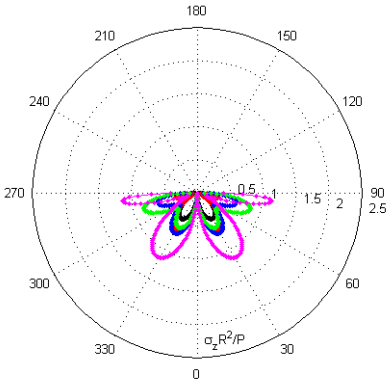
180
210
150
240
120
270
90
300
60
330
30
0
0.5
1
1.5
2
2.5
$\sigma_z R^2/P$

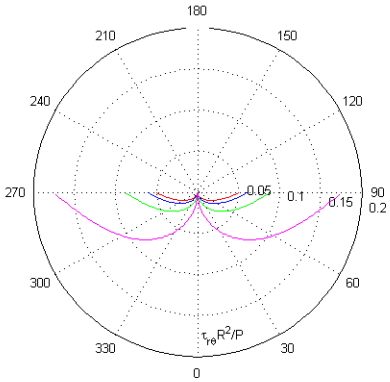
180
210
150
240
120
270
90
300
60
330
30
0
0.05
0.1
0.15
0.2
$\tau_{r\theta} R^2/P$

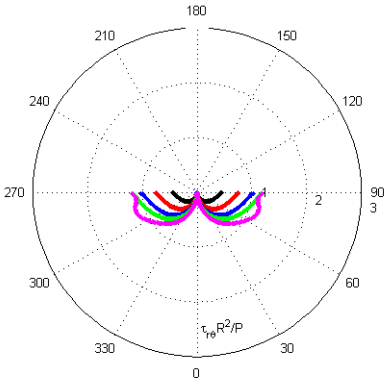
180
210
150
240
120
270
90
300
60
330
30
0
1
2
3
$\tau_{r\theta} R^2/P$

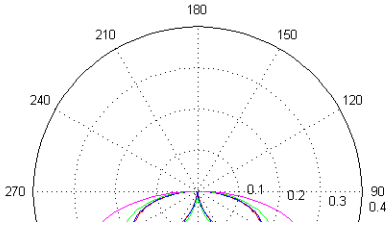
180
210
150
240
120
270
90
300
60
330
30
0
0.1
0.2
0.3
0.4

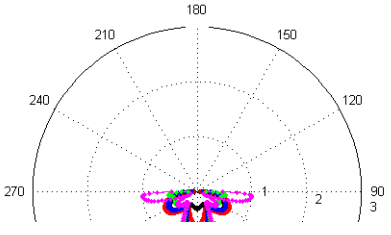
180
210
150
240
120
270
90
300
60
330
30
0
1
2
3

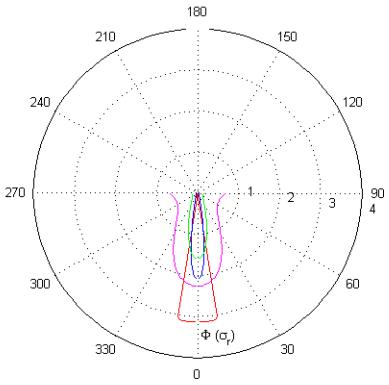
180
210
150
240
120
270
90
300
60
330
30
0
1
2
3
4
Φ (σr)

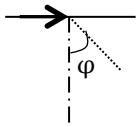
φ

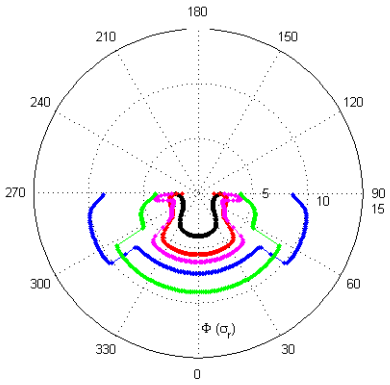
180
210
150
240
120
270
90
300
60
330
30
0
5
10
15
Φ (σr)

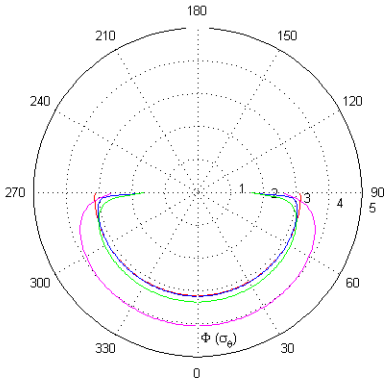
180
210
150
240
120
270
90
300
60
330
30
0
1
2
3
4
5
Φ (σθ)

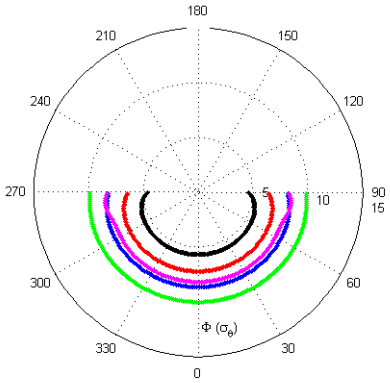
180
210
150
240
120
270
90
300
60
330
30
0
5
10
15
Φ (σθ)

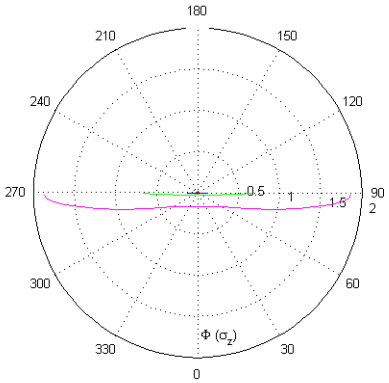
180
210
150
240
120
270
90
300
60
330
30
0
0.5
1
1.5
2
Φ (σz)

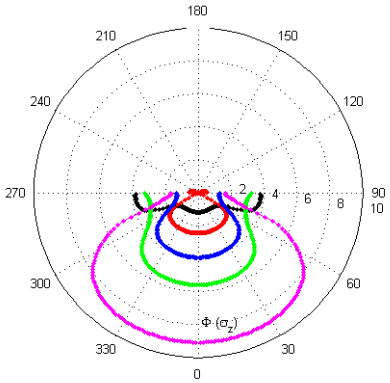
180
210
150
240
120
270
90
300
60
330
30
0
2
4
6
8
10
Φ (σz)

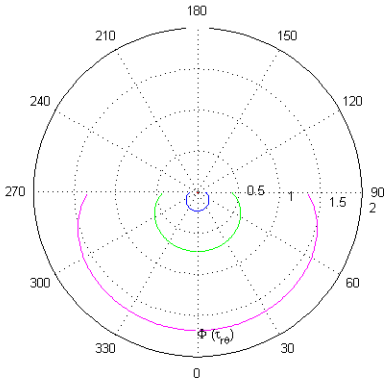
180
210
150
240
120
270
90
300
60
330
30
0
0.5
1
1.5
2
Φ (τrθ)

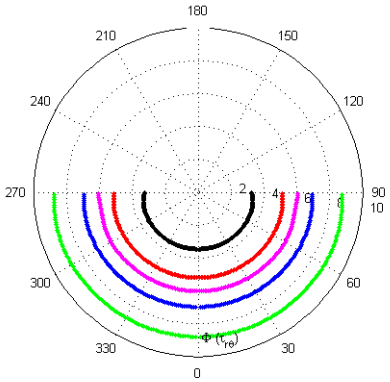
180
210
150
240
120
270
90
300
60
330
30
0
2
4
6
8
10
Φ (τrθ)

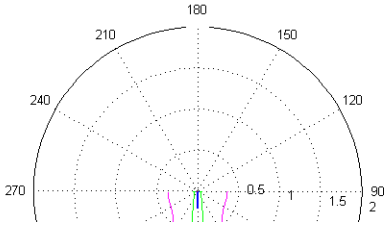
180
210
150
240
120
270
90
300
60
330
30
0
0.5
1
1.5
2

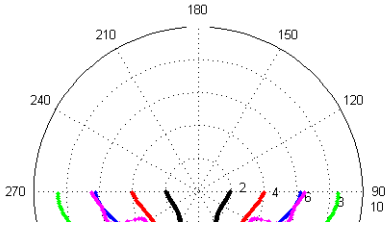
180
210
150
240
120
270
90
300
60
330
30
0
2
4
6
8
10

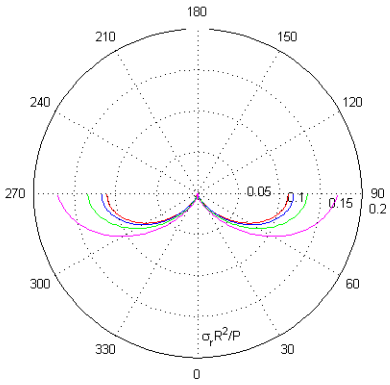
180
210
150
240
120
270
90
300
60
330
30
0
0.05
0.1
0.15
0.2
$\sigma_r R^2/P$

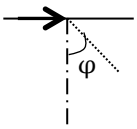
φ

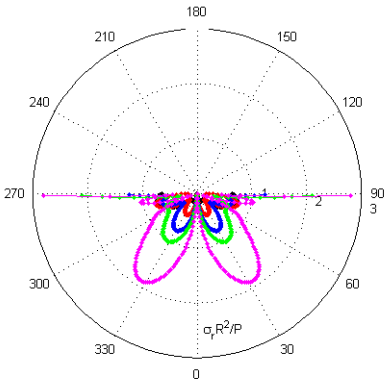
180
210
150
240
120
270
90
300
60
330
30
0
1
2
3
$\sigma_r R^2/P$

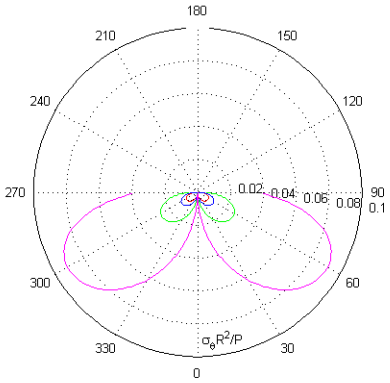
180
210
150
240
120
270
90
300
60
330
30
0
0.02
0.04
0.06
0.08
0.1
$\sigma_\theta R^2/P$

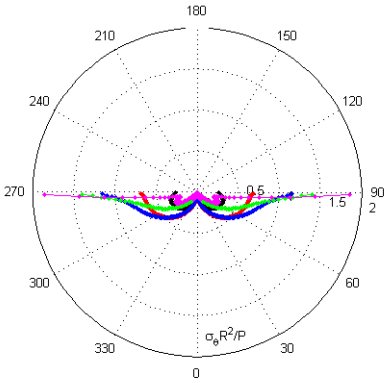
180
210
150
240
120
270
90
300
60
330
30
0
0.5
1.5
2
$\sigma_\theta R^2/P$

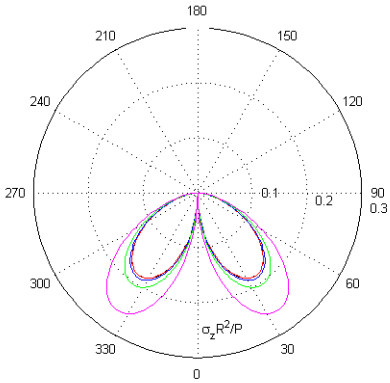
180
210
150
240
120
270
90
300
60
330
30
0
0.1
0.2
0.3
$\sigma_z R^2/P$

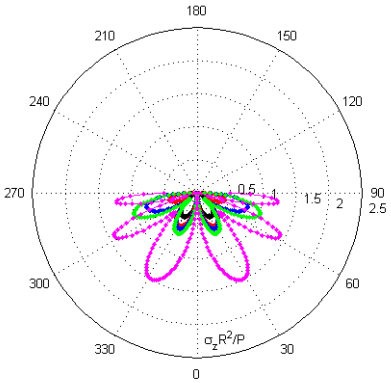
180
210
150
240
120
270
90
300
60
330
30
0
0.5
1
1.5
2
2.5
$\sigma_z R^2/P$

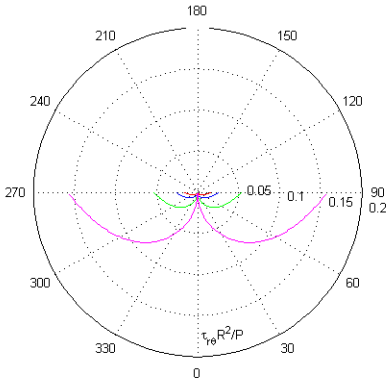
180
210
150
240
120
270
90
300
60
330
30
0
0.05
0.1
0.15
0.2
$\tau_{r\theta} R^2/P$

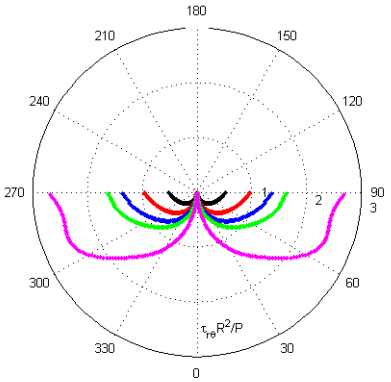
180
210
150
240
120
270
90
300
60
330
30
0
1
2
3
$\tau_{r\theta} R^2/P$

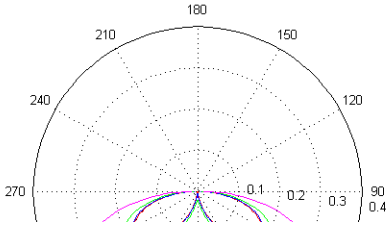
180
210
150
240
120
270
90
0.1
0.2
0.3
0.4

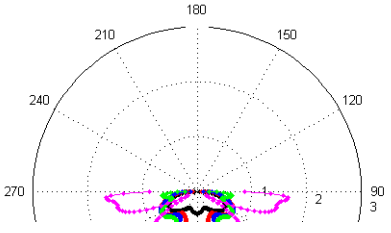
180
210
150
240
120
270
90
1
2
3

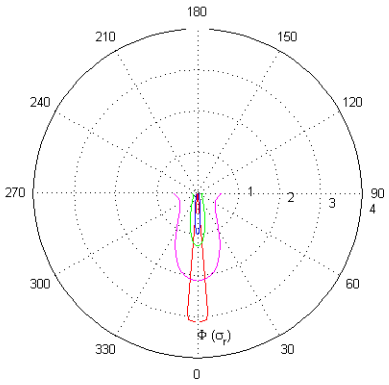
180
210
150
240
120
270
90
300
60
330
30
0
1
2
3
4
Φ (σr)

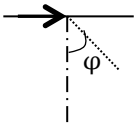
φ

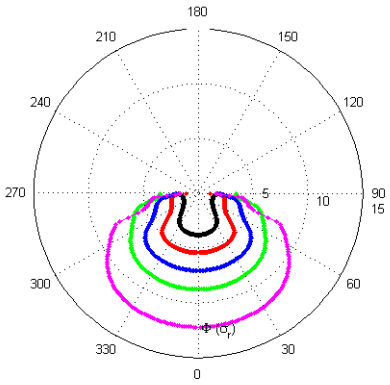
180
210
150
240
120
270
90
300
60
330
30
0
5
10
15
Φ (σr)

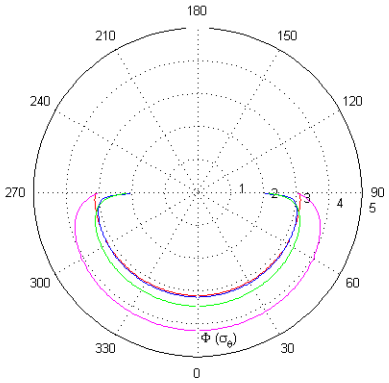
180
210
150
240
120
270
90
300
60
330
30
0
1
2
3
4
5
Φ (σθ)

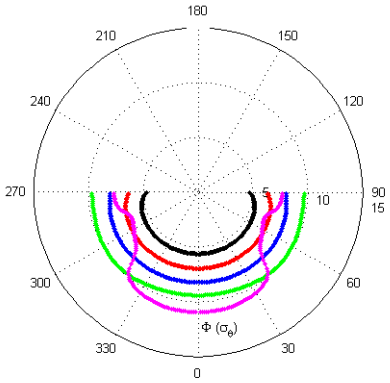
180
210
150
240
120
270
90
300
60
330
30
0
5
10
15
Φ (σθ)

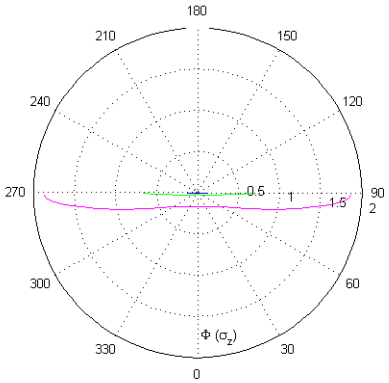
180
210
150
240
120
270
90
300
60
330
30
0
0.5
1
1.5
2
Φ (σz)

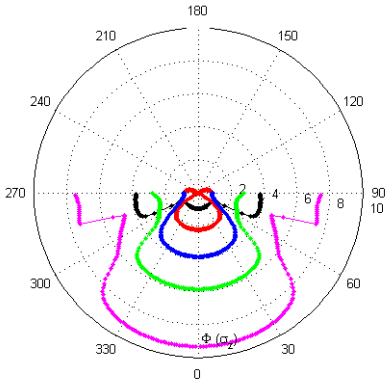
180
210
150
240
120
270
90
300
60
330
30
0
2
4
6
8
10
Φ (σz)

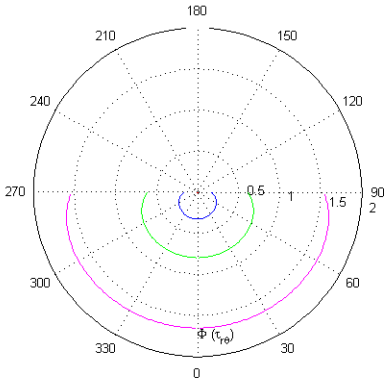
180
210
150
240
120
270
90
300
60
330
30
0
0.5
1
1.5
2
Φ (τrθ)

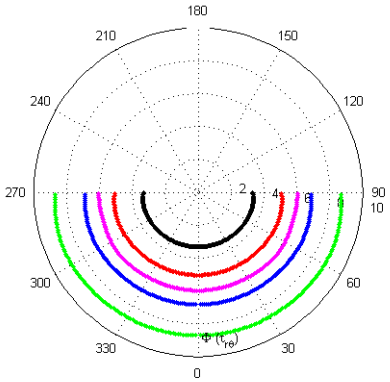
180
210
150
240
120
270
90
300
60
330
30
0
2
4
6
8
10
Φ (τrθ)

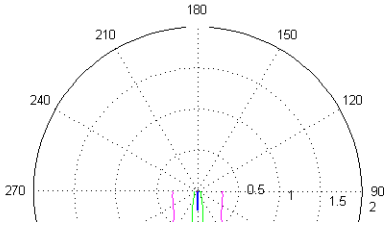
180
210
150
240
120
270
90
300
60
330
30
0
0.5
1
1.5
2

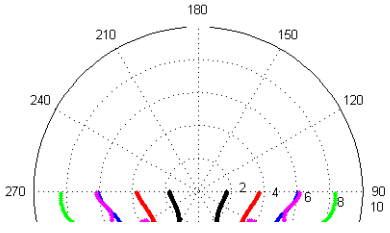
180
210
150
240
120
270
90
300
60
330
30
0
2
4
6
8
10

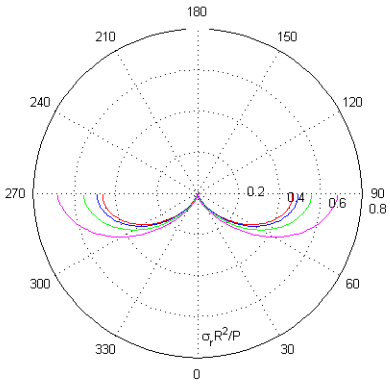
180
210
150
240
120
270
90
300
60
330
30
0
0.2
0.4
0.6
0.8
$\sigma_r R^2/P$

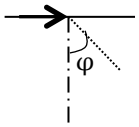
φ

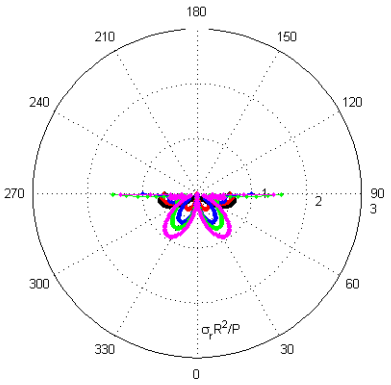
180
210
150
240
120
270
90
300
60
330
30
0
1
2
3
$\sigma_r R^2/P$

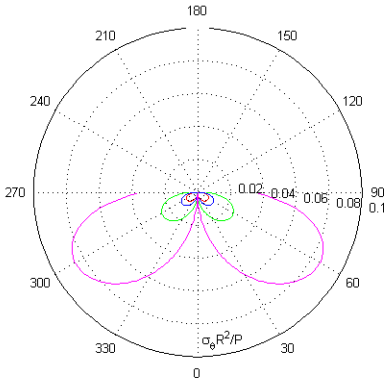
180
210
150
240
120
270
90
300
60
330
30
0
0.02
0.04
0.06
0.08
0.1
$\sigma_\theta R^2/P$

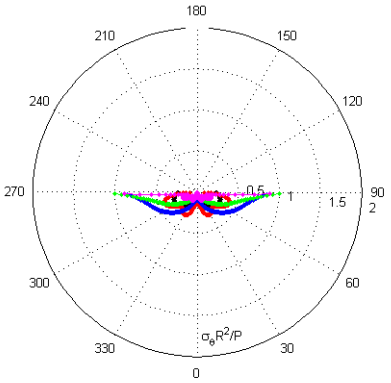
180
210
150
240
120
270
90
300
60
330
30
0
0.5
1
1.5
2
$\sigma_\theta R^2/P$

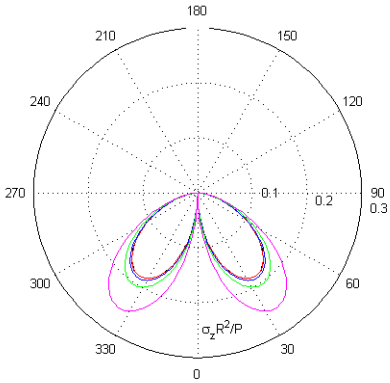
180
210
150
240
120
270
90
300
60
330
30
0
0.1
0.2
0.3
$\sigma_z R^2/P$

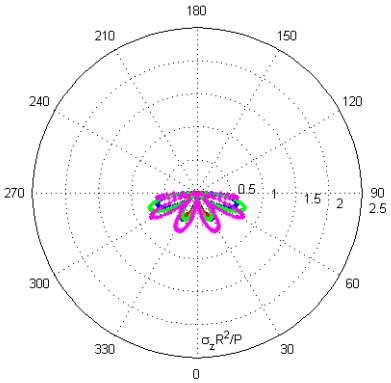
180
210
150
240
120
270
90
300
60
330
30
0
0.5
1
1.5
2
2.5
$\sigma_z R^2/P$

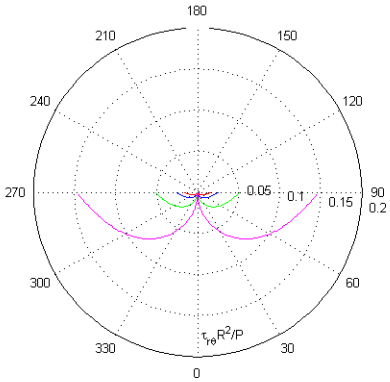
180
210
150
240
120
270
90
300
60
330
30
0
0.05
0.1
0.15
0.2
$\tau_{r\theta} R^2/P$

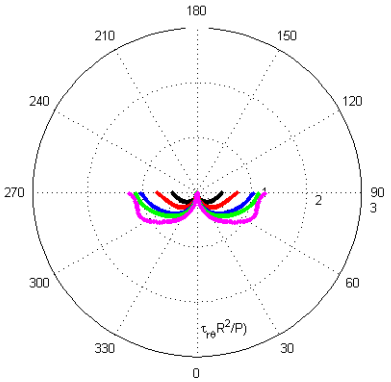
180
210
150
240
120
270
90
300
60
330
30
0
2
3
$\tau_{r\theta} R^2/P)$

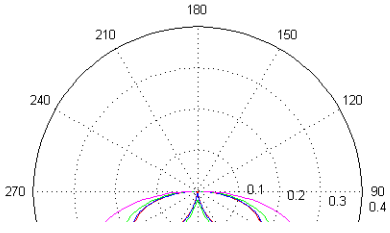
180
210
150
240
120
270
90
300
60
330
30
0
0.1
0.2
0.3
0.4

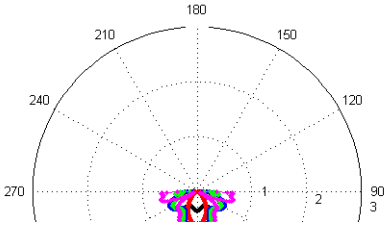
180
210
150
240
120
270
90
300
60
330
30
0
1
2
3

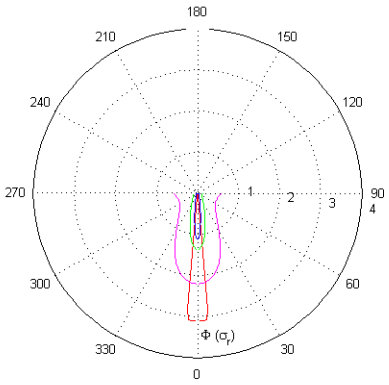
180
210
150
240
120
270
90
300
60
330
30
0
1
2
3
4
Φ (σr)

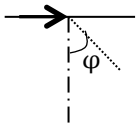
φ

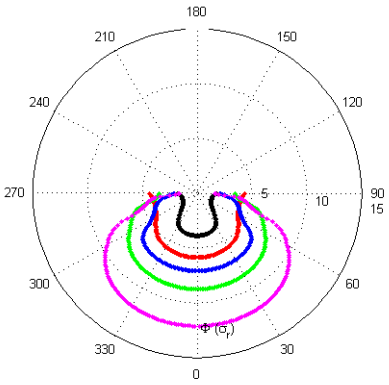
180
210
150
240
120
270
90
300
60
330
30
0
5
10
15
Φ (σr)

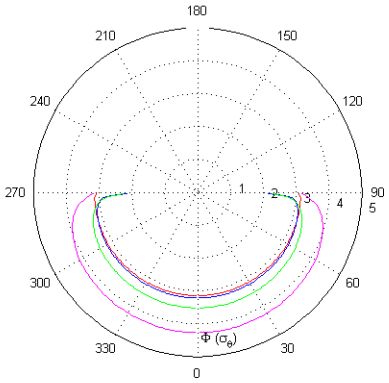
180
210
150
240
120
270
90
300
60
330
30
0
1
2
3
4
5
Φ (σθ)

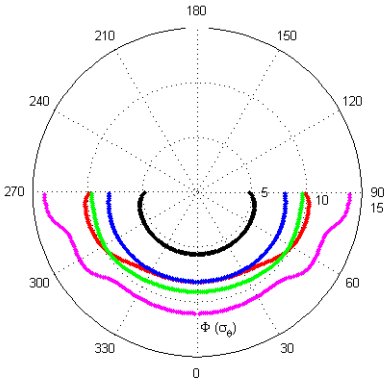
180
210
150
240
120
270
90
300
60
330
30
0
5
10
15
Φ (σθ)

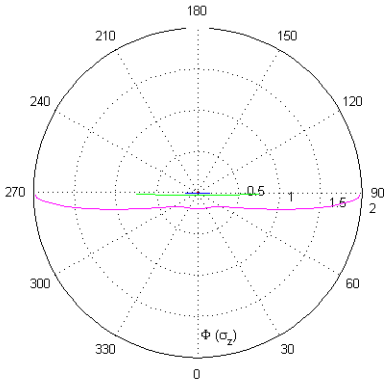
180
210
150
240
120
270
90
300
60
330
30
0
0.5
1
1.5
2
Φ (σz)

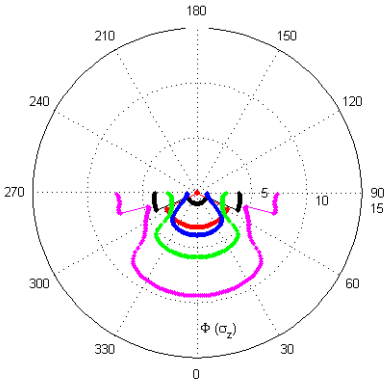
180
210
150
240
120
270
90
300
60
330
30
0
5
10
15
Φ (σz)

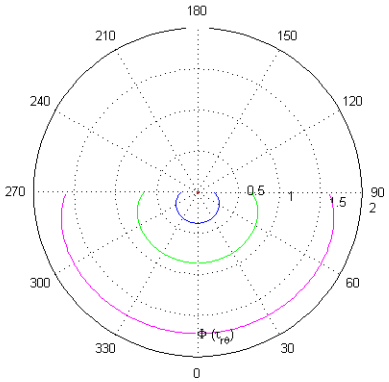
180
210
150
240
120
270
90
300
60
330
30
0
0.5
1
1.5
2
Φ (τrθ)

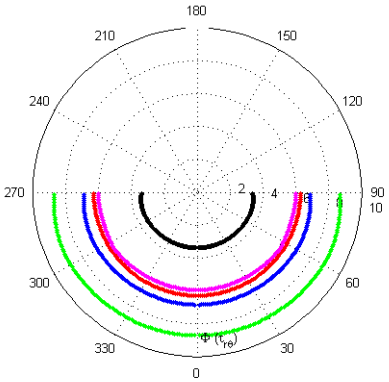
180
210
150
240
120
270
90
300
60
330
30
0
2
4
6
8
10
Φ (τrθ)

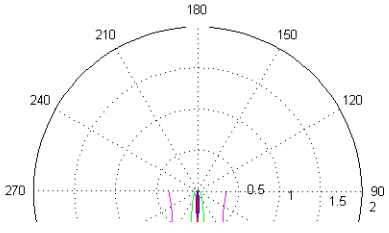
180
210
150
240
120
270
90
0.5
1
1.5
2

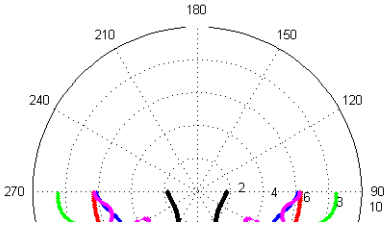
180
210
150
240
120
270
90
2
4
6
8
10

Stress amplitudes are found to have upper limits of about 2.25 P/R^2 for σ_z and about $2.5P/R^2$ for τ_{rz} in the examined frequency range. The number of lobes in the stress bulbs increases with frequency, from one under static conditions to four and six at $(\omega R/V_s) = 20$ for σ_z and Poisson's ratios of 0.34 and 0.45, respectively, and from two in the static case to three and four at the highest considered dimensionless frequency for τ_{rz}. As mentioned previously, this pattern can be explained on the basis of successive zones of destructive and constructive wave interference, which is expected to become more pronounced as frequency increases, leading to multi-lobe, flower-like bulbs. The number of bulbs may increase indefinitely as the frequency approaches infinity. Similar changes are also observed for the other four stress components, σ_r, σ_θ, $\tau_{r\theta,}$ *and* $\tau_{\theta z}$.

In general, phase angle patterns grow radially with increases in dimensionless frequency. As discussed earlier, the phase shift values correspond approximately to the dimensionless frequency ($\omega R/V$) computed with the propagation velocity of the dominant wave type for a given aperture angle. For instance, for τ_{rz}, at aperture angle of 0°, phase angle values are close to ($\omega R/V_S$) since shear waves are the dominant travelling waves in this case. For higher aperture angles there is a minor decrease in phase angle values due to presence of P-waves travelling at velocities higher than that of shear waves. However, the amount of reduction illustrates combined effects of different wave types rather than pure propagation of P-waves. Moreover, worthy of comment are the nearly perfect semi-circle phase patterns associated with some of the stress components (i.e. σ_θ, $\tau_{r\theta,}$ *and* $\tau_{\theta z}$). Although the phase values are slightly smaller than $\omega R/V_S$, the constant phase patterns indicate either perfect shear waves as controlling, or a relatively constant combination of different wave types.

Finally, for the azimuthal angle of 180°, the amplitudes of stress components are the same as that of 0°; however, the phase angles are different by a value of π for σ_r, σ_θ, and σ_z yet the same for τ_{rz}.

To help interpret the results, with reference to Figures 3.18 and 3.19, consider the example of a point within the soil media located at x = 7.07 m, y = 0 m and z = - 7.07 m. This point is located at radial distance R = 10 m from the point of application of the vertical load at a vertical angle of φ = 45 degrees. If V_S = 100 m/s and (ω = 60) rad/s, the dimensionless frequency is ($\omega R/V_S$) = 6. In Figure 3.20, the ray along an aperture angle of 45 degrees intersects the vertical and shear stress bulbs for ($\omega R/V_S$) = 6 (i.e. marked red curve) at dimensionless values of 0.5 and 0.8, respectively. For a unit vertical point load (P = 1 kN), vertical and shear stress amplitudes are obtained by dividing the aforementioned values by R^2 (i.e., σ_z = 5 kN/m^2 and τ_{rz} = 8 kN/m^2). The corresponding phase angles are 2.54π and π for vertical and shear components, respectively. At zero frequency (static case), the corresponding stresses are 2 and 1.8 kN/m^2 and the phase angles are zero.

The results from Figures 3.22 and 3.26 and Figures 3.24 and 3.28 can be compared to show the effects of Poisson's ratio on stress bulbs; while Figures 3.22 and 3.24 and Figures 3.26 and 3.28 can be used to investigate damping effects. The most critical effects of Poisson's ratio are summarized in Figure 3.30, which shows that an increase of Poisson's ratio causes no perceptible change in stress bulb amplitudes or phase angles for aperture angles associated with shear wave propagation (approximately 0º to 20º). However, Poisson's ratio increases produce stress amplitude increases and decreases for aperture angles associated with P-wave (20º − 60º) and Rayleigh wave (60º to 90º) propagation, respectively. Our interpretation is that in the high-ν case, the higher bulk moduli of the soil 'attracts' more P-wave propagation (at the expense of

Rayleigh wave energy), thereby modifying stress amplitudes associated with these wave types. These effects are most apparent for relatively high values of dimensionless frequencies ($\omega R/V_S$ = 10, 20).

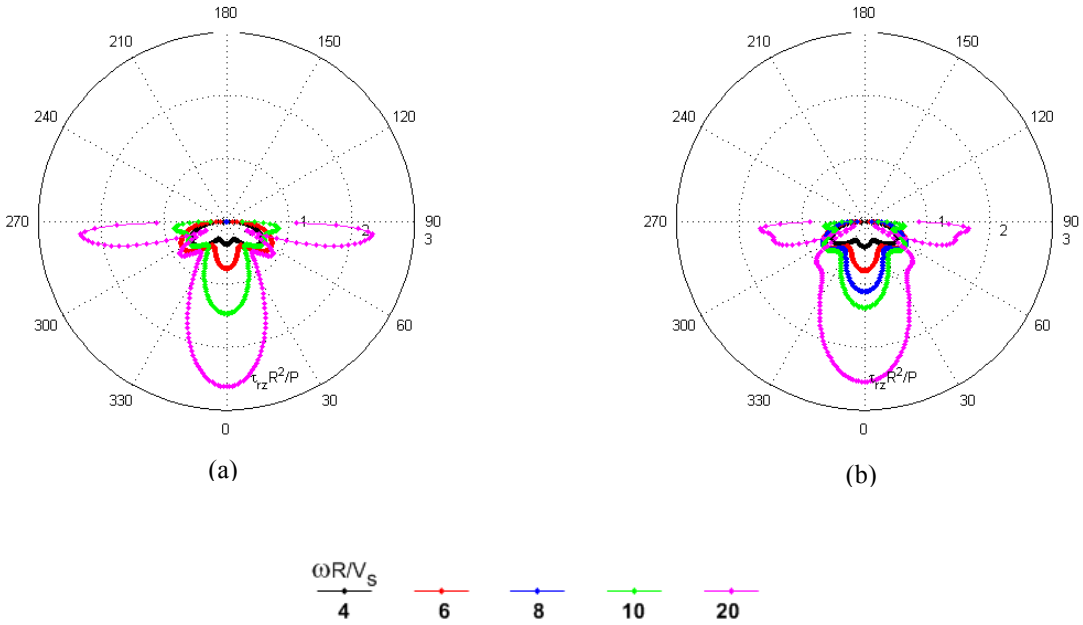

Figure 3.30: Stress amplitudes due to horizontal point load, ξ = 1%; (a) v = 0.34, (b) v=0.45

Figure 3.31 shows the most critical effects of increasing soil damping ratio. As expected, there is a reduction of stresses with increasing damping, which are more obvious for high values of dimensionless frequencies ($\omega R/V_S = 4 - 10$). Aside from stress reductions, increasing damping also serves to smooth the dramatic sharpness in dimensionless stress bulbs for high values of dimensionless frequencies.

It should be noted that the complete sets of results corresponding to 1° increments of azimuthal angle are available in the digital text files (i.e. libraries) and will be used in Chapter 5 to extend the point load solutions to the distributed load cases.

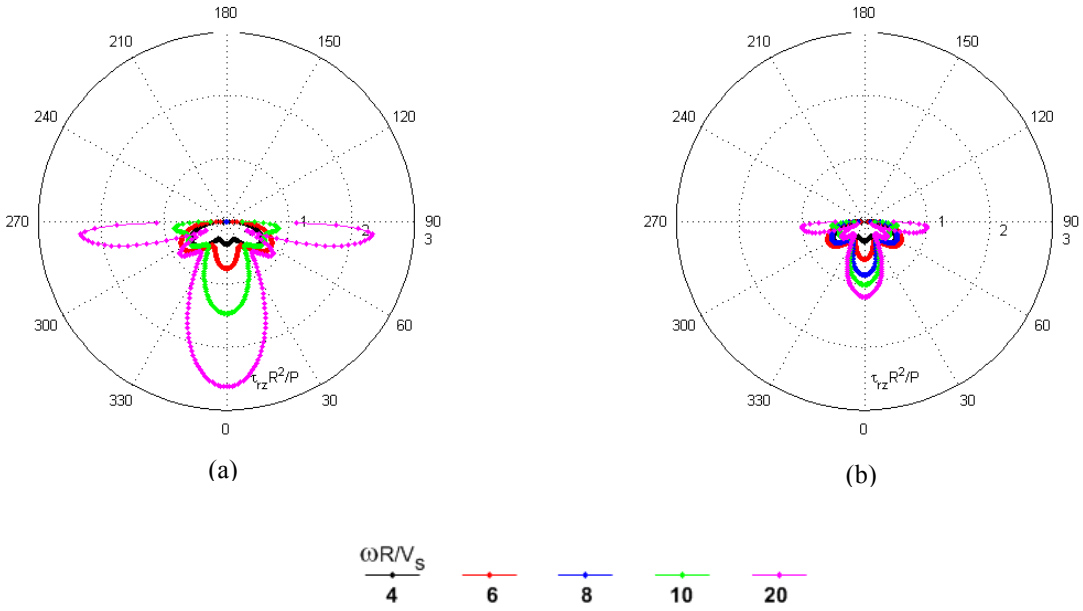

Figure 3.31: Stress amplitudes due to horizontal point load, v = 0.34; (a) ξ = 1%, (b) ξ = 5%

3.5 CONCLUSIONS

The value of dimensionless stress, ($\sigma_{ij}R^2/P$), within foundation soil underlying a harmonic vertical point load at ground surface is a function of dimensionless frequency, aperture angle, damping, and Poisson's ratio. For the harmonic horizontal point load case, an extra dimensionless value of azimuthal angle should be added to the equation. The following conclusions may be drawn for both load types (emphasizing the vertical and shear components):

- For ($\omega R/V_S$) < 1, dynamic effects range from negligible to moderate for both vertical and shear stress components and could probably be ignored.
- For ($\omega R/V_S$) ≈ 2 to 4, the general shapes of the stress distributions are similar to those for the static case, but the stress amplitudes are increased by about 70% for the vertical component and 50% for shear component in vertical load case, and are increased by about 50% for vertical component and 80% for shear component in horizontal load case.

- For ($\omega R/V_S$) > 4, stress patterns deviate substantially from the static case and follow a more complex pattern, due to constructive and destructive interference of the travelling waves.
- Increase of Poisson's ratio causes no perceptible change in stress bulb amplitudes or phase angles for aperture angles associated with shear wave propagation However, Poisson's ratio increases produce stress amplitude increases and decreases for aperture angles associated with P-wave and Rayleigh wave propagation, respectively. Our interpretation is that in the high-ν case, the higher bulk moduli of the soil 'attracts' more P-wave propagation (at the expense of Rayleigh wave energy), thereby modifying stress amplitudes associated with these wave types.
- Reduction in stress values is a natural outcome of soil damping ratio. However, this effect is more obvious for higher dimensionless frequencies. In other words, higher damping ratio values alleviate the dramatic sharpness in dimensionless stress bulbs with high dimensionless frequencies and cause smoother stress patterns.

4 Stress beneath Dynamically Applied Two-Dimensional Vertical and Horizontal Line Loads

In geotechnical engineering many elements of infrastructure are modeled using two-dimensional (2-D) configurations. Some examples include strip foundations, retaining structures, dams, and earthen levees. To complete the library of fundamental stress solutions and to lay the ground work for the general stress solutions arising from combinations of loads on foundations, this chapter concerns the problem of a 2-D half-space under dynamically applied surface line loads. As discussed earlier in Chapter 2, the corresponding static case is known as the Flamant problem (Saad, 2009) for which analytical solutions are available for both stresses and displacements. The goals of this chapter are to (1) extend the Flamant solutions to the dynamic regime, by considering harmonic vertical and horizontal 2-D line loads applied on the surface of a visco-elastic half-space, (2) develop general normalization schemes to facilitate ease of application, and (3) provide insight into the physics of SSI-induced stresses in two-dimensional problems and thereby take initial steps towards a simplified procedure for evaluating seismic stress demands in foundation soil. It should be mentioned that this problem was also considered by Lamb in 1904 paper, yet no solutions for stresses were considered.

In this chapter, similar to Chapter 3, the Buckingham theorem (Buckingham, 1914) is applied to the static and dynamic problems of vertical and horizontal line loads imposed on the

surface of a 2-D half-space to determine the number of dimensionless parameters. Such parameters are then selected with regards to characteristic properties of the system and are investigated through the numerical analyses. The commercial program ISoBEM (2012) was employed to perform the numerical analyses. The verification of the solutions is performed by comparing the static stress results to the Flamant's solution (Saad, 2009). There are no dynamic solutions against which to compare our results.

Upon verification, the final analyses are performed for a large set of parameters including dimensionless frequencies ($\omega R/V_S$) ranging from 0 to 20, Poisson's ratios of 0.34 and 0.45, and soil damping values of 1% and 5%. The solutions are then illustrated in the form of dimensionless stress bulbs for amplitude and phase angles. A discussion is also presented on the effects of Poisson's ratio, damping, and most importantly, dimensionless frequency on the stress response of a soil mass due to applied dynamic 2-D line loads.

4.1 DIMENSIONLESS PARAMETERS OF LINE LOAD PROBLEMS

As discussed in Chapter 3, the fundamental units are length *[L]* and force *[F]* in static problems and are length *[L]*, force *[F]*, and time *[T]* in dynamic ones. In the following sections, the solutions to vertical and horizontal Flamant problems are presented for the static and dynamic cases.

4.1.1 Dimensional Analysis of the Classical Flamant Problem

The vertical and horizontal classical Flamant problems are illustrated in Figure 4.1.

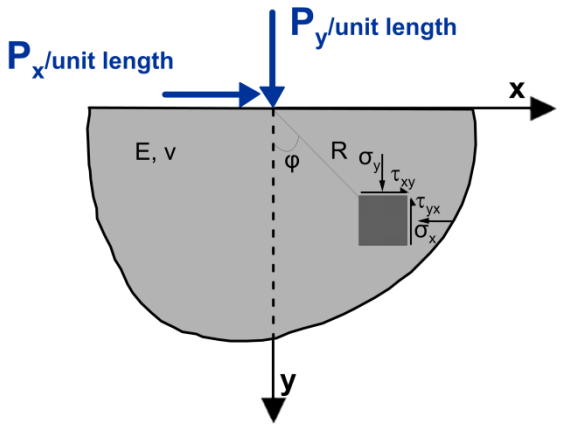

Figure 4.1: Schematic illustration of Flamant problem

In this figure the position of an arbitrary element within the 2-D elastic soil medium (with Young's modulus E and Poisson's ratio v) is defined by radial distance from the point of application of line load P (origin of axes), and the aperture angle φ in the x-y plane. Hence, in this problem three parameters, E, R, and P have two fundamental units, i.e. length *[L]* and force *[F]*. Two intrinsically dimensionless parameters, φ and v, complete the definition of the physical system. Accordingly, the number of dimensionless groups required to define this problem is given as (where Q refers to the number of intrinsically dimensionless parameters):

$$(N-M)+Q=(3-2)+2=3 \tag{4.1}$$

Therefore, the solution to the classical Flamant problem must be represented by an equation involving three dimensionless parameters, two of which are known (φ and v). Additional steps are required to identify the third parameter. Equation 4.2 shows the stress response, σ_{ij}, of a soil element, with the associated units appearing in Equation 4.3. It should be noted that due to 2-D nature of the problem, the dimension for the applied surface load is *[F/L]*, which is different from the problems described in Chapter 3 where the load had units of *[F]*.

$$\sigma_{ij}=P^{\alpha}E^{\beta}R^{\gamma}g(\varphi,\nu) \tag{4.2}$$

$$[\frac{F}{L^2}]=[\frac{F}{L}]^{\alpha}[\frac{F}{L^2}]^{\beta}[L]^{\gamma} \tag{4.3}$$

Parameters α, β, and γ are determined through dimensional analysis per Equation 4.3. Equation 4.4 provides two equations and three unknowns.

$$\begin{aligned} 1&=\alpha+\beta \\ -2&=-2\beta+\gamma \end{aligned} \tag{4.4}$$

The linearity of the problem requires $\alpha = 1$. Values of β and γ are then obtained as 0 and -1, respectively, resulting in:

$$\sigma_{ij}=\frac{P}{R}g(\varphi,\nu) \tag{4.5}$$

Equation 4.5 reveals the independence of stresses to the Young's modulus of the 2-D half-space, as mentioned in Chapter 2. This equation is rewritten in dimensionless form as Equation 4.6 where the third dimensionless parameter is ($\sigma_{ij}R/P$). In other words, for an element located at distance R from the 2-D vertical or horizontal static line loads applied at the ground surface, dimensionless stresses depend only on aperture angle and, possibly, ν. This is confirmed by the exact stress solution to the Flamant problem as shown in Equations 4.7 to 4.9 for vertical load and in Equations 4.10 to 4.12 for horizontal load in dimensionless forms.

$$\frac{\sigma_{ij}R}{P}=g(\varphi,\nu) \tag{4.6}$$

$$\frac{\sigma_x R}{P_y}=-\frac{2}{\pi}\sin^2\varphi\cos\varphi \tag{4.7}$$

$$\frac{\sigma_y R}{P_y} = -\frac{2}{\pi}\cos^3\varphi \tag{4.8}$$

$$\frac{\tau_{xy} R}{P_y} = -\frac{2}{\pi}\sin\varphi\cos^2\varphi \tag{4.9}$$

$$\frac{\sigma_x R}{P_x} = -\frac{2}{\pi}\sin^3\varphi \tag{4.10}$$

$$\frac{\sigma_y R}{P_x} = -\frac{2}{\pi}\sin\varphi\cos^2\varphi \tag{4.11}$$

$$\frac{\tau_{xy} R}{P_x} = -\frac{2}{\pi}\sin^2\varphi\cos\varphi \tag{4.12}$$

The independence of the right-hand side of the above solutions to R indicates *self-similarity* of the problem, as it reduces the number of independent variables from two (i.e., φ, R) to one (φ), which greatly simplifies the governing equations such that an ordinary differential equation is sufficient to solve the problem instead of partial differential equations. This remarkable property is discussed in detail by Barenblatt (1996). The elegance of this approach is more pronounced when it comes to problems for which solutions are not fully available in closed-form. The dynamic Flamant problem lacks an exact closed form solution, as discussed in the following section. While the static stress solutions are independent of Young's modulus and Poisson's ratio of the half-space materials, the latter will not hold for dynamic loads.

4.1.2 Dimensional Analysis for 2-D Dynamic Vertical and Horizontal Line Load Problems

In the dynamic counterpart to the Flamant problem, shown in Figure 4.2, the line loads are periodic with amplitude P and angular frequency ω. Radial distance (R), shear wave velocity (V_S), shear modulus (G), and mass density of the soil medium (ρ) are other essential parameters.

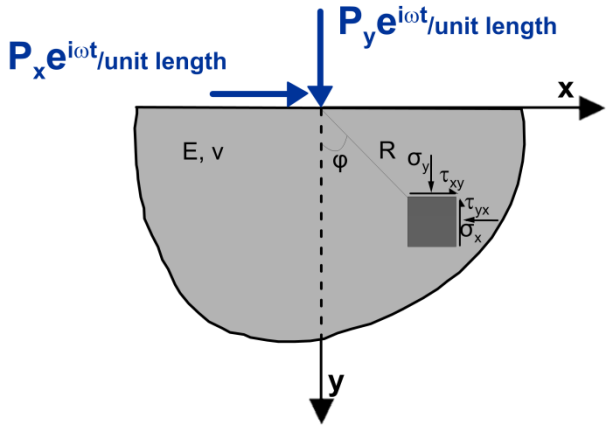

Figure 4.2: 2-D dynamic vertical and horizontal line load problems

Since G, V_S and ρ are correlated, only two of them should be considered as fundamental parameters resulting in a total of five ($N = 5$). There are three fundamental dimensions, length *[L]*, force *[F]*, and time *[T]*, ($M = 3$). There are three intrinsically dimensionless parameters v, ξ, and φ ($Q = 3$). Accordingly, the number of dimensionless group is:

$$(N-M)+Q=(5-3)+3=5 \tag{4.13}$$

Hence, in addition to the three intrinsically dimensionless parameters and ($\sigma_{ij}R/P$), another dimensionless parameter is required to fully describe the dynamic solution. Similar to Chapter 3, this parameter is selected to be dimensionless frequency ($\omega R/V_S$). As shown in Equation 4.14 in the 2-D dynamic problem ($\sigma_{ij}R/P$) is a function of soil v and ξ, aperture angle, and dimensionless frequency.

$$\frac{\sigma_{ij}R}{P} = g\left(\varphi, \nu, \xi, \frac{\omega R}{V_s}\right) \tag{4.14}$$

4.2 Numerical Technique and Software Verification

As discussed previously, numerical analyses are required to evaluate the functional dependence of dimensionless stress in Eq. 4.14 on the indicated controlling variables. This approach is taken because solving the governing differential equation of the system analytically is a formidable task. We use the software package ISoBEM (2012) for these analyses.

The accuracy of ISoBEM analyses are verified for the static vertical and horizontal Flamant problems. We also verify the applicability of the proposed stress normalization. There are no prior solutions against which to compare computed dynamic stresses.

4.2.1 Verification of ISoBEM Analyses – Static Flamant Problem

The accuracy of ISoBEM analyses are verified for the 2-D static vertical and horizontal loading problems by comparing to published solutions presented in Section 4.1.1. Results are shown in Figure 4.3, which compare horizontal, vertical, and shear stress components from ISoBEM analyses to Flamant's solution. For this comparison, stresses are calculated by ISoBEM for a total of 20 internal nodes. These nodes are located 1m below the surface boundary. The element type applied for these analyses are considered to be Three-node Quadratic Line (3QL) element. As shown in this figure, there is nearly perfect compatibility between the stress fields obtained from the Flamant's closed-form solutions and ISoBEM.

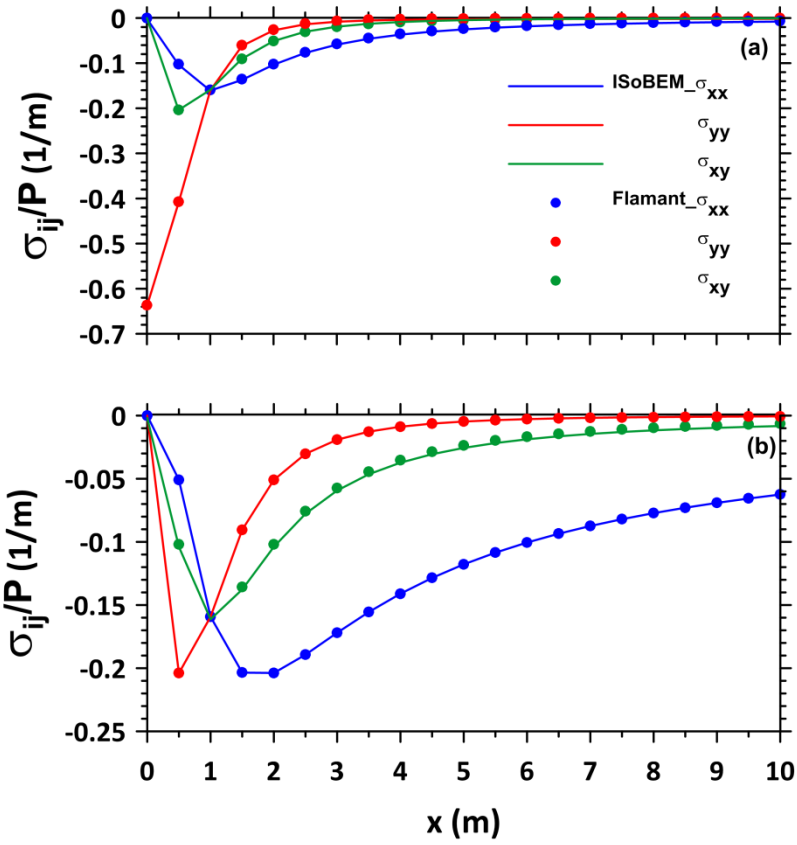

Figure 4.3: Comparison between ISoBEM analytical solution for classical Flamant problem for (a) vertical load and (b) horizontal load. Results apply for: y = -1, ρ = 1.8 Mg/m^3, V_S = 300 m/s, v = 0.34

4.2.2 Verification of ISoBEM Analyses - Normalization

The final verification is conducted to test the normalization of the dynamic stress results with respect to ($\sigma_{ij}R/P$) and ($\omega R/V_S$). For this purpose, three models were built in ISoBEM representing different values of frequencies, shear wave velocities, and radial distances, yet identical sets of dimensionless frequencies, ($\omega R/V_S$). Table 4.1 summarizes the three models used for normalization verifications for vertical and horizontal loads.

Table 4.1: ISoBEM 2-D models used to verify normalization for vertical and horizontal loads; v = 0.34, ξ = 1%

	Model 1			Model 2			Model 3		
$\omega R/V_S$	ω (rad/s)	V_S (m/s)	R (m)	ω (rad/s)	V_S (m/s)	R (m)	ω (rad/s)	V_S (m/s)	R (m)
0.5	98.06	100.0	0.51	49.75	100.0	1.00	49.75	149.6	1.50
1	196.1	100.0	0.51	99.50	100.0	1.00	99.50	149.6	1.50
2	392.2	100.0	0.51	199.0	100.0	1.00	199.0	149.6	1.50
4	784.5	100.0	0.51	398.0	100.0	1.00	398.0	149.6	1.50
6	1177	100.0	0.51	597.0	100.0	1.00	597.0	149.6	1.50
8	1569	100.0	0.51	796.0	100.0	1.00	796.0	149.6	1.50
10	1961	100.0	0.51	995.0	100.0	1.00	995.0	149.6	1.50

Corresponding stress amplitudes are presented in Figures 4.4 and 4.5 in non-normalized and normalized forms for vertical and horizontal 2-D point load cases, respectively. The results support the proposed normalization scheme.

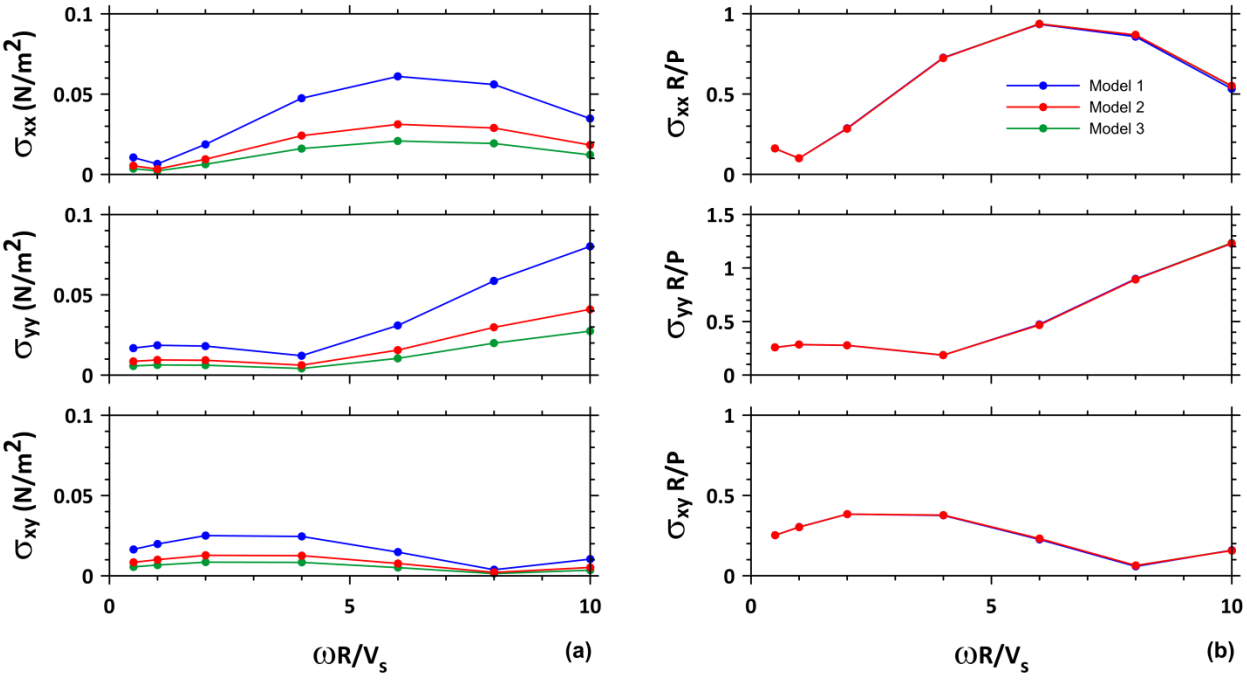

Figure 4.4: Checks of stress normalization using ISoBEM analyses for the conditions described in Table 4.1 for vertical 2-D line load case; (a) stress components (b) normalized stress components

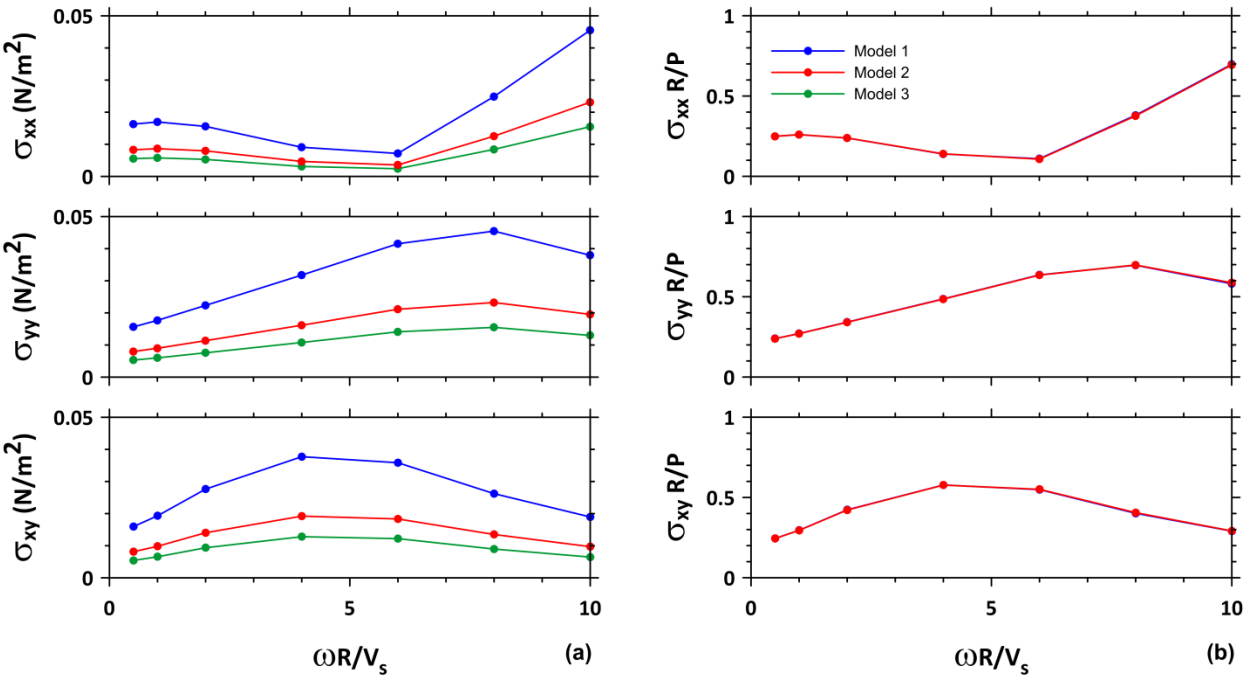

Figure 4.5: Checks of stress normalization using ISoBEM analyses for the conditions described in Table 4.1 for horizontal 2-D line load case; (a) stress components (b) normalized stress components

4.3 A DIMENSIONLESS PRESENTATION OF DYNAMIC STRESS FIELDS

In this section I present the stress responses produced by vertical and horizontal oscillating 2-D line loads on the surface of a visco-elastic half-space. Stresses are presented in dimensionless form for any location inside the soil mass as:

$$\frac{\sigma_{ij} R}{P} = g\left(\varphi, \nu, \xi, \frac{\omega R}{V_s}\right) \tag{4.15}$$

Similar to the models discussed in Chapter 3, a total of 40 combinations of dimensionless frequencies, damping, and Poisson's ratios are used in suites of analyses that are designed to cover the likely parameter range for practical applications. The locations of internal points are

selected such that a full range of aperture angles from 0° to 90° are covered. Such combinations are summarized in four major groups in Table 4.2.

Table 4.2: Summary of model setups in ISoBEM for dynamic 2-D point load analysis

Group	Model	φ (°)	$\omega R/V_s$	ω (rad/s)	V_s (m/s)	R (m)	ν	ξ
1	1-10	0 - 90	0 - 20	0 - 12000	300	0.5	0.34	0.01
2	11-20	0 - 90	0 - 20	0 - 12000	300	0.5	0.34	0.05
3	21-30	0 - 90	0 - 20	0 - 12000	300	0.5	0.45	0.01
4	31-40	0 - 90	0 - 20	0 - 12000	300	0.5	0.45	0.05

The models in ISoBEM are set up as 2-D using three-node Quadratic Line (3QL) element types. The 3QL elements are the most common element types in 2-D boundary element problems. These elements apply quadratic interpolation functions to represent both boundary geometry and boundary variables (i.e. traction and displacement) (Mottershead, 2013). Three components of dynamic stress amplitudes and phase angles are generated and plotted as polar graphs. Amplitudes and phase angles of stress components are presented in Figures 4.8 to 4.15 for the vertical line load case and in Figures 4.16 to 4.23 for the horizontal line load case. To illustrate the effect of dimensionless frequency on the shape of stress bulbs, results are shown in two groups corresponding to ($\omega R/V_S$) = 0 to 2 (left column) and ($\omega R/V_S$) = 4 to 20 (right column).

In these figures, the values read around the radial lines correspond to dimensionless stress amplitudes ($\sigma_{ij}R/P$). To get the dimensional stress values for a specific frequency at a specific location, one should properly calculate the dimensionless frequency ($\omega R/V_S$) then read from the graph the corresponding dimensionless stress values knowing radial distance (R) and aperture angle (φ). The de-normalization should then be performed with respect to known value of vertical point load (P) and R.

In the figures corresponding to phase angles, the values read around the radial lines represent the actual phase angle in units of radians. The phase angles are associated with the time shift between the surface load time series and the stress time series at the point of interest. As discussed in Chapter 3, 1-D wave propagation theory indicates a phase shift is $\omega R/V$ for waves travelling at speed V. When wave propagation is dominated by shear waves, the phase shift should be $\omega R/V_S$, which is referred to as dimensionless frequency throughout this dissertation.

To help interpret the phase angle behavior, consider the case of the vertical stress component, σ_y, due to a vertical oscillatory surface line load (Figure 4.6) and the shear stress component, τ_{xy}, due to horizontal oscillatory surface line load (Figure 4.7). The 2-D models in ISoBEM are set up to investigate phase angles at different aperture angles, and the results in Figures 4.6 and 4.7 apply for φ = 0, 10, 45, 70, and 85 deg.

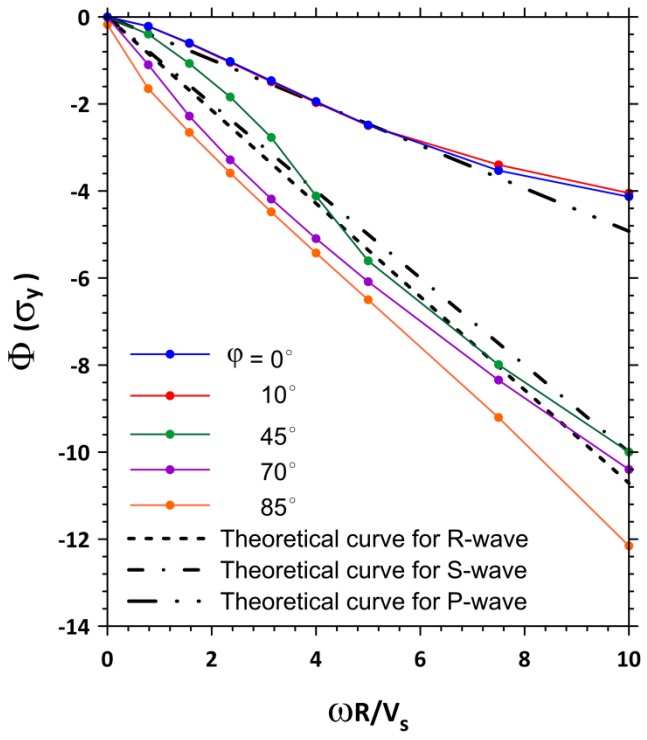

Figure 4.6: Phase angle variation for vertical stress component due to vertically oscillating line load, v = 0.34, ξ = 1%

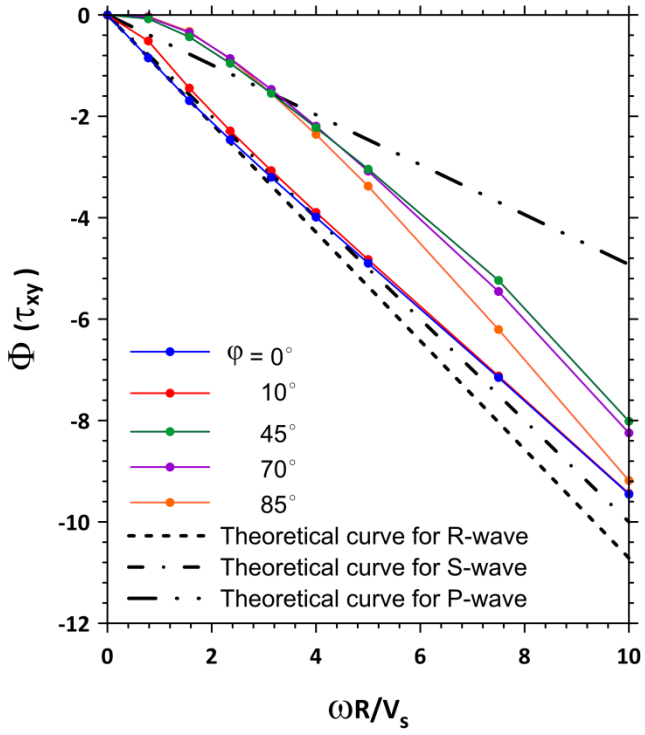

Figure 4.7: Phase angle variation for shear stress component due to horizontally oscillating line load, v = 0.34, ξ = 1%

The values of phase angles are negative indicating the time lag of stresses with respect to the applied loads. Moreover, at points along the vertical axis, i.e. aperture angle of 0°, one would expect: (1) for applied vertical loads, a dominant effect of P-waves on vertical stress components, resulting in phase angles being approximately equivalent to the theoretical value of $\omega R/V_P$; (2) for applied horizontal loads, a dominant effect of S-waves on shear stress components, resulting in phase angles being approximately ($\omega R/V_S$). Figures 4.6 and 4.7 show that these expected behaviors are observed with minor deviations for aperture angles of 0 and 10 degrees. As aperture angles increase to values ≥ 45 degrees, phase shifts for the vertical load case more nearly match those for theoretical S-waves or Rayleigh waves and phase shifts for the horizontal load case more nearly match those for theoretical P-waves.

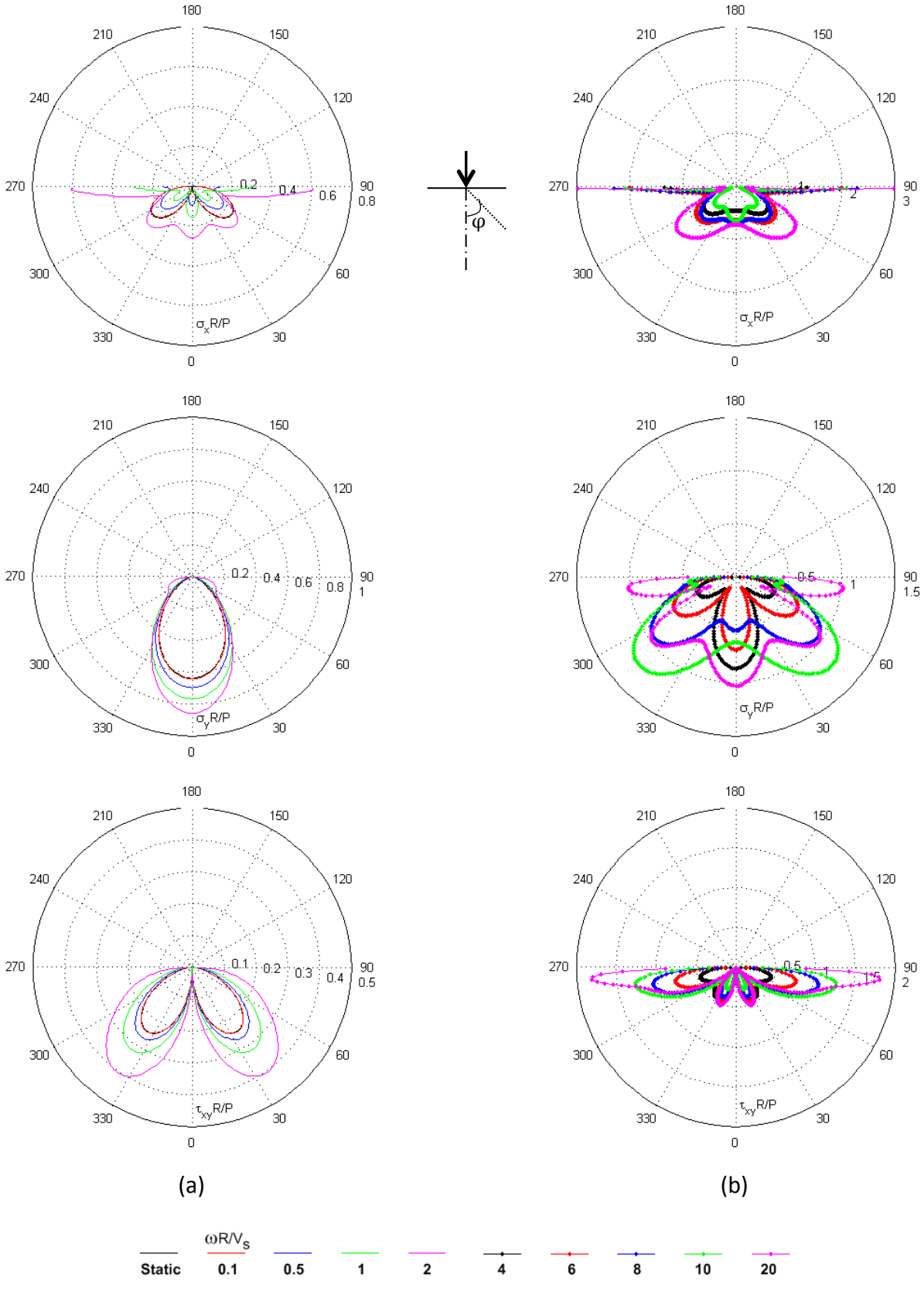

Figure 4.8: Stress amplitude bulbs due to vertical 2-D line load, v = 0.34, ξ = 1%; (a) $\omega R/V_S$ = 0 (static) to 2, (b) $\omega R/V_S$ = 4 to 20

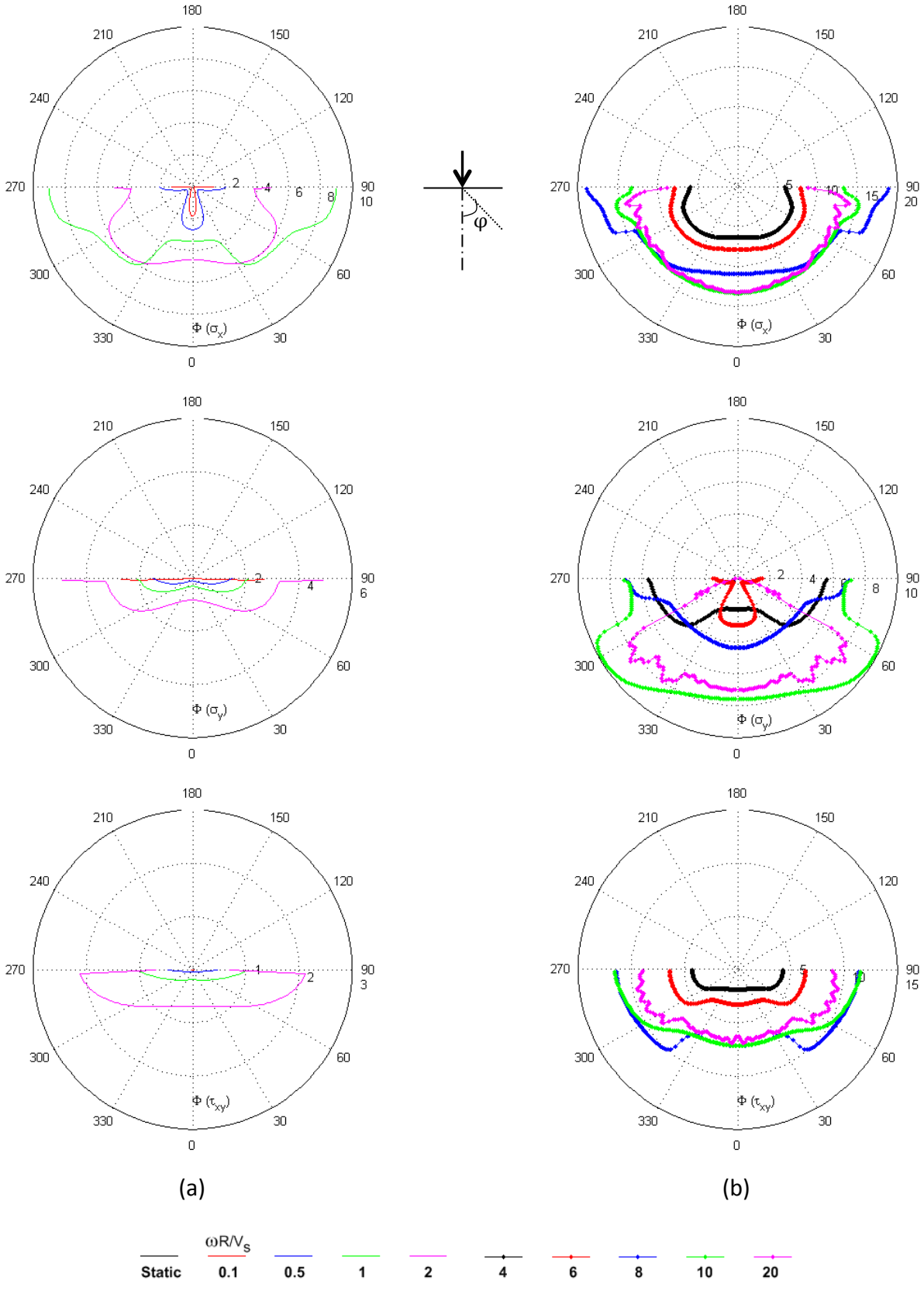

Figure 4.9: Phase angle bulbs due to vertical 2-D line load, v = 0.34, ξ = 1%; (a) $\omega R/V_S$ = 0 (static) to 2, (b) $\omega R/V_S$ = 4 to 20

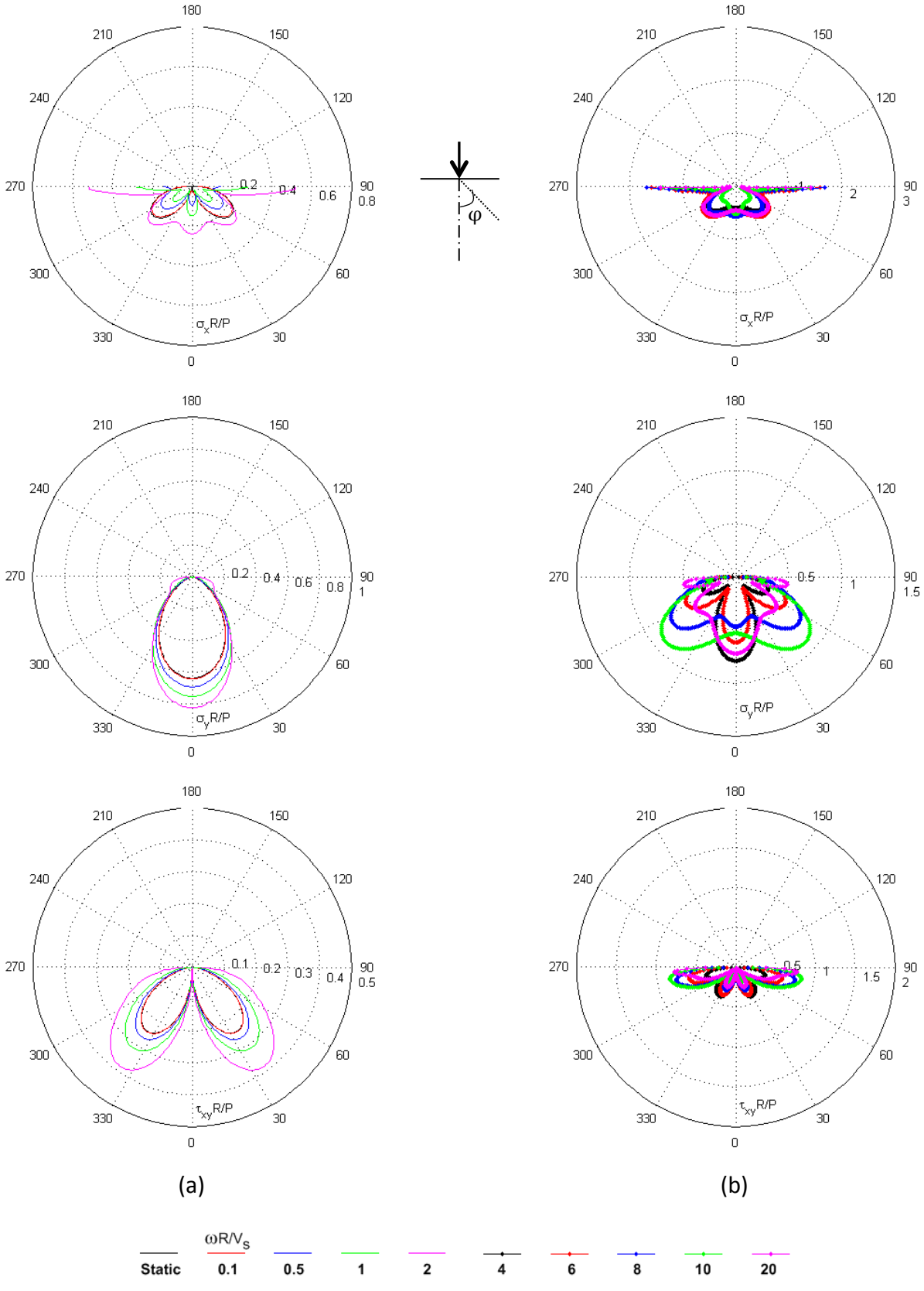

Figure 4.10: Stress amplitude bulbs due to vertical 2-D line load, v = 0.34, ξ = 5%; (a) $\omega R/V_S$ = 0 (static) to 2, (b) $\omega R/V_S$ = 4 to 20

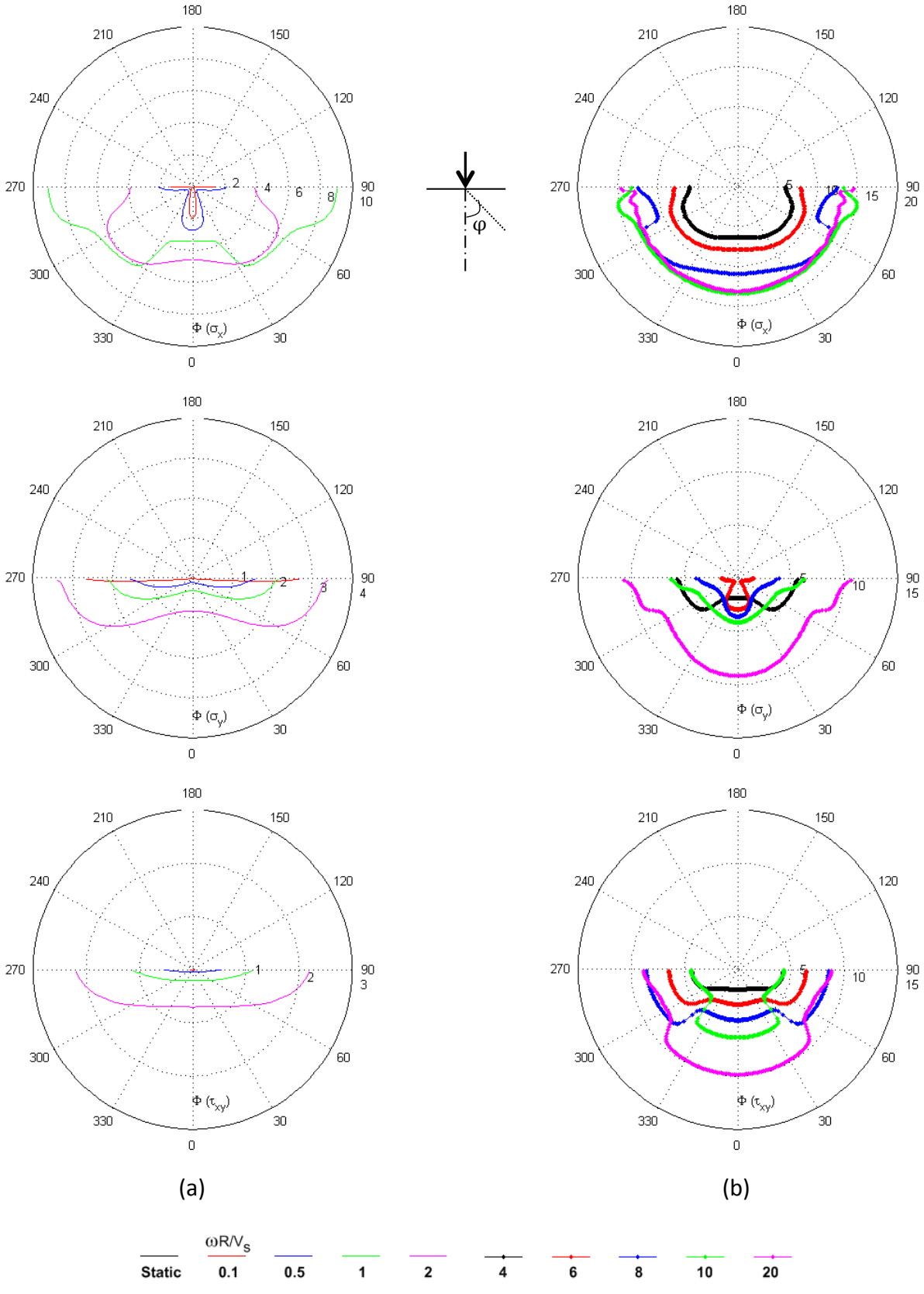

Figure 4.11: Phase angle bulbs due to vertical 2-D line load, v = 0.34, ξ = 5%; (a) $\omega R/V_S$ = 0 (static) to 2, (b) $\omega R/V_S$ = 4 to 20

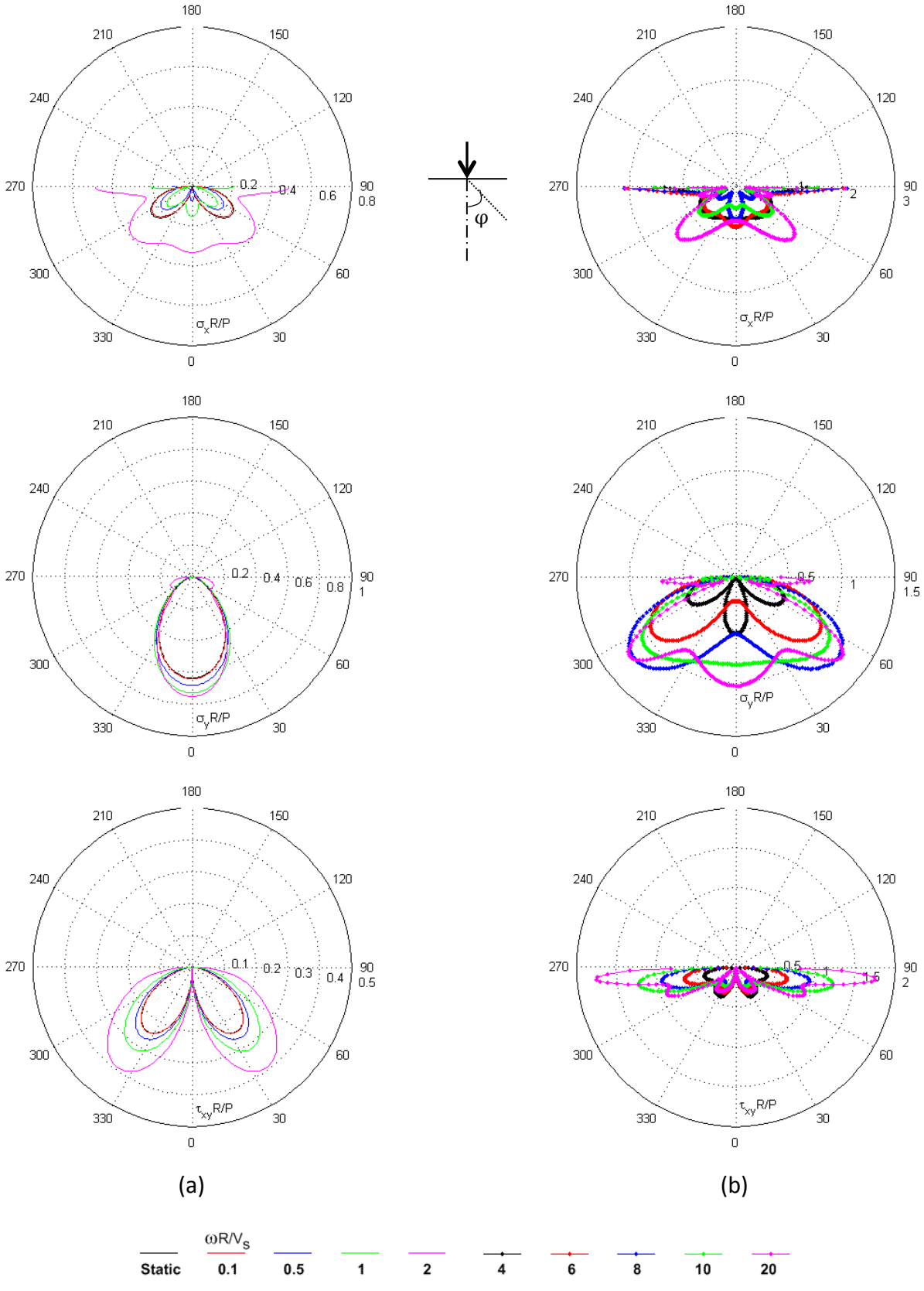

Figure 4.12: Stress amplitude bulbs due to vertical 2-D line load, v = 0.45, ξ = 1%; (a) $\omega R/V_S$ = 0 (static) to 2, (b) $\omega R/V_S$ = 4 to 20

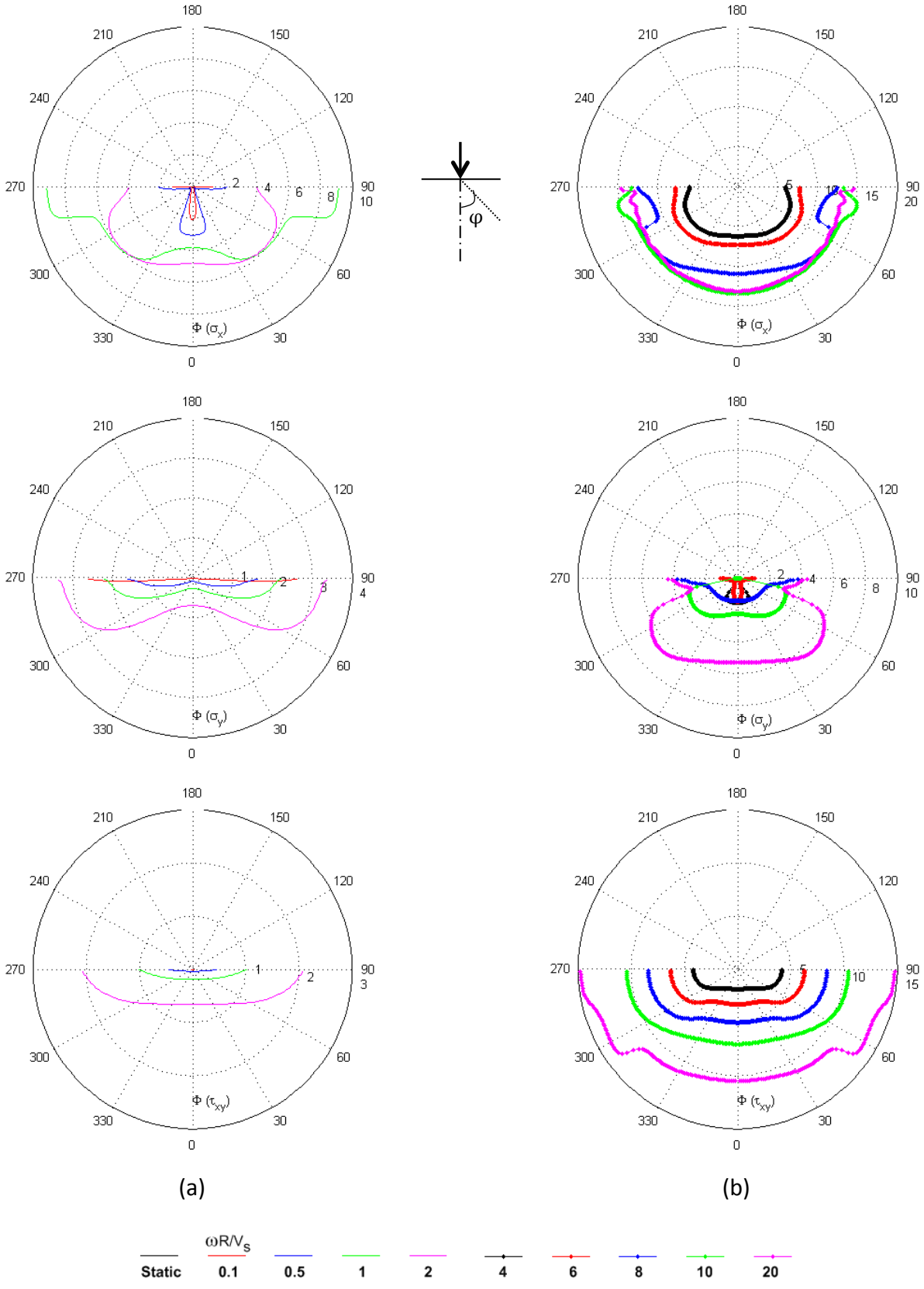

Figure 4.13: Phase angle bulbs due to vertical 2-D line load, v = 0.45, ξ = 1%; (a) $\omega R/V_S$ = 0 (static) to 2, (b) $\omega R/V_S$ = 4 to 20

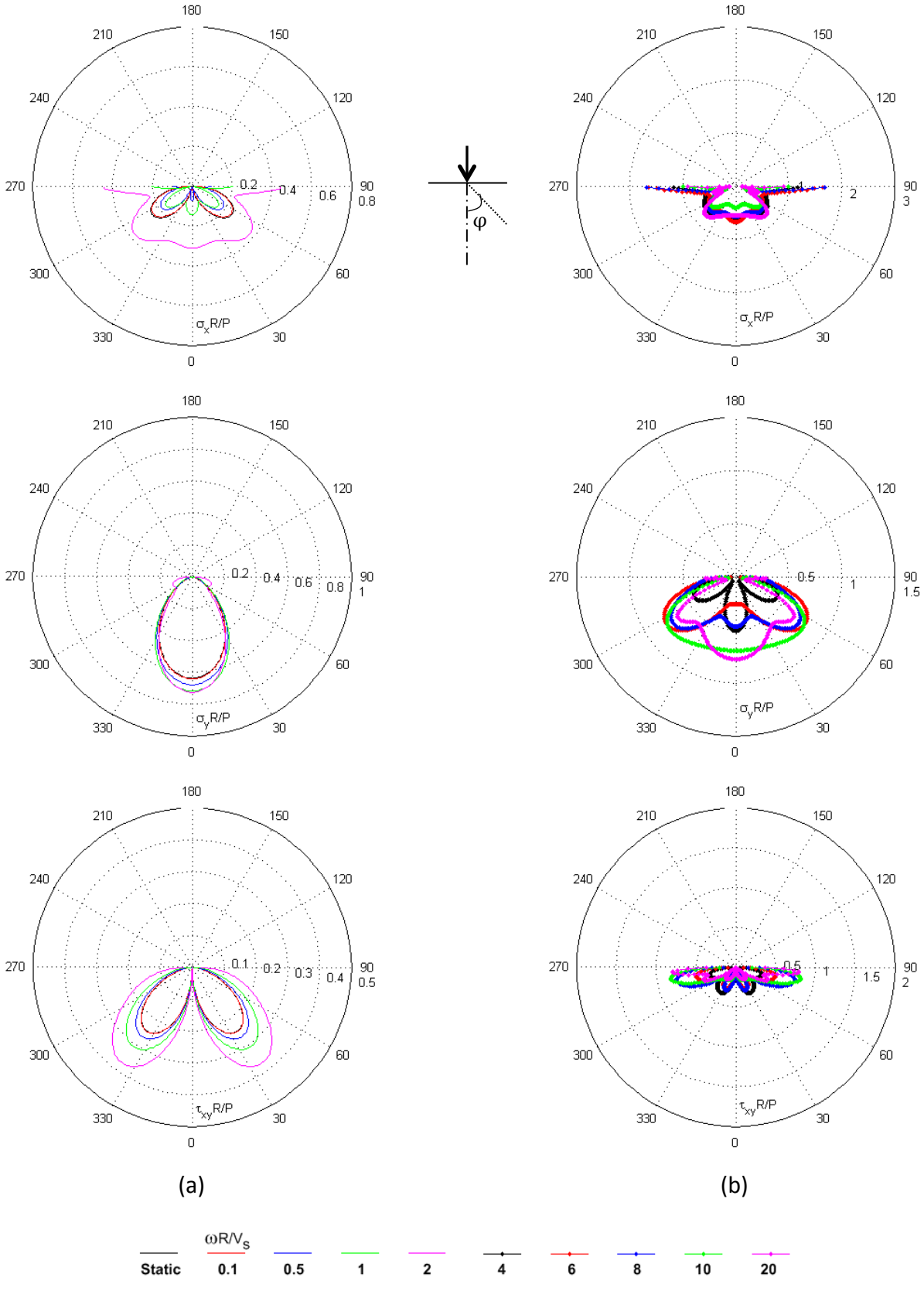

Figure 4.14: Stress amplitude bulbs due to vertical 2-D line load, v = 0.45, ξ = 5%; (a) $\omega R/V_S$ = 0 (static) to 2, (b) $\omega R/V_S$ = 4 to 20

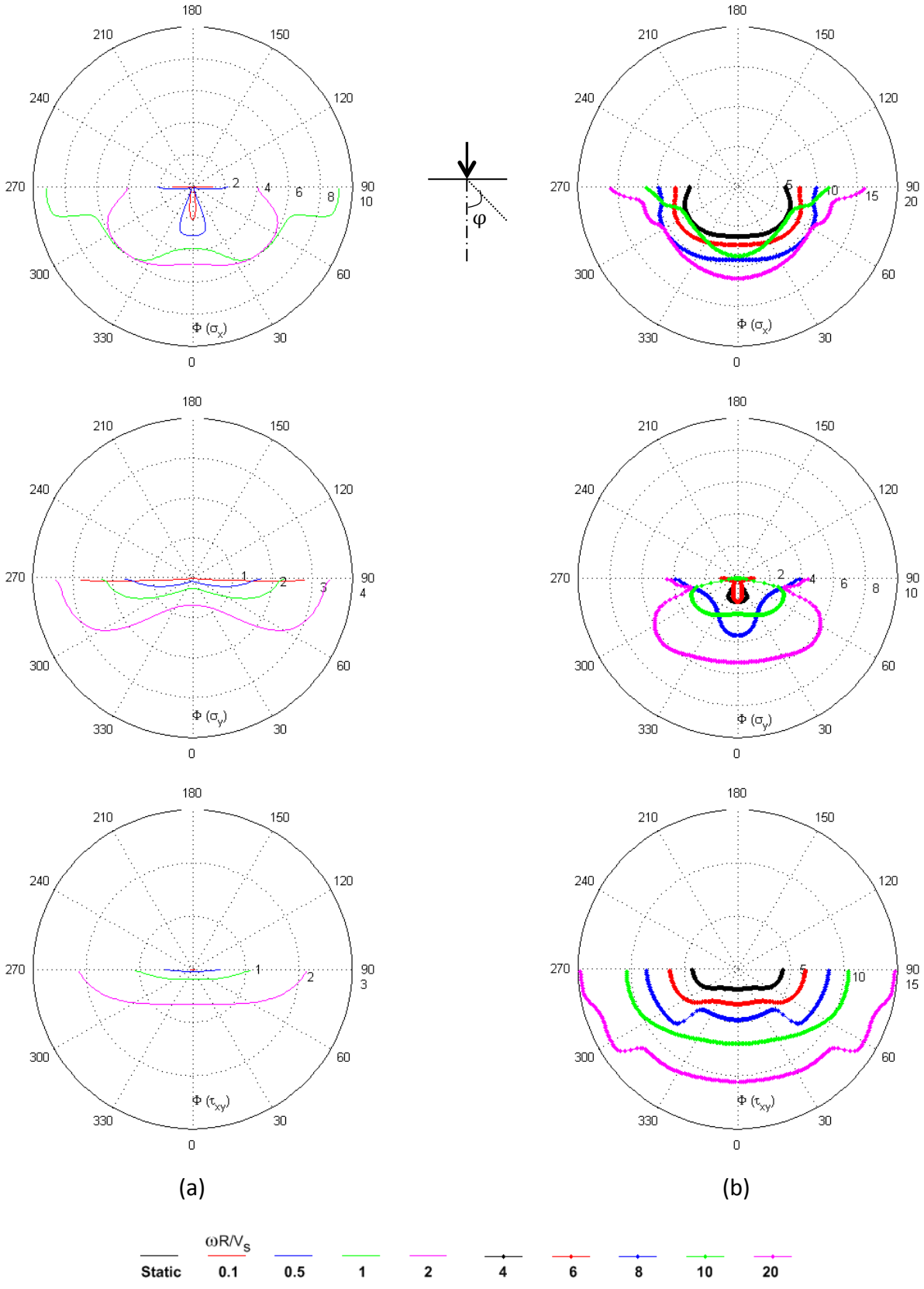

Figure 4.15: Phase angle bulbs due to vertical 2-D line load, v = 0.45, ξ = 5%; (a) $\omega R/V_S$ = 0 (static) to 2, (b) $\omega R/V_S$ = 4 to 20

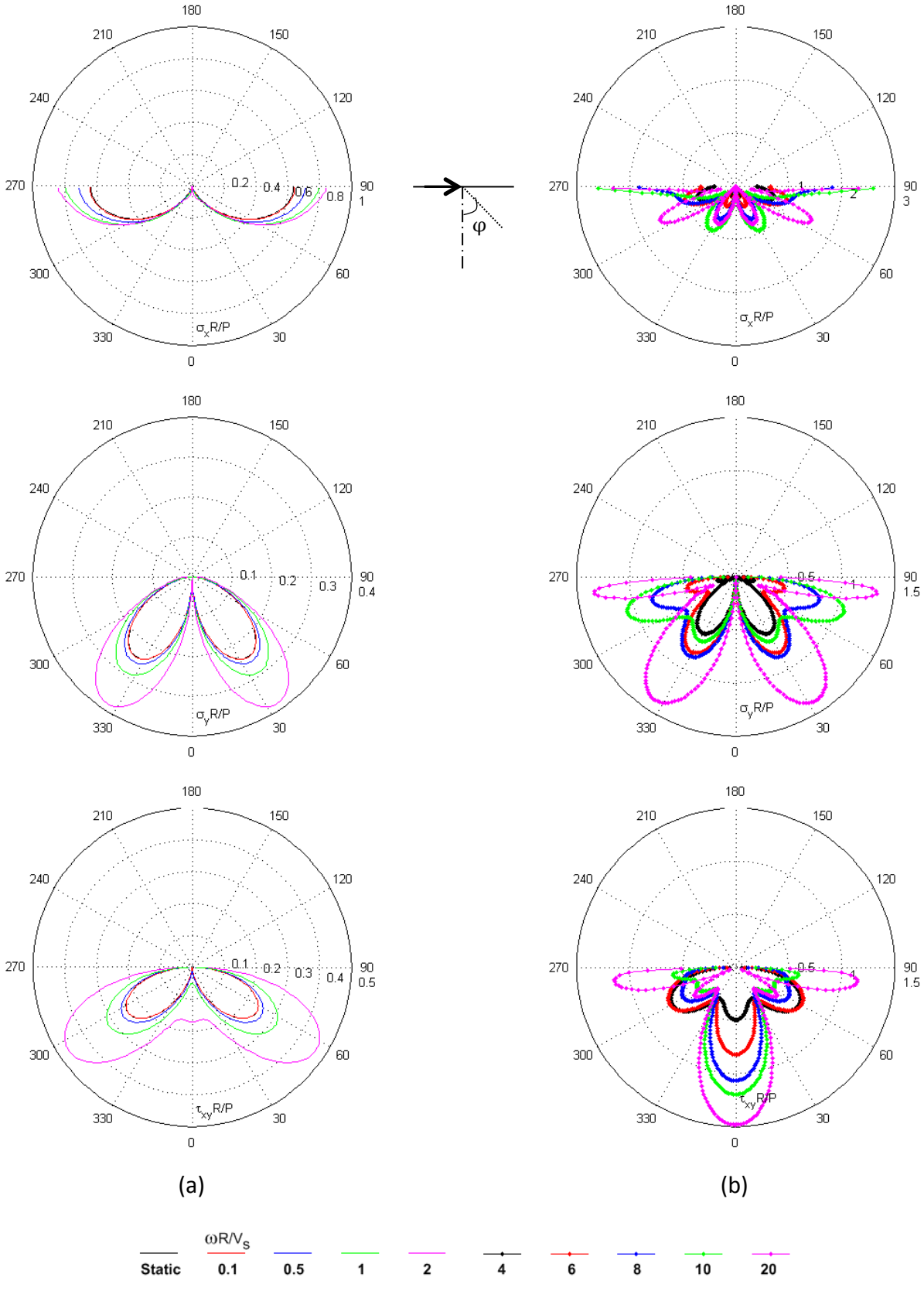

Figure 4.16: Stress amplitude bulbs due to horizontal 2-D line load, v = 0.34, ξ = 1%; (a) $\omega R/V_S$ = 0 (static) to 2, (b) $\omega R/V_S$ = 4 to 20

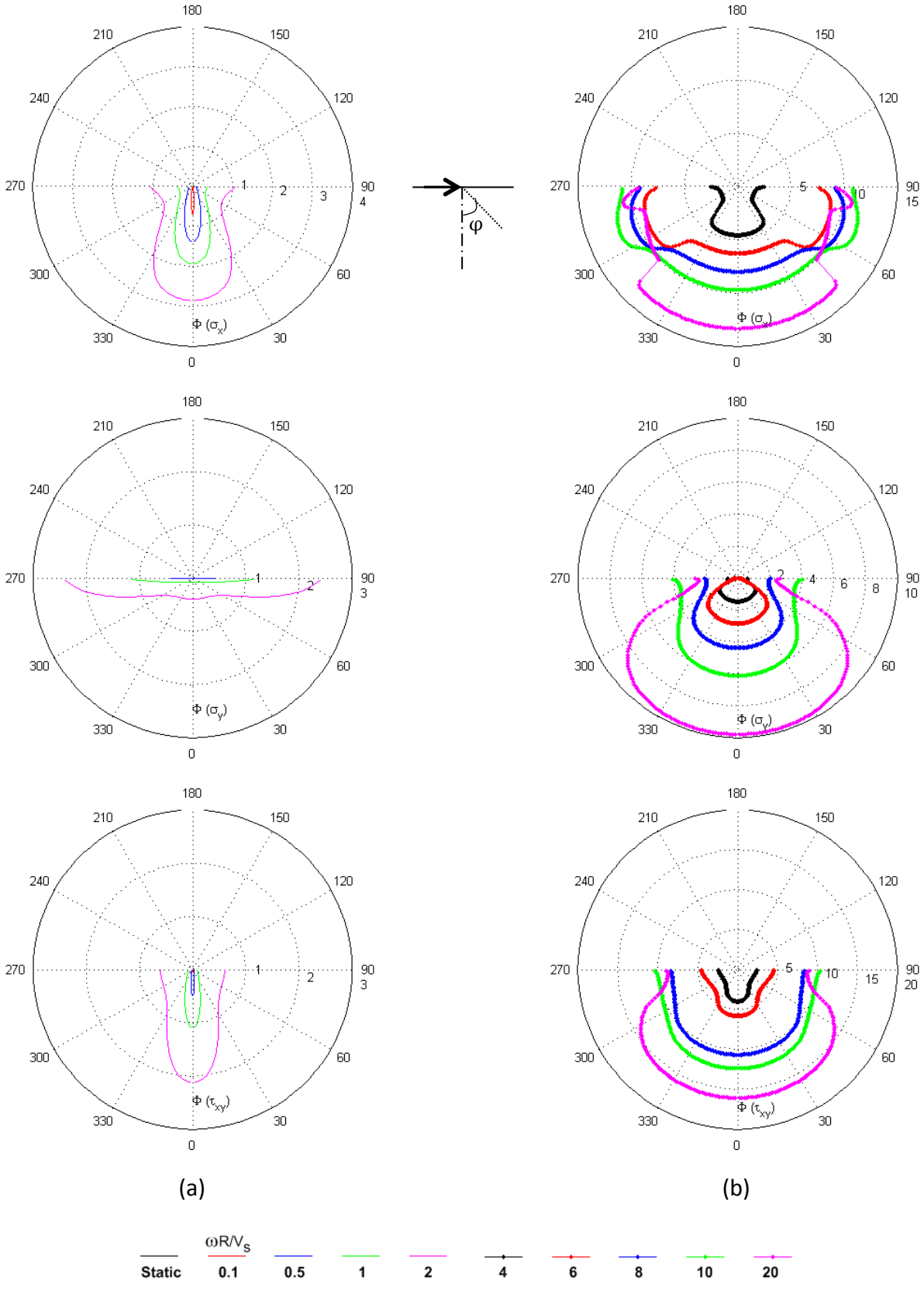

Figure 4.17: Phase angle bulbs due to horizontal 2-D line load, v = 0.34, ξ = 1%; (a) $\omega R/V_S$ = 0 (static) to 2, (b) $\omega R/V_S$ = 4 to 20

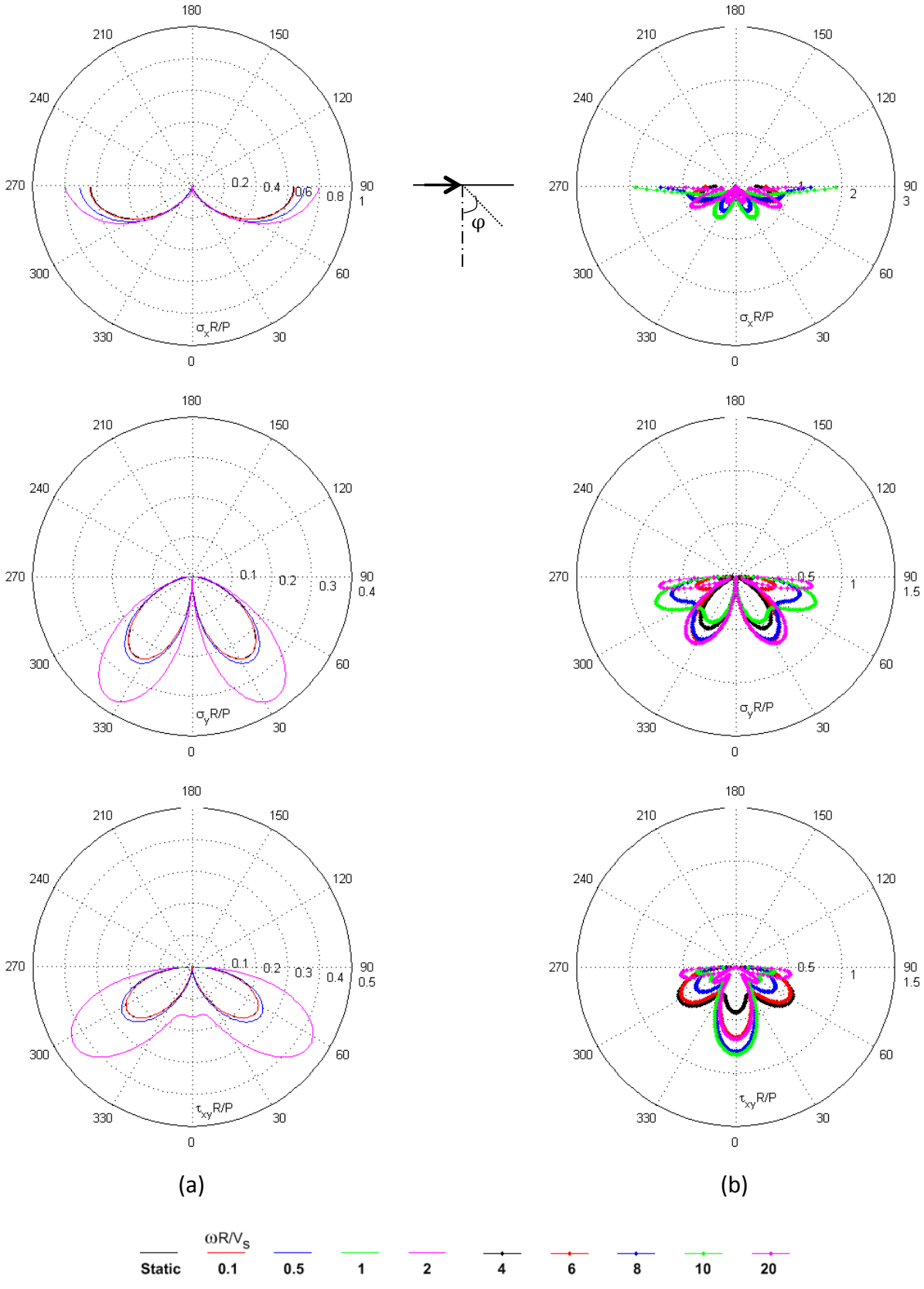

Figure 4.18: Stress amplitude bulbs due to horizontal 2-D line load, v = 0.34, ξ = 5%; (a) $\omega R/V_S$ = 0 (static) to 2, (b) $\omega R/V_S$ = 4 to 20

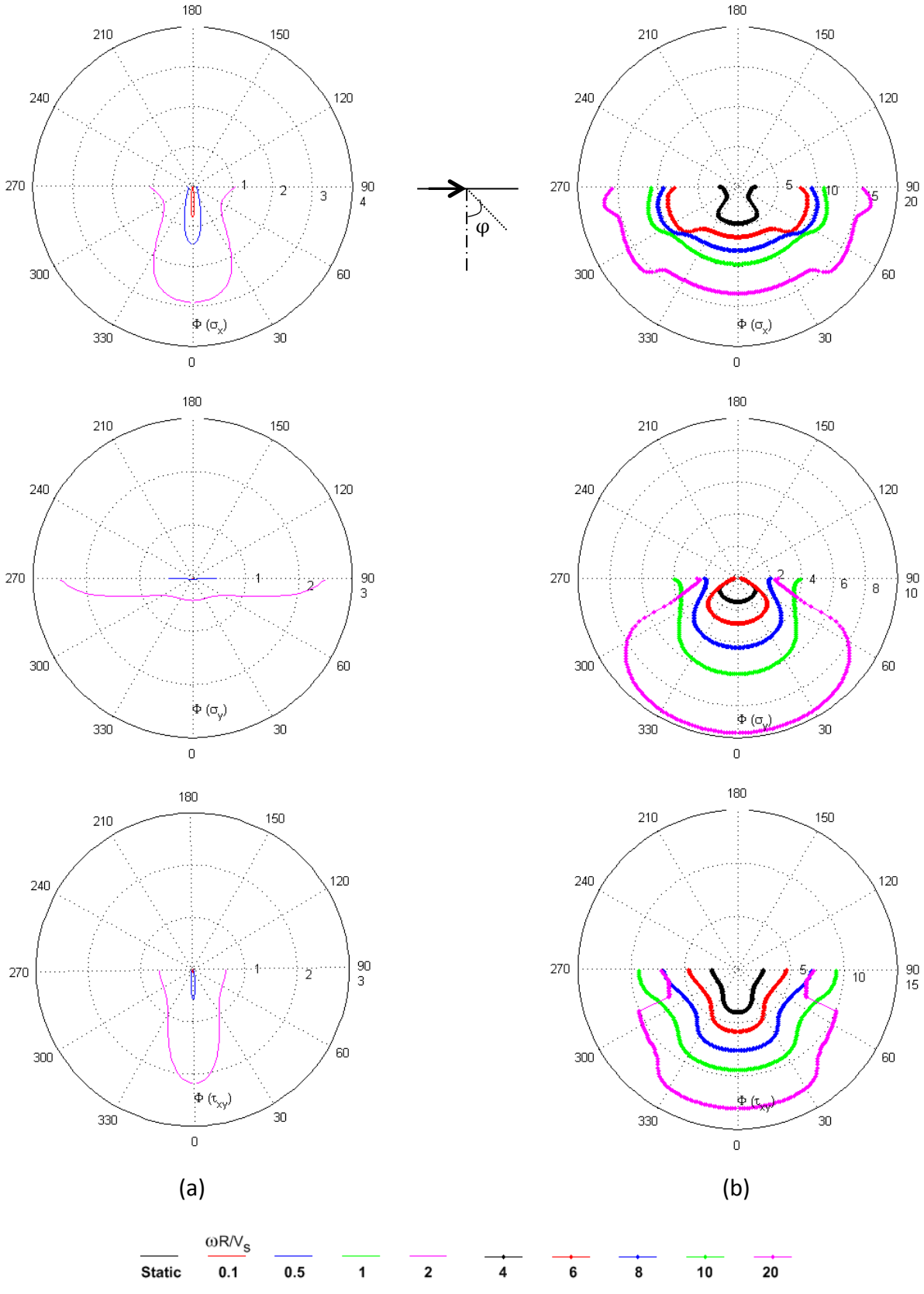

Figure 4.19: Phase angle bulbs due to horizontal 2-D line load, v = 0.34, ξ = 5%; (a) $\omega R/V_S$ = 0 (static) to 2, (b) $\omega R/V_S$ = 4 to 20

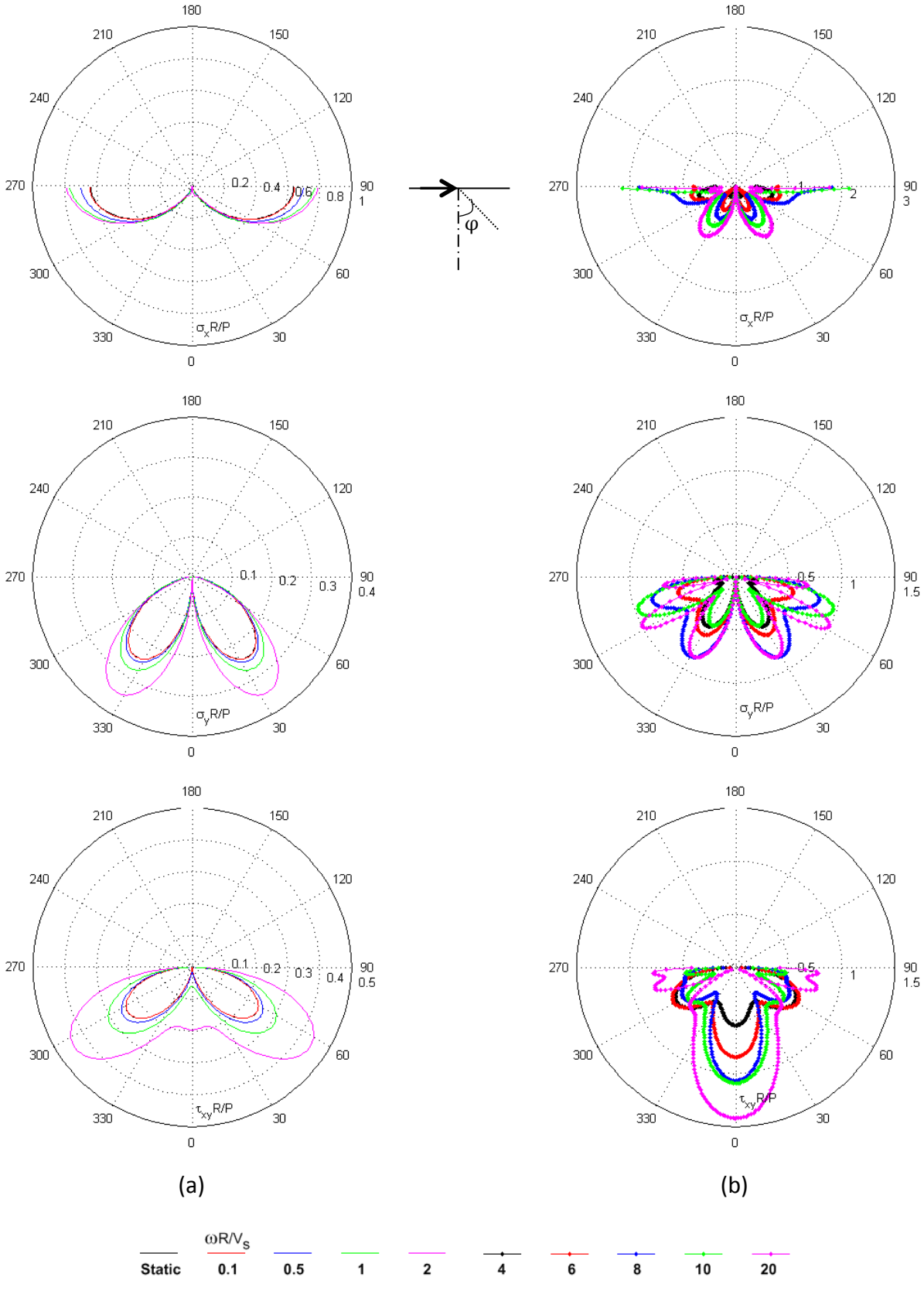

Figure 4.20: Stress amplitude bulbs due to horizontal 2-D line load, v = 0.45, ξ = 1%; (a) $\omega R/V_S$ = 0 (static) to 2, (b) $\omega R/V_S$ = 4 to 20

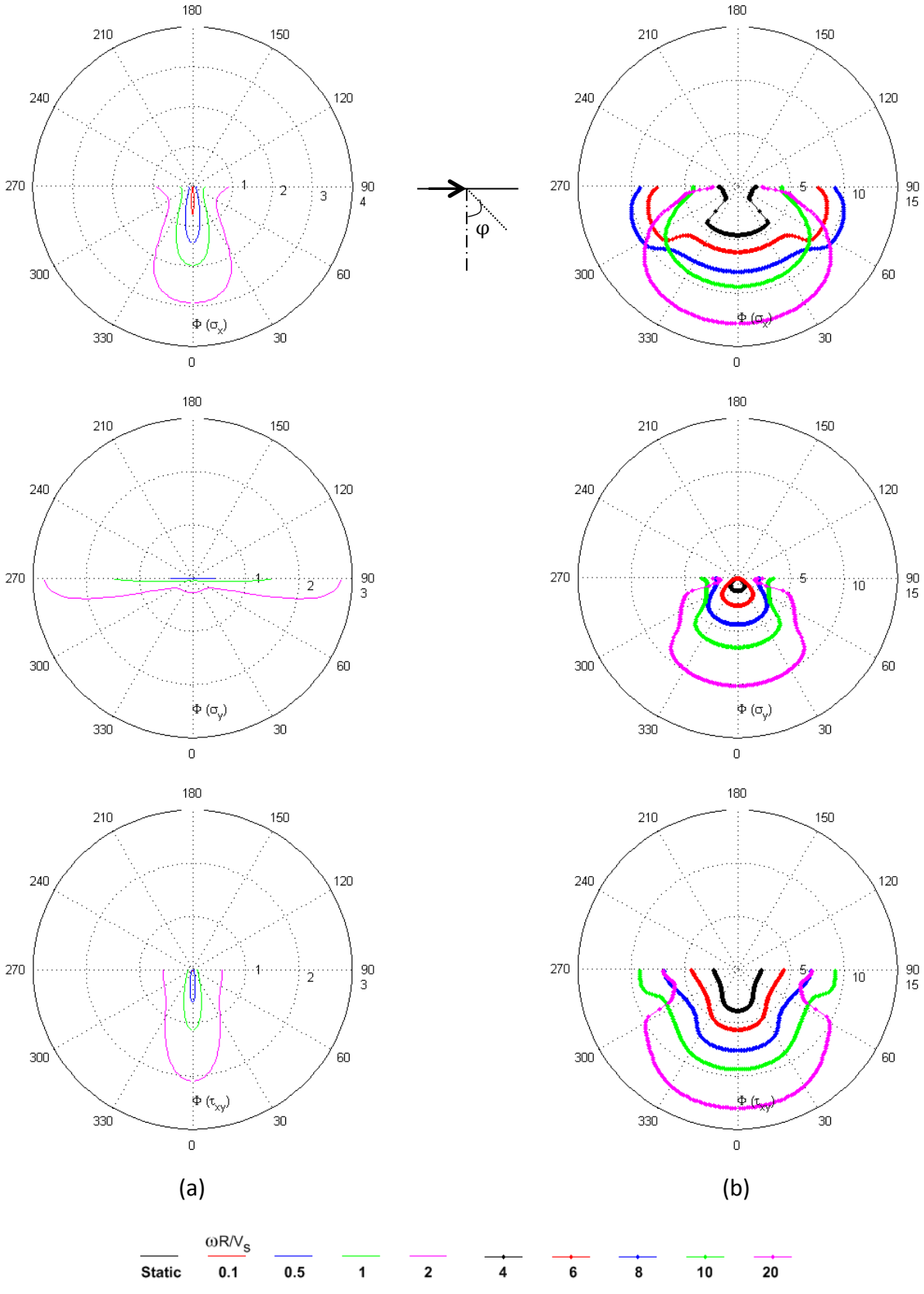

Figure 4.21: Phase angle bulbs due to horizontal 2-D line load, v = 0.45, ξ = 1%; (a) $\omega R/V_S$ = 0 (static) to 2, (b) $\omega R/V_S$ = 4 to 20

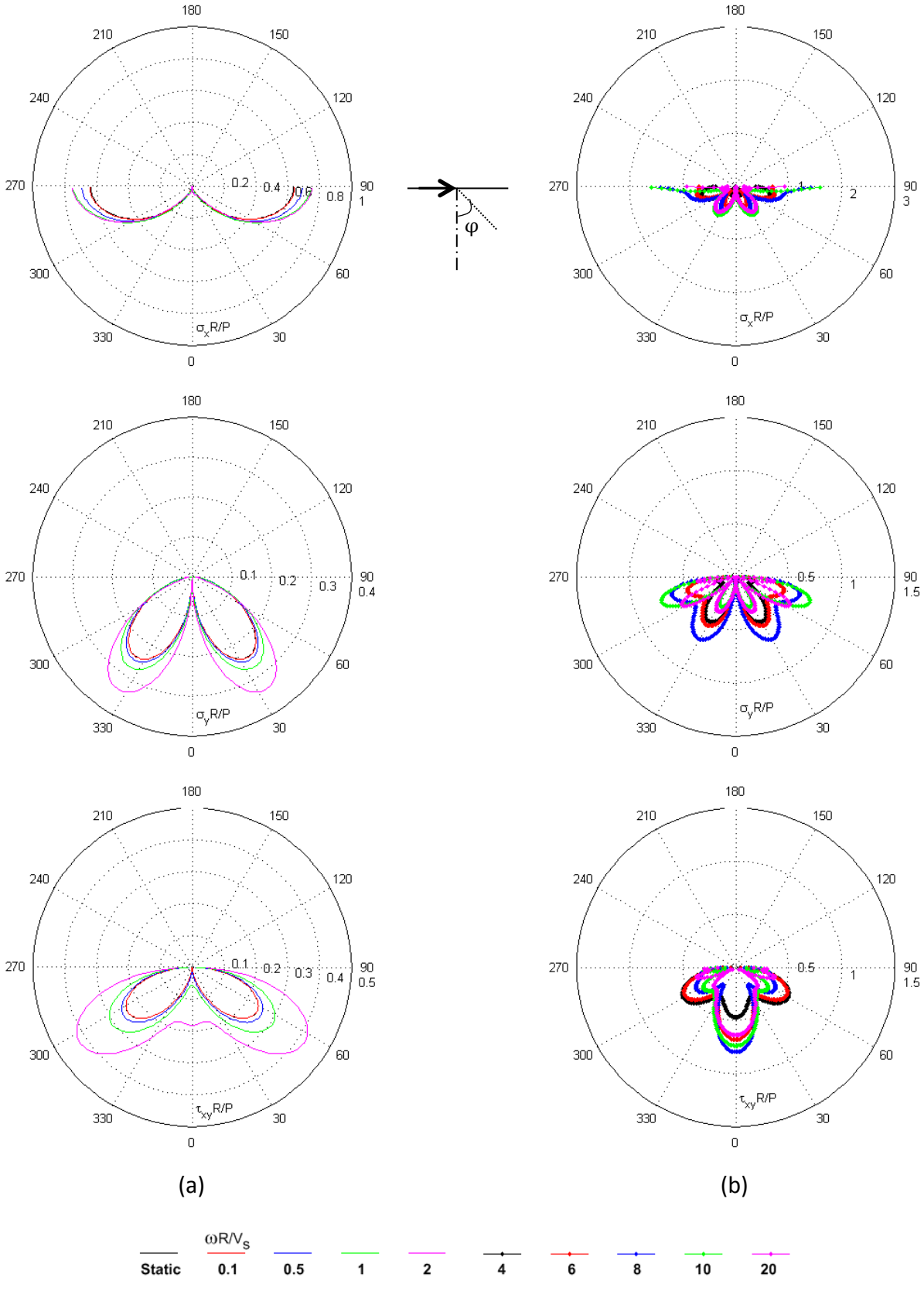

Figure 4.22: Stress amplitude bulbs due to horizontal 2-D line load, v = 0.45, ξ = 5%; (a) $\omega R/V_S$ = 0 (static) to 2, (b) $\omega R/V_S$ = 4 to 20

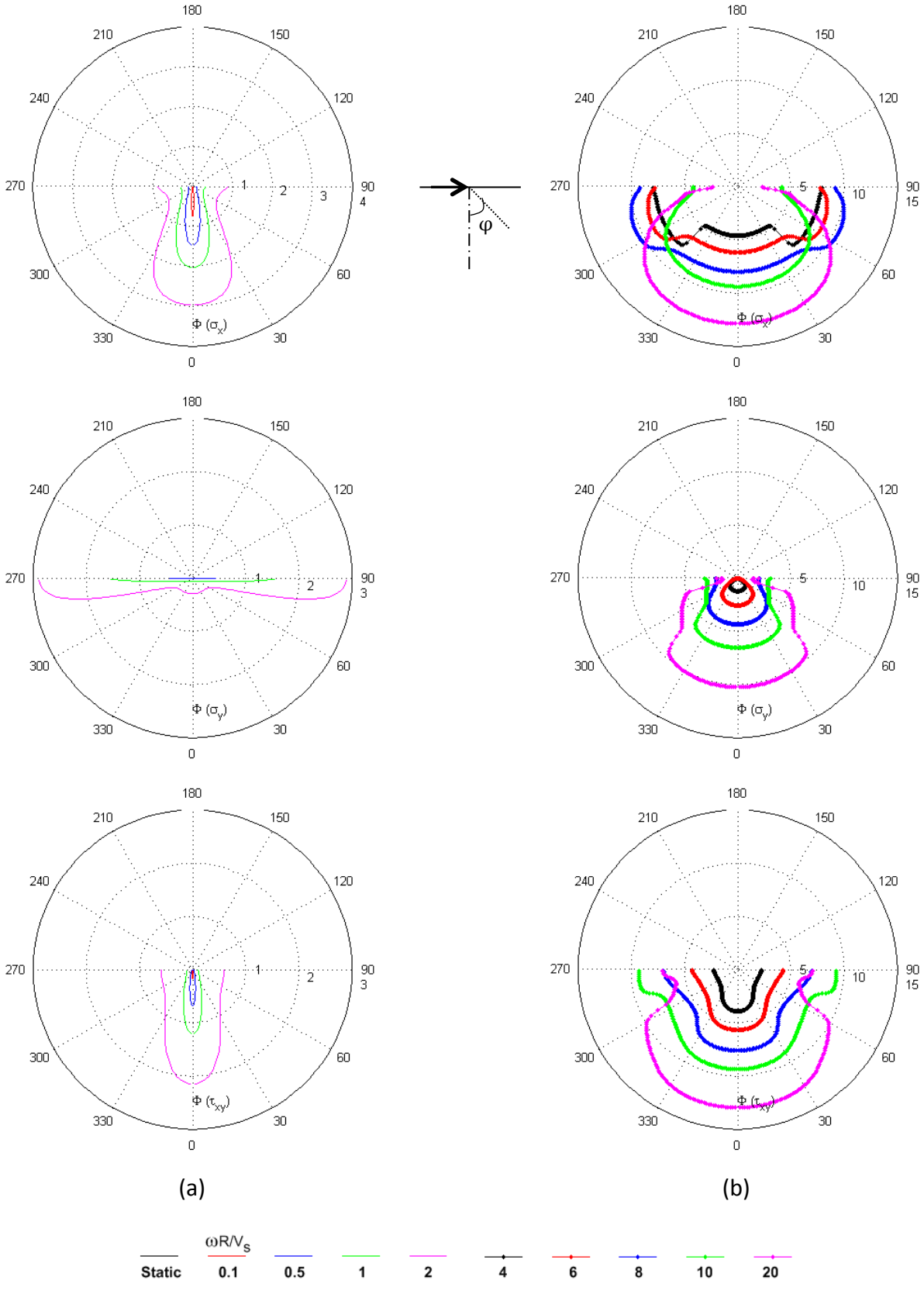

Figure 4.23: Phase angle bulbs due to horizontal 2-D line load, v = 0.45, ξ = 5%; (a) $\omega R/V_S$ = 0 (static) to 2, (b) $\omega R/V_S$ = 4 to 20

As shown in these figures, in the examined frequency range, stress amplitudes are found to have upper limits that far exceed the corresponding static values in both vertical and horizontal line load cases. Similar to the point load stress solutions described in Chapter 3, line loads produce successive zones of destructive and constructive wave interference that complicates the patterns of stress bulbs as frequency increases. We hasten to add that although the overall patterns are similar in line and point load problems, the stress bulbs penetrate deeper into the soil mass in line load cases compared to the point load ones. This fact is related to line load problems requiring 2-D wave propagation; hence the dissipation of energy only occurs in the *x*-*y* plane. In the case of a point load (Chapter 3), the wave propagation occurs in three-dimensional space, leading to more rapid geometric spreading of wave energy. To illustrate these differences, consider the example of a vertical line load for which P = 1 kN/m, $\omega R/V_S$ = 2 rad/sec, and $\varphi = 0^{\circ}$. With reference to Figure 4.8, where $\xi = 0.01$ and $\nu = 0.34$, the normalized vertical stress value is $\sigma_y R/P$ = 0.85. Assuming the same values for force, dimensionless frequency, aperture angel, damping, and Poisson's ratio shown in Figure 3.10, the normalized vertical stress is $\sigma_z R^2/P$ = 0.7, where P has the unit of force. Considering same value of radial distance for both cases (R=1m):

$$\begin{aligned} &\text{vertical line load} \rightarrow \frac{\sigma_y R}{P} = 0.85 \rightarrow \sigma_y = 0.85 \ \ kN/m^2 \\ &\text{vertical point load} \rightarrow \frac{\sigma_z R^2}{P} = 0.70 \rightarrow \sigma_z = 0.70 \ \ kN/m^2 \end{aligned} \tag{4.16}$$

These results confirm that at the same radial distance from the source load, stresses from vertical line loads exceed those for vertical point loads; put another way, stress bulbs penetrate deeper into the soil mass for 2-D problems than for the 3-D case.

In general, phase angle patterns grow radially with increases of dimensionless frequency, which is expected. As discussed earlier, the phase shift should be roughly equivalent to the dimensionless frequency appropriate to the dominant wave type for the aperture angle under consideration. For instance, for vertical stress component, σ_y, due to a vertical line load, phase angle values are close to ($\omega R/V_S$) at aperture angles of 30°- 60°, whereas higher aperture angles ($\varphi > 60°$) produce a minor increase in phase angles due to the dominance of Rayleigh waves. In addition, for the vertical load case the phase bulbs at aperture angles near 0° have a dimple indicating a decrease in phase value, which is due to the predominance of P-waves along the y-axis.

For the case of a horizontally oscillating surface load, the shear stress component, τ_{xy}, at aperture angle near 0° are close to ($\omega R/V_S$) due to the dominance of shear waves in this case. For higher aperture angles there is a minor decrease in phase angle values due to the presence of P-waves travelling at faster velocities. However, the amount of reduction illustrates combined effects of different wave types rather than pure propagation of P-waves.

The results from Figures 4.8 and 4.12 and Figures 4.10 and 4.14 can be compared to show the effects of Poisson's ratio on stress bulbs; while Figures 4.8 and 4.10 and Figures 4.12 and 4.14 can be used to investigate damping effects. The most critical effects of Poisson's ratio are summarized in Figure 4.24, which shows that an increase of Poisson's ratio causes no perceptible change in stress bulb amplitudes or phase angles for aperture angles associated with shear wave propagation (approximately 0º to 20º). However, Poisson's ratio increases produce stress amplitude increases and decreases for aperture angles associated with P-wave (20º − 60º) and Rayleigh wave (60º to 90º) propagation, respectively. Our interpretation is that in the high-ν case, the higher bulk moduli of the soil 'attracts' more P-wave propagation (at the expense of

Rayleigh wave energy), thereby modifying stress amplitudes associated with these wave types. These effects are most apparent for relatively high values of dimensionless frequencies ($\omega R/V_S$ = 10, 20).

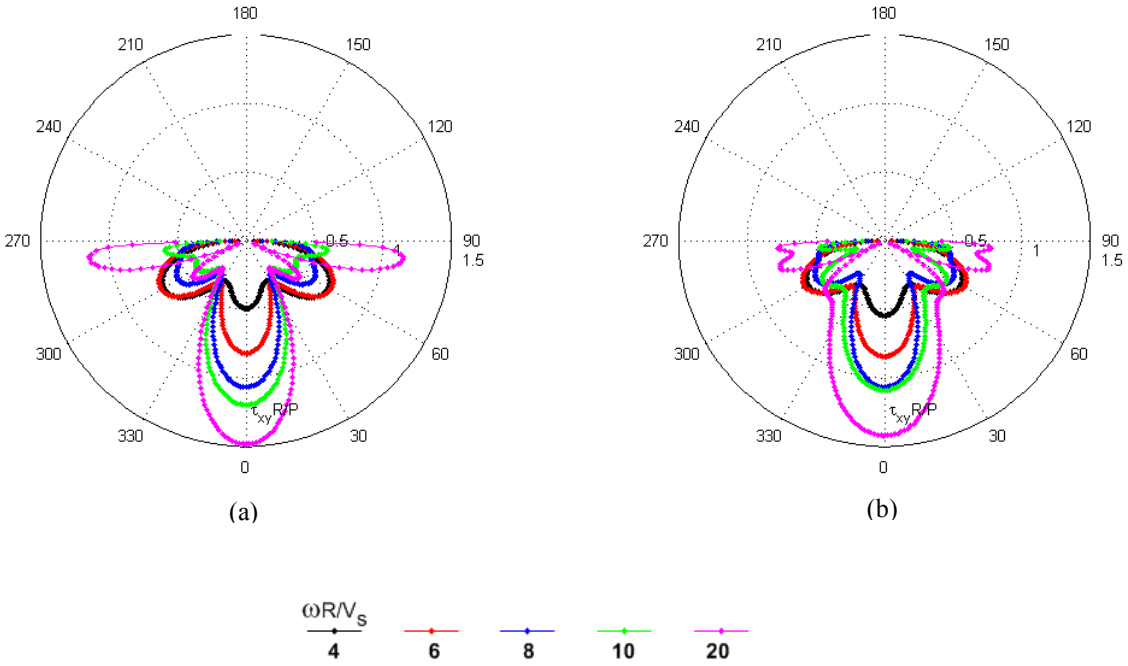

Figure 4.24: Stress amplitudes due to vertical line load, ξ = 1%; (a) v = 0.34, (b) v=0.45

Figure 4.25 shows the most critical effects of increasing soil damping ratio. As expected, there is a reduction of stresses with increasing damping, which are more obvious for high values of dimensionless frequencies ($\omega R/V_S$ = 4 − 10). Aside from stress reductions, increasing damping also serves to smooth the dramatic sharpness in dimensionless stress bulbs for high values of dimensionless frequencies.

It should be noted that the complete sets of results corresponding to 1° increments of azimuthal angle are available in the digital text files (i.e. libraries) and will be used in Chapter 5 to extend the point load solutions to the distributed load cases.

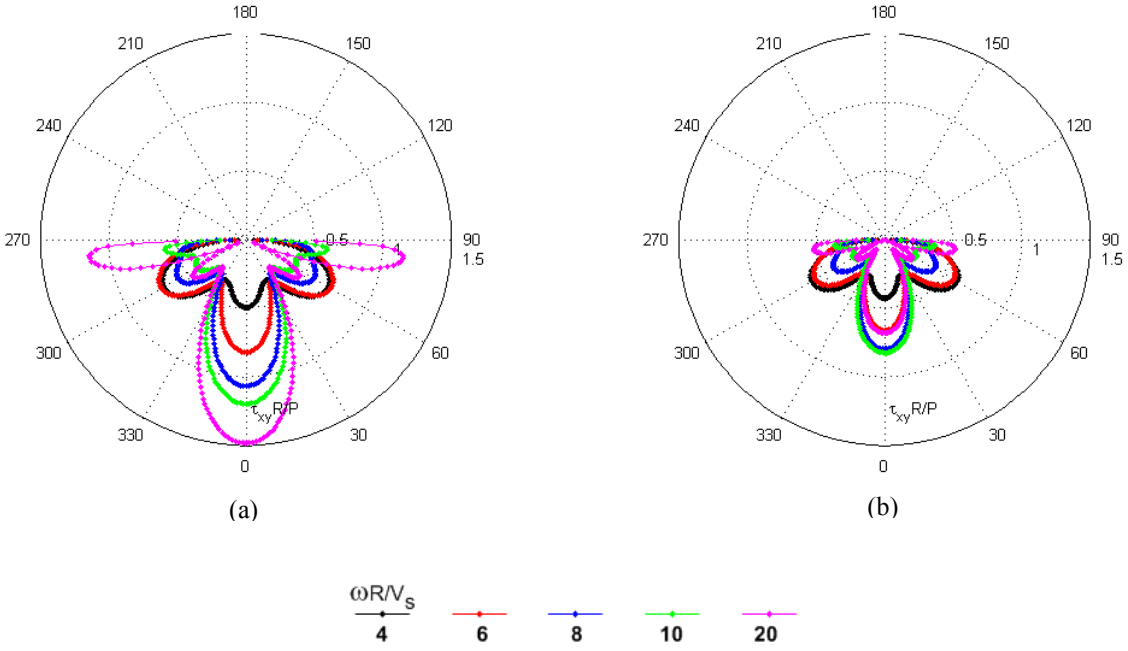

Figure 4.25: Stress amplitudes due to vertical line load, v = 0.34; (a) ξ = 1%, (b) ξ = 5%

4.4 CONCLUSIONS

Values of dimensionless stress, ($\sigma_{ij}R/P$), within foundation soils underlying harmonic vertical and horizontal line loads at the ground surface are a function of dimensionless frequency, aperture angle, damping, and Poisson's ratio. The following conclusions may be drawn for both load types (emphasizing the vertical and shear components):

- For ($\omega R/V_S$) < 1, dynamic effects range from negligible to moderate for both vertical and shear stress components and could probably be ignored.
- For ($\omega R/V_S$) ≈ 2 to 4, the general shapes of the stress distributions are similar to those for the static case, but the stress amplitudes are increased by about 80%.

- For ($\omega R/V_S$) > 4, stress patterns deviate substantially from the static case and follow a more complex pattern, due to constructive and destructive interference of the travelling waves.
- Increase of Poisson's ratio causes no perceptible change in stress bulb amplitudes or phase angles for aperture angles associated with shear wave propagation However, Poisson's ratio increases produce stress amplitude increases and decreases for aperture angles associated with P-wave and Rayleigh wave propagation, respectively. Our interpretation is that in the high-ν case, the higher bulk moduli of the soil 'attracts' more P-wave propagation (at the expense of Rayleigh wave energy), thereby modifying stress amplitudes associated with these wave types.
- Reduction in stress values is a natural outcome of soil damping ratio. However, this effect is more obvious for higher dimensionless frequencies. In other words, higher damping ratio values alleviate the dramatic sharpness in dimensionless stress bulbs with high dimensionless frequencies and cause smoother stress patterns.

5 Dynamic Interface and Within-soil Stresses due to Distributed Surface Loads

Most elements of infrastructure impose loads on the ground surface through foundations of finite area, which may require formal treatment of the distributed nature of the loads across the foundation area. The goal of this chapter is to obtain the stress distribution in the soil medium due to distributed loading that is applied dynamically. Foundations are often idealized at two extremes of rigidity – perfectly flexible and rigid. The evaluation of within-soil stresses from flexible foundations is rather trivial, if computationally expensive; all loads applied to the foundation are idealized as point or line loads, allowing the solutions from Chapters 3 and 4 to be applied sequentially across all foundation loads and dynamic stresses at any point are obtained through summation of their respective complex-valued components.

Rather, in this chapter, I begin with an overview of available stress solutions for the soil-rigid foundation interface from the literature, most of which is applicable to static loads. I describe a relatively limited body of literature for cyclic loading of rigid foundations, and proceed to present the results of ISoBEM simulations for this problem. The results are presented in the form of graphs as well as parametric equations for pressures at the soil-rigid foundation interface (these solutions do not apply for stresses at depth within the soil body).

To evaluate within-soil dynamic stresses, the devised interface stresses can be converted to input surface loads to simulate the effects of vibration of a rigid foundation. Moreover, to

facilitate simplified modeling of this problem in Matlab, I demonstrate how the principle of superposition can be applied via integration of the fundamental dynamic stress solutions presented in Chapters 3 and 4 to obtain within-soil dynamic stresses resulting from surficial loads applied at different ground surface locations. This implementation is only developed currently for uniform surface loads (analogous to the flexible foundation problem). The accuracy of the currently implemented solutions is verified by comparison to stress solutions obtained by direct modeling of uniform distributed loads using ISoBEM.

5.1 STRESS DISTRIBUTIONS AT THE SOIL-RIGID FOUNDATION INTERFACE

In the following sections, I describe available static stress solutions at the soil-rigid foundation interface for two types of circular and rigid foundations. I then perform ISoBEM simulations for each case to evaluate dynamic stresses directly beneath the cyclically loaded rigid foundation.

5.1.1 Circular Rigid Foundation on Elastic Half-space

Schiffman and Aggarwala (1961) were the first to evaluate the vertical contact pressure directly beneath a rigid circular foundation. Their results apply for the conditions of a foundation on the surface of a homogeneous, elastic and isotropic half-space. The foundation is exposed to static vertical load (shown in Figure 5.1 where $\omega = 0$), producing stresses described by,

$$\sigma_z = \frac{P}{2\pi a\sqrt{a^2 - r^2}} \tag{5.1}$$

where r is the radial distance from the center, a is the radius of the circular foundation, and P is the applied vertical load.

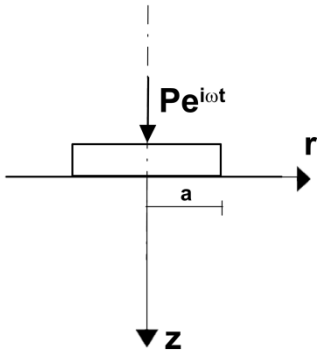

Figure 5.1 Symmetrical vertical loading of rigid circular foundation

The dynamic counterpart to the aforementioned problem, shown in Figure 5.1 ($\omega > 0$), is investigated using ISoBEM. As shown in Figure 5.2, I first verify the accuracy of ISoBEM analyses for the static vertical problem relative to the classical solution of Schiffman and Aggarwala (1961). In Figure 5.2, interface stresses are normalized by the average stress $P/(\pi a^2)$ and location r is normalized by radius a. There is nearly perfect compatibility between the stress fields obtained from the closed-form solutions and ISoBEM. The results indicate that the stress near the center of the footing is only half of the average stress. The interface stresses exceed the average only for $r/a > 0.8$. The singularity at the edge of the footing ($r/a = 1$) is typical "corner" behavior encountered in elasticity problems. In practical applications, the stress at the edge will always be finite due to local yielding of the soil material and lack of perfectly rigid behavior in the foundation elements. In this light, elasticity solutions are seen to provide lower bounds for stresses close to the center of the footing and upper bounds close to the edge. Interestingly, the stress distribution in Equation 5.1 is independent of the elastic constants of the half-space.

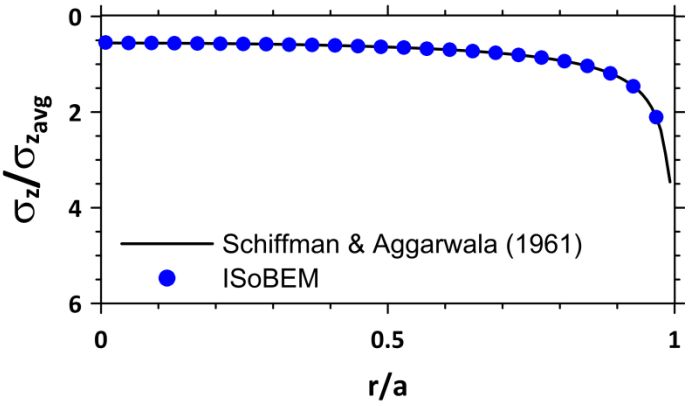

Figure 5.2 Comparison between ISoBEM and analytical solution for vertical contact pressure of a circular rigid foundation under static vertical loading ($\sigma_z/\sigma_{z_{avg}} = 1/(2\sqrt{1-(r/a)^2})$)

For dynamic problems, I define the dimensionless frequency using the characteristic dimension of the problem, which is the radius of the circular foundation. Hence, the dimensionless frequency is selected to be ($\omega a/V_S$). Sung (1953) and Bycroft (1956) present approximate solutions suggesting that dynamic stresses are well approximated by static solutions at low frequencies ($\omega a/V_S$ < 1.5), where the foundation dimension is small compared to the wavelength of stress waves emitted from the soil-foundation interface. As shown in Figure 5.3, the transition from the static behavior is first evident at $\omega a/V_S$ = 1.0. Hence, $\omega a/V_S \leq 0.5$ is taken as equivalent to the static solution.

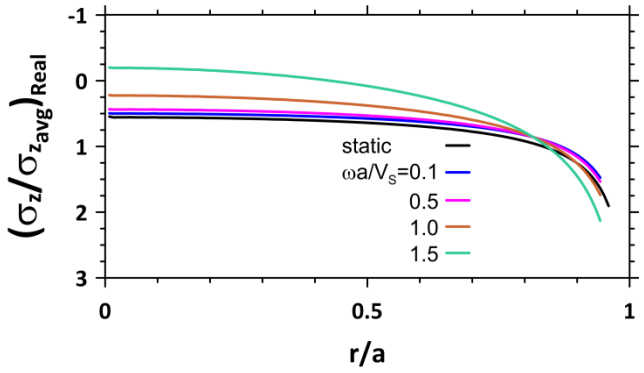

Figure 5.3 Comparison between static and dynamic behavior for vertical contact pressure of a circular rigid foundation

To investigate the dependence of contact stresses on frequency, axisymmetric models in ISoBEM were developed to simulate tractions at the soil-foundation interface for circular rigid foundation on the surface of an elastic half-space. The simulations are performed for dimensionless frequencies ranging from 0.1 − 10. Vertical stress components for nine dimensionless frequencies are shown in Figures 5.4 in terms of their real and imaginary parts.

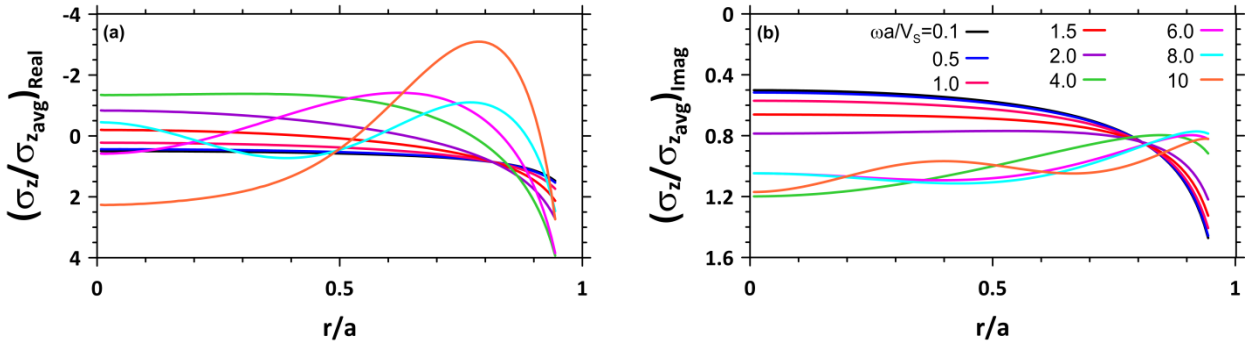

Figure 5.4 Dynamic vertical stress distribution at soil-foundation interface of a rigid circular foundation under vertical cyclic loading (a) Real part, (b) Imaginary part

To establish equations for practical use corresponding to these stress distributions, polynomials are fitted to each curve. The polynomials are of order six,

$$\sigma_z = \sum_{i=1}^{6} c_i x^i \tag{5.2}$$

where x is the dimensionless location (r/a). For stress distribution at soil-foundation interface of a rigid circular foundation under vertical cyclic loading with dimensionless frequency of ($\omega a/V_S \leq 0.5$), one should use Equation 5.1 for the real part while keeping imaginary part as zero. For higher dimensionless frequencies (for $\omega a/V_S \geq 0.5$), Equation 5.2 should be used for which the coefficients are presented in Tables 5.1 and 5.2, respectively.

5.1 Dynamic vertical stress distribution polynomial coefficients at soil-foundation interface of a rigid circular foundation under vertical cyclic loading – Real Part

Dimensionless Freq. (ωa/Vs)	c_0	c_1	c_2	c_3	c_4	c_5	c_6
0.5	-0.45	-0.76	9.32	-43.9	100	-107	44.2
1.5	-0.17	-1.23	15.8	-72.3	165	-177	73
2	-0.79	-1.71	22.2	-99.7	228	-244	100
4	-1.28	-3.03	35.8	-178	413	-439	180
6	0.66	-3.58	33.5	-215	509	-533	216
8	-0.37	-3.35	55.2	-164	229	-219	108
10	2.32	-2.77	26.6	-145	350	-477	255

Table 5.2 Dynamic vertical stress distribution polynomial coefficients at soil-foundation interface of a rigid circular foundation under vertical cyclic loading – Imaginary Part

Dimensionless Freq. (ωa/Vs)	c_0	c_1	c_2	c_3	c_4	c_5	c_6
1.5	0.67	-0.59	7.18	-34.4	78.6	-84.0	34.4
2	0.79	-0.51	6.05	-29.8	68.1	-72.7	29.7
4	1.20	-0.31	2.91	-18.4	42.4	-44.9	18.2
6	1.05	-0.21	3.11	-11.6	23.2	-26.0	11.4
8	1.05	-0.18	2.90	-10.1	20.3	-24.1	10.9
10	1.16	0.02	-3.10	-4.44	43.6	-65.3	28.8

The coefficients of the polynomials are also plotted as a function of dimensionless frequency for real and imaginary parts in Figure 5.5, and are presented in form of equations in Tables 5.3 and 5.4. Using these coefficients, the devised surface stresses can then be readily computed.

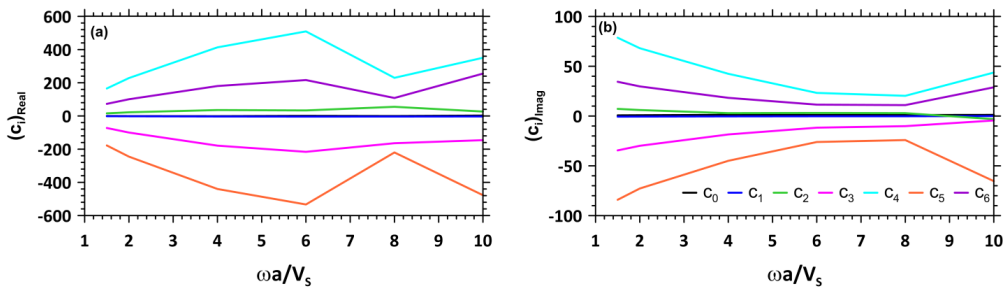

Figure 5.5 Polynomials coefficients for equations of dynamic vertical stress distribution at soil-foundation interface of a rigid circular foundation under cyclic loading (a) Real part, (b) Imaginary part

5.3 Polynomials coefficients for equations of dynamic vertical stress distribution at soil-foundation interface of a rigid circular foundation under cyclic vertical loading – Real Part

	$c = \sum_{i=1}^{5} a_i (\frac{\omega a}{V_s})^i$
c_0	$y = 0.0054x^5 - 0.1294x^4 + 1.0806x^3 - 3.5885x^2 + 3.8921x - 0.9668$
c_1	$y = -0.0002x^5 + 0.0059x^4 - 0.0565x^3 + 0.3547x^2 - 1.7963x + 0.8289$
c_2	$y = -0.0484x^5 + 1.1538x^4 - 9.6679x^3 + 33.475x^2 - 37.813x + 24.356$
c_3	$y = -0.0731x^5 + 1.7588x^4 - 15.197x^3 + 64.284x^2 - 174.12x + 87.188$
c_4	$y = 0.4434x^5 - 10.53x^4 + 89.343x^3 - 349.49x^2 + 731.48x - 397.47$
c_5	$y = -0.518x^5 + 12.189x^4 - 102.7x^3 + 399.07x^2 - 822.15x + 447.15$
c_6	$y = 0.191x^5 - 4.4302x^4 + 36.864x^3 - 142.35x^2 + 298.84x - 158.4$

5.4 Polynomials coefficients for equations of dynamic vertical stress distribution at soil-foundation interface of a rigid circular foundation under cyclic vertical loading – Imaginary Part

	$c = \sum_{i=1}^{5} a_i (\frac{\omega a}{V_s})^i$
c_0	$y = -0.0007x^5 + 0.0197x^4 - 0.1919x^3 + 0.78x^2 - 1.1114x + 1.1353$
c_1	$y = 1E\text{-}04x^5 - 0.0024x^4 + 0.0234x^3 - 0.1221x^2 + 0.419x - 1.0112$
c_2	$y = 0.0015x^5 - 0.0488x^4 + 0.5113x^3 - 1.9101x^2 + 0.6903x + 8.9523$
c_3	$y = 0.0067x^5 - 0.1744x^4 + 1.7325x^3 - 8.7467x^2 + 27.276x - 60.649$
c_4	$y = -0.0135x^5 + 0.4055x^4 - 4.394x^3 + 22.715x^2 - 68.069x + 142.47$
c_5	$y = 0.0071x^5 - 0.2587x^4 + 3.1698x^3 - 18.362x^2 + 62.86x - 146.42$
c_6	$y = -0.0009x^5 + 0.0542x^4 - 0.8181x^3 + 5.6279x^2 - 22.673x + 58.24$

The accuracy of the approximation of dynamic vertical stress distribution using polynomial is examined using direct modeling in ISoBEM and is shown in Figure 5.6.

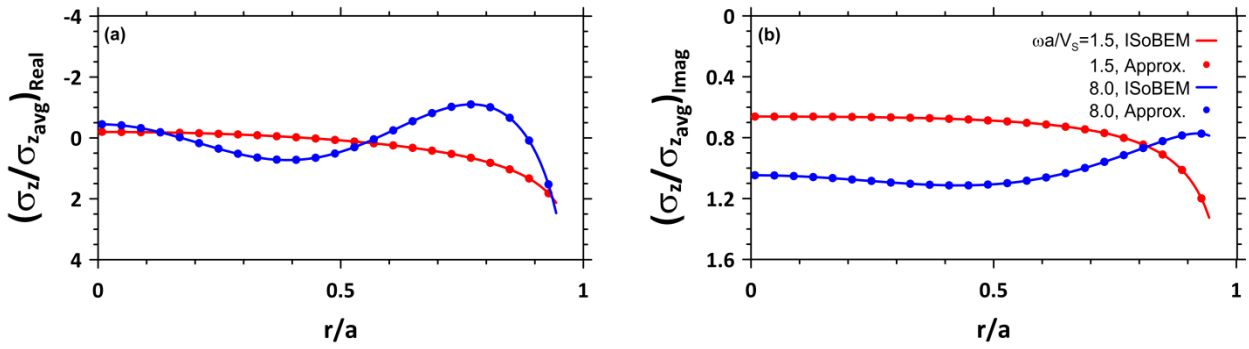

Figure 5.6 Verification of the accuracy of polynomials solutions (Approx.) for dynamic vertical stress distribution at soil-foundation interface of a rigid circular foundation under cyclic loading (a) Real, (b) Imaginary parts

It should be noted that we attempted the horizontal and moment cases for the circular foundation, but we encountered some difficulties. These two cases will be evaluated further in future research.

5.1.2 Strip Rigid Foundation on Elastic Half-space

Borowicka (1939) presented a static solution for the vertical contact pressure directly beneath a rigid strip foundation subjected to symmetrical vertical static loading (shown in Figure 5.5 where ω = 0). The results apply for a smooth (zero friction at soil interface) rigid foundation of width 2b on the surface of a homogeneous, isotropic half-space and are given by,

$$\sigma_y = \frac{2P}{\pi b\sqrt{1-\left(\frac{x}{b}\right)^2}} \tag{5.3}$$

where x is the horizontal distance from the footing centerline and P is the applied vertical load per unit footing length. The order of the singularity at $x=b$ is the same as at $r=a$ in the 3-D problem. As before, no elastic constants for the soil medium appear in the solution.

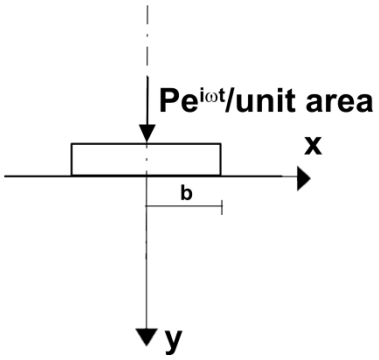

Figure 5.7 Symmetrical vertical loading of rigid strip foundation

The dynamic counterpart to problem in Figure 5.5 ($\omega > 0$) is investigated using ISoBEM. As shown in Figure 5.8, I first verify the accuracy of ISoBEM analyses by comparing the static result to the solution provided by Borowicka (1939). In Figure 5.8, interface stresses are normalized by the average stress $P/(2b)$ and location x is normalized by half-width b. There is nearly perfect compatibility between the stress fields obtained from the closed-form solutions and ISoBEM. Interestingly, the contact stress at the center of the footing is somewhat higher than in the 3-D problem ($2/\pi$ instead of 1/2).

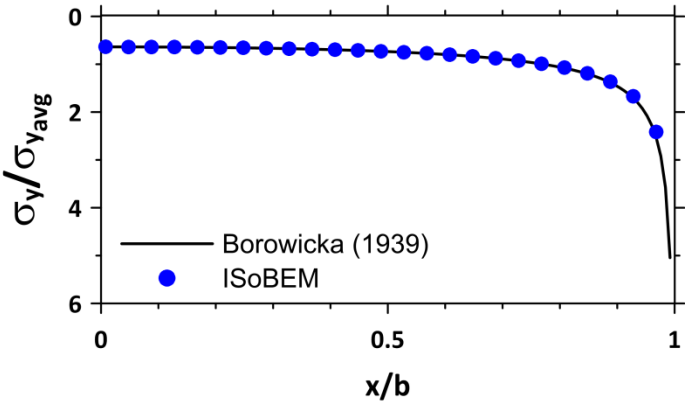

Figure 5.8 Comparison between ISoBEM and analytical solution for vertical contact pressure of a rigid strip foundation under static vertical loading ($\sigma_y/\sigma_{y_{avg}} = 2b/(\pi\sqrt{1-(x/b)^2}$)

Similar to the case of circular rigid foundation, the dimensionless frequency is selected to be ($\omega b/V_S$). Two-dimensional models in ISoBEM were developed to simulate soil-foundation interface stresses for a rigid strip foundation on surface of an elastic half-space for dimensionless frequency ranging from $0.1 - 10$. The stress components corresponding to these dimensionless frequencies are shown in Figures 5.9 for both real and imaginary parts.

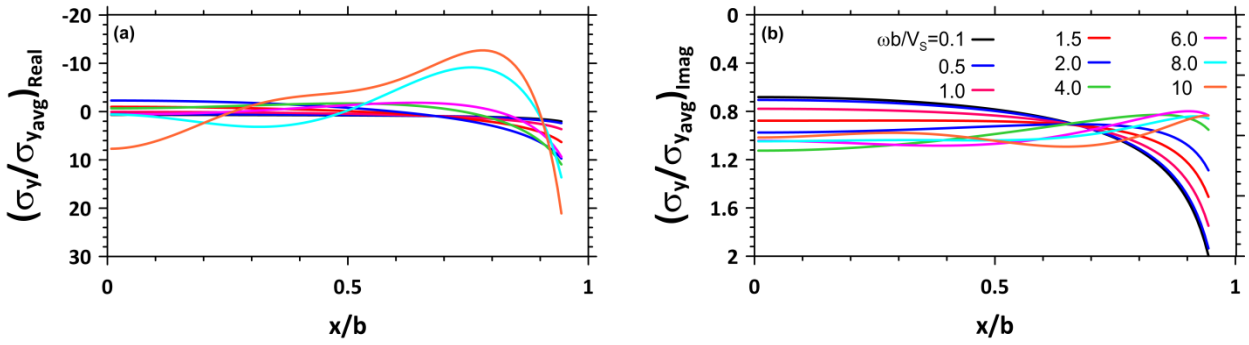

Figure 5.9 Dynamic vertical stress distribution at soil-foundation interface of a rigid strip foundation under cyclic vertical loading (a) Real part, (b) Imaginary part

The corresponding coefficients of the stress distribution equations are presented in Tables 5.5 and 5.6 for real and imaginary parts, respectively (for $\omega b/V_S \geq 1.5$). These coefficients are also plotted as a function of dimensionless frequency in Figure 5.10, and are presented in form of equations in Tables 5.7 and 5.8. Using these coefficients, the devised surface stresses can be readily computed.

Table 5.5 Dynamic vertical stress distribution polynomial coefficients at soil-foundation interface of a strip rigid foundation under cyclic vertical loading– Real Part

Dimensionless Freq. (ωa/Vs)	c_0	c_1	c_2	c_3	c_4	c_5	c_6
1.5	-0.91	-3.38	49.0	-222	507	-543	223
2	-2.17	-6.12	78.5	-354	810	-867	356
4	-0.49	-8.33	92.5	-491	1139	-1207	493
6	0.78	-8.60	95.2	-501	1129	-1195	497
8	1.00	-19.9	284	-1023	1685	-1652	761
10	7.78	-2.09	-139	-285	2612	-4503	2374

Table 5.6 Dynamic vertical stress distribution polynomial coefficients at soil-foundation interface of a strip rigid foundation under cyclic vertical loading – Imaginary Part

Dimensionless Freq. (ωa/Vs)	c_0	c_1	c_2	c_3	c_4	c_5	c_6
1.5	0.89	-0.64	7.75	-37.7	86.0	-91.9	37.6
2	0.98	-0.51	5.94	-30.0	68.6	-73.2	29.9
4	1.13	-0.31	3.27	-18.7	42.6	-45.4	18.5
6	1.04	-0.22	3.24	-12.4	25.0	-27.9	12.2
8	1.05	-0.19	2.19	-12.4	32.9	-39.3	16.6
10	1.01	-0.07	0.14	-8.08	36.6	-51.3	22.5

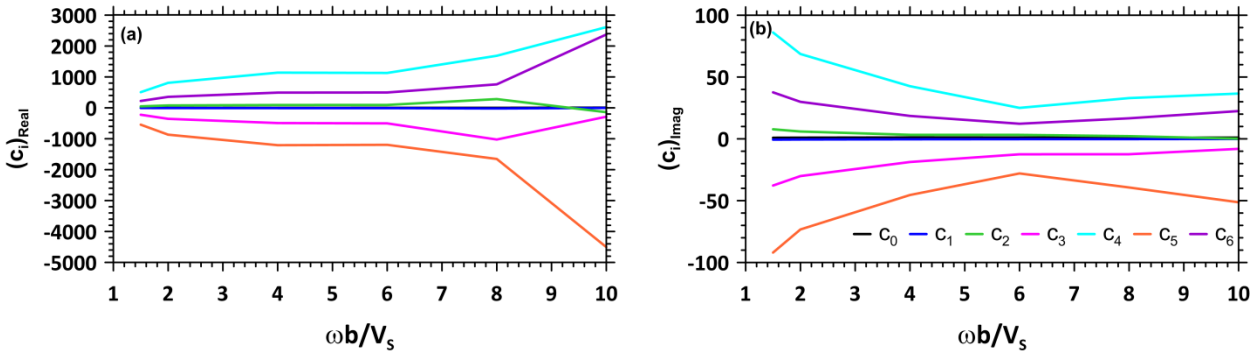

Figure 5.10 Polynomials coefficients for equations of dynamic vertical stress distribution at soil-foundation interface of a strip rigid foundation under cyclic vertical loading (a) Real part, (b) Imaginary part

5.7 Polynomial coefficients for equations of dynamic vertical stress distribution at soil-foundation interface of a strip rigid foundation under cyclic vertical loading – Real Part

	$c = \sum_{i=1}^{5} a_i (\frac{\omega a}{V_s})^i$
c_0	$y = -0.0028x^5 + 0.1068x^4 - 1.4096x^3 + 8.2339x^2 - 20.496x + 15.547$
c_1	$y = 0.0151x^5 - 0.3147x^4 + 2.0972x^3 - 4.3297x^2 - 3.5792x + 6.1308$
c_2	$y = -0.3014x^5 + 6.4497x^4 - 46.521x^3 + 128.87x^2 - 88.09x + 17.83$
c_3	$y = 0.7289x^5 - 15.589x^4 + 108.95x^3 - 257.45x^2 - 65.304x + 160.89$
c_4	$y = -0.1384x^5 + 1.2872x^4 + 29.092x^3 - 420.56x^2 + 1787.5x - 1331.6$
c_5	$y = -0.6207x^5 + 15.746x^4 - 170.65x^3 + 964.04x^2 - 2757.8x + 1925.5$
c_6	$y = 0.3159x^5 - 7.6653x^4 + 79.352x^3 - 429.79x^2 + 1188.5x - 824.15$

5.8 Polynomial coefficients for equations of dynamic vertical stress distribution at soil-foundation interface of a strip rigid foundation under cyclic vertical loading – Imaginary Part

	$c = \sum_{i=1}^{5} a_i (\frac{\omega a}{V_s})^i$
c_0	$y = -0.0002x^5 + 0.0056x^4 - 0.0456x^3 + 0.1205x^2 + 0.0685x + 0.6434$
c_1	$y = 0.0002x^5 - 0.0062x^4 + 0.0686x^3 - 0.3748x^2 + 1.0619x - 1.5914$
c_2	$y = 0.0002x^5 + 0.0048x^4 - 0.214x^3 + 2.3011x^2 - 9.8079x + 17.981$
c_3	$y = 0.0173x^5 - 0.4884x^4 + 5.239x^3 - 27.12x^2 + 71.699x - 99.568$
c_4	$y = -0.0516x^5 + 1.4272x^4 - 14.762x^3 + 72.657x^2 - 181.25x + 237.38$
c_5	$y = 0.054x^5 - 1.4982x^4 + 15.534x^3 - 76.76x^2 + 192.51x - 253.21$
c_6	$y = -0.0197x^5 + 0.5521x^4 - 5.8063x^3 + 29.279x^2 - 75.286x + 101.6$

I next turn my attention to an important problem for dynamic applications for which no classical solution is available in the literature for the static case – horizontal loading applied to a strip foundation. The problem geometry, depicted in Figure 5.11, is antisymmetric. The corresponding stresses at soil-rigid foundation interface are presented in Figure 5.12 for real and imaginary parts. As before, the normalizing average stress used in Figure 5.12 is $P/(2b)$. The polynomial coefficients associated with these stress distributions are presented in Tables 5.9 and 5.10 for real and imaginary parts, respectively. These coefficients are also plotted as a function of dimensionless frequency in Figure 5.13 (for $\omega b/V_S \geq 1.5$), and are presented in form of equations in Tables 5.11 and 5.12.

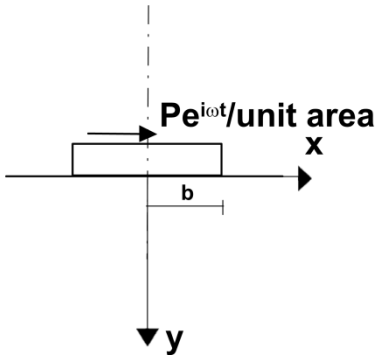

Figure 5.11 Antisymmetric horizontal loading of rigid strip foundation

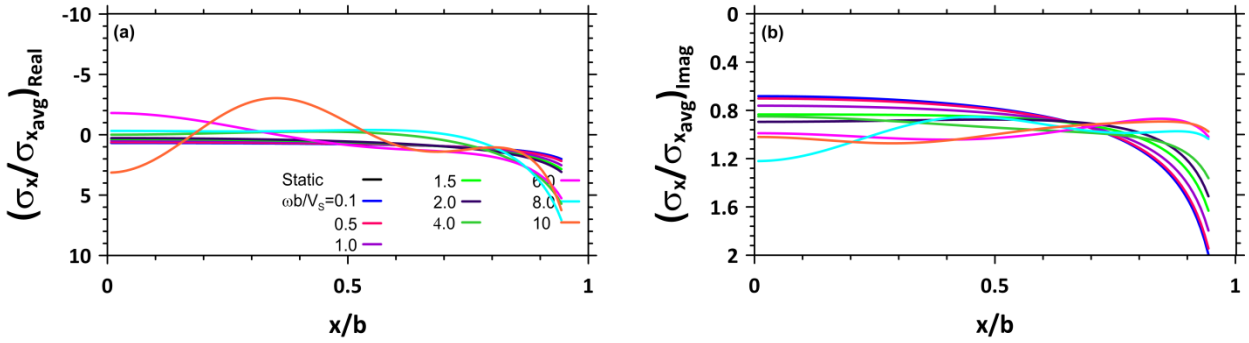

Figure 5.12 Static and dynamic horizontal stress distribution at soil-foundation interface of a rigid strip foundation under horizontal cyclic loading: (a) Real part, (b) Imaginary part

Table 5.9 Static and dynamic horizontal stress distribution polynomial coefficients at soil-foundation interface of a rigid strip foundation under horizontal cyclic loading – Real Part

Dimensionless Freq. (ωa/Vs)	c_0	c_1	c_2	c_3	c_4	c_5	c_6
static	0.83	-6.87	77.37	-347	735	-727	272
1.5	0.38	-1.53	19.2	-88.6	202	-216	88.8
2	0.31	-1.70	21.3	-98.9	225	-241	99.2
4	0.07	-3.81	43.1	-223	519	-550	224
6	-1.73	-3.58	60.4	-188	354	-387	174
8	-0.21	-5.34	64.8	-304	671	-711	298
10	2.84	15.7	-310	798	-298	-792	599

Table 5.10 Dynamic horizontal stress distribution polynomial coefficients at soil-foundation interface of a rigid strip foundation under horizontal cyclic loading – Imaginary Part

Dimensionless Freq. (ωa/Vs)	c_0	c_1	c_2	c_3	c_4	c_5	c_6
1.5	0.85	-0.73	8.84	-42.7	97.4	-104	42.6
2	0.91	-0.67	7.89	-38.9	88.9	-95.0	38.8
4	0.86	-0.52	6.76	-30.0	67.3	-72.7	30.0
6	0.99	-0.36	5.00	-20.1	41.2	-44.7	19.2
8	1.22	-0.19	-1.65	-19.0	80.8	-101	41.7
10	1.03	-0.72	10.27	-42.0	74.3	-62.4	20.6

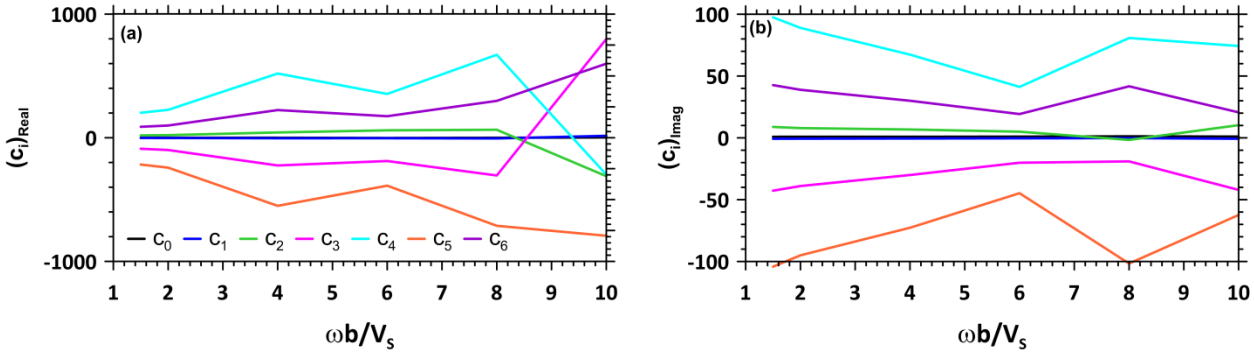

Figure 5.13 Polynomials coefficients for equations of dynamic horizontal stress distribution at soil-foundation interface of a rigid strip foundation under horizontal cyclic loading: (a) Real part, (b) Imaginary part

5.11 Polynomial coefficients for equations of dynamic vertical stress distribution at soil-foundation interface of a strip rigid foundation under cyclic horizontal loading – Real Part

	$c = \sum_{i=1}^{5} a_i (\frac{\omega a}{V_s})^i$
c_0	$y = -0.0047x^5 + 0.1236x^4 - 1.149x^3 + 4.6134x^2 - 8.1341x + 5.4884$
c_1	$y = 0.0129x^5 - 0.3106x^4 + 2.7727x^3 - 11.194x^2 + 19.358x - 13.263$
c_2	$y = -0.1195x^5 + 2.6537x^4 - 22.173x^3 + 86.198x^2 - 144.61x + 104.48$
c_3	$y = 0.778x^5 - 18.968x^4 + 170.62x^3 - 690.88x^2 + 1196.2x - 814.16$
c_4	$y = -1.5781x^5 + 40.287x^4 - 375.84x^3 + 1560.2x^2 - 2742.5x + 1881.7$
c_5	$y = 1.2845x^5 - 34.137x^4 + 328.78x^3 - 1397.6x^2 + 2484.3x - 1744.5$
c_6	$y = -0.3923x^5 + 10.868x^4 - 108.1x^3 + 470.98x^2 - 846.31x + 611.35$

5.12 Polynomial coefficients for equations of dynamic vertical stress distribution at soil-foundation interface of a strip rigid foundation under cyclic horizontal loading – Imaginary Part

	$c = \sum_{i=1}^{5} a_i (\frac{\omega a}{V_s})^i$
c_0	$y = 0.0002x^5 - 0.0077x^4 + 0.0958x^3 - 0.5124x^2 + 1.1857x - 0.0615$
c_1	$y = -0.0001x^5 + 0.0024x^4 - 0.0107x^3 - 0.0054x^2 + 0.1929x - 0.982$
c_2	$y = 0.0076x^5 - 0.1568x^4 + 1.0632x^3 - 2.6495x^2 + 0.5968x + 11.054$
c_3	$y = 0.0076x^5 - 0.2418x^4 + 2.6598x^3 - 13.076x^2 + 33.681x - 71.611$
c_4	$y = -0.0945x^5 + 2.3601x^4 - 21.177x^3 + 85.575x^2 - 167.64x + 216.56$
c_5	$y = 0.1303x^5 - 3.2079x^4 + 28.406x^3 - 113.18x^2 + 215.19x - 252.75$
c_6	$y = -0.0538x^5 + 1.323x^4 - 11.726x^3 + 46.93x^2 - 89.699x + 104.84$

As can be observed in Figure 5.14 although values are not the same, vertical stress distributions at soil-foundation interface of a rigid strip foundation under vertical cyclic loading follow the same trend as horizontal stress distribution at soil-foundation interface of a rigid strip foundation under horizontal cyclic loading.

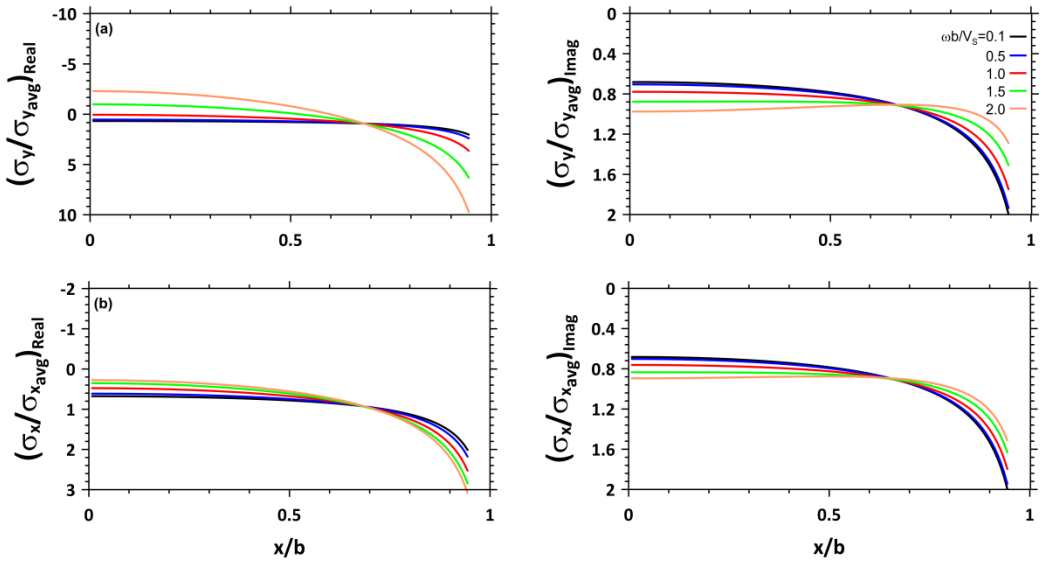

Figure 5.14 Comparison between stress distribution at soil-foundation interface of a rigid strip foundation under (a) vertical load, (b) horizontal load

Finally, I consider the antisymmetric problem of moment applied to a strip foundation, the geometry of which is depicted in Figure 5.15. Mushelishvili (1963) present the static solution to this problem, which is given by,

$$\sigma_y = \frac{-Mx}{\pi b^4 \sqrt{1-\left(\frac{x}{b}\right)^2}} \tag{5.4}$$

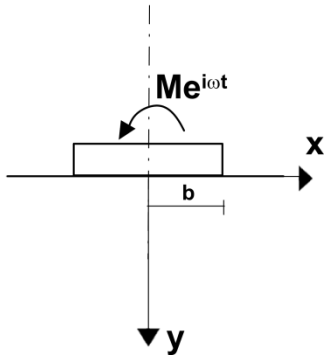

Figure 5.15 Moment loading of rigid strip foundation

Two-dimensional models in ISoBEM were developed to simulate soil-foundation interface stresses from applied moment for a rigid strip foundation on surface of an elastic half-space for dimensionless frequency ranging from 0.1 − 10. As shown in Figure 5.16, I first verify the accuracy of ISoBEM results through comparison to the static solution provided by Muskhelishvili (1963). There is nearly perfect compatibility between the stress fields obtained from the closed-form solution and ISoBEM. Note that due to antisymmetry, the contact normal stress at the center of the footing is zero.

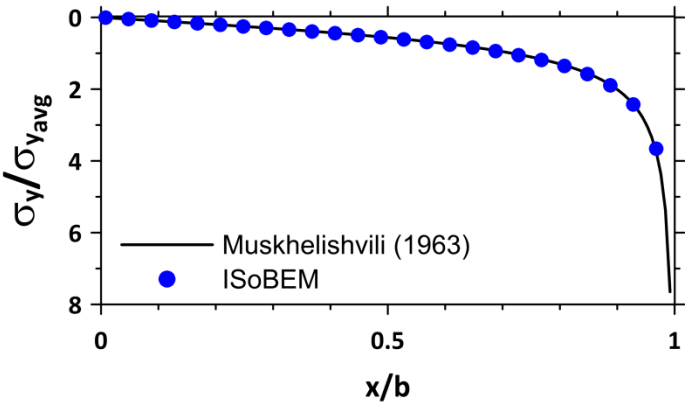

Figure 5.16 Comparison between ISoBEM and analytical solution for vertical contact pressure of a rigid strip foundation under static moment loading

The corresponding real and imaginary parts of cyclic stresses at the soil-rigid foundation interface are presented in Figure 5.17. Similar to previous cases, the coefficients of polynomials corresponding to these stress distributions are presented in Tables 5.13 and 5.14 for real and imaginary parts, respectively (for $\omega b/V_S \geq 1.5$) , and are presented in form of equations in Tables 5.15 and 5.16.

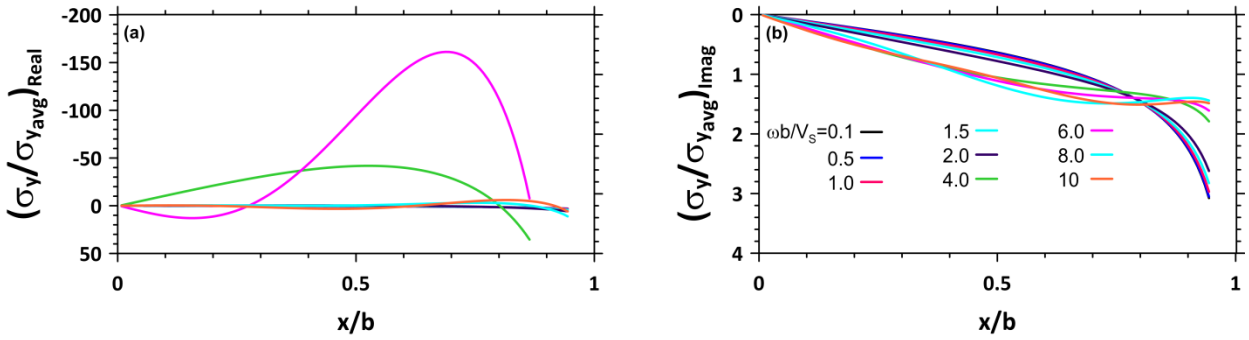

Figure 5.17 Dynamic vertical stress distribution at soil-foundation interface of a rigid strip foundation under moment cyclic loading (a) Real part, (b) Imaginary part

Table 5.13 Dynamic vertical stress distribution polynomial coefficients at soil-foundation interface of a rigid strip foundation under moment loading – Real Part

Dimensionless Freq. (ωa/Vs)	c_0	c_1	c_2	c_3	c_4	c_5	c_6
1.5	0.05	-2.53	31.1	-149	344	-369	152
2	0.08	-5.43	47.5	-227	526	-565	232
4	1.33	-154	563	563	7022	-7922	3534
6	0.78	61.0	939	939	1241	-11282	5337
8	0.25	-14.9	126	126	12236	-1543	744
10	0.13	-9.38	31.2	31.2	-131.5	-433	449

Table 5.14 Dynamic vertical stress distribution polynomial coefficients at soil-foundation interface of a rigid strip foundation under moment loading – Imaginary Part

Dimensionless Freq. (ωa/Vs)	c_0	c_1	c_2	c_3	c_4	c_5	c_6
1.5	0.02	-0.06	16.8	-81.5	186	-199	81.8
2	0.01	0.30	14.9	-72.4	164	-176	72.3
4	0.00	1.91	8.19	-41.7	89.8	-94.8	38.9
6	0.00	1.91	6.61	-27.1	61.6	-69.5	29.3
8	0.00	1.62	2.61	-7.01	26.2	-44.6	22.7
10	0.00	2.08	10.3	-66.4	157	-161	59.6

5.15 Polynomial coefficients for equations of dynamic vertical stress distribution at soil-foundation interface of a strip rigid foundation under cyclic moment loading – Real Part

	$c = \sum_{i=1}^{5} a_i (\frac{\omega a}{V_s})^i$
c_0	$y = -0.0029x^5 + 0.0844x^4 - 0.8866x^3 + 4.0877x^2 - 7.7489x + 5.0633$
c_1	$y = 0.8543x^5 - 22.956x^4 + 223.36x^3 - 954.39x^2 + 1728.9x - 1092.7$
c_2	$y = 0.8695x^5 - 18.387x^4 + 119.79x^3 - 242.28x^2 + 132.52x + 59.649$
c_3	$y = 0.0194x^5 + 6.404x^4 - 149.26x^3 + 1085x^2 - 2714x + 1951.8$
c_4	$y = -42.966x^5 + 1108.8x^4 - 10399x^3 + 43315x^2 - 77200x + 48497$
c_5	$y = -5.5806x^5 + 87.13x^4 - 102.04x^3 - 2971x^2 + 9316.7x - 7713.7$
c_6	$y = 3.4707x^5 - 63.521x^4 + 266x^3 + 473.75x^2 - 2738.5x + 2591.3$

5.16 Polynomial coefficients for equations of dynamic vertical stress distribution at soil-foundation interface of a strip rigid foundation under cyclic moment loading – Imaginary Part

	$c = \sum_{i=1}^{5} a_i (\frac{\omega a}{V_s})^i$
c_0	$y = -1E-05x^5 + 0.0004x^4 - 0.0049x^3 + 0.0295x^2 - 0.0859x + 0.0971$
c_1	$y = -0.0015x^5 + 0.0452x^4 - 0.478x^3 + 2.1202x^2 - 3.1922x + 1.3541$
c_2	$y = 0.0113x^5 - 0.284x^4 + 2.5723x^3 - 9.9975x^2 + 13.056x + 12.381$
c_3	$y = -0.0443x^5 + 1.0514x^4 - 9.0613x^3 + 33.475x^2 - 35.984x - 77.248$
c_4	$y = -0.0443x^5 + 1.0514x^4 - 9.0613x^3 + 33.475x^2 - 35.984x - 77.248$
c_5	$y = 0.1015x^5 - 2.4552x^4 + 21.603x^3 - 81.054x^2 + 88.614x + 174.2$
c_6	$y = -0.1005x^5 + 2.504x^4 - 22.79x^3 + 88.462x^2 - 102.68x - 179.02$

5.2 WITHIN-SOIL STRESSES FROM DISTRIBUTED DYNAMIC SURFACE LOADS

5.2.1 Motivations and Methodology

In Chapters 3 and 4, dynamic stress solutions were developed for vertical and horizontal point and line loads. These solutions are stored as different libraries corresponding to developed loading cases, where each library contains several text files presenting dimensionless stresses (i.e., $\sigma_{ij}R^2/P$ or $\sigma_{ij}R/P$ and corresponding phase angles for point and line loading) as a function of aperture angle (φ) for specific values of dimensionless frequency, Poisson's ratio, and damping ($\omega R/V_S$, ν, ξ). The goal of this chapter is to apply the principle of superposition using those fundamental dynamic stress solutions to obtain within-soil stress distributions due to surficial loads applied at different locations on the ground surface. I first develop and implement the integrations in a Matlab code. I then verify the accuracy of the code by comparing to available solutions for static problems as well as to stress solutions obtained by direct modeling of distributed loads using ISoBEM for dynamic problems.

5.2.2 Distributed Vertical Point Load Problems: Methodology and Verification

In Chapter 3 I presented fundamental dynamic stress solutions for vertical and horizontal point loads. The results were presented as dimensionless (normalized) stresses in graphical form, but

the numerical values for stress amplitudes and phase angles are also stored in digital libraries. In this section, superposition techniques are applied for the case of distributed vertical point loads. The same logistics apply to the problem of horizontal point load with consideration of azimuthal angle (θ) and the corresponding Matlab code can provide results for this case as well. The normalized stress solution for the vertical point load problem is:

$$\frac{\sigma_{ij}R^2}{P} = f_{ij}\left(\xi, \nu, \varphi, \frac{\omega R}{V_s}\right) \tag{5.5}$$

where function f_{ij} represents the complex-valued stress distribution including real and complex parts (or, equivalently, amplitudes and phase angles). The within-soil stress solution due to circular surficial loading is developed by discretizing the circular foundation as shown in Figure 5.15. The following equations present the area dA_k of a random small element and the force applied on that element from a radially varying surface load σ_k.

$$dA_k = \left(\frac{r_1 d\theta_1 + r_2 d\theta_2}{2}\right)(r_2 - r_1) \tag{5.6}$$

$$dP_k = \sigma_k \left(dA_k\right) \tag{5.7}$$

where σ_k is the applied stress on the k^{th} increment. For the case of a uniform load applied to a flexible foundation, σ_k is independent of radius (and hence subscript k) because the stress distribution at the soil-foundation interface matches that applied to the surface. For the case of a rigid foundation, the radial distribution of interface pressures is obtained using the procedures given in Section 5.2. Within-soil stresses for any stress component σ_{ij} are computed by summation over all N elements:

$$\sigma_{ij} = \sum_{k=1}^{N}\left[\frac{P_k}{R_k^2} f_{ij}\left(\xi, \nu, \varphi_k, \frac{\omega R_k}{V_s}\right)\right] = \sum_{k=1}^{N}\left[\frac{\sigma_k A_k}{R_k^2} f_{ij}\left(\xi, \nu, \varphi_k, \frac{\omega R_k}{V_s}\right)\right] \tag{5.8}$$

The summation in Equation 5.8 is applied using the stress solutions expressed as real and complex parts (because it is not useful to sum phase angles).

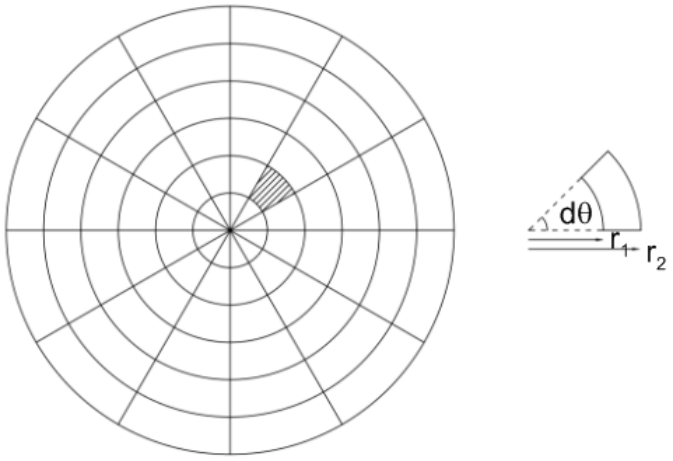

Figure 5.18 Discretization of a circular distributed load area

In order to verify the presented integration (summation) methodology, I compare against published solutions for the static problem. Those solutions are based on similar principles of integration as applied here, in this case of the Boussinesq's solution and with the integration performed over a circular area representing a perfectly flexible foundation (Poulos and Davis, 1974). Because of complexities associated with evaluating inverse integral transforms (or directly integrating Boussinesq's solution), closed-form solutions are only available for σ_z, σ_r, and σ_θ along the z-axis ($r = 0$). Because the solution is for a flexible foundation, the vertical stress p is constant over the radius a of the foundation. The resulting stresses from Poulos and Davis (1974) are,

$$\sigma_z = p\left[1-\left(\frac{1}{1+\left(\frac{a}{z}\right)^2}\right)^{\frac{3}{2}}\right] \tag{5.9}$$

$$\sigma_r = \sigma_\theta = -\frac{p}{2}\left[(1+2\nu)-\frac{2(1+\nu)z}{(a^2+z^2)^{1/2}}+\frac{z^3}{(a^2+z^2)^{3/2}}\right] \tag{5.10}$$

Numerical solutions for all components of stress, strain, and displacement are tabulated by Ahlvin and Ulery (1962). Shear stresses are given by,

$$\tau_{rz} = pG_1 \tag{5.11}$$

where G_1 is presented in Table 5.9.

Results from the published solutions are compared to those obtained using the aforementioned Matlab integration code in Figure 5.19. The two results are nearly identical. It should be noted, however, that this comparison does not test that the code maintains proper phasing, since the static component is real-valued.

Table 5.17: Function "G_1"- Adapted from Ahlvin and Ulery (1962)

r/a z/a	0	0.2	0.4	0.6	0.8	1	1.2	1.5	2	3	4	5	6	7	8	10	12	14
0	0	0	0	0	0	.31831	0	0	0	0	0	0	0	0	0	0	0	0
0.1	0	.00315	.00802	.01951	.06682	.31405	.05555	.00865	.00159	.00025	.00007	.00003						
0.2	0	.01163	.02877	.06441	.16214	.30474	.13592	.03060	.00614	.00091	.00026	.00010	.00005	.00003	.00002			
0.3	0	.02301	.05475	.11072	.21465	.29228	.18216	.05747	.01302	.00201	.00059							
0.4	0	.03460	.07883	.14477	.23442	.27779	.20195	.08233	.02138									
0.5	0	.04429	.09618	.16426	.23652	.26216	.20731	.10185	.03033	.00528	.00158	.00063	.00030	.00016	.00009	.00004	.00002	.00001
0.6	0	.04966	.10729	.17192	.22949	.24574	.20496	.11541										
0.7	0	.05484	.11256	.17126	.21772	.22924	.19840	.12373	.04718									
0.8	0	.05590	.11225	.16534	.20381	.21295	.18953	.12855										
0.9	0	.05496	.10856	.15628	.18904	.19712	.17945	.28881										
1	0	.05266	.10274	.14566	.17419	.18198	.16884	.12745	.06434	.01646	.00555	.00233	.00113	.00062	.00036	.00015	.00007	.00004
1.2	0	.04585	.08831	.12323	.14615	.15408	.14755	.12038	.06967	.02077	.00743	.00328	.00159	.00087	.00051			
1.5	0	.03483	.06688	.09293	.11071	.11904	.11830	.10477	.07075	.02599	.01021	.00460	.00235	.00130	.00078	.00033	.00016	.00009
2	0	.02102	.04069	.05721	.06948	.07758	.08067	.07804	.06275	.03062	.01409	.00692	.00369	.00212	.00129	.00055	.00027	.00015
2.5	0	.01293	.02534	.03611	.04484	.05119	.05509	.05668	.05117	.03099	.01650	.00886	.00499	.00296	.00185	.00082	.00041	.00023
3	0	.00840	.01638	.02376	.02994	.03485	.03843	.04124	.04039	.02886	.01745	.01022	.00610	.00376	.00241	.00110	.00057	.00032
4	0	.00382	.00772	.01149	.01480	.01764	.02004	.02271	.02475	.02215	.01639	.01118	.00745	.00499	.00340	.00167	.00090	.00052
5	0	.00214				.00992		.01343	.01551	.01601	.01364	.01105	.00782	.00560	.00404	.00216	.00122	.00073
6	0					.00602		.00845	.01014	.01148	.01082	.00917	.00733	.00567	.00432	.00243	.00150	.00092
7	0					.00396			.00687	.00830	.00842	.00770	.00656	.00539	.00432	.00272	.00171	.00110
8	0					.00270			.00481	.00612	.00656	.00631	.00568	.00492	.00413	.00278	.00185	.00124
9	0					.00177			.00347	.00459	.00513	.00515	.00485	.00438	.00381	.00276	.00192	.00133
10	0							.00199	.00258	.00351	.00407	.00420	.00411	.00382	.00346			

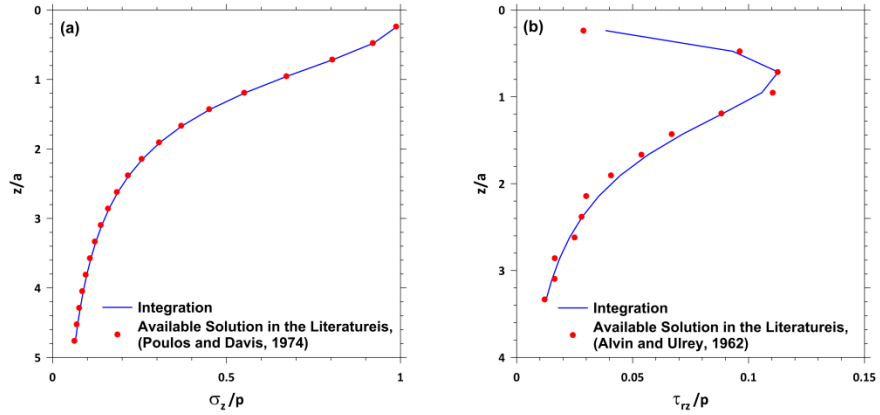

Figure 5.19 Comparison between stress solutions obtained from integration and available solutions in the literature for vertical distributed circular load (a) Vertical, (b) Shear stress components (r = 0, p =1 kN/m^2, v = 0.33)

To verify the integration methodology in Equation 5.8 for the harmonic loading problem, including proper summation of real and complex values of within-soil stresses, I compare results from the Matlab code with those obtained directly from ISoBEM. The problem considered is a perfectly flexible circular foundation on a uniform, isotropic half-space. Outcomes for vertical and shear stresses at three frequencies are presented in Figures 5.20 to 5.25. The comparisons are excellent for the real parts. There are differences between the imaginary components that become larger (as a percent error) as frequency decreases. However, when viewed as a fraction of the real part, the differences between the imaginary components are small. Moreover, the differences in

the imaginary components decreases as the dimensionless frequency increases, and the imaginary values increase and contribute more to the amplitude values. The errors are thought to result from the interpolation of the point load solution in Matlab.

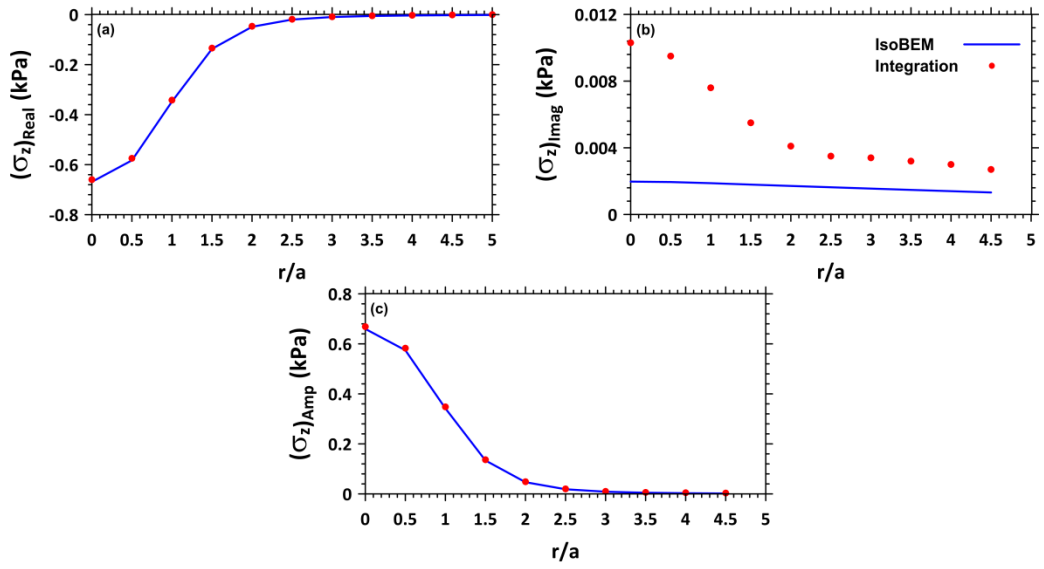

Figure 5.20 Comparison between vertical stress solutions obtained from integration and direct modeling in ISoBEM for vertical distributed circular load (a) Real part, (b) Imaginary part, and (c) Amplitude (z = -1 m, p =1 kN/m^2, v = 0.34, $\omega a/V_S$ = 0.2)

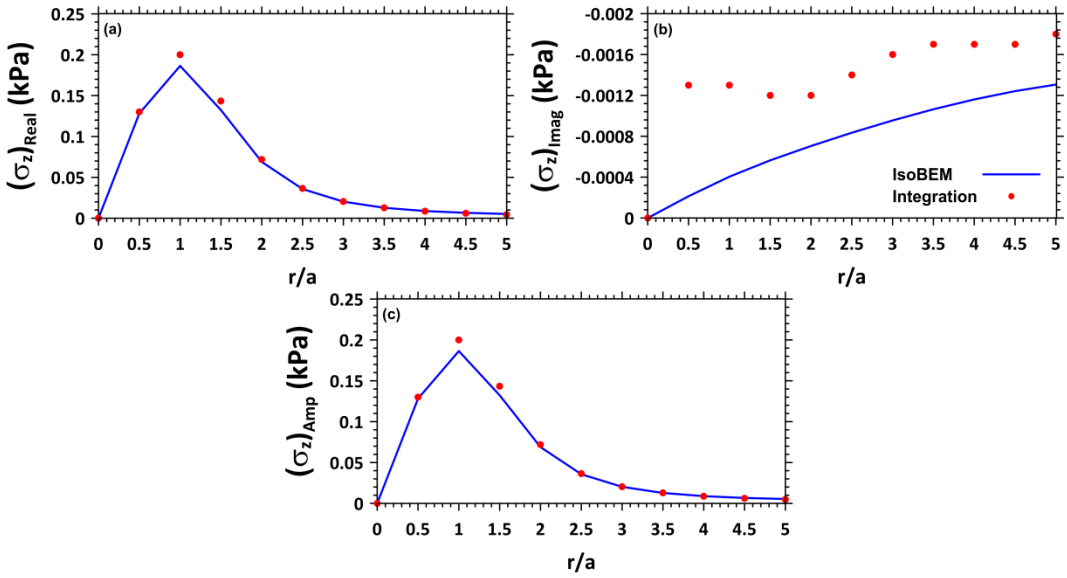

Figure 5.21 Comparison between shear stress solutions obtained from integration and direct modeling in ISoBEM for vertical distributed circular load (a) Real part, (b) Imaginary part, and (c) Amplitude (z = -1 m, p =1 kN/m^2, v = 0.34, $\omega a/V_S$ = 0.2)

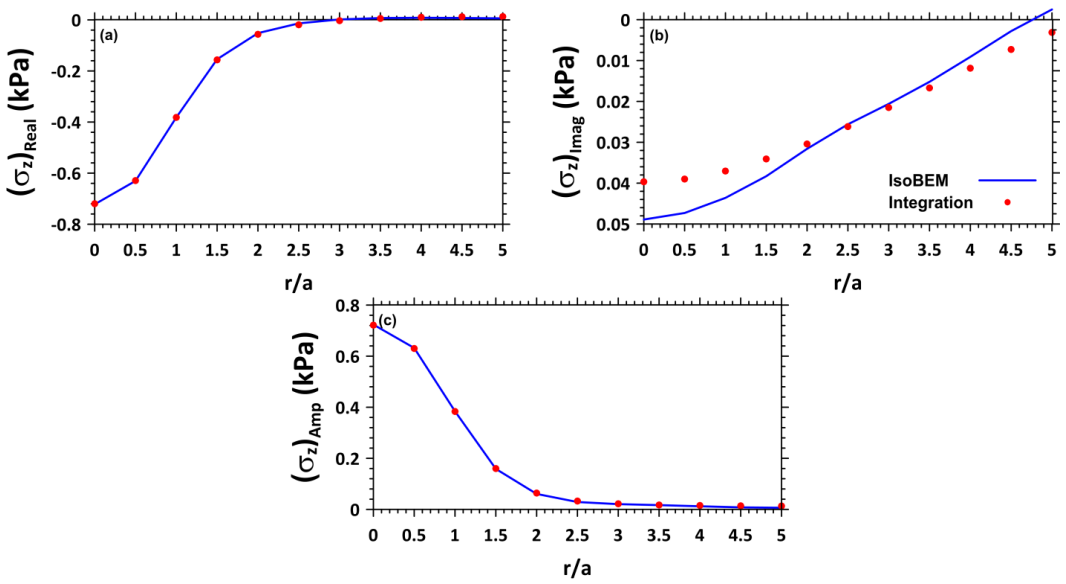

Figure 5.22 Comparison between vertical stress solutions obtained from integration and direct modeling in ISoBEM for vertical distributed circular load (a) Real part, (b) Imaginary part, and (c) Amplitude (z = -1 m, p =1 kN/m^{2}p, v = 0.34, $\omega a/V_S$ = 0.5)

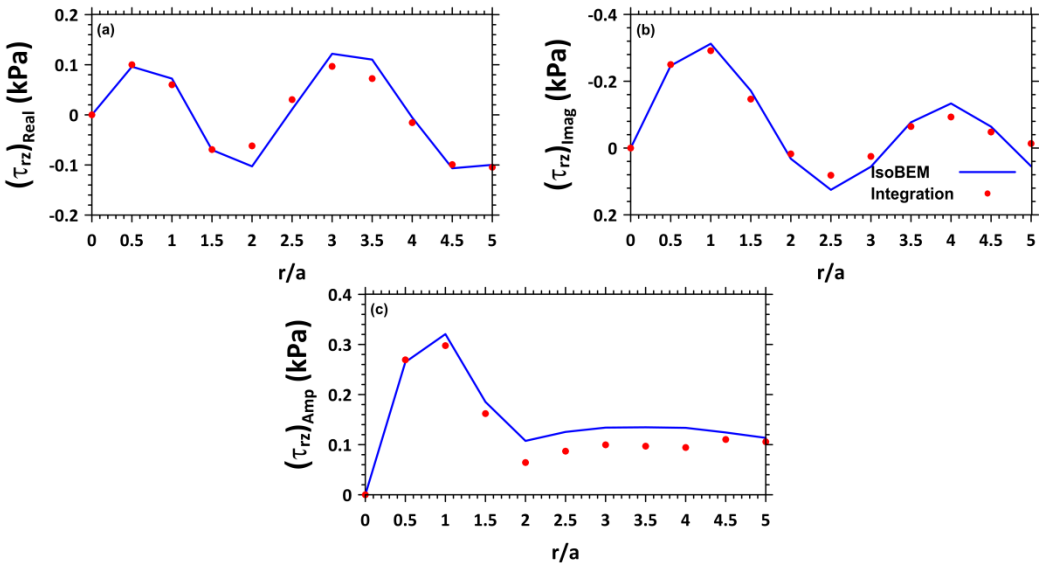

Figure 5.23 Comparison between shear stress solutions obtained from integration and direct modeling in ISoBEM for vertical distributed circular load (a) Real

part, (b) Imaginary part, and (c) Amplitude (z = -1 m, p =1 kN/m^{2}p, v = 0.34, $\omega a/V_S$ = 0.5)

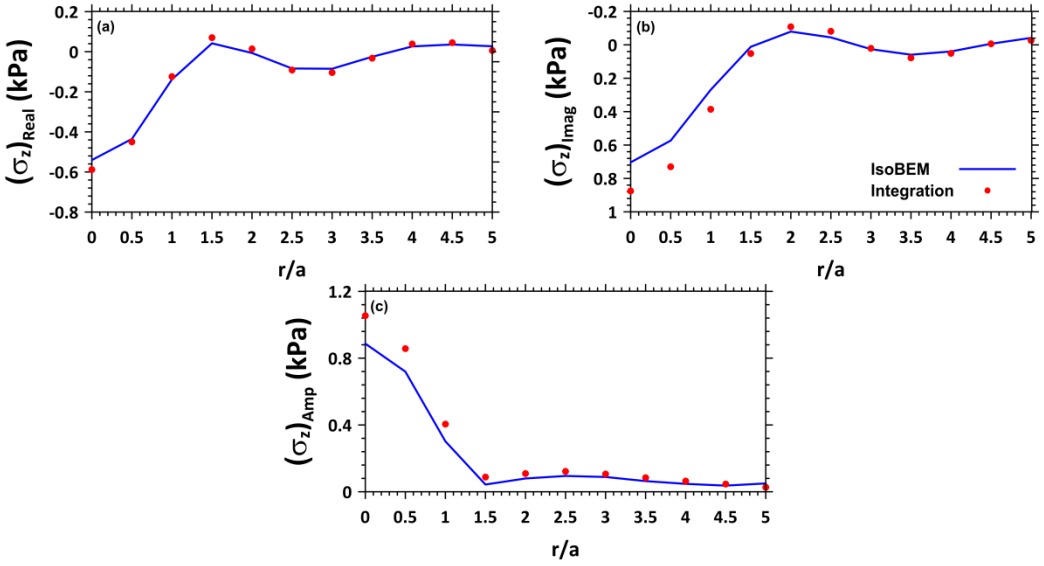

Figure 5.24 Comparison between vertical stress solutions obtained from integration and direct modeling in ISoBEM for vertical distributed circular load (a) Real part, (b) Imaginary part, and (c) Amplitude (z = -1 m, p =1 kN/m^2, v = 0.34, $\omega a/V_S$ = 2.0)

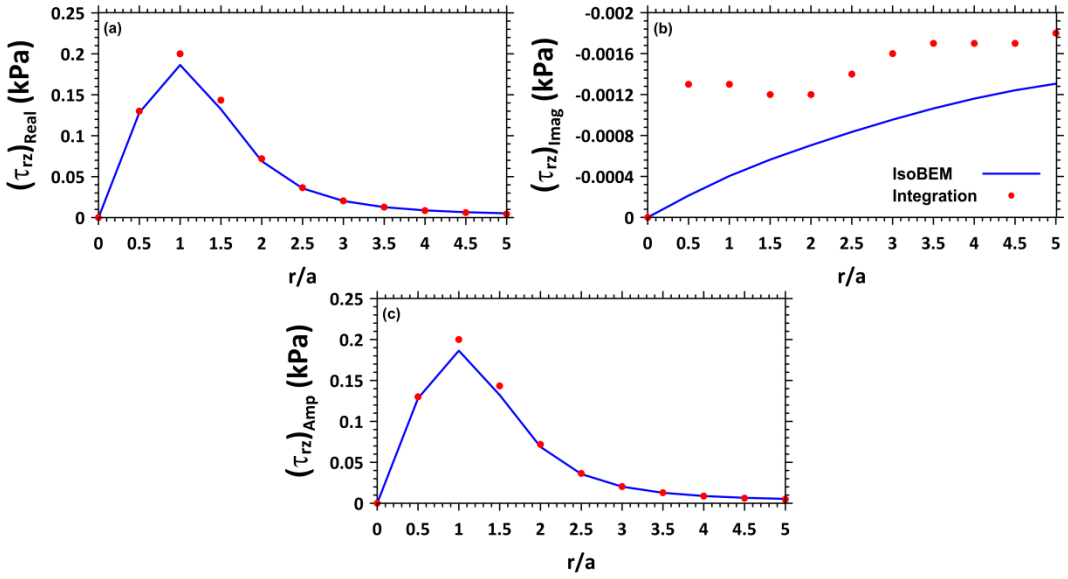

Figure 5.25 Comparison between shear stress solutions obtained from integration and direct modeling in ISoBEM for vertical distributed circular load (a) Real part, (b) Imaginary part, and (c) Amplitude (z = -1 m, p =1 kN/m^2, v = 0.34, $\omega a/V_S$ = 2.0)

5.2.3 Distributed Vertical and Horizontal Line Load Problems: Methodology and Verification

In Chapter 4 I presented fundamental dynamic stress solutions for vertical and horizontal line loads on strip foundations. The results were presented graphically and numerical values were stored for the complex-valued stresses in multiple libraries. In this section, the application of superposition techniques is presented for the case of vertical and horizontal line loads. The normalized stress solution for a line load of P (force/length) is as follows:

$$\frac{\sigma_{ij} R}{P} = f_{ij}\left(\xi, \nu, \varphi, \frac{\omega R}{V_s}\right) \tag{5.12}$$

where function f_{ij} represents the complex-valued stress distribution including real and complex parts (or, equivalently, amplitudes and phase angles).

I consider the problem of uniformly distributed vertical and horizontal loading of a flexible strip foundation, as shown in Figure 5.26. The length of a random small element (k^{th} increment) and the load acting upon it are,

$$L_k = dx \tag{5.13}$$

$$P_k = \sigma_k L_k \tag{5.14}$$

where σ_k is the applied stress on the k^{th} increment, which may be constant for the case of a uniform foundation but will vary with x for a rigid foundation. Within-soil stresses for any stress component σ_{ij} are computed by summation over all N elements:

$$\sigma_{ij} = \sum_{k=1}^{N}\left[\frac{P_k}{R_k} f_{ij}\left(\xi, \nu, \varphi_k, \frac{\omega R_k}{V_s}\right)\right] = \sum_{k=1}^{N}\left[\frac{\sigma_k L_k}{R_k} f_{ij}\left(\xi, \nu, \varphi_k, \frac{\omega R_k}{V_s}\right)\right] \tag{5.15}$$

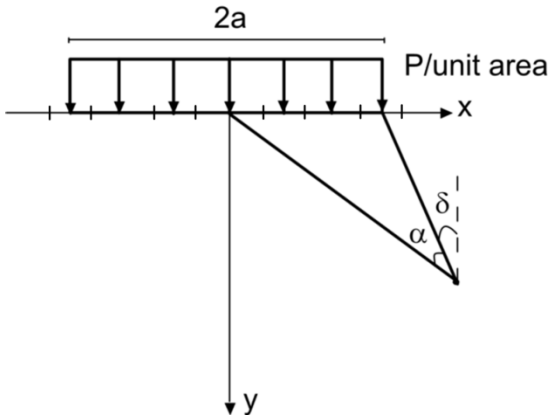

Figure 5.26 Discretization of a strip distributed load area

As with the 3D problem the integration methodology is verified against published solutions for the static problem by Poulos and Davis (1974), as follows:

$$\sigma_x = \frac{P}{\pi}\left[\alpha - \sin\alpha\cos(\alpha + 2\delta)\right] \tag{5.16}$$

$$\sigma_y = \frac{P}{\pi}\left[\alpha + \sin\alpha\cos(\alpha + 2\delta)\right] \tag{5.17}$$

$$\tau_{xy} = \frac{P}{\pi}\left[\sin\alpha\sin(\alpha + 2\delta)\right] \tag{5.18}$$

Results from these published solutions are compared to those obtained using the integration code in Figure 5.27-5.28 for vertical and horizontal strip loads, respectively. The two results are nearly identical, but as before, this verification does not pertain to phasing.

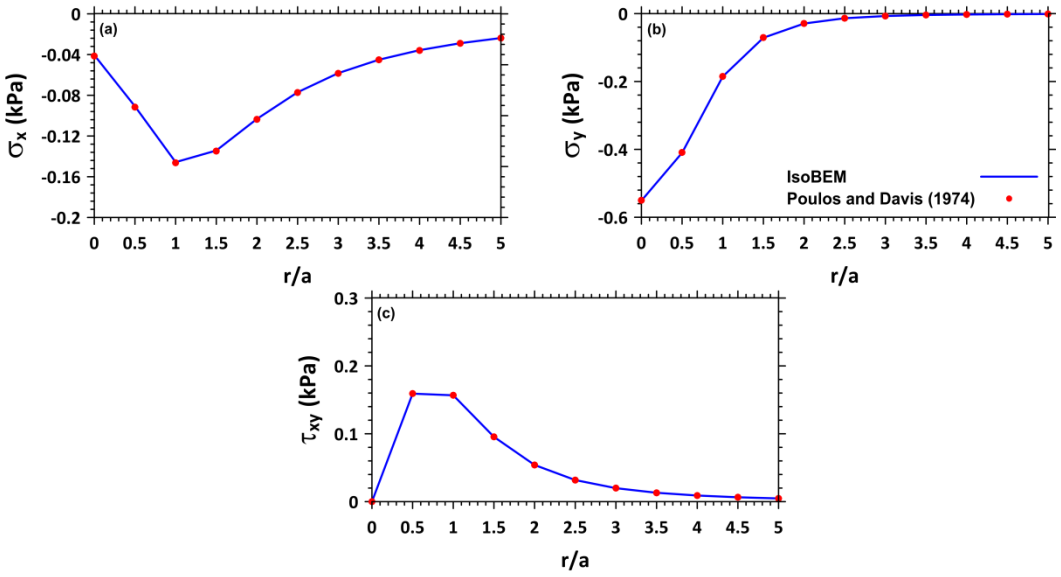

Figure 5.27 Comparison between static stress solutions obtained from integration and analytical solutions for vertical distributed strip load (a) Vertical, (b) Horizontal, and (c) Shear stress components (y = -1 m, p =1 kN/m^2)

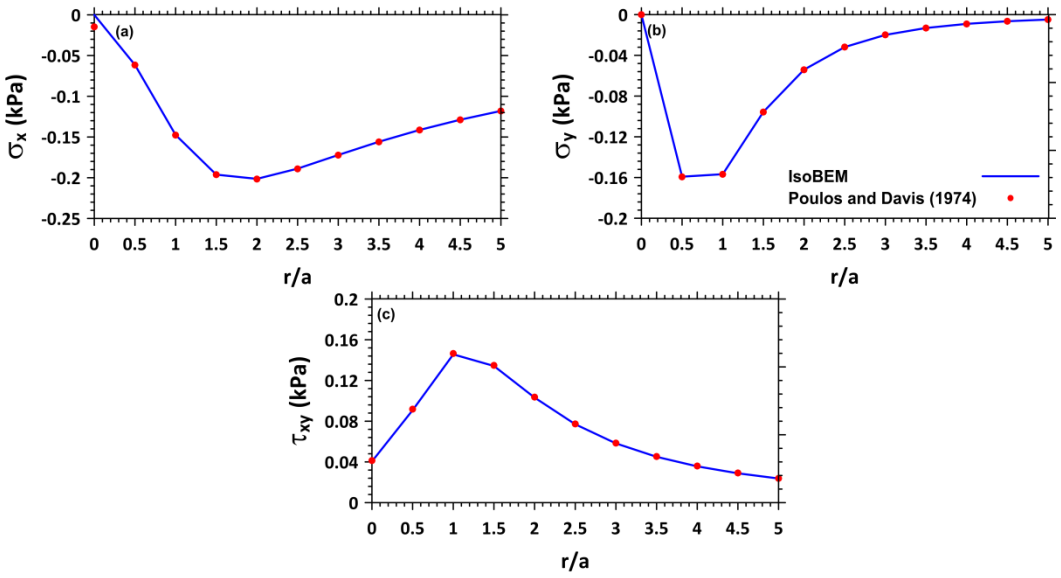

Figure 5.28 Comparison between static stress solutions obtained from integration and analytical solutions for horizontal distributed strip load (a) Vertical, (b) Horizontal, and (c) Shear stress components (y = -1 m, p =1 kN/m^2)

To verify the integration methodology in Equation 5.15 for the harmonic loading problem, including proper summation of real and complex values of within-soil stresses, I

compare to results obtained from directly from ISoBEM. The problem considered is a vertically loaded perfectly flexible strip foundation on a uniform, isotropic halfspace. Outcomes for vertical and shear stresses at two frequencies are presented in Figures 5.29 to 5.32.

The comparisons are excellent for the real parts. There are large differences between the imaginary components at both of the considered frequencies. However, since dimensionless frequencies are small ($\omega b/V_s$ = 0.2, 0.5) the differences between imaginary components are small when viewed as a fraction of the real part. Moreover, the differences in the imaginary components decreases as the dimensionless frequency increases, and the imaginary values increase and contribute more to the amplitude values. This is more pronounced for higher values of frequencies as presented for the case of vertical circular load in Section 5.2.2. The errors are thought to result from the interpolation of the line load solution in Matlab.

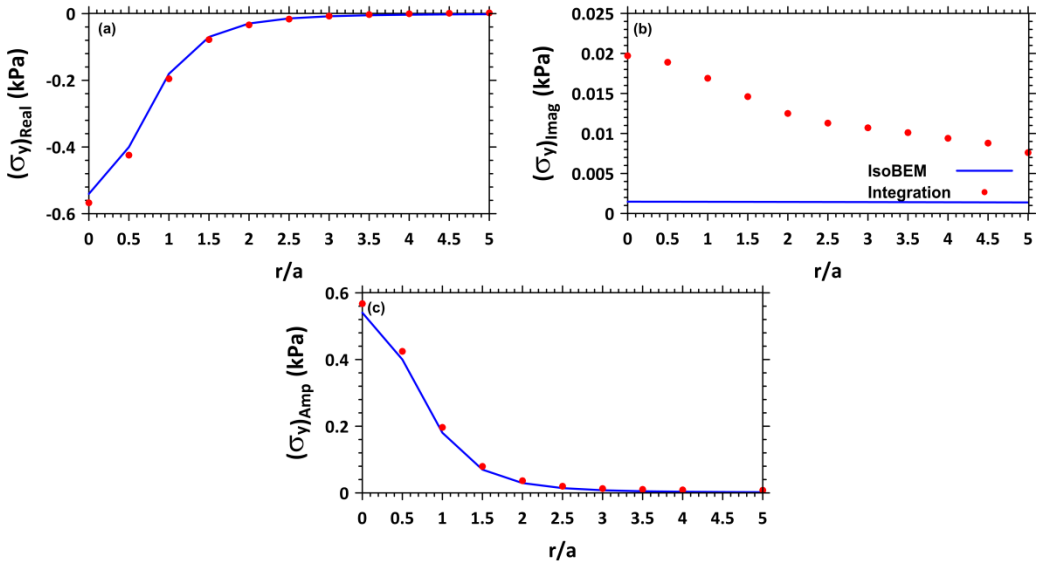

Figure 5.29 Comparison between vertical stress solutions obtained from integration and direct modeling in ISoBEM for vertical distributed strip load (a) Real part, (b) Imaginary part, and (c) Amplitude (y = -1 m, p = 1 kN/m^2, v = 0.34, ωb/Vs = 0.2)

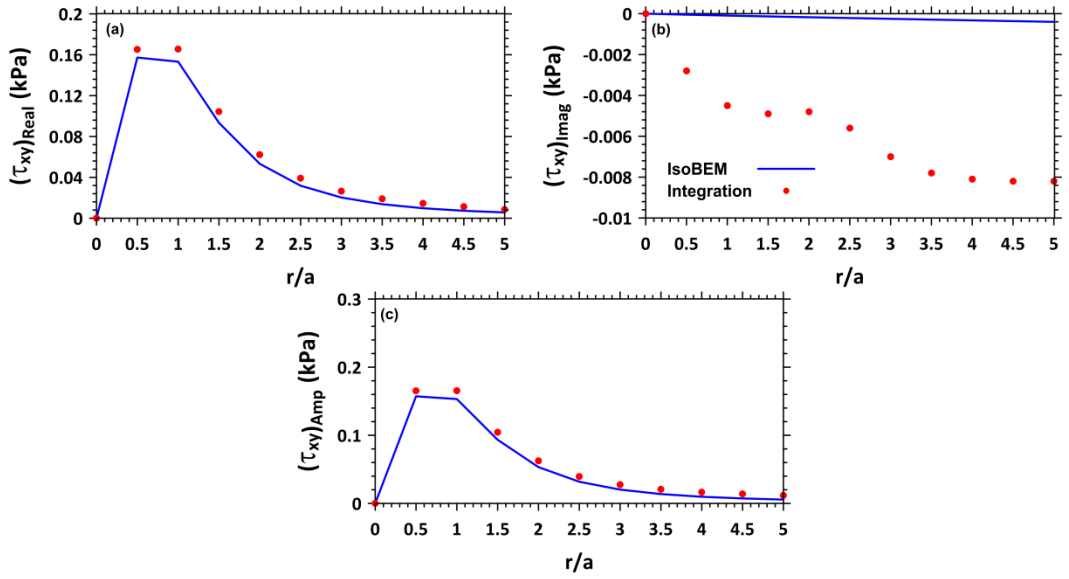

Figure 5.30 Comparison between shear stress solutions obtained from integration and direct modeling in ISoBEM for vertical distributed strip load (a) Real part, (b) Imaginary part, and (c) Amplitude (y = -1 m, p = 1 kN/m2, v = 0.34, ωb/Vs = 0.2)

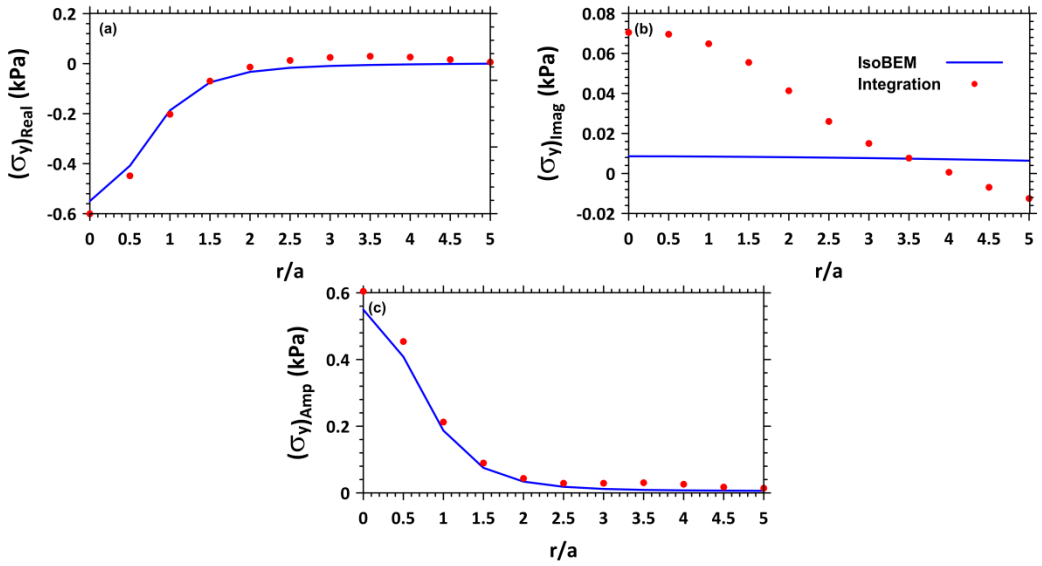

Figure 5.31 Comparison between vertical stress solutions obtained from integration and direct modeling in ISoBEM for vertical distributed strip load (a) Real part, (b) Imaginary part, and (c) Amplitude (y = -1 m, p = 1 kN/m^2, v = 0.34, $\omega b/V_S$ = 0.5)

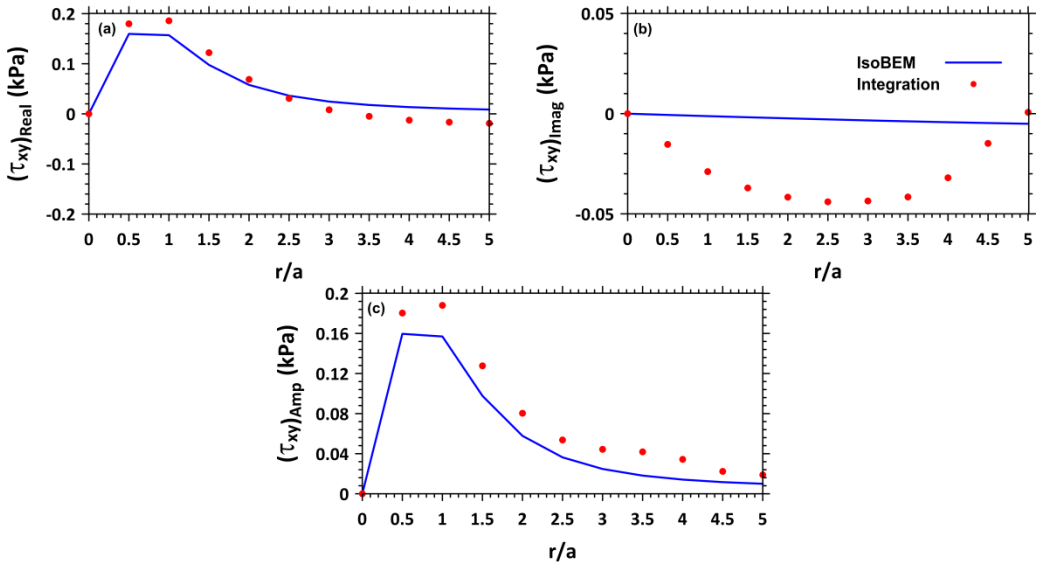

Figure 5.32 Comparison between shear stress solutions obtained from integration and direct modeling in ISoBEM for vertical distributed strip load (a) Real part, (b) Imaginary part, and (c) Amplitude (y = -1 m, p = 1 kN/m^2, v = 0.34, $\omega b/V_S$ = 0.5)

To conclude, for both cases of circular and strip loading, the integration techniques appear to work well for static and dynamic problems involving uniform surface loads. Overall, the real parts and amplitudes compared better with those from direct modeling of distributed loading in ISoBEM. This will cause negligible errors in amplitude, but can affect phase angles. We believe the source of this error lies in the interpolation process preformed in Matlab code and as the numbers get larger, the interpolation errors get smaller. Finally, it should be noted that this approach can be easily extended to a more general type of loads, such as non-uniform or non-symmetric loads.

6 CONCLUSIONS AND RECOMMENDATIONS

6.1 SCOPE OF THE RESEARCH

The objective of this research was to evaluate the impacts of soil-structure interaction on the seismic stress demands in soil materials beneath the foundation, referred to as 'foundation soils'. The goals of this study were to show how the presence of a structure affects wave propagation in the vicinity of the foundation due to SSI and to propose rigorous procedures by which to assess these demands due to vertical or horizontal point loads, line loads, or distributed loads acting within a foundation area.

Following the introduction of the SSI problem from the structural standpoint, this research began by asking –*what is the effect of the vibrating structure on the foundation soil*? – to discuss how the presence of a structure causes the characteristics of wave propagation and associated stress/strains to deviate from the free-field condition as a result of kinematic and inertial effects (Chapter 1). To answer this question the initial steps were to overview of the historical development of analytical and numerical expressions for the response of a solid medium to static and dynamic loads on the soil medium, and to identify some shortcomings of those solutions for the present application (Chapter 2).

For harmonically applied surface loads (horizontal and vertical, point and line) acting on a visco-elastic half-space, the governing equations were solved numerically using the Boundary Element Method via a well-verified software platform (ISoBEM). The results are interpreted

within a framework derived from dimensional analysis considerations, specifically applying the Buckingham π theorem to determine the dimensionless fundamental parameters applicable to these problems. The results produces by this software were verified by comparing to available solutions in the literature. Verification was also conducted for the normalization of the dynamic stress results with respect to proposed dimensionless parameters. The variations of the six components of the three-dimensional stress tensor with respect to the identified fundamental parameters were then investigated through suites of sensitivity analyses. Results for stress amplitudes were presented in the form of stress bulbs. Time delays between surface loads and stresses were represented with phase shifts, which were also presented in a graphical form (Chapters 3 and 4).

For the case of rigid foundations, in order to obtain the surface loads applied to foundation soils, and to simulate the effects of vibration of a rigid foundation, the simulations were performed to evaluate the dynamic stress distributions directly beneath rigid foundations subject to cyclic loading. The results were presented in the form of graphs as well as parametric equations. Moreover, the principle of superposition was applied to fundamental dynamic stress solutions in order to obtain the resulting stress distributions in the soil medium due to surficial loads applied at different locations on the ground surface. The accuracy of the integration techniques was verified by comparing to the available solutions as well as the stress solutions obtained by direct modeling of distributed loads using ISoBEM. The corresponding computational tools were implemented in MATLAB (Chapter 5).

6.2 RESEARCH FINDINGS AND RECOMMENDATIONS

6.2.1 Chapter 2: Historical Development

Fully analytical solutions are available in the literature for the problems of static vertical and horizontal point and line loads on an elastic half-space. In case of surficial static distributed load, due to complexities associated with evaluating inverse integral transforms (or directly integrating static solutions), closed-form solutions are only available at limited locations relative to the point load (i.e., at the ground surface and directly beneath the load). Numerical solutions are available for all stress components.

In case of dynamic problems, mostly known as Lamb's problem (Lamb, 1904) for the case of point and line loads, the analytical solutions are limited to: (1) some specific load types (i.e. mostly impulsive point loads), (2) displacements and not stresses, and (3) locations along the ground surface or directly beneath the load, but not at other aperture angles. Although the formulation in most of the problems the formulation for the integral transforms is exact, the aforementioned limitations are due to complexities associated with evaluating the inverse integrals transforms.

An excellent contribution is presented by Schepers et al. (2010) to deal with some numerical problems associated with evaluation of the inverse integrals for the problem of harmonic vertical and horizontal point load applied on the surface of an elastic or viscoelastic half-space. The solutions are also provided in the form of stresses. However, the pressure bulbs in this work are limited to a few numbers of frequencies as well as a nominal shear wave velocity of 100 m/s. Nevertheless, the presented stress results are strongly functions of dimensional frequencies and nominal shear wave velocity. If any other values of shear wave velocity or

frequency are of interest, rigorous scaling adjustment procedures need to be performed in order to get the corresponding stress outputs.

6.2.2 Chapter 3: Stress beneath Dynamically Applied Vertical and Horizontal Point Loads

In this chapter, the Buckingham π theorem (Buckingham, 1914) was discussed as part of the normalization scheme. This theorem was applied to the static and dynamic problems of vertical and horizontal point loads imposed on the surface of the half-space to determine the number of dimensionless parameters. With regards to characteristic properties of the systems, the value of dimensionless stress, ($\sigma_{ij}R^2/P$), within foundation soil underlying a static vertical point load at ground surface was found to be a function of aperture angle and Poisson's ratio. For the static horizontal point load case, an extra dimensionless value of azimuthal angle was added to the equation.. The proposed normalizations were confirmed by comparing to analytical solutions to the Boussinesq and the Cerruti problems.

Boundary Element Method (BEM) was selected as the numerical method of analysis. The commercial program ISoBEM (2012) was employed as the main software throughout this work. The analyses in this part of research included two cases for dynamically applied vertical and horizontal point loads on the surface of an elastic half-space. For the corresponding dynamic problems, two more parameters were selected to be dimensionless frequency and damping ratio. The proposed normalizations were confirmed by direct modeling in ISoBEM such that normalized graphs of stresses match well once the aforementioned dimensionless parameters are the same.

The verification of the solutions in the point load problems was performed by comparing the stress results to the Boussinesq's solution (Boussinesq, 1885), Cerruti's solution (Cerruti,

1882), and Lamb's problem solution by Schepers et al. (2010) and Esmaeilzadeh et al. (2015). Upon verification, the final analysis was performed for a large set of parameters including dimensionless frequencies ($\omega R/V_S$) ranging from 0 to 20, Poisson's ratios of 0.34 and 0.45, and soil damping values of 1% and 5%, to account for sand and incompressible clay soils, respectively. The solutions were then illustrated in the form of dimensionless stress bulbs for amplitude and phase angles.

For ($\omega R/V_S$) < 1, dynamic effects ranged from negligible to moderate for both vertical and shear stress components and were suggested to be ignored. For ($\omega R/V_S$) ≈ 2 to 4, the general shapes of the stress distributions were similar to those for the static case, but the stress amplitudes were increased by about 70% for the vertical component and 50% for shear component in vertical load case, and were increased by about 50% for vertical component and 80% for shear component in horizontal load case. For ($\omega R/V_S$) > 4, stress patterns deviated substantially from the static case and followed a more complex pattern, due to constructive and destructive interference of the travelling waves.

Increase of Poisson's ratio caused no perceptible change in stress bulb amplitudes or phase angles for aperture angles associated with shear wave propagation However, Poisson's ratio increases produced stress amplitude increases and decreases for aperture angles associated with P-wave and Rayleigh wave propagation, respectively. Our interpretation was that in the high-ν case, the higher bulk moduli of the soil 'attracted' more P-wave propagation (at the expense of Rayleigh wave energy), thereby modifying stress amplitudes associated with these wave types.

Reduction in stress values was the expected outcome of soil damping ratio. However, this effect was more obvious for higher dimensionless frequencies. In other words, higher damping

ratio values alleviated the dramatic sharpness in dimensionless stress bulbs with high dimensionless frequencies and caused smoother stress patterns.

In general, phase angle patterns growed radially with increases in dimensionless frequency. The phase shift values corresponded approximately to the dimensionless frequency ($\omega R/V$) computed with the propagation velocity of the dominant wave type for a given aperture angle. For instance, for τ_{rz}, at aperture angle of 0°, phase angle values were close to ($\omega R/V_S$) since shear waves were the dominant travelling waves in this case. For higher aperture angles there was a minor decrease in phase angle values due to presence of P-waves travelling at velocities higher than that of shear waves. However, the amount of reduction illustrated combined effects of different wave types rather than pure propagation of P-waves. Moreover, worthy of comment were the nearly perfect semi-circle phase patterns associated with some of the stress components (i.e. σ_θ, $\tau_{r\theta}$, *and* $\tau_{\theta z}$). Although the phase values were slightly smaller than $\omega R/V_S$, the constant phase patterns indicated either perfect shear waves as controlling, or a relatively constant combination of different wave types.

Finally in the case of horizontal point load, for the azimuthal angle of 180°, the amplitudes of stress components were the same as that of 0°; however, the phase angles were different by a value of π for σ_r, σ_θ, and σ_z yet the same for τ_{rz}.

6.2.3 Chapter 4: Stress beneath Dynamically Applied Two-Dimensional Vertical and Horizontal Line Loads

In this chapter, similar to Chapter 3, the Buckingham theorem (Buckingham, 1914) was applied to the static and dynamic problems of vertical and horizontal line loads imposed on the surface of a 2-D half-space to determine the number of dimensionless parameters. With regards to

characteristic properties of the systems, the value of dimensionless stress, ($\sigma_{ij}R/P$), within foundation soil underlying a static vertical or horizontal line load at ground surface was found to be a function of aperture angle, and Poisson's ratio, damping ration, and dimensionless frequency. These parameters were investigated through the numerical analyses in ISoBEM. The verification of the solutions was performed by comparing the static stress results to the Flamant's solution (Saad, 2009). There were no dynamic solutions available in the literature against which to compare our results. Verification of normalization was performed similar to the case of point loads in Chapter 3. Upon verification, the final analyses are performed for a large set of parameters including dimensionless frequencies ($\omega R/V_S$) ranging from 0 to 20, Poisson's ratios of 0.34 and 0.45, and soil damping values of 1% and 5%. The solutions are then illustrated in the form of dimensionless stress bulbs for amplitude and phase angles.

For ($\omega R/V_S$) < 1, dynamic effects range from negligible to moderate for both vertical and shear stress components and could probably be ignored. For ($\omega R/V_S$) ≈ 2 to 4, the general shapes of the stress distributions were similar to those for the static case, but the stress amplitudes were increased by about 80%. For ($\omega R/V_S$) > 4, stress patterns deviated substantially from the static case and followed a more complex pattern, due to constructive and destructive interference of the travelling waves.

Increase of Poisson's ratio caused no perceptible change in stress bulb amplitudes or phase angles for aperture angles associated with shear wave propagation However, Poisson's ratio increases produced stress amplitude increases and decreases for aperture angles associated with P-wave and Rayleigh wave propagation, respectively. Our interpretation was that in the high-ν case, the higher bulk moduli of the soil 'attracted' more P-wave propagation (at the

expense of Rayleigh wave energy), thereby modifying stress amplitudes associated with these wave types.

Reduction in stress values was expected as the outcome of soil damping ratio. However, this effect was more obvious for higher dimensionless frequencies. In other words, higher damping ratio values alleviated the dramatic sharpness in dimensionless stress bulbs with high dimensionless frequencies and cause smoother stress patterns.

Although the overall patterns were similar in line and point load problems, the stress bulbs penetrated deeper into the soil mass in line load cases compared to the point load ones. This fact was found to be related to line load problems requiring 2-D wave propagation; hence the dissipation of energy only occurred in the *x*-*y* plane. In the case of a point load (Chapter 3), the wave propagation occurred in 3-l space, leading to more rapid geometric spreading of wave energy.

In general, phase angle patterns growed radially with increases of dimensionless frequency. The phase shift was expected to be roughly equivalent to the dimensionless frequency appropriate to the dominant wave type for the aperture angle under consideration. For instance, for vertical stress component, σ_y, due to a vertical line load, phase angle values were close to ($\omega R/V_S$) at aperture angles of 30°- 60°, whereas higher aperture angles (φ > 60°) produced a minor increase in phase angles due to the dominance of Rayleigh waves. In addition, for the vertical load case the phase bulbs at aperture angles near 0° had a dimple indicating a decrease in phase value, which was found to be due to the predominance of P-waves along the y-axis. For the case of a horizontally oscillating surface load, the shear stress component, τ_{xy}, at aperture angle near 0° were close to ($\omega R/V_S$) due to the dominance of shear waves in this case. For higher aperture angles there was a minor decrease in phase angle values due to the presence of P-waves

travelling at faster velocities. However, the amount of reduction illustrated combined effects of different wave types rather than pure propagation of P-waves.

6.2.4 Chapter 5: Dynamic Stress Distribution due to Distributed Surficial Loads

In this chapter, I began with an overview of available stress solutions for the soil-rigid foundation interface from the literature, most of which was applicable to static loads. I proceeded to present the results of ISoBEM simulations for cyclic loading of rigid foundations. The results were presented in the form of graphs as well as parametric equations for pressures at the soil-rigid foundation interface (these solutions do not apply for stresses at depth within the soil body).

To evaluate within-soil dynamic stresses, the devised interface stresses were recommended to be converted to input surface loads to simulate the effects of vibration of a rigid foundation. Moreover, to facilitate simplified modeling of this problem in Matlab, I demonstrated how the principle of superposition can be applied via integration of the fundamental dynamic stress solutions presented in Chapters 3 and 4 to obtain within-soil dynamic stresses resulting from surficial loads applied at different ground surface locations. The accuracy of these solutions was verified by comparison to stress solutions obtained by direct modeling of distributed loads using ISoBEM.

For the stress solutions due to harmonically applied point or line loads, it is recommended to use the graphical solutions with consideration of examples provided in Chapters 3 and 4.

For the stress solutions due to harmonically applied distributed solutions, it is recommended to either use integration techniques presented in Chapter 5, or to contact authors for the access to Matlab codes. It should be mentioned that the Matlab codes will be eventually

available at UCLA Department of Civil and Engineering website under supervision of Professor Jonathan Stewart and Professor Scott Brandenberg.

6.3 RECOMMENDATIONS FOR THE FUTURE RESEARCH

The following are recommendations for future research:

- Devise procedures for predicting seismic stress demands that account for both SSI and 1-D wave propagation effects with consideration of phase differences between the two stress demands.
- Validation of the proposed procedure against test data such as centrifuge modeling of levee structure resting atop soft organic peat.
- Validation of the proposed procedure against direct simulations in FEM (Esmaeilzadeh et al. (2015) or LS-DYNA) or FDM (FLAC).
- Validation of the proposed procedure against case histories to confirm the calculated dynamic stress demand can predict the triggering of liquefaction in real events.
- Extending the proposed procedure to evaluate the stress distribution at soil-foundation interface of a circular rigid foundation under cyclic horizontal and moment load.
- Extending the proposed procedure to evaluate the within-soil pressure for the rigid foundation problem.
- Study the effects of inhomogeneous soils and soil non-linearity on the proposed procedure.

REFERENCES

Ahlvin, R. G., Ulery, H. H. (1962). Tabulated values for determining the complete pattern of stresses, strains, and deflections beneath a uniform circular load on a homogeneous half space. *Highway Research Board Bulletin*.

Allaby, A., Allaby, M. (Eds.). (2008). *Oxford dictionary of earth sciences*. Oxford: Oxford University Press.

Ashford, S. A., Boulanger, R. W., Donahue, J. L., Stewart, J. P., Kokusho, T., Lee, W., & Yoshimine, M. (2011). Geotechnical quick report on the Kanto Plain region during the March 11, 2011, Off Pacific Coast of Tohoku earthquake, Japan. *Geotechnical Extreme Events Reconnaissance (GEER)*.

Banerjee, P. K., & Wilson, R. B. (1989). Industrial applications of boundary element methods. London and New York, Elsevier Applied Science (Developments in Boundary Element Methods-5), 1989, 309.

Barenblatt, G. I. (1996). Scaling, self-similarity, and intermediate asymptotics: dimensional analysis and intermediate asymptotics (Vol. 14). Cambridge University Press.

Bao, H., Bielak, J., Ghattas, O., Kallivokas, L. F., O'Hallaron, D. R., Shewchuk, J. R., & Xu, J. (1998). Large-scale simulation of elastic wave propagation in heterogeneous media on parallel computers. Computer methods in applied mechanics and engineering, 152(1), 85-102.

Bielak, J., 1976. Modal analysis for building-soil interaction, J. Eng. Mech. 102, 771–786.

Bray, J. D., Stewart, J. P. (principal authors). (2000). Damage patterns and foundation performance in Adapazari. *Earthquake Spectra*, *16*(S1), 163-189.

Bekefi, G., & Barrett, A. H. (1987). Waves in dielectrics. 6.5 in Electromagnetic Vibrations, Waves, and Radiation.

Bolt, B. A., & Bolt, B. A. (1993). Earthquakes and geological discovery. New York: Scientific American Library.

Borowicka, H. (1939). Druckverteilung unter elastischen Platten. Archive of Applied Mechanics, 10(2), 113-125.

Boussinesq, J. (1885). Application des potentiels à l'étude de l'équilibre et du mouvement des solides élastiques: principalement au calcul des déformations et des pressions que produisent, dans ces solides, des efforts quelconques exercés sur une petite partie de leur surface ou de leur intérieur: mémoire suivi de notes étendues sur divers points de physique, mathematique et d'analyse. Gauthier-Villars.

Brown, S. F. (1967). Stresses and deformations in flexible layered pavement systems subjected to dynamic loads (Doctoral dissertation, University of Nottingham).

Buckingham, E. (1914). On physically similar systems; illustrations of the use of dimensional equations. Physical Review, 4(4), 345-376.

Bycroft, G. N. (1965). Forced Vivrations of a rigid circular plate on a semi-infinite elastic space and on an elastic stratum. Philosophical Transactions of the Royal Society of London A: Mathematical, Physical and Engineering Sciences, 248(948), 327-368.

Cagniard, L. (1939). "Réflexion et réfraction des ondes séismiques progressives", *Gauthier-Villars*, Paris

Cerruti, V. (1882). Ricerche intorno all'equilibrio dei corpi elastici isotropi. *Reale Accademia dei Lincei, Roma*, *13*, 1882.

Chao, C.C. (1960). Dynamical response of an elastic half-space to tangential surface loadings, *Journal of Applied Mechanics*, ASME, **27**, 559-567.

Chu, D. B., Stewart, J. P., Lee, S., Tsai, J. S., Lin, P. S., Chu, B. L., ... & Wang, M. C. (2004). Documentation of soil conditions at liquefaction and non-liquefaction sites from 1999 Chi–Chi (Taiwan) earthquake. *Soil Dynamics and Earthquake Engineering*, *24*(9), 647-657.

Cubrinovski, M., Bradley, B., Wotherspoon, L., Green, R., Bray, J., Wood, C., ... & Wells, D. (2011). Geotechnical aspects of the 22 February 2011 Christchurch earthquake.

Dashti, S., Bray, J. D., Pestana, J. M., Riemer, M., & Wilson, D. (2009). Mechanisms of seismically induced settlement of buildings with shallow foundations on liquefiable soil. *Journal of geotechnical and geoenvironmental engineering*.

Davis, R. O., Selvadurai, A. P. S. (1996). Elasticity and Geomechanics.

De Hoop, A.T. (1960). "A modification of Cagniard's method for solving seismic pulse problems", *Applied Science Research*, Section B, **8**, 349-356.

Douglas, A., Hudson, J. A., & Blamey, C. (1972). A quantitative evaluation of seismic signals at teleseismic distances—III Computed P and Rayleigh wave seismograms. Geophysical Journal International, 28(4), 385-410

Ellison, K.C., Masroor, A.M. Almufti, I., Willford, M, O'Riordan, N (2015). Structure-Soil-Structure Interaction Analysis in a Highly Seismic, Dense Urban Regeneration Zone, presented

at 6th International Conference on Earthquake Geotechnical Engineering, New Zealand, 2015. Christchurch, NZ.

Eringen, A. C., Suhubi, E.S. (1975). *Elastodynamics*, Academic Press, Volume II (Linear Theory).

Esmaeilzadeh Seylabi, E., Jeong, C., Taciroglu, E. (2015). On numerical computation of impedance functions for rigid soil-structure interfaces embedded in heterogeneous half-spaces, Computers and Geotechnics, 10.1016/j.compgeo.2015.11.001

Favata, A. (2012). On the Kelvin problem. *Journal of Elasticity*, *109*(2), 189-204.

Ghiglia, D. C., & Pritt, M. D. (1998). *Two-dimensional phase unwrapping: theory, algorithms, and software* (Vol. 4). New York:: Wiley.

Graff, K. F. (1975). *Wave motion in elastic solids*. Courier Dover Publications.

Hardy, M. S. A., Cebon, D. (1994). Importance of speed and frequency in flexible pavement response. *Journal of engineering mechanics*, *120*(3), 463-482.

Hashash, Y.M.A., Musgrove, M.I., Harmon, J.A., Groholski, D.R., Phillips, C.A., and Park, D. (2015) "DEEPSOIL 6.1, User Manual".

Heidarzadeh, B., Mylonakis, G. Stewart, J.P, (2015). Stresses Beneath Dynamically Applied Vertical Point Loads, presented at 6th International Conference on Earthquake Geotechnical Engineering, New Zealand, 2015. Christchurch, NZ.

Hughes, T. J. (2012). The finite element method: linear static and dynamic finite element analysis. Courier Dover Publications.

ISoBEM: *Boundary Element Method Package*. http://bemsands.com, 2012.

Jennings, P. C., & Bielak, J. (1973). Dynamics of building-soil interaction.Bulletin of the Seismological Society of America, 63(1), 9-48.

Kausel, E. (2012). Lamb's problem at its simplest. Proceedings of the Royal Society A: Mathematical, Physical and Engineering Science, 469(2149).

Kausel, E. (2006). Fundamental solutions in elastodynamics: a compendium. Cambridge University Press.

Kelvin, L. (1848). Note on the integration of the equations of equilibrium of an elastic solid. Cambridge and Dublin Mathematical Journal, 3, 87-89.

Lamb, H. (1904). On the propagation of tremors over the surface of an elastic solid. Philosophical Transactions of the Royal Society of London. Series A, Containing Papers of a Mathematical or Physical Character, 1-42.

Miller, G. F., & Pursey, H. (1954). The field and radiation impedance of mechanical radiators on the free surface of a semi-infinite isotropic solid.Proceedings of the Royal Society of London. Series A. Mathematical and Physical Sciences, 223(1155), 521-541.

Mooney, H.M. (1974). Some numerical solutions for Lamb's problem, *Bulletin of the Seismological Society of America*, **64** (2), 473-491.

Mottershead, J. E. (Ed.). (2013). Modern Practice in Stress and Vibration Analysis: Proceedings of the Conference Held at the University of Liverpool, 3–5 April 1989. Elsevier.

Muskhelishvili, N. I. (1966). Some basic problems of the mathematical theory of elasticity. Nauka, Moscow, 1(966), 2.

Nikolaou, S., & Go, J. (2009). Site-Specific Seismic Studies for Optimal Structural Design: Part II–Applications. Structure magazine, 2009-12.

NIST (2012). Soil-structure interaction for building structures, *Report No. NIST GCR 12-917-21*, National Institute of Standards and Technology, U.S. Department of Commerce, Washington D.C. Project Technical Committee: Stewart, JP (Chair), CB Crouse, T Hutchinson, B Lizundia, F Naeim, and F Ostadan.

Oudry, J., Roth, S., Lebaal, N., Chamoret, D., & Shakourzadeh, H. (2012). Mesh density and mesh orientation dependence of FE model submitted to low–frequency vibration. International Journal of Computer Applications in Technology, 43(2), 101-109.

Pekeris, C.L. (1955). The seismic surface pulse, Proceedings of the National Academy of Sciences of the United States of America, **41** (7), 469-480.

Peng, Y., Zhou, D. (2013). Modelling of cutting force on a viscoelastic body for surgical simulation. In *Proceedings of the 2013 Grand Challenges on Modeling and Simulation Conference* (p. 14). Society for Modeling & Simulation International.

Peng, Y., Zhou, D. (2012). Stress Distributions Due to a Concentrated Force on Viscoelastic Half-Space. *Journal of Computation & Modeling*, *2*(3).

Pekeris, C.L. (1955). The seismic surface pulse, Proceedings of the National Academy of Sciences of the United States of America, **41** (7), 469-480.

Poulos, H. G., Davis, E. H. (1974). Elastic Solutions for Soil and Rock Mechanics, John Wiley.

Richards, P.G. (1979). Elementary solutions to Lamb's problem for a point source and their relevance to three-dimensional studies of spontaneous crack propagation, *Bulletin of the Seismological Society of America*, **69** (4), 947-956.

Roach, G. F. (1982). Green's functions. AMC, 10, 12.

Sadd, M. H. (2009). Elasticity: theory, applications, and numerics. Academic Press.

Schepers, W., Savidis, S., Kausel, E. (2010). Dynamic stresses in an elastic half-space. *Soil Dynamics and Earthquake Engineering*, *30*(9), 833-843.

Schiffman, R. L., & Aggarwala, D. B. (1961, July). Stresses and displacements produced in a semi-infinite elastic solid by a rigid elliptical footing. InProceedings of the 5th international conference on soil mechanics and foundation engineering (Vol. 1, pp. 795-801).

Shafiee, A., Stewart, J. P., & Brandenberg, S. J. (2015). Reset of Secondary Compression Clock for Peat by Cyclic Straining. Journal of Geotechnical and Geoenvironmental Engineering, 141(3), 02815001.

Stokes, G.G.(1849).On the dynamical theory of diffraction. Transactions ofthe Cambridge PhilosophicalSociety, 9, 1–62.

Su, K., Sun, L., Hachiya, Y., & Maekawa, R. (2008). Analysis of shear stress in asphalt pavements under actual measured tire-pavement contact pressure.*Proceedings of the 6th ICPT, Sapporo, Japan*, 11-18.

Sung, Tse Yung. Vibrations in semi-infinite solids due to periodic surface loading. Diss. Harvard University, 1953.

Talybly, L. K. (2010). Boussinesq's viscoelastic problem on normal concentrated force on a half-space surface. *Mechanics of Time-Dependent Materials*, *14*(3), 253-259.

Veletsos, A. S., & Meek, J. W. (1974). Dynamic behaviour of building-foundation systems. Earthquake Engineering & Structural Dynamics, 3(2), 121-138.

Veletsos, A. S., & Nair, V. V. (1975). Seismic interaction of structures on hysteretic foundations. Journal of the Structural Division, 101(1), 109-129.

Weisstein, Eric W. (2007) "Cylindrical Coordinates." From MathWorld—A Wolfram Web Resource. http://mathworld.wolfram.com/CylindricalCoordinates.html

Wolf, J. P., & Deeks, A. J. (2004). Foundation vibration analysis: A strength of materials approach. Butterworth-Heinemann.

Wolf, J. P. (1994). Foundation vibration analysis using simple physical models. Pearson Education.

Woods, R. D. (1968). Screening of surface waves in soils. *Am Soc Civil Engr J Soil Mech.*